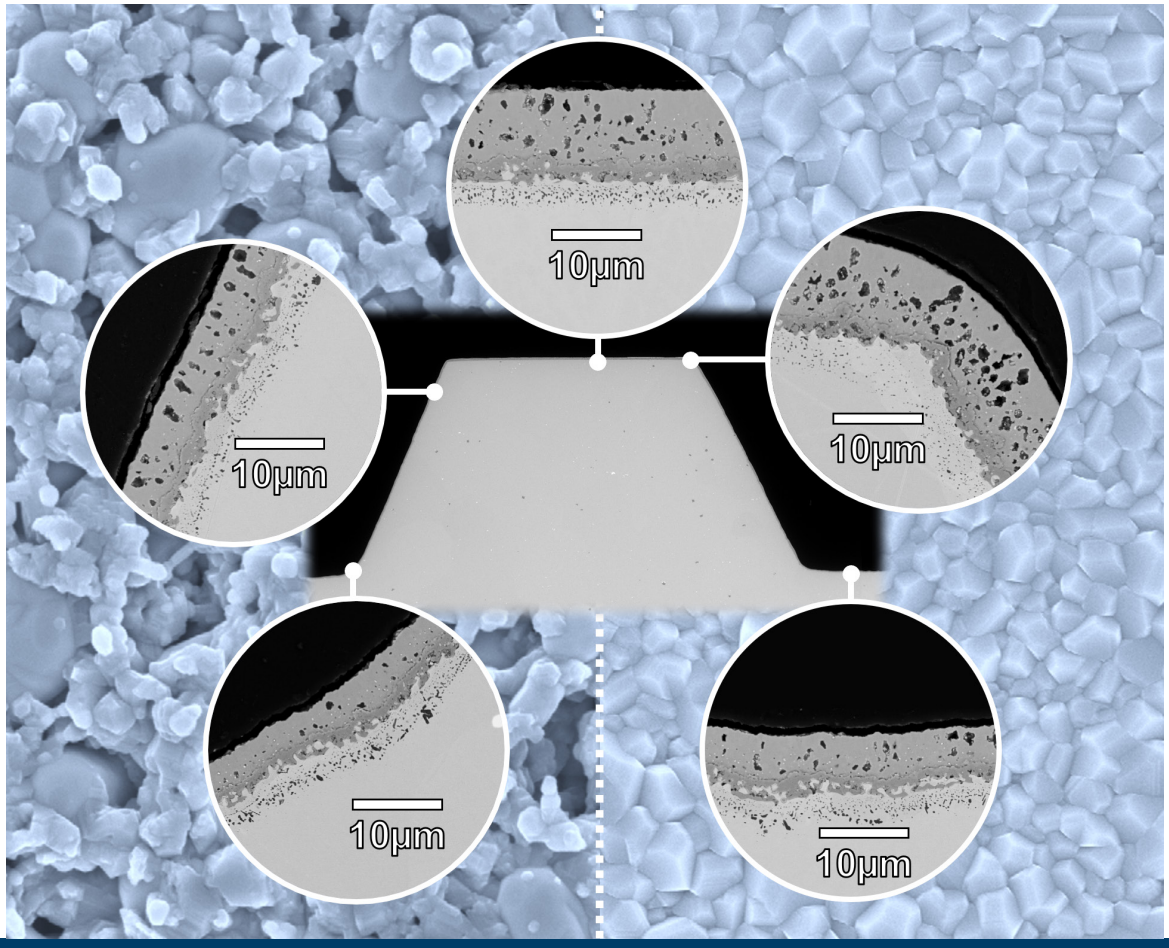

Cost-reduced and Sustainable Interconnects and their Coatings for Solid Oxide Cells

Martin Hilger

Energie & Umwelt / Energy & Environment
Band / Volume 732
ISBN 978-3-95806-989-3

Mitglied der Helmholtz-Gemeinschaft

JÜLICH
Forschungszentrum

Schriften des Forschungszentrums Jülich
Reihe Energie & Umwelt / Energy & Environment Band / Volume 732

Forschungszentrum Jülich GmbH
Institute of Energy Materials and Devices (IMD)
Werkstoffsynthese und Herstellungsverfahren (IMD-2)

Cost-reduced and Sustainable Interconnects and their Coatings for Solid Oxide Cells

Martin Hilger

Schriften des Forschungszentrums Jülich
Reihe Energie & Umwelt / Energy & Environment Band / Volume 732

ISSN 1866-1793 ISBN 978-3-95806-989-3

Bibliografische Information der Deutschen Nationalbibliothek.
Die Deutsche Nationalbibliothek verzeichnet diese Publikation in der
Deutschen Nationalbibliografie; detaillierte Bibliografische Daten
sind im Internet über http://dnb.d-nb.de abrufbar.

Herausgeber und Vertrieb:	Forschungszentrum Jülich GmbH Zentralbibliothek, Verlag 52425 Jülich Tel.: +49 2461 61-5368 Fax: +49 2461 61-6103 zb-publikation@fz-juelich.de www.fz-juelich.de/zb
Umschlaggestaltung:	Grafische Medien, Forschungszentrum Jülich GmbH
Druck:	Grafische Medien, Forschungszentrum Jülich GmbH
Copyright:	Forschungszentrum Jülich 2026

Schriften des Forschungszentrums Jülich
Reihe Energie & Umwelt / Energy & Environment, Band / Volume 732

D 82 (Diss. RWTH Aachen University, 2026)

ISSN 1866-1793
ISBN 978-3-95806-988-6 (Print)
ISBN 978-3-95806-989-3 (E-Book)

Vollständig frei verfügbar über das Publikationsportal des Forschungszentrums Jülich (JuSER)
unter www.fz-juelich.de/zb/openaccess.

Abstract

Transitioning towards greenhouse-gas-neutral energy systems and economies relies critically on renewable energy technologies. Hydrogen is indispensable both as an energy carrier and as a chemical reactant, and water electrolysis powered by renewable sources is a key pathway. Due to their high efficiency, solid oxide cells (SOCs) are a particularly attractive technology. At the same time, the high operating temperatures restrict material choices and impose severe impact on components. Together with the still limited competitiveness compared with other electrolyzer technologies, this is a central reason why large-scale industrial deployment was not achieved yet. Steel components play a major role in this context, especially the interconnect, which accounts for a substantial share of material use and cost.

Within the EU-funded project NOUVEAU, this work targeted the development of interconnect concepts towards lower costs and improved sustainability. The focus was on both the interconnect steel and the required protective coatings. Beyond mitigating steel oxidation, suppressing the release of volatile Cr(VI) species is essential, as these cause severe degradation of the air electrode (Cr poisoning). Based on the state of the art and the reference system established in Jülich, three strategies were pursued: (i) enabling thin-sheet interconnect designs by employing non-destructive coating methods, (ii) reducing coating thickness while maintaining protectivity, and (iii) using lower-cost and more environmentally friendly materials, including conventional steels and Co-free coating compositions.

These goals were addressed on the process side through the development and comparison of coating technologies and on the materials side through the evaluation of alternative steels and spinel compositions. The benchmark was the established Jülich system, a $MnCo_{1.9}Fe_{0.1}O_4$ (MCF) spinel coating applied by atmospheric plasma spraying (APS) on Crofer22APU or Crofer22H. In parallel, the established suspension-based wet powder spraying (WPS) route was continued. As a further scalable and resource-efficient alternative, electrophoretic deposition (EPD) was involved, developed, and systematically benchmarked against APS and WPS. EPD process development started from the reference combination and was subsequently transferred to the conventional ferritic steel AISI430 and to the Co-free spinel $CuMn_{1.8}Ni_{0.2}O_4$ (CMN).

To obtain continuous layers with dense or closed-porous microstructures, single-step and two-step heat-treatment routes were investigated, with the first step of the two-step schedules conducted in a reducing atmosphere. The aim was to integrate the final oxidizing step into stack joining and thereby embed the process chain into established manufacturing flows. Application-related boundary conditions were addressed, including coating of flow-field geometries, compatibility with adjacent glass sealants, and maintaining protective functionality across the process chain and subsequent SOC operation.

Performance was evaluated through qualitative and quantitative investigations of chromium evaporation, corrosion behavior, and electrical properties. Two exposure studies (up to 500 h and 3000 h) enabled comparisons between EPD, WPS, and APS. Under the investigated conditions at 800°C, the Co-free CMN variant exhibited markedly lower protectivity than MCF. For AISI430, the formation of a continuous, insulating SiO_2 layer at the steel surface proved to be a key limitation, resulting in substantially poorer electrical performance than for Crofer steels. In contrast, two-step treated MCF-EPD coatings showed exceptional protection and integrity and were competitive with the literature. WPS provided a similar protective effect and, together with EPD, outperformed the APS reference. For uniform coating of real gas-distributor geometries, EPD proved particularly suitable, as the line-of-sight limitation of APS – and to some extent WPS – was significantly reduced. The optimized MCF-EPD coatings were also transferred to stack components, and basic SOFC stack functionality was demonstrated by i/V characteristics.

For a robust technology selection, the technical assessment was complemented by an ecological perspective. APS, WPS, and EPD were compared along their process chains up to an application-ready coated component using life cycle assessment. Suspension-based routes showed clear advantages over APS, including reduced greenhouse-gas emissions and acidification potential. The strongest effect was observed for EPD, which reduced minerals and metals consumption by about a factor of 40 compared with APS in the considered scenario. This is primarily driven by much lower coating thicknesses and enhanced material efficiency during deposition.

Overall, this work demonstrates that the interconnect, as a major cost driver for SOCs, can be addressed effectively through combined process- and materials-based strategies. Suspension-based coating technologies were identified as both technically effective and environmentally favorable, with EPD emerging as a particularly promising option. At the same time, key limitations of Co-free spinels and conventional steels under the investigated conditions were identified, and directions for further development were outlined.

Kurzfassung

Auf dem Weg hin zu einem treibhausgasneutralen Energie- und Wirtschaftssystem spielt der Umstieg auf erneuerbare Energietechnologien eine zentrale Rolle. Wasserstoff ist dabei sowohl als Energieträger als auch als chemischer Reaktant unerlässlich. Ein Schlüsselpfad ist die Elektrolyse von Wasser unter Nutzung regenerativer Energiequellen. Aufgrund ihrer hohen Effizienz stellen Festoxidzellen (Solid oxide cells, SOCs) eine besonders attraktive Technologie dar. Gleichzeitig begrenzen hohe Betriebstemperaturen die Werkstoffauswahl und belasten Komponenten stark. Zusammen mit der bislang gegenüber anderen Elektrolyseurtechnologien eingeschränkten Wettbewerbsfähigkeit ist dies ein zentraler Grund für die noch ausbleibende großindustrielle Umsetzung. Eine wesentliche Rolle spielen dabei die Stahlkomponenten, insbesondere der Interkonnektor, die einen Hauptanteil am Materialeinsatz und an den Kosten trägt.

Die vorliegende Arbeit setzte im Rahmen des EU-finanzierten NOUVEAU-Projekts an dieser Stelle an und zielte darauf ab, Interkonnektoren in Richtung geringerer Kosten und gesteigerter Nachhaltigkeit weiterzuentwickeln. Im Fokus standen sowohl der Interkonnektor-Stahl als auch die erforderlichen Schutzschichten. Neben der Verringerung der Stahloxidation ist insbesondere die Rückhaltung volatiler Cr(VI)-Spezies relevant, da diese luftseitig zu einer erheblichen Degradation der Elektrode führen (Cr-Vergiftung). Ausgehend vom Stand der Technik und der in Jülich etablierten Referenz wurden drei Strategien verfolgt: (i) die Ermöglichung dünnwandiger Interkonnektor-Designs durch schonende Beschichtungsverfahren, (ii) die Verringerung der Schutzschichtdicke bei equivalenter Schutzwirkung und (iii) die Nutzung preisgünstiger und umweltfreundlicher Materialien, darunter konventionelle Stähle und Co-freie Beschichtungswerkstoffe.

Die Arbeit adressierte diese Ziele prozessseitig durch die Entwicklung und den Vergleich geeigneter Beschichtungsverfahren und materialseitig durch die Untersuchung alternativer Stähle und Spinell-Zusammensetzungen. Als Benchmark diente das in Jülich etablierte System einer Beschichtung des Spinells $MnCo_{1.9}Fe_{0.1}O_4$ (MCF), aufgebracht mittels atmosphärischem Plasmaspritzen (APS) auf Crofer22APU bzw. Crofer22H. Ergänzend wurde das bereits etablierte suspensionsbasierte Nasspulverspritzen (Wet powder spraying, WPS) weitergeführt. Als weitere skalierbare und ressourcenschonende Alternative wurde die elektrophoretische Abscheidung (Electrophoretic deposition, EPD) einbezogen, entwickelt und systematisch gegen APS und WPS abgeglichen. Die EPD-Prozessentwicklung erfolgte zunächst auf Basis der Referenzkombination und wurde anschließend auf den konventionellen ferritischen Stahl AISI430 sowie auf den Co-freien Spinell $CuMn_{1.8}Ni_{0.2}O_4$ (CMN) übertragen.

Zur Einstellung kontinuierlicher Schichten mit dichten beziehungsweise geschlossenporösen Mikrostrukturen wurden ein- und zweistufige Wärmebehandlungsrouten untersucht, wobei bei den zweistufigen Programmen der erste Schritt in

reduzierender Atmosphäre durchgeführt wurde. Ziel war es, den finalen oxidierenden Schritt in die Stack-Fügung zu integrieren und die Prozessführung dadurch in bestehende Fertigungsketten einbetten zu können. Dabei wurden auch Randbedingungen für die Anwendung adressiert, darunter die Beschichtung von Gasverteilerstrukturen, die Kompatibilität zu angrenzenden Glaslotdichtungen sowie die Aufrechterhaltung der Schutzwirkung über die Prozesskette und den anschließenden SOC-Betrieb.

Die Bewertung erfolgte über qualitative und quantitative Untersuchungen zu Cr-Verdampfung, Korrosionsverhalten und elektrischen Eigenschaften. Zwei Auslagerungsstudien (bis 500 h bzw. 3000 h) ermöglichten den Vergleich von EPD mit WPS und APS. Dabei zeigte sich, dass die Co-freie CMN-Variante unter den betrachteten Bedingungen bei 800°C eine deutlich geringere Schutzwirkung als MCF aufweist. Für AISI430 erwies sich die Ausbildung einer kontinuierlichen, isolierenden SiO_2-Schicht an der Stahloberfläche als wesentliche Einschränkung, die zu einer deutlich schlechteren elektrischen Leistung gegenüber Crofer-Stählen führt. Demgegenüber zeigten insbesondere zweistufig behandelte MCF-EPD-Beschichtungen sehr gute Schutz- und Integritätseigenschaften und schnitten im Literaturvergleich wettbewerbsfähig ab. WPS zeigte eine ähnliche Schutzwirkung und setzte sich gemeinsam mit EPD von der APS-Referenz ab. In der gleichmäßigen Beschichtung realer Gasverteilergeometrien wurde EPD als besonders geeignet herausgestellt, da der line-of-sight-Effekt von APS und in Teilen auch von WPS deutlich reduziert ist. Die optimierten MCF-EPD-Beschichtungen wurden zudem auf Stack-Komponenten übertragen. Die grundlegende Funktionsfähigkeit eines SOFC-Stack-Laufs wurde anhand von i/V-Kennlinien demonstriert.

Für eine belastbare Technologieauswahl wurde die rein technische Perspektive um eine ökologische Bewertung ergänzt. APS, WPS und EPD wurden entlang ihrer Prozessketten bis zur einsatzbereiten beschichteten Komponente in einer Lebenszyklusanalyse verglichen. Dabei ergab sich ein klarer Vorteil der suspensionsbasierten Verfahren gegenüber APS, unter anderem hinsichtlich Treibhausgasemissionen und Versauerungspotenzial. Besonders deutlich war der Effekt für EPD, das im betrachteten Szenario den Verbrauch metallischer und mineralischer Rohstoffe gegenüber APS um etwa den Faktor 40 reduzierte. Ausschlaggebend dafür sind deutlich geringere Schichtdicken und eine hohe Materialeffizienz in der Abscheidung.

Insgesamt konnte die Arbeit zeigen, dass sich die Interkonnektor-Komponente als wesentlicher SOC-Kostentreiber durch kombinierte prozess- und materialseitige Strategien gezielt adressieren lässt. Suspensionsbasierte Beschichtungsverfahren wurden als technisch effektiv und ökologisch vorteilhaft herausgearbeitet, wobei EPD als besonders vielversprechende Option hervorsticht. Gleichzeitig wurden unter den betrachteten Bedingungen zentrale Schwachstellen Co-freier Spinelle und konventioneller Stähle identifiziert und Ansatzpunkte für die weitere Entwicklung aufgezeigt.

Table of Contents

Already published Parts of this Work

(1) Hilger, M., et al., *Towards sustainable interconnects for solid oxide cells: An integrated technical and environmental evaluation of coating methods.* Journal of Power Sources, 2025. 659; 238471.

(2) Hilger, M., et al., *Electrophoretic Deposition of Protective Spinel Coatings for Solid Oxide Cell Interconnects – Towards Stack Integration*. Journal of the Electrochemical Society, 2026. 173; 034509.

Conference Contributions

Hilger, M., et al., *Electrophoretic Deposition of Protective Coatings for Cost-reduced Solid Oxide Cell Interconnects.* Poster presented at the second Jülich-Twente summit, Enschede, Netherlands, November 13th and 14th, 2023.

Hilger, M., et al., *Electrophoretic Deposition of Protective Coatings for Cost-reduced Solid Oxide Cell Interconnects.* Oral presentation at the 99th annual conference of the German Ceramic Society (DKG99), Höhr-Grenzhausen, Germany, September 8th – 11th, 2024.

Hilger, M., et al., *Electrophoretic Deposition of Protective Coatings for Solid Oxide Cell Interconnects.* Oral presentation at the third Jülich-Twente summit, Jülich, Germany, March 26th and 27th, 2025.

Hilger, M., et al., *Functional Ceramic Coatings for Solid Oxide Cell Interconnects via Electrophoretic Deposition.* Oral presentation at the 19th Solid Oxide Fuel Cell world conference (SOFC-XIX), Stockholm, Sweden, July 13th – 18th, 2025.

Portions of this thesis are based on material, previously published in the above listed peer-reviewed, open-access journal articles, of which the author is the first author. Data, figures and text from these publications have been partially or fully incorporated throughout the thesis, in some cases either re-organized, condensed, or modified with supplementary content.

The contributions of the two already published peer-review publications (1/2) are reflected in the core sections 2–4. Thereby, the contents related to the comparison of the involved coating technologies are mainly derived from paper (1), considering both the theoretical background and the methodology as well as the results and discussion section. Paper (2) was fundamental for the contents related to the closer comparison of the EPD coatings, including various characterization techniques and the related background.

As both publications are available open-access and the author retains copyright, a formal reprint permission remains not required. This declaration is made in the interest of enhancing transparency.

1. Introduction

The anthropogenic climate crisis already poses one of the most profound ecological catastrophes of global extend, which in its destructive impact on civil order aggravates ongoingly. While, due to the extensive combustion of fossil energy carriers, the concentration of the major contributing greenhouse gas (GHG) CO_2 up to 2025, compared to pre-industrial age, increased from 280 ppm to more than 420 ppm, the past three years showed as the three hottest since records began.[1,2] The continuously progressing heat-up thereby inevitably requires adaptation to the direct consequences, i.e., rising sea level, extreme weather events, increasing in frequency and strength, and thus, necessarily associated migration movement.[3]

To preserve the chance of stabilizing the global climate system, and by this avoiding uncontrolled aggravation of the underlying dynamics, drastic reduction towards net-zero of GHG emissions is necessary. Especially industrialized nations in the Global North, as those of the European Union (EU), and specifically Germany, bare pronounced responsibility. On the one hand they are least affected of climate crisis (in contrast to countries in the Global South), while on the other hand, however, they are the dominating contributors considering historically cumulative emissions.[4] This creates a responsibility, which is reflected in the Paris Agreement from the 21st Conference of Parties to the United Nations Framework Convention on Climate Change in 2015, which derives in an earlier arrival at net-zero emissions and transactions in less-emitting nations.[5]

In times of national isolationism and a globally manifesting authoritarian and fossil back-lash, an additional responsibility evolves for the EU in drawing a counter-project. And even though political trends might not be directed fully opposite, the core measures to tackle the climate crisis even bring vast potential for local economies and geo-political independence. On the track towards net-zero, a central pillar is built by decarbonizing energy systems by the expanded use of renewable sources. By further replacing fossil energy carriers as coal, oil and gas, energy-related emissions, currently adding up to 83% of the German national GHG emissions[6], not only a major lever in terms of reducing emissions can be activated. Shifting towards power generation from wind, water and solar, can also enhance European, national, or even municipal energy autonomy.[7]

The volatile nature of renewable sources on the one hand, and specific requirements in distinct sectors, as chemical or metallurgical industry, as well as transport or mobility, on the other hand create a necessity for the conversion of energy and its temporary storage in a non-electrical form ("Power-to-X"). Here, transfer into chemical energy is crucial, as it applies to batteries. However, also hydrogen plays a pivotal role as chemical energy carrier, which – produced via water electrolysis, using renewable energy (then labelled *green*) and converted back to electric power when required – can serve as buffer. More importantly,

green hydrogen is essential for specific sectors, as those stated above, to be decarbonized at all.[8]

While hydrogen consumption grows continuously and currently the major fraction results from fossil sources, not more than 1% is considered green, stressing the need for cost-effective, large-scale electrolyzers.[9] Within the portfolio of relevant technologies – which can co-exist and offer specific benefits each – solid oxide cells (SOCs) are of special interest due to exceptionally high efficiencies, especially when applied in power-heat-coupling systems.[10] Though, according to the pending scale to industrial use, and closely connected, their lack in competitiveness to several other green hydrogen technologies, SOCs yet see a substantial challenge to exploit their potential.

In SOC technology, a set of structural components around the interconnect, manufactured from steel, present a key hurdle. In contrast to the remaining, name-giving oxide ceramic components, this shows up considering both costs, but also resource consumption. With a share of up to 82 and 94% in the overall cost and resource use, respectively, (within the operation-relevant unit, and depending on the specific design), the interconnect however represents an impactful lever as well.[11] Moreover, this group of components is associated with key degradation phenomena within the SOC, necessitating the use of protective coatings. This motivates considering these components with respect to durability and thereby overall sustainability, in addition to economical and resource efficiency.[12]

Employing several strategies, this aspect should be tackled by the present work, which was conducted within the Horizon Europe-funded project NOUVEAU (Novel Electrode Coatings and Interconnect) under the grant agreement N°101058784. The work proceeded in close collaboration with two doctoral research works, those of D. Vakhrameev (Forschungszentrum Jülich, IMD-1) and K. El Jardali (IMDEA Energy, Mostoles, Spain), conducted within the framework of NOUVEAU in parallel. These works were focusing in-depth on the degradation behavior of the steels and the protectivity of coatings, developed here, and on a comprehensive evaluation of environmental impacts, associated with the processes, relevant in NOUVEAU, as well as specifically in the present thesis, respectively.

This work will first introduce into SOC technology and outline the role of the interconnect as a central component, as well as the associated problems to tackle. Following up, the pursued strategies are worked out, and the required theoretical groundwork is provided. The next section presents the investigated material systems, experimental methodologies, and characterization techniques. Subsequently, the obtained findings are presented and discussed. To conclude, key insights are summarized, limitations are estimated, and an outlook on the implementability of the developments is presented.

2. Theoretical Background

This chapter sets out the fundamentals required for the developments in this work. It first sketches the SOC technology and positions the focal component – the interconnect – together with associated questions, governing mechanisms, and technological approaches. It then points to avenues for a more cost-effective and sustainable design.

2.1. Solid Oxide Cells (SOCs)

Solid oxide cells are one of several complementary technologies for hydrogen production and power generation. While each class has its own operating specifics and application space, fuel cells and electrolyzers in general share the same core idea: interconverting chemical and electrical energy in opposite directions. Water is split into H_2 and O_2 under an applied voltage in the electrolyzer, and the reverse reaction proceeds electrochemically in the fuel cell to form water with a potential drop. The half-reactions occur at the electrodes, which are separated by an ion-conducting, electronically insulating electrolyte.

Fuel-cell families are typically distinguished by the ionic charge carrier in the electrolyte, usable process gases, and operating temperature. The major classes are alkaline fuel cells (AFCs), proton exchange membrane fuel cells (PEM-FCs), molten carbonate fuel cells (MCFCs), and solid oxide fuel cells (SOFCs). A schematic comparison is shown in Figure 1.

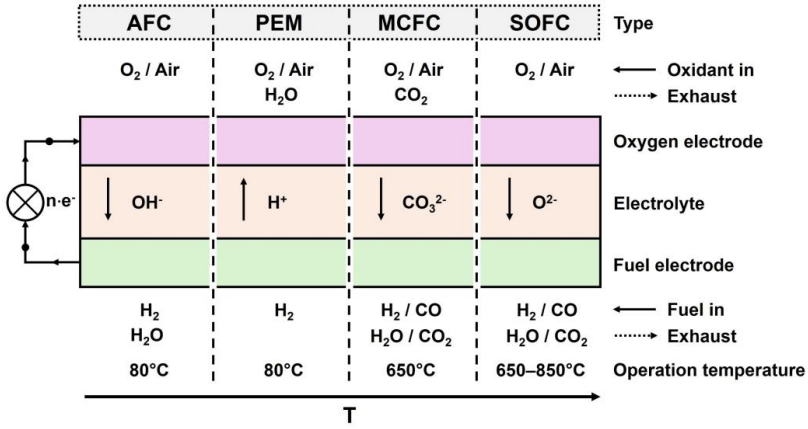

Figure 1: Schematic of the four main fuel cell technologies and their operational specifications, including charge carriers, fuels/oxidants and operating temperature. Own graphic derived from[13].

A similar comparison applies to electrolysis cells (without a molten-carbonate-based technology, whereas anion exchange membranes (AEM) emerge as an additional relevant candidate). Most technologies require design choices specific to the operating mode. SOCs however stand out as both modes can be realized on the same device – reversible SOCs

(rSOCs) – which aligns well with energy systems driven by renewable sources. Their high operating temperatures enable internal reforming and thus a broad portfolio of fuels, including hydrocarbons (C_xH_y). In SOEC operation, next to CO_2 electrolysis, synthesis gas (H_2 + CO) can also be produced, which is widely utilized in chemical industry.[10]

High temperatures are demanding for durability and material cost, yet they also unlock enhanced efficiency through accelerated electrochemistry and combined heat-and-power integration. SOFCs can provide valuable waste heat in residential systems, and SOECs can couple to hot off-gas streams in industrial settings such as steel production.[14]

Realizing these benefits requires a clear view of operating principles, the roles of components on the cell- and a higher level, materials and manufacturing routes, and the failure mechanisms that emerge. This section aims to build that foundation.

2.1.1. Operating principle of SOCs

As fuel cells and electrolyzers in principle, SOCs split the overall electrochemical conversion into two half-reactions while blocking electron transport through the electrolyte, which establishes a potential difference. In fuel-cell mode the reaction proceeds spontaneously and generates a current. In electrolysis mode external work drives the reaction in reverse. Water is produced as steam in the SOFC and split into H_2 and O_2 in the SOEC. Owing to the close analogy, SOFC is used here for illustration. The global reaction, including the released Gibbs free energy ΔG_0, (Eq. 2.1) and the half-reactions (Eqs. 2.2 and 2.3) at the electrodes can be defined as the following:

$$H_2 + \frac{1}{2} O_2 \rightarrow H_2O\,(g)\,;\, \Delta G_0 = -237.09\ \mathrm{kJ \cdot mol^{-1}} \tag{2.1}$$

$$\text{Fuel electrode (anode): } H_2 + O^{2-} \rightarrow H_2O + 2\,e^- \tag{2.2}$$

$$\text{Air electrode (cathode): } \frac{1}{2} O_2 + 2\,e^- \rightarrow O^{2-} \tag{2.3}$$

Oxidation occurs at the fuel electrode (here anode, Eq. 2.2), reduction at the air electrode (here cathode, Eq. 2.3). In electrolysis mode directions and electrode polarity are reversed. In both SOFC and SOEC, ionic charge transport inside the cell is carried by oxygen ions in the electrolyte, and overall charge balance is maintained by an external electronic circuit. A schematic of SOFC and SOEC operation with labelled components and gas streams is shown in Figure 2.

Next to classical oxygen-ion conducting cells, proton-conducting cells (PCCs) are a parallel line of development with lower technology readiness but attractive features, including lower operating temperatures and direct, dry hydrogen production at the hydrogen electrode.[15] As this work however focuses on oxygen-ion conducting SOCs, detailed mechanisms and materials of PCCs are not treated. Several aspects of SOC operation nevertheless translate, while the atmospheric changes and cooler operation lead to slightly different system-level constraints with implications for structural components.

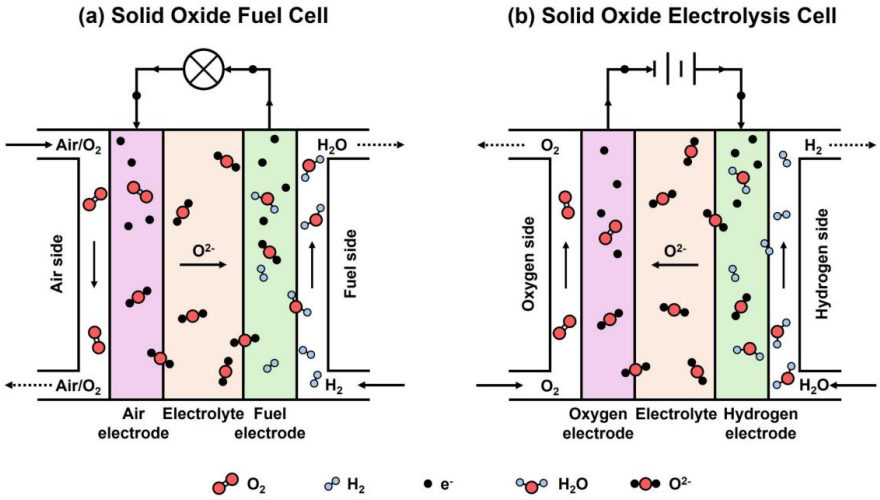

Figure 2: Schematic of an SOFC (a) and SOEC (b) functional cell unit and its reactant flows; layer thicknesses not proportional. Own illustration.

To implement the functional principle of SOCs in practice, the cells are realized in various layer configurations, material sets, and geometries for efficient integration at a higher level. The next sections survey the most relevant configurations, material solutions, and the specific developments considered in this work.

2.1.2. SOC configurations, cell types and materials

As the name implies, all functional layers in solid oxide cells are based on oxide ceramics. Each layer serves a distinct role, which translates into specific requirements for material selection and microstructure. Layer compounds are typically built on a mechanically supporting substrate, and the chosen support usually classifies the cell type (e.g., electrode-supported or electrolyte-supported; cf. later, Figure 3). The overall design is anchored by the electrolyte. Its strict requirement profile – high ionic conductivity, electronic insulation, and long-term stability under oxidizing and reducing conditions – is met by only a few materials. Consequently, the electrodes and their compositions are arranged and selected with the electrolyte at the center of the design space.

Beyond chemical and structural stability during long-term exposure, adjacent functional layers must be chemically and thermo-mechanically compatible with the electrolyte, in particular with a well-matching coefficient of thermal expansion (CTE). At the same time, electron and oxygen-ion transport, together with gas permeation in the porous electrodes, must be maintained. Table 1 provides an overview of requirements for each functional layer, along with common material choices and relevant specifications.

Table 1: Functional layers, their requirements, established candidate materials and their specifications for SOCs.[16,17]

Layer	Requirements	Materials	Specifications
Electrolyte	Oxygen ion conducting, electrically insulating, gas-tight, mechanically and chemically stable in oxidizing and reducing atmospheres	YSZ GDC	YSZ as best compromise candidate for T > 700°C GDC electrically conducting at high T and reducing atmospheres, better ionic conduction than YSZ for T < 700°C
Fuel electrode	Transporting fuel/open-porous, oxygen-ion and electron conducting, catalytic activity	Ni-YSZ Ni-GDC	Cermets of percolating metal (Ni) and fluorite (YSZ/GDC) phase and pore network, Ni-YSZ is most established
Air electrode	Transporting oxidant/ open-porous, oxygen-ion and electron conducting, catalytic activity	LSM LSC(F)	Mixed ionic-electronic conducting (MIEC) perovskites, pore network, LSM earlier solution, LSC(F) better at lower T
Air-side contacting	Transporting oxidant, stabilizing electrical connection, levelling out height differences	LSM LSC(F)	Chemical compatibility with air electrode, larger pore sizes for oxidant distribution, large thickness for height buffering
Barrier layer	Hindering interaction of electrolyte and air electrode, gas-tight, oxygen-ion conducting	GDC	Blocks Sr and Co diffusion and prevents secondary phase formation at electrolyte

*__YSZ:__ Yttria-stabilized zirconia (3 mol% Y_2O_3 for partially stabilized (3YSZ) or 8 mol% Y_2O_3 for fully stabilized ZrO_2 (8YSZ)); __GDC:__ Gadolinium-doped ceria (typically 10 mol% Gd in CeO_2); __LSM:__ Lanthanum-strontium-manganite ((La,Sr)MnO_3); __LSC(F):__ Lanthanum-strontium-(iron-)cobaltite ((La,Sr)(Co(Fe))O_3).

While the literature covers a broad palette of material solutions – alternative stabilization or doping of zirconia and ceria, mixed-conducting perovskites on the fuel side, and air electrodes with enhanced degradation stability – the set summarized here reflects the state of the art. In particular, the YSZ-based system with a Ni-YSZ cermet fuel electrode and La-Sr perovskites on the air side remains the most widely used combination.[16] It has also proven the most robust for industrialization.[18] CTEs in such stacks typically fall within a narrow corridor of $10–13\times10^{-6}\ K^{-1}$, which lowers the risk of thermo-mechanical stress during manufacturing, operation, and thermal cycling.[19,20]

The choice of the mechanically supporting layer is a key design decision and underpins the classification of SOC concepts. The support can be integrated into a functional layer or realized as a largely passive structural layer. Historically, the first architecture was the electrolyte-supported cell (ESC), which uses a comparatively thick, load-bearing electrolyte on which the remaining functional layers are deposited. To

overcome the high ohmic losses – and thus the need for temperatures above ~800°C – alternative concepts displaced the support from the electrochemically active core unit.[21]

Therefore, the fuel-electrode-supported cell (FESC) was developed. Here, a separate, thicker layer on the fuel side – made of a Ni-based cermet with a coarse microstructure – provides mechanical support, robust contacting, and gas transport pathways.[21]

Subsequently, the metal-supported cell (MSC) emerged, placing an electrochemically inert metallic substrate on the fuel side as the primary support and thus further removing the structural function from the active zone.[22] Heat spreads efficiently in the metallic base, which shortens start-up times. The downside however is limited durability of porous metals under SOC conditions, so operation is often constrained to lower temperatures, typically below ~650°C, and thereby to pure process gases.[21] A schematic comparison of the concepts ESC, FESC, and MSC is shown in Figure 3.

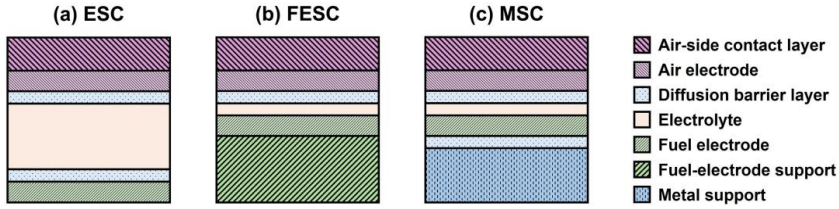

Figure 3: Schematic illustration of the three most established SOC support configurations: (a) Electrolyte-supported cell (ESC), (b) fuel electrode-supported cell (FESC), and (c) metal-supported cell (MSC), including the characteristic layers. Layer thicknesses not proportional. Own illustration derived from[17].

Practical deployment requires embedding the functional cell units into a higher-level structure that distributes gas flows uniformly and ensures reliable electrical contacting. To reach application-relevant voltages, energy densities, and hydrogen production rates, compact assemblies with large active area per system volume are essential. Among several models, two basic configurations dominate. In the tubular concept, functional layers are deposited concentrically on a tube, separating gases between the inner channel and the shell. In the planar concept, flat cell packages are assembled into a "stack," where a full-area connecting unit contacts neighboring cells electrically and, at the same time, separates and distributes the gases: the interconnect. The interconnect is thus central in the planar design, whereas in tubular cells its role is limited to the length of a single tube. A schematic comparison is shown in Figure 4.

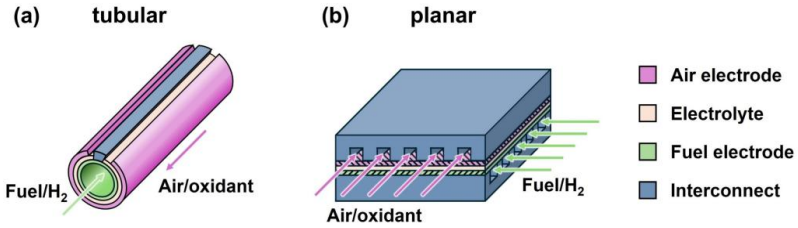

Figure 4: Schematics of (a) the tubular and (b) the planar SOC configuration. Own illustration derived from[16].

Tubular stacks offer specific advantages – efficient fuel utilization, pressurized operation, and fewer non-functional parts – yet planar stacks have proven more practical. They are simpler to manufacture with established ceramic processes and can achieve high volumetric energy densities. They are well advanced in research and industrial development.[18]

SOC concepts developed at Forschungszentrum Jülich likewise use the planar configuration and are therefore the focus here. Although successive generations differ in geometry, size, layer thicknesses and microstructures, and performance, they share a common foundation: FESC architecture with a YSZ electrolyte and a Ni-YSZ cermet on the fuel side (fuel electrode and support layer). As this system is widely studied and considered state-of-the-art, the conclusions are broadly transferable. In the current Jülich baseline cell, the Ni-YSZ support is about 500 µm thick. Functional layers are much thinner, with electrolyte and GDC barrier in the few-micrometer range, and electrodes on the order of 10 µm or more. LSC or LSCF are standard for the air electrode and the adjacent contact layer, the latter typically near 100 µm in thickness.[11,21]

Achieving the intended layer functions depends on producing uniform and reproducible microstructures with consistent integrity and precisely controlled thickness. This, in turn, rests on selecting and controlling suitable manufacturing processes, which are the key to building high-performance SOCs.

2.1.3. Ceramic manufacturing processes

Established manufacturing routes for functional layers in SOCs – both in commercial concepts and in research – aim at industrial feasibility, i.e., integration into mass production with low reject rates, high reproducibility, and automation potential. Suspension-based processes are particularly relevant, as they enable high throughput and are widely used across ceramic processing.

Suspension-based processes

These methods are based on dispersing ceramic particles – from nanometers up to micrometers – in a liquid, typically organic, medium. Organic additives such as binders and plasticizers are added to tune rheology and green-body properties. The most common routes are tape casting for large-area, self-supporting green sheets on the order of several 100 cm^2 up to m^2 (with subsequent post-processing to final size) and screen printing for thin functional layers up to a few 100 cm^2 on pre-existing substrates.[23–25]

In tape casting, comparatively low-viscosity, shear-thinning slurries are applied to a sacrificial carrier film and drawn under a doctor blade that sets the thickness. After evaporation of volatile components, a uniform green tape remains, and multiple layers can be deposited sequentially.

Screen printing uses higher-viscosity, likewise shear-thinning pastes that are pressed with a squeegee through a screen defined by mesh size and thickness onto the substrate, followed by drying. Layer-by-layer deposition is also feasible. The method is closely related to the printing process established in the textile industry, holding the same name.

Suspension-based routes are typically used for porous functional layers – supports and electrodes – though dense layers such as electrolytes and barrier layers can also be produced.[23,26] Beyond particle-size distributions, suspension composition and process parameters, a critical step for achieving the target microstructures is the thermal post-treatment, namely sintering.

Sintering

Sintering is a heat treatment below the melting point of the highest-melting constituent during which porosity decreases. Shrinkage and densification occur, and a weakly bonded particle assembly evolves into a coherent, stronger network. Typical temperatures for technical and refractory ceramics exceed 1400°C, whereas specialized functional ceramics, as in SOCs, can be processed several hundred degrees lower.[27] Debindering and sintering often proceed in a single heat-treatment step. The driving force is minimization of the system enthalpy. Four dominant mechanisms can be identified during the evolution from powder to a consolidated body[27]:

(i) **Reduction of surface energy:** decreasing specific surface area during particle coalescence.

(ii) **Reduction of interfacial energy:** decreasing specific interfaces and grain boundaries.

(iii) **Relaxation of gradients:** equalizing concentration differences and electrostatic potentials.

(iv) **Relief of mechanical stresses.**

These driving forces suffice to enable mass transport, however heat markedly accelerates the underlying mechanisms. Material transport can proceed by sublimation and deposition, surface diffusion, and volume diffusion. Pore elimination is linked to shrinkage and can occur by plastic flow, grain-boundary diffusion, or volume diffusion from grain boundaries.[27] A graphical overview of the mechanisms is shown in Figure 5.

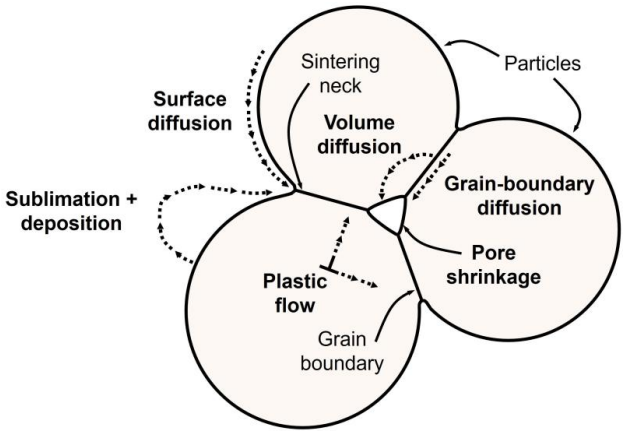

Figure 5: Schematic of transport phenomena during the (solid state) sintering. Own illustration derived from[28].

Sintering typically begins with "welding" of particles that were previously only loosely or mechanically compacted, governed by surface diffusion and sublimation/re-sublimation. With increasing temperature, newly formed grain boundaries grow into necks. Longer holding times or higher temperatures promote grain-boundary diffusion, which heals defects such as dislocations at boundaries. Neck growth – by this mechanism and by high-temperature volume diffusion – drives substantial shrinkage. As sintering proceeds, grains approach their ideal rounded cuboctahedral shape. Mean grain size and contact number increase. Once closed porosity is reached – if achievable for the chosen powder and thermal schedule – residual pores are expelled, largely by grain-boundary diffusion, and final density is approached.

Selecting suitable sintering schedules – heating rates, dwell temperatures and times, as well as atmosphere – is essential for tailored microstructures. In multilayer assemblies with different compositions and targets, this is particularly challenging. Cell manufacturing can use sequential fabrication and sintering, co-sintering of stacked green layers, or a combination. The overarching goals – flat, defect-free cells and defined layer-wise microstructures – are difficult to achieve under the constraints of interacting layers and complex stress states.

Interdiffusion during multi-hour high-temperature steps can degrade or even destroy functionality, so this risk should be minimized. One avenue is to use specialized sintering techniques that shorten times and/or localize heat input. Examples include laser and flash-lamp sintering, whereas pressure- or electric-field-assisted routes are also feasible approaches. These options can be attractive from economical and ecological perspectives as well but generally lack the technological readiness and scalability to play a role in manufacturing yet.

Where very thin layers, tightly defined compositions or microstructures, or especially high densities are required – and interdiffusion must be avoided – classical suspension-based routes with subsequent sintering may be insufficient. In such cases, specialized deposition

techniques are used. For tailored electrolytes or barrier layers, typically stabilized zirconia or doped ceria, vacuum-based processes with deposition from the vapor phase are common.[25,29]

Vapor deposition processes

In vapor deposition, the coating substance deposits from the gas phase in a vacuum onto the substrate. A distinction is made mainly between physical vapor deposition (PVD) and chemical vapor deposition (CVD). For SOC functional layers, PVD is common, with the deposition atmosphere supplied in the target chemical composition by definition.[30] Sputtering is widely used and ejects atoms from a target by ion impacts from a noble-gas plasma, typically Argon. Magnetron sputtering, enhanced by an applied magnetic field, is particularly common.[31]

CVD methods are also used in selected cases. Unlike PVD, precursors are introduced that react at the substrate surface to form a continuous film of the target composition. Despite higher process complexity, the key advantage of PVD/CVD is direct deployability, often without further thermal steps.[32]

After completion of the compound of all functional layers, the cell is integrated into the higher-level structure, the stack. Component compatibility and thermal processing remain critical for ceramic-cell integrity.

2.1.4. Stack architecture, components and assembly

Beyond the elementary cell packages discussed above, additional parts are required to realize the series connection of cells in the stack. The Jülich planar concept with fuel-electrode-supported cells serves as the reference here, as it is central to the practical work. Series connection is achieved by linking several single repeating units (SRUs), in which each cell is contacted on both sides by a conductive interconnect. On the air side, a porous ceramic contact layer provides the electrical and mechanical interface. On the fuel side, Ni meshes are commonly used, as in operation they can weld to the Ni-based cermets and at the same time distribute the fuel gas/hydrogen. Gas distribution on the air side is typically provided by structures integrated into the interconnect component.[11]

Cells are laterally enclosed by frames that also act structurally and help distribute process gases along the stack height. The base plate and end plate form the outer enclosure and the interfaces for gas connections and higher-level system integration. Interconnects, frames, and base/end plates are key elements from several perspectives and are a focus of this work. Their roles, requirements, and practical issues are analyzed in the following sections.

Sealing plays an essential role in reliable stack operation. Sealants tie all parts into a coherent assembly and prevent short-circuiting as well as uncontrolled gas leakage and reaction. In planar stacks they are indispensable. Depending on the design, interconnects, frames, and cell edges must be joined, and different sealant types within a single stack can be appropriate. Glass sealants are most commonly used.[33] They are applied as suspension-based

pastes or as preformed green tapes. During stack assembly – the joining step consolidating all components – the glass sealant partially crystallizes into a dimensionally stable glass-ceramic. The sealant must remain stable under long-term pressure and under both air- and fuel-side atmospheres, moreover it must be thermo-mechanically compatible with adjacent parts, in particular with respect to CTE matching.[33]

For SOC applications, borosilicate glasses are generally recommended. Typical compositions contain 45–55 mol% SiO_2 and 5–15 mol% B_2O_3. Additions of 20–30 mol% BaO, MgO, and SrO are common to reduce interdiffusion between cell and glass sealant. Al_2O_3, Y_2O_3, or La_2O_3 are also used in the range of 10–15 mol%, and small amounts of further oxides are employed to tailor properties – for example Nd_2O_3 and ZnO to adjust or raise the CTE and thermo-mechanical stability, TiO_2 and ZrO_2 to stimulate crystallization, and NiO and CuO to enhance adhesion. Often a single addition is related to several impact categories.[33]

At Forschungszentrum Jülich, a Ca-Ba-silicate glass with YSZ fibers as filler is established for stack sealing and is applied as screen-printed green foils. Details on composition, development, and application technique are reported elsewhere[34,35]. The placement of the glass-sealant foils – together with the other stack components – is shown schematically for the representative Jülich F10 design, incorporating 10 × 10 cm^2 cells, depicted as a four-layer example in partially exploded view in Figure 6.

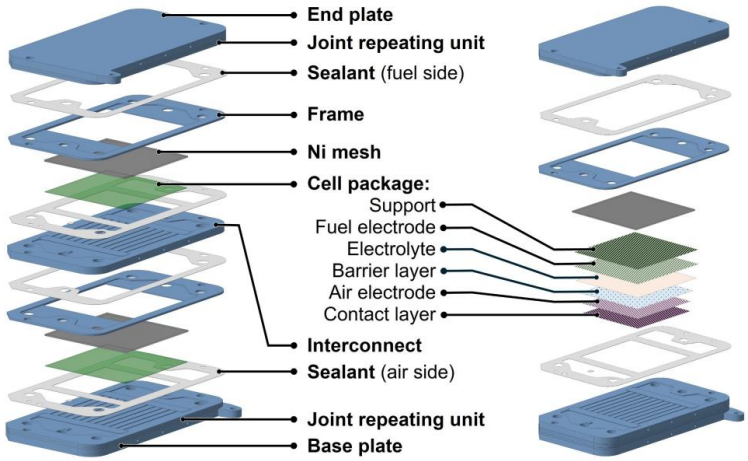

Figure 6: Technical drawing of a Jülich four-layer F10-type SOC stack, incorporating two joint and two exploded SRUs, and highlighting the layered structure of the functional cell. Drawings provided by W. A. Mertens (FZJ-ITE).

After assembly of all components, consolidation into a gas-tight unit proceeds together with electrical contacting within each SRU and between SRUs. This stack assembly step can be carried out at the start of operation. The process must promote the desired crystallization of the glass solder while preserving the integrity of the other parts, particularly the cells. At Jülich, joining is typically performed after multistep heating for

gradual debindering of the glass-sealant foils and uniform heating of all parts, followed by a 100 h dwell at 850°C. A detailed description is provided in Section 3.4.2.

To operate a joined stack, one or more stacks – each comprising several SRUs – are integrated into the overall system. The system further consists of additional components that sustain and regulate operation, including process-gas supply, steam generators, heat exchangers, electrical wiring, sensors, and control electronics. These are often summarized as the periphery or balance-of-plant components (BoP). An overview of a Jülich system is given in the Supplementary Information (cf. SI 1).

Viewed against the broader system, the interconnect may seem secondary, yet it remains an integral and structurally indispensable part of the stack. Its design and materials face demanding requirements. The following chapters examine its role and the associated challenges in detail.

2.1.5. Role and requirements of interconnects

Building on the stack architecture outlined above, the interconnect (often termed bipolar plate) performs two core tasks within each SRU. It links cells electrically in series and it separates and distributes fuel and oxidant across the active area. End plates face nearly the same boundary conditions – even if they do not connect adjacent cells – and are therefore considered implicitly below. Frames follow the same logic in pared-down, purely structural form. The resulting task portfolio and requirements for the interconnect can be concluded as the following[36,37]:

(i) **Electrical and thermal conduction:** Reliable electronic connection of cells in series and sufficient thermal conductivity for stable stack operation.

(ii) **Gas tightness:** Effective separation and distribution of fuel and oxidant gases, preventing uncontrolled reactions.

(iii) **Thermo-mechanical compatibility:** Matching CTE with adjacent components to minimize thermal stress during operation and cycling.

(iv) **Chemical stability:** Resistance to decomposition and volatilization under elevated temperatures, aggressive gas atmospheres and continuous streams.

(v) **Corrosion resistance:** Prevention of high-temperature corrosion and formation of protective oxide scales to ensure long-term performance.

(vi) **Geometrical and structural functionality:** Integration of flow-field structures with dimensional stability and reliable contact within the stack architecture.

(vii) **Mechanical stability:** Adequate strength and creep resistance under operational loads over long service times.

As the name implies, the interconnect must join cells while conducting heat and electricity. Thermal conductivities on the order of 5 $W \cdot m^{-1} \cdot K^{-1}$ are commonly cited as a target.[36] Literature often mentions electrical conductivities around 1 $S \cdot cm^{-1}$, yet in practice the relevant metric is the area-specific resistance of a component with representative thickness.[36] Values should remain below 50 $m\Omega \cdot cm^2$.[36–38]

Gas tightness underpins safe and efficient operation. The interconnect must suppress leakage and mixing process gases that would cause pressure losses, performance penalties, or hazardous reactions. A dense structure, with at most a very small fraction of closed pores, is required.

Thermo-mechanical compatibility is critical from first heat-up through steady operation and cycling. A mismatch in CTE with adjacent parts – especially the ceramic cell and its electrolyte – inevitably drives stresses that can degrade performance or cause failure. For Ni-YSZ based cells, preferred CTEs lie around $10–13 \times 10^{-6}\ K^{-1}$.[19,20,36]

Chemical stability and corrosion resistance are closely linked. The interconnect should avoid uncontrolled secondary phases, limit the release of volatile species into the gas streams, and form only stable, low-resistive surface layers under air- and fuel-side conditions. Uncontrolled corrosion raises resistance, harms interfaces, and shortens service life.

Geometrical and structural functionality ties requirements back to manufacturability. The material and process must realize the intended flow-field features with dimensional stability and robust, low-resistance contacts within the stack architecture.

Mechanical stability completes the profile. The interconnect must retain shape under compressive load at elevated temperature and over long times. Adequate creep resistance is needed to preserve geometry and function across the stack lifetime.

Considering these requirements – together with economic and availability constraints – the literature outlines several material and process options. The following sections review these routes.

2.1.6. Material solutions for interconnects

The requirement profile for interconnects is demanding and tightly coupled to the remaining stack components. Long-term exposure to elevated temperatures and aggressive oxidizing and reducing atmospheres narrows the field of viable materials. A straightforward starting point – given the ceramic cell materials – is to consider oxide ceramics for the interconnect itself.

Ceramic interconnects

Early stack developments explored ceramic interconnects, with lanthanum chromites ($LaCrO_3$) at the forefront.[39,40] At the high operating temperatures of early SOCs, near 1000°C, these perovskites were attractive thanks to their stability and well-matched CTEs. Though their drawbacks proved substantial. Processing is difficult and costly, mechanical strength is limited, and – most critically for today's sub-800°C operation – the p-type

ceramics offer insufficient electrical performance compared to competing material classes such as metals.[38,40]

Metal interconnects

As cell concepts, materials, and microstructures advanced, operating temperatures dropped and widened the material palette to include metallic alloys. Metals combine higher mechanical strength and easier manufacturability with superior electrical conductivity at lower temperatures and lower cost, making them highly attractive. Two constraints accompany this shift. Metals oxidize by forming surface oxide scales that must remain sufficiently conductive and mechanically stable, and their CTEs – strongly tied to crystal structure – are typically higher than those of oxide ceramics.[36,37]

The CTE constraint excludes classes with excellent mechanical properties but poor thermo-mechanical compatibility, notably Ni-base superalloys and austenitic stainless steels. Both crystallize face-centered cubic (fcc) and can reach CTEs up to ~20×10^{-6} K^{-1} to 800°C.[36] Chromium-rich systems such as Cr-base alloys or ferritic stainless steels are body-centered cubic (bcc) and show CTEs in the range of ~$11–12.5\times10^{-6}$ K^{-1} and ~$11.5–14\times10^{-6}$ K^{-1}, respectively, across the relevant temperature interval. [36]

As long-term stability relies on self-passivation, the formation and properties of surface oxides are central. Scale chemistry and kinetics can be influenced by alloy composition and processing, which provides a lever for design.

Oxidation kinetics of metals

Thermodynamics predicts which metallic or oxide phases are stable for a given temperature and oxygen partial pressure, often visualized in Ellingham diagrams via the Gibbs free energies. The oxidation process itself is governed by kinetics and proceeds in three stages, schematically shown in Figure 7.

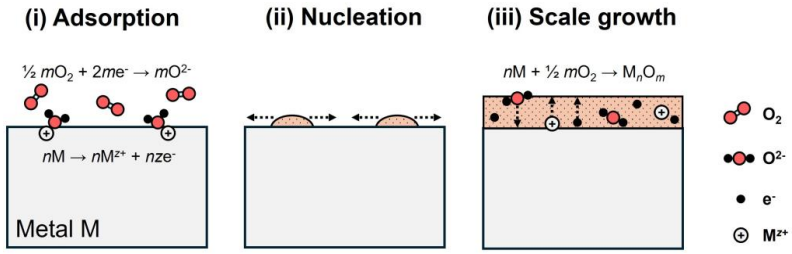

Figure 7: Schematic illustration of the oxide-scale formation on a metal surface, including the three main steps: (i) adsorption, (ii) oxide nucleation, and (iii) scale growth. Own illustration adapted from[41].

First, oxygen from the atmosphere adsorbs on the metal surface. After charge transfer, O^{2-} and M^{n+} ions form and establish ionic bonding. Next, the oxide nucleates at the metal-gas interface and grows laterally into a continuous scale. These early steps depend on crystallographic orientation, defects, surface condition, and impurities in gas and metal. Once a continuous layer separates metal and atmosphere, further growth proceeds by solid-

state diffusion of M^{n+} and/or O^{2-} through the scale. Depending on the dominant diffusing species, growth is *inward* or *outward*.[41]

At high temperatures, most metals exhibit parabolic scale growth, which is often established by monitoring the mass gain experimentally. Wagner's theory provides a classic description. The parabolic law for mass gain Δm (g) reads

$$\Delta m^2 = k_p t + A \tag{2.4}$$

where k_p ($g^2 \cdot h^{-1}$) is the parabolic rate constant, t (h) is the exposure time, and A (g^2) is the integration constant. For dense scales, and neglecting oxygen solubility in the metal, diffusion through the oxide is rate determining. Growth slows as thickness increases.[42]

Such behavior defines a *protective* oxide scale. If the forming scale is porous and gas-phase oxygen transport dominates rather than ionic diffusion, a near-linear mass gain is observed. The scale is then *non-protective*.[43]

Layered scales can form depending on alloy chemistry, as individual elements favor different oxides. A continuous chromia layer (Cr_2O_3) is particularly desirable because its electrical conductivity is comparatively higher than that of FeO/Fe_3O_4, SiO_2, or Al_2O_3 under SOC conditions.[41,44]

Chromium-base alloys offer excellent corrosion resistance by forming extensive Cr_2O_3, exemplified by Ducrolloy (Cr-5Fe-1Y_2O_3; Plansee, Breitenwang, Austria).[45] Their disadvantages are however lower electrical conductivity, difficult processing, and high cost. In contrast, ferritic stainless steels have moved in focus. With chromium contents above ~15 wt% they likewise form Cr_2O_3, yet they are far easier to process and less expensive.[36,37]

Ferritic stainless steels

Self-passivating ferritic stainless steels combine good thermo-mechanical compatibility and plausible conductivity with straightforward manufacturing and comparatively low cost. Meanwhile they are considered state-of-the-art for interconnects. Chromium contents typically range from ~16–23 wt%. Bespoke interconnect steels with ~22 wt% Cr are designed to maintain a sufficient Cr reservoir for long-term operation, while conventional Cr-forming ferritic stainless steels often lie near 16–19 wt%.[36,46]

Beyond Fe and Cr, additional alloying elements are decisive for tailoring the property profile, for defining viable processing routes, and ultimately for cost.[36] Some elements also enter as residuals from steelmaking and can adversely affect performance.

Manganese is a common minor addition, typically below about 1 wt%. During exposure it diffuses through the chromia scale and forms a continuous $(Mn,Cr)_3O_4$ spinel layer. Besides other benefits, this layer increases electrical conductivity by more than an order of magnitude compared to bare Cr_2O_3.[44,47]

Silicon and aluminum often occur in small amounts as residual elements in conventional grades not optimized for high-temperature electrical service.[48] In interconnects they are problematic because they can form SiO_2 or Al_2O_3 sub-scales beneath

the chromia. These oxides are highly resistive and thereby drastically increase area-specific resistance (ASR).[44,49–51] A SiO_2 sub-scale can also cause adhesion issues due to CTE mismatch with the steel.[52] Avoiding such residuals requires vacuum melting, which is expensive and therefore generally limited to tailor-made grades. Alternatively, silicon can be bound in beneficial, isolated phases to suppress SiO_2 formation.[49] Additions of refractory elements such as W, Mo, or Nb promote Laves phases, for example $(Fe,Cr(Si))_2(Nb,W,Mo)$, which both immobilize Si and enhance creep resistance and hardness by impeding dislocation motion.[51,53]

Titanium – like Cr, Nb, W, and Mo – is also used to stabilize the bcc structure at elevated temperatures. Through localized oxidation or precipitation beneath the oxide scale, Ti can further improve scale adhesion.[54]

Finally, reactive elements such as La, Ce, Y, or Sc are introduced in very small concentrations to enhance oxidation resistance and oxide-scale adhesion.[55–57] The so-called "reactive-element effect" is attributed to segregation of these atoms at chromia grain boundaries, partial blocking of diffusion pathways, and a possible shift from outward to inward growth mechanisms.[55,58,59] Reported effective levels are as low as 0.01–0.5 wt%.[55] A schematic of oxidation mechanisms in ferritic stainless steels as a function of composition is shown in Figure 8.

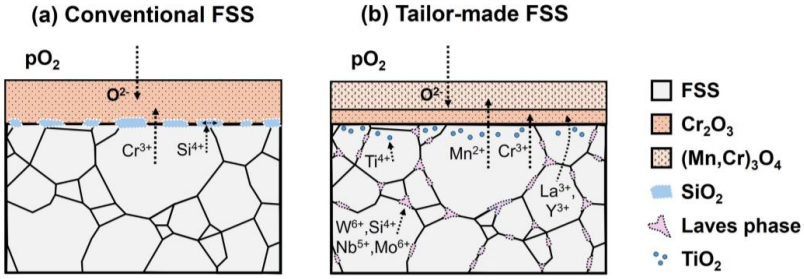

Figure 8: Schematic of the oxidation kinetics of different ferritic stainless steel (FSS) types; (a) Conventional grade with medium Cr content, no substantial Mn addition and residual Si, and (b) tailor-made grade for SOC application, combining high Cr and defined Mn concentration, addition of refractory elements for Laves phase formation and Si binding, and doping of reactive elements and Ti for oxide-scale tuning. Own illustration.

Conventional grades widely discussed for interconnects include AISI430, AISI441, and AISI444. Their challenges are a smaller chromium reservoir and often less controlled Si and Al levels, which threaten long-term stability and low ASR. In response, tailored steels were developed that incorporate high Cr, deliberate Mn and reactive-element additions, and active management of Si and Al – either by exclusion or binding. Examples are ZMG232 (Proterial Ltd., Tokyo, Japan), Sanergy™ HT (Alleima, Sandviken, Sweden), and Plansee ITM (Plansee, Breitenwang, Austria). The latter was used in a Jülich SOFC stack, performing over 100 kh.[60] The Crofer family was developed jointly by Forschungszentrum Jülich and Thyssen-Krupp (today produced by VDM Metals). Crofer22APU features

~22 wt% Cr with very low Si and Al contents. Crofer22H was later introduced for thinner sheets under higher mechanical requirements. Compared to its predecessor it exhibits improved creep strength and higher tolerance to Si through Laves-phase formation. Crofer steels remain a widely established option, especially in research.

Whether conventional or tailor-made, all grades face demanding long-term exposure in SOC stacks. Understanding the relevant degradation mechanisms is therefore essential for developing effective mitigation strategies.

2.2. Degradation phenomena related to the interconnect

Addressing degradation – alongside competitiveness and operational flexibility – is a central task in SOC research and development. Limited long-term stability under operating conditions, i.e., gradual loss of stack performance up to functional failure, arises from multiple mechanisms distributed across the stack. Their relevance depends on cell type, operational mode, and especially temperature. In oxygen-ion conducting SOCs, thermally accelerated diffusion and interdiffusion dominate.

Typical examples include diffusion of electronically conductive species into the electrolyte with associated electronic leakage, or formation of $SrZrO_4$ at the electrolyte-barrier layer interface caused by Sr migrating from the air electrode.[61] On the fuel side, microstructural changes in the Ni cermet – Ni agglomeration and Ni migration – are widely reported. The latter reduces the population of active triple phase boundaries and with it the catalytic area.[62] A major strategy, in parallel to materials and microstructural optimization, is to lower operating temperature towards the intermediate range around 600°C (IT-SOCs) to drastically slow down degradation kinetics.[63]

Temperature and gas atmospheres place comparable stress on metallic stack parts. Air-side conditions are particularly severe, combining ambient humidity with high oxygen partial pressure and continuous flow. These factors make the interconnect and other steel components vulnerable. While further temperature reductions are pursued in classical SOCs and PCCs, and gas compositions further differ in PCC operation, the oxygen-ion SOC around 800°C remains the most relevant case for industrial implementation and for which mechanisms are best documented. The degradation phenomena that are directly or indirectly linked to the interconnect are therefore crucial aspects for long-term stable and efficient stack operation and are therefore examined in the following sections.

2.2.1. High-temperature corrosion

The oxidation and corrosion behavior of ferritic stainless steels in SOC environments – discussed in Section 2.1.6 and illustrated in Figure 8 – underpins their suitability via self-passivation. Unchecked thickening of the chromia scale, however, increases electrical resistance and drives ohmic losses during long-term operation. Additional corrosion effects emerge under harsh conditions and therefore require separate treatment.

Oxide-scale spallation

Often, metal oxidation is treated as a continuous parabolic process. This rests on the assumption of dense, cohesive scales with good adhesion to the substrate. Local disturbances can disrupt this ideal behavior and trigger abrupt, non-uniform growth or even scale detachment (called spallation).

As chromia and spinel ($(Mn,Cr)_3O_4$) layers thicken during exposure at high temperature, stresses can build up, especially if pores and cracks develop near the scale-metal interface. Thermal cycling amplifies the risk due to CTE mismatch in the layered scale-metal compound. Sudden local delamination exposes unprotected metal, which then corrodes rapidly. The result can be local contact loss and a stepwise increase in ASR. Detached flakes may also damage nearby cell components.[38] Figure 9a sketches the spallation mechanism.

Breakaway corrosion

Local chromium depletion beneath spalled areas can propagate damage in a cascade. Closely related is a second disruptive mode with far-reaching consequences: breakaway corrosion.

When the protective top layer weakens or conditions are particularly harsh – very high temperature, strong air flow – progressive chromium depletion near the surface can cross a critical threshold. Iron-rich oxides then form preferentially. These phases are non-protective and often grow as voluminous, open-porous or sponge-like structures. The phenomenon spreads, induces local stresses, and can cause cracking, delamination, contact loss, and sharp increases in resistance. Growth follows an approximately linear law, which reflects gas-phase access through the porous scale. This breakaway corrosion is a key failure mechanism that must be mitigated.[41] The process is sketched in Figure 9b.

Dual-atmosphere effect

Air-side oxidation is the primary corrosion load for interconnect steels under SOC conditions. Fuel-side corrosion in reducing atmospheres is usually less critical, since metallic contact to the Ni mesh remains stable. Long-term exposure to oxidizing on one side and reducing on the other can nevertheless alter the steel response. The literature discusses this so-called "dual-atmosphere effect" with mixed conclusions.[64]

Yang et al. first reported in 2003 that air-side corrosion of ferritic steel plates was altered when the reverse side was exposed to fuel gas at 800°C.[65] Iron-rich oxides were observed on the air side. Follow-up studies variously confirmed similar or stronger effects[66,67], while others saw little to no impact[68–71]. Later work indicated that the effect can be even more pronounced near 600°C.[72,73]

Hydrogen involvement is broadly accepted, given its diffusion through the steel. A single, general mechanism however remains unresolved. One view is that hydrogen incorporation into the oxide alters defect chemistry and increases cation diffusivity.[67,68] Other proposals include local steam generation at the interface that mechanically disturbs

scale formation[74], or hydrogen blocking chromium diffusion to the surface, which hinders continuous chromia formation.[73] Figure 9c provides a schematic of the dual-atmosphere effect, including the main explanatory approaches.

Given the contradictory findings and open questions, further study is necessary, along with development of mitigation strategies. The effect will likely be more relevant for thinner interconnects where through-thickness diffusion acts over shorter distances. Thick designs, such as the Jülich F10 concept with millimeter-scale plates (cf. Figure 6), are expected to be less sensitive than sheet formats below roughly half a millimeter.

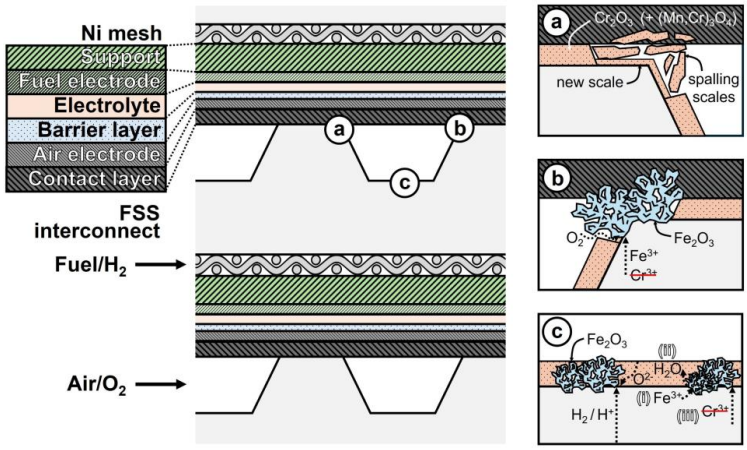

Figure 9: Schematic illustration of the three main degradation mechanisms of FSS interconnects related to high-temperature corrosion: (a) oxide scale spallation, (b) breakaway corrosion, and (c) the dual-atmosphere effect, including the explanation approaches of (i) defect chemistry altering, (ii) retained Cr-ion diffusion, and (iii) steam-induced chromia formation blockade. Illustration leans in style towards Jülich FESC F10 stack design.

2.2.2. Chromium evaporation and poisoning of air electrodes

Beyond gas-driven attack of the interconnect and inward migration of species, another major degradation route originates in the steel and moves outward. Volatile chromium species evolve from the interconnect, enter the gas stream, and poison the air electrode. Chromium evaporation and ensuing air-electrode poisoning have been debated for decades and remain central to interconnect-related degradation.[75–77]

The self-passivating chromia layer on high-chromium steels provides essential corrosion resistance, yet SOC operating conditions – elevated temperature, high oxygen partial pressure, and ambient humidity– promote volatilization of Cr(VI) species. These gaseous species traverse the air electrode. The atmospheric conditions strongly influence the type of species, and depending on pO_2 and pH_2O, the following reactions proceed[75]:

$$Cr_2O_3\,(s) + \tfrac{3}{2}\,O_2\,(g) \rightarrow 2\,CrO_3\,(g) \qquad (2.5)$$

$$Cr_2O_3\,(s) + \tfrac{3}{2}\,O_2\,(g) + 2\,H_2O\,(g) \rightarrow 2\,CrO_2(OH)_2\,(g) \qquad (2.6)$$

The volatilization of CrO_3 is favored above ~1000°C. In the presence of water however, $CrO_2(OH)_2$ evolves well below that temperature. Below ~900°C, $CrO_2(OH)_2$ is the dominant volatile species.[43,78,79] Next to temperature and humidity, gas flow conditions further influence evaporation rates.

Deposited chromium compounds form within the air-side contacting system, the air electrode, and the barrier layer. Depending on the chosen materials, different poisoning pathways yield secondary phases.[75] The key distinction arises from how Sr is bound in the two common air-electrode families, (La,Sr(Ca))MnO_3 and (La,Sr)(Co,Fe)O_3,which leads to different locations and impacts of phase formation.

For (La,Sr(Ca))MnO_3 electrodes, chromia and spinel phases, Cr_2O_3 and $(Mn,Cr)_3O_4$, preferentially form at triple phase boundaries (TPBs) at the air-electrode-electrolyte interface. In the common LSM system, initial Cr-Mn-O nuclei arise via[75]:

$$CrO_2(OH)_2\,(g) + Mn'_{Mn} \rightarrow (Cr\text{-}Mn\text{-}O)nuclei + H_2O\,(g) \qquad (2.7)$$

Here Mn'_{Mn} denotes Mn^{2+} in the LSM lattice in Kröger-Vink notation. Growth of Cr_2O_3/$(Mn,Cr)_3O_4$ proceeds from these nuclei. Because TPBs are here crucial for the air-electrode reaction, their blockage is particularly detrimental to cell performance.[75]

For LSC(F) electrodes, weaker Sr binding leads to chromate formation near the surface of the air electrode or contact layer and also within the electrode bulk, but not only concentrated at the electrolyte interface. Moreover, in contrast to the LSM system, this area is less crucial for the catalytic reaction due to the enhanced overall surface activity, resulting from faster oxygen surface exchange kinetics in the LSC(F) system. Nucleation of (Cr-Sr-O) occurs on segregated SrO according to[75]:

$$CrO_2(OH)_2\,(g) + SrO \rightarrow (Cr\text{-}Sr\text{-}O)nuclei + H_2O\,(g) \qquad (2.8)$$

This route is kinetically faster than in LSM due to the lower chemical stability, yet the more distributed deposition, accompanied with the enhanced surface activity, tends to be less damaging than the TPB-targeted LSM case.[75,80] Figure 10 schematizes the processes.

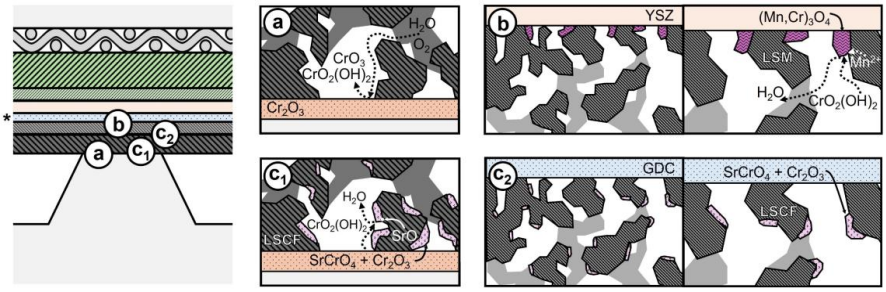

Figure 10: Schematics of Cr evaporation and poisoning mechanisms at air side; (a) Evaporation from chromia scale, (b) poisoning in LSM system at TPBs, and (c) poisoning in LSCF system, (1: near chromia scale, and 2: near barrier layer). Light-grey sections representing background. Own illustration, layer indication analogous to Figure 9. *LSM-air-electrode system typically operating without barrier layer.

Beyond the mechanisms outlined above, which can be considered established knowledge, a recent study[81] by Kindelmann et al. using atomically resolved TEM and spectroscopy points to additional nanoscale processes at the air-electrode/barrier interface during extremely long operation with an LSCF air electrode. Based on in-depth analyses of material from the previously mentioned 100 kh SOFC long-run stack, the authors observed not only pronounced $SrCrO_4$ crystals at the LSCF-GDC interface but also upon then unreported, multiply substituted Ce-oxide appearing as continuous nanoscale precipitates. Although this phenomenon seems to emerge only after very long operating times and remains limited in spatial extent, the delamination of the air electrode from the electrolyte/barrier layer – linked by the authors to this effect – is regarded as a central cause of long-term performance degradation.[81] Accordingly, even for the LSC(F) system, which is often considered as more resistant to chromium poisoning, volatile Cr species are shown to be problematic over long timescales and require closer attention.

Besides the damages in the cell, chromium evaporation also depletes the near-surface Cr reservoir in the steel, which weakens corrosion resistance over time.[75] This couples back to phenomena such as oxide-scale spallation and breakaway corrosion. Mass change can capture this interplay experimentally. Oxidation alone yields parabolic mass gain, whereas chromium loss produces an approximately linear mass decrease. Their superposition – often partially compensating – is commonly termed *paralinear* behavior.[82,83]

2.2.3. Electrical and mechanical contact degradation

Finally, the air-side electrical and mechanical contact at the interconnect-electrode interface can degrade as active contact area diminishes. This contributes directly to stack-performance loss and constitutes an additional degradation pathway.

Even under compressive load, an SOC stack can experience a gradual loss of effective contact area between interconnect and cell. The result is an increase in contact resistance, diminishing utilization of the electrode surface with local overpotentials, and, conversely, insufficient contacting and mechanical stresses from non-uniform load distribution.

Beyond corrosion phenomena that reshape the interconnect surface – oxide-scale spallation, breakaway corrosion, and, to a minor extent, the dual-atmosphere effect – long-term structural changes of the steel, such as high-temperature creep, are critical for sustained performance. This aspect ties closely to alloy composition and the resulting mechanical properties. It also depends on interconnect design, including flow-field geometry and especially component thickness, as well as manufacturing precision, for example the initial flatness and conformity of the central interconnect areas.

Moreover, the contacting approach matters. Stacks can be assembled with a contact layer that is pre-sintered on the cell, or with a compliant contact that consolidates during the stack joining step and imprints onto the flow-field structure.

2.2.4. Mitigation strategies

A range of strategies can be applied not only to optimize stack contacting but also to address corrosion and chromium evaporation. Mitigation spans operating conditions as well as materials and design choices.

Strengthening durability against the degradation mechanisms discussed above benefits from a coordinated set of measures. A major route – relevant across components and aligned with easier integration in industrial thermal processes – is the reduction of operating temperature towards ~600°C for IT-SOCs.[63] Lower temperature defuses many thermally accelerated interconnect degradation modes (yet dependent on the exact steel composition). Because water vapor in the air stream is a key driver of steel corrosion and chromium evaporation, drying the air stream could be another lever.[12]

With respect to interconnect design, avoiding sharp flow-field features helps to reduce local chromium depletion, breakaway corrosion, and oxide-scale spallation. Smoother geometries also distribute mechanical stresses more evenly, which supports scale stability. Still, composition remains a powerful lever. As outlined in Section 2.1.6, thermo-mechanical stability, corrosion resistance, and stable electrical conductivity – by suppressing highly resistive phases – can be tuned through targeted alloying. Beyond corrosion and conductivity, the formation of a $(Mn,Cr)_3O_4$ top layer, promoted by a sufficient Mn content, can improve chromium retention. Compared to chromia, the spinel can lower chromium release by up to a factor of 3.[84,85] This principle is used in tailored steels such as the Crofer grades, and is also reported for certain conventional grades like AISI409 and AISI441.[46]

On the cell side, material and microstructure choices can increase tolerance to chromium. As noted in Section 2.2.2, differences in poisoning mechanisms between LSM and LSCF matter. LSCF is more reactive, yet volatile chromium tends to be captured near the air-electrode contact surface, rather than depositing preferentially at TPBs as in LSM, which reduces functional damage.[75] Barrier-layer microstructures can be optimized to further suppress $SrCrO_4$ deposition at TPBs. A "cleaning effect" has been proposed, where CrO_3 or $SrCrO_4$ volatilize in the presence of H_2O at microstructurally tuned GDC layers.[75]

The most effective approach however is to prevent volatile chromium species from leaving the steel in the first place. In the same step, inward oxygen transport and thus steel corrosion can be prevented. For this purpose, air-side protective coatings on interconnect flow-field structures – and on all metal surfaces exposed to the air stream – are the most established solution. They are well studied in multiple variants and intervene at each step of the degradation chain.

Fuel-side coatings may also be considered in the context of the dual-atmosphere effect, although research remains early and the magnitude of the effect is still under debate. Moreover, fuel side contacting remains stable as solid Ni-steel bond. In contrast, air-side

protective coatings are the most promising and most widely pursued strategy, being examined in detail in the following section.

2.3. Protective coatings for interconnects

Within this established strategy to enhance long-term durability, a range of material systems and deposition methods has been explored for effective interconnect protective coatings. This chapter outlines the prerequisites on the materials side and for the deposition routes and surveys corresponding solutions discussed in the literature. It also opens the perspective for new coating approaches – considering limitations of established methods and parallel developments of the interconnect component.

2.3.1. Functional requirements and selection of coating materials

The requirements for the coating – which govern both the chosen material system and the deposition method – form a complex profile. The decisive points can be summarized as the following[36,37]:

(i) **Chemical and thermo-mechanical compatibility:** Avoiding unwanted phase formation with steel and cell, as well as stresses induced by CTE mismatch.

(ii) **Low area-specific resistance:** Minimizing ohmic losses in the stack through high intrinsic conductivity and efficient contacting.

(iii) **Slowed oxidation kinetics:** Reducing oxygen ingress via physical or microstructural characteristics of the coating system.

(iv) **Suppression of chromium evaporation:** Closing diffusion and gas transport pathways of volatile Cr(VI) species or binding Cr in the coating.

(v) **Continuous, dense and homogeneous coatings:** Enabling uniform and integer layer formation with low/closed porosity, also over complex flow-field geometries.

The selected material must inherently provide the basic properties. Under the harsh requirements, oxide-ceramic layers stand out for long-term stability – either applied as such or formed *in-situ* by oxidation to equilibrium under SOC operating conditions. Within oxides, three groups have been prominent and remain active research topics: perovskites, reactive element oxides or rare earth element oxides, and spinels. Composites such as infiltrate-matrix systems or multilayers are investigated as well.[12,36] A schematic of the crystal structures is shown in Figure 11.

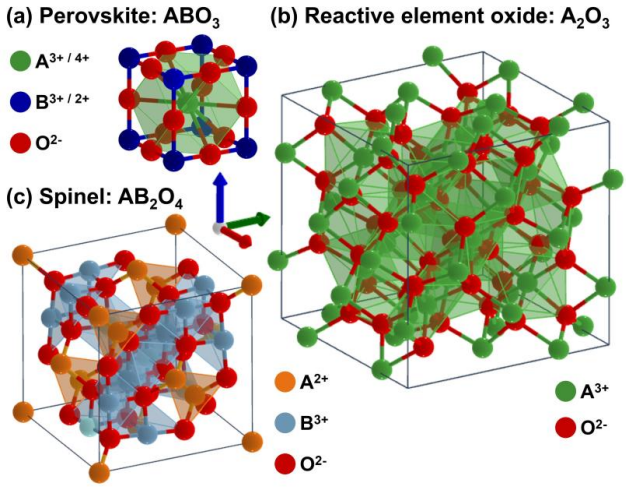

Figure 11: Crystal structures of the relevant oxide classes, as discussed for interconnect coating materials: (a) Perovskite, (b) reactive element oxides (corundum-like), and (c) spinel structure. Drawings created at and extracted from The Materials Project[86] (an open-source software web application).

Perovskites follow the general stoichiometry ABO_3, with A as lower-valent cations such as La, Sr, or Ca and B as higher-valent transition-metal cations such as Mn, Co, Fe, and also Cr. They are in principle mixed ionic-electronic conductors (MIECs), yet specific compositions are mainly conducting electrons. Under SOC-relevant conditions of temperature and pO_2, oxygen-ion transport proceeds via vacancy hopping and electronic transport via hole conduction (small-polaron hopping, p-type conduction).[20] This mixed conduction is a challenge for protection because oxygen transport is only weakly impeded.

Lanthanum chromite ($LaCrO_3$) was a natural starting point because it was already used for all-ceramic interconnects. Other La-based systems were further examined: lanthanum-strontium manganite ($La_{1-x}Sr_xMnO_3$), lanthanum-strontium cobaltite ($La_{1-x}Sr_xCoO_3$), and lanthanum-strontium ferrite ($La_{1-x}Sr_xFeO_3$).[36] These groups exhibit CTEs compatible with adjacent components – particularly ferritic stainless steels – around $10\times10^{-6}\ K^{-1}$ at 800°C, whereas conductivities remain unsuitable, unless temperatures towards 1000°C are applied.[37,40] Moreover, especially for Cr-containing and, more generally, La-based perovskites, the limited oxygen-barrier effect coincides with high diffusivity and poor retention of volatile Cr.[36] Although perovskites are processable by standard ceramic routes and provide adequate stability and thermo-mechanical compatibility, the weak barrier can only be countered, if at all, by very thick coatings. Perovskites are therefore not the preferred choice and have largely been superseded in research.

Reactive element oxides (REOs) are oxides of trivalent cations – classically rare earth elements such as La, Y, or Nd – with a corundum-like A_2O_3 structure.[36] Even nanometer-thin films have been reported to improve oxidation behavior by slowing scale growth and

enhancing adhesion, which prevents oxide-scale spallation.[87–89] Improvements in electrical performance with respect to ASR have also been observed in several studies.[87,90,91] REOs are not good electronic conductors per se, yet at small thickness the insulating effect is negligible compared with the benefit of reduced oxygen transport that is linked to their low oxygen-vacancy concentration. Cerium is a special case (discussed further in Section 2.3.2) since mixed valence enables small-polaron hopping between Ce^{3+} and Ce^{4+}. A major hurdle for Ce and the REO group more in general is permeability to volatile chromium species, which makes stand-alone use as a protective coating unsuitable.[90] Significant progress has nevertheless been achieved by combining REO layers with a second coating: namely spinels.

Spinels have the general formula AB_2O_4, where A is typically divalent and B trivalent, occupying tetrahedral and octahedral sites, respectively, in a face-centered cubic oxygen lattice.[36] Selection and proportioning of A and B tune electrical and thermo-mechanical properties. Spinels generally exhibit high conductivities under relevant conditions, with transport assumed to proceed by hopping on octahedral sites.[92] Mixed-valent occupancy of these sites is essential for good electrical properties. This also underlies the oxidation-induced electrical behavior of Mn-containing ferritic steels – where a $(Mn,Cr)_3O_4$ spinel forms above the corundum-like Cr_2O_3 scale. Although spinel conductivity exceeds that of Cr_2O_3, it remains far below that of coating-grade systems because Cr occurs only as Cr^{3+} and strongly prefers octahedral sites.[44,93–95] Consequently, chromia scale thickness typically dominates ASR in spinel-coated systems, and suppressing its growth is key.[96]

Spinel candidates include e.g. the systems Cu-Fe[94,97], Co-Fe[94,98], and Ni-Fe[94,99]. Mn-based spinels are however most significant – particularly Mn-Co[36,100] – and among Co-free compositions Cu-Mn.[12,36] $(Mn,Co)_3O_4$ stands out for chromium retention and stable, low ASR.[100–102] At 800°C, reported conductivities are 6.4–60 $S \cdot cm^{-1}$ with CTEs of 11.5–14.4×10^{-6} K^{-1} up to 800°C.[94] Both stoichiometries, $MnCo_2O_4$ and $Mn_{1.5}Co_{1.5}O_4$ are common, whereby extensive efforts target property optimization by doping. Rare earth elements such as La or Y have been used[103–105], while transition metals such as Ni and especially Cu or Fe are most frequently utilized.[100]

In a systematic study across Mn_2O_3 – Co_3O_4 – Fe_2O_3, within his PhD thesis Kiefer in 2007 at Forschungszentrum Jülich[106] found similarly good electrical properties for Fe-doped $MnCo_{1.9}Fe_{0.1}O_4$ (MCF) and undoped $MnCo_2O_4$ (MCO), with conductivities generally decreasing upon Fe addition. MCF showed a better CTE match to steel (12.5×10^{-6} K^{-1} to 800°C) when compared with MCO (14.3×10^{-6} K^{-1}), and was therefore identified as the preferred composition. Since then, MCF has been the Jülich standard, applied by various deposition techniques[107–109] and established for long-term stack tests.[110–112]

As the reliance on Co poses ecological, social, and economic challenges due to its scarcity and critical supply situation, avoiding Co is a common goal.[113,114] $(Mn,Cu)_3O_4$

spinels have therefore long been explored, with Fe and Ni as typical dopants. Analogous to the Mn-Co-Fe system, Kiefer systematically studied Mn_2O_3 – Fe_2O_3 – CuO and identified $CuMn_{1.9}Fe_{0.1}O_4$ (CMF) as the best choice regarding phase stability, and electrical and thermo-mechanical properties.[106] Reported hurdles include CTE changes during thermal cycling – linked to cubic-tetragonal transformations. For CMF, averaged CTEs of 10.2 and 12.6×10^{-6} K^{-1} are found for heating to 800°C in air and subsequent cooling, respectively. Multiphase constitution has also been reported elsewhere, however not as an exclusion criterion considering potentially mechanically induced damage.[115,116]

To further enhance performance and stability of $(Cu,Mn)_3O_4$, Basu's group proposed Ni doping as particularly beneficial[117–121] and suggested $CuMn_{1.8}Ni_{0.2}O_4$ with an electrical conductivity of 100 $S\cdot cm^{-1}$.[120,121] Explicit thermal expansion data for this exact composition are not available. Ling and Petric reported a CTE of 11.6×10^{-6} K^{-1} for a closely related spinel and emphasized the overall compatibility of Cu-Mn spinels with SOC stack materials.[94] Some studies indicate comparatively weak chromium retention for $(Cu,Mn)_3O_4$ at SOC air side conditions.[120,122] However, datasets for doped variants remain limited – and their potential may yet be realized, strongly motivated from an ecological standpoint.

When fixing a coating material, compatibility with available deposition methods must also be considered, as route and execution are decisive for achieving the targeted protection. Coatings must be applied to steel-component areas directly exposed to the corrosive air-side atmosphere – primarily flow fields and gas inlets and outlets on interconnects and frames. An exemplary configuration is shown for Jülich F10 components in Figure 12.

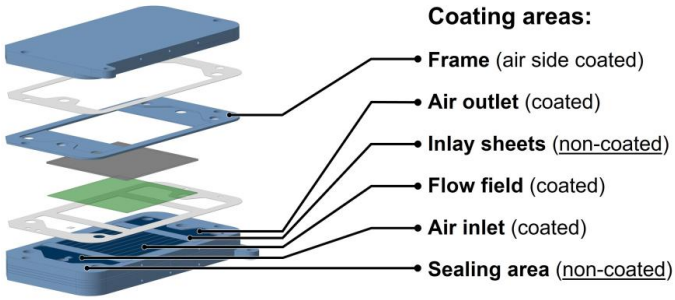

Figure 12: Technical drawing of four-layer F10 stack with protective coating applied in specific areas on the air side of critical steel parts, highlighted in dark blue. Drawing provided by W. A. Mertens (FZJ-ITE).

To confine application to the relevant zones, accurate local deposition must be possible or implemented by masking. Provided precise, integral, and uniform layers can be formed on relevant geometries and component formats, the choice of deposition method remains relatively open, whereas specific methods have been established in the past.

2.3.2. State-of-the-art coating technologies

Numerous methods for applying protective coatings have been discussed, each with specific advantages and hurdles. Routes used for SOC functional ceramic layers include paste-based methods such as screen printing and roller painting.[123–125] These, however, impose geometric constraints that hinder thin, uniform layers on complex flow fields. Further approaches include thermal spraying, suspension-based processes, and gas-phase deposition – particularly PVD methods.[12,126,127]

A notable commercial option is the Ce-Co PVD coating by Alleima (Sandviken, Sweden), already implemented at industrial scale.[128] It offers excellent long-term stability (even over >70.000 h)[129,130], chromium retention, and ASR reduction.[131–134] The bilayer results from a multistage roll-to-roll PVD process. A 10 nm Ce layer is followed by roughly 600 nm Co.[128] The Ce layer promotes adhesion and oxidation protection, while the Co layer suppresses chromium evaporation.[132] Forming to final interconnect geometry must be done after coating, which confines this route to thin-sheet designs that allow pre-coated strip. Moderate deformation can be tolerated without severely impairing protection.[135] Functionally, the Co top layer transforms via Co_3O_4 into a classical $(Mn,Co)_3O_4$ spinel under SOC air-side exposure – driven by Mn diffusion from the steel and oxygen uptake.[101] Presence of Mn as an alloying element is therefore required. Alleima's standard substrate is the ferritic stainless-steel grade AISI441 (Sanergy™ HT), although Crofer grades can also be coated.[136]

Two further methods with strong industrial use history and a decades-long record at Forschungszentrum Jülich are atmospheric plasma spraying (APS), a thermal spray process, and wet powder spraying (WPS), a suspension-based process. MCF-APS coatings are the proven Jülich standard and have provided effective protection for stack runs over more than 30,000 h of operation[112,137] WPS with Mn-base spinel (Mn_3O_4) as a Cr getter has been employed in the previously named 100 kh long-run stack[60] and was recently advanced for MCF[107]. Both technologies are used in this work and are briefly outlined with respect to deposition mechanisms and layer formation. Methodological specifics are discussed later in Section 3.2.

Atmospheric Plasma Spraying (APS)

Atmospheric Plasma Spraying is a thermal spray process for producing metallic or ceramic coatings with thicknesses from a few tens of micrometers up to about one millimeter.[138,139] The feedstock – introduced as powder, rod, or wire – enters a hot gas stream, is (partially) molten, and accelerated in this state towards the substrate to be coated. The hot gas stream is generated by igniting a plasma via an applied voltage between a central cathode and an annular anode.[138,139] Various plasma gases and their mixtures can be used. Argon, helium, hydrogen, and nitrogen are common choices. Unlike low-pressure and

vacuum plasma spraying, where the atmosphere has little influence on coating composition, APS in ambient air promotes oxidation of both the coating material and the substrate.[126] A schematic of an APS system in operation and the according layer formation is shown in Figure 13.

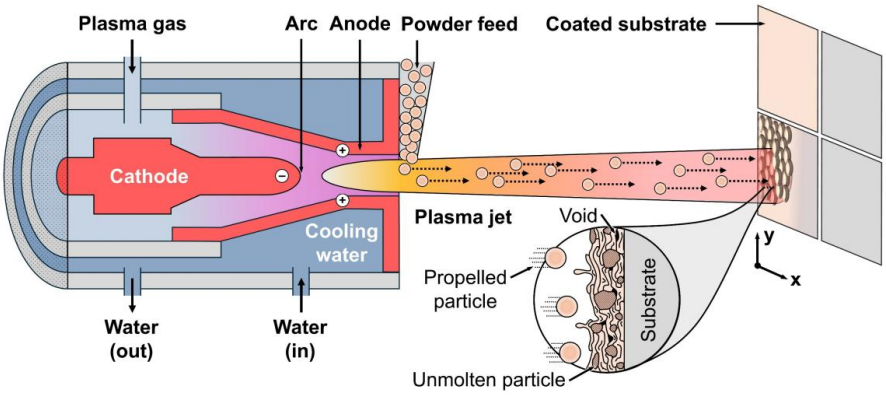

Figure 13: Schematic depiction of the APS coating process, indicating the key parameters and the layer formation process and characteristics. Own illustration, derived from[140].

Beyond ambient pressure, several process parameters govern the resulting coating. Gas selection, via dissociation temperatures for multi-atomic gases such as H_2 and N_2 and via ionization temperatures, controls the plasma energy content and thus the energy transferred to the injected material. Argon is typically the primary plasma gas due to its favorable ignitability (i.e. a comparably low breakdown voltage to generate the plasma)[141], while hydrogen and nitrogen are employed as secondary gases to adjust transport coefficients. Spray distance is equally critical: too short stand-offs can lead to insufficient particle melting; too long distances favor premature solidification – both detrimental to coating build-up.[138,139]

Matching the injection velocity of the feedstock to the hot-gas velocity is important to achieve central melting of the particles. For non-planar substrates such as interconnects, the spray angle is an additional key factor for achieving complete coverage. Deliberate variation of the angle during processing, by coordinated motion of the substrate and/or spraying robot, can improve deposition on complex geometries. For powder injection, a narrow particle-size distribution supports uniform melting and acceleration. Particle geometry and mass likewise affect melting and flight behavior and must therefore be reflected in parameter selection.[138,139]

APS coatings exhibit a characteristic microstructure arising from partial melting and high particle velocities of ~200 $m \cdot s^{-1}$.[142] Upon impact, particles flatten into splats and rapidly solidify. Solidification is completed before the next layer forms. Together with mechanical constraint at the substrate, this induces thermally driven stresses.[143] Stress

relaxation often manifests as cracking[144], and both such cracks and incompletely molten particles contribute to (open) porosity.[145,146] High cooling rates can retain metastable high-temperature phases at room temperature.[147] For MCF coatings this corresponds to the rock-salt $(Mn,Co,Fe)_1O_1$ structure. Subsequent aging can transform this phase back to the spinel structure accompanied by volume increase, which compensates prior porosity and markedly densifies the coating.[148] In SOC stack operation, the prevailing atmospheres favor this transformation, and pore closure can occur already during stack joining and start-up.[147,148] Accordingly, MCF-APS coatings are deployable in the as-sprayed, untreated state.

Several factors nevertheless limit APS for applying interconnect protective coatings. Although variable spray angles help address complex geometries, the line-of-sight nature of APS, accentuated by the high particle velocities, poses challenges on uneven surfaces such as steep flanks and sharp edges (as present for the Jülich F10 interconnect, cf. Figure 6). Ensuring continuous coverage often necessitates comparatively high coating thicknesses, increasing material consumption. Additional losses arise from overspray in industrial application on real parts and from non-adhering material. A particularly critical limitation is the restricted suitability for thin, structured sheets. The substantial mechanical and thermal loads during deposition raise the risk of deformation and lasting damage to both substrate and coating. Since thin-sheet formats are especially relevant for industrial SOCs, attention is shifting towards resource-efficient deposition methods with lower impact on the substrate, notably suspension-based approaches such as WPS.

Wet Powder Spraying (WPS)

In the WPS process, ceramic powder, typically mixed with a binder and solvent, is atomized and sprayed at ambient pressure and temperature onto substrates to form continuous coatings, ranging from a few up to several tens of micrometers or even 100 µm. The ceramic powder provides the desired material properties, while the binder stabilizes the suspension and promotes particle adhesion during spraying. The solvent adjusts the viscosity of the suspension to enable efficient spray application and uniform coating formation. The choice of binder and solvent is critical for achieving optimal coating quality and uniformity. Using fine powders with narrow particle size distributions is moreover crucial to guarantee the dispersion of powder and additives for continuous atomization and spraying through a nozzle.

Coatings are typically applied in multiple layers to enable controlled build-up and to achieve uniform quality. In addition to the choice of the suspension constituents and their concentrations, several process and equipment parameters are crucial to obtain the targeted coating properties. Appropriate settings of air flow, nozzle geometry, and spray distance are key to ensure homogeneous layer formation. The traverse speed of the spray head or stage and the number of layers control the final thickness. A schematic of the WPS process with key parameters and layer formation is given in Figure 14.

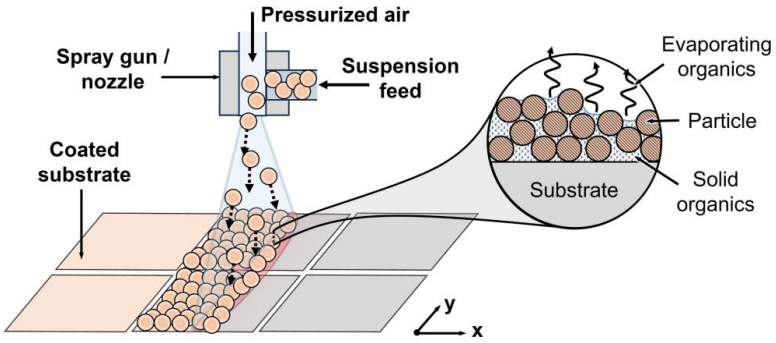

Figure 14: Schematic of the WPS coating process, indicating the key parameters and the layer formation process and characteristics. Own illustration.

Unlike APS coatings, WPS coatings are initially deposited in a loose, non-densified (green) state and require subsequent heat treatment to achieve stability and desired properties. After drying, thermal treatments can be used to remove the residual volatile (organic) components from the coating and sinter the deposited powder to a continuous, dense, pure ceramic layer. While heat treatments are necessary for the deployment of WPS-coated components, appropriate thermal processing steps can also be chosen to tailor the microstructural properties as desired.[149,150] In this regard it has been shown in various works that two-step treatments, including a first step in reducing atmospheres (containing H_2) and a subsequent one in oxidizing atmospheres (as air), are beneficial to achieve this goal.[124,151] This procedure, often referred to as "reactive sintering" is broadly used to densify ceramic coatings, derived from suspension-based processes and is discussed in detail in Section 2.4. This was established by Wolff et al. for the MCF-WPS coatings as well, enabling closed porosity and adequate protectivity of the developed coatings.[107] Comparable developments were reported by Hong et al. on non-doped Mn-Co spinel coatings.[152]

The WPS technique is particularly suitable for depositing thin, continuous ceramic coatings on large-scale and structured components, such as interconnects. Although the suitability to achieve uniform coating thicknesses on complex geometries, also enabled by variation of spraying angles, is more pronounced than for APS, WPS remains a line-of-sight process. Accordingly, highly challenging features such as sharp edges and steep flanks pose hurdles, especially when aiming for low coating thicknesses. Beyond particle flow during deposition, this is accentuated by the viscous characteristics of the coating after deposition. Agglomeration of particles after atomization or on the substrate surface can cause defects that lead to coating failure, while, similar to APS, overspray in industrial manufacturing limits resource efficiency. As particle characteristics however remain rather unaffected from spraying impact, in contrast to APS, powder recycling seems more feasible and could at least be relevant in large-scale manufacturing facilities.

Considering the listed hurdles and drawbacks of the highlighted commercial and established coating technologies, together with emerging requirements for coating systems of modern and future interconnect types, attention can be directed towards novel coating approaches. From this, a requirements profile for next-generation coatings can be derived to guide the selection of suitable technologies.

2.3.3. Requirements for next-generation coatings

Building on the requirements outlined in Section 2.3.1, boundary conditions for interconnect protective coatings remain governed by processability of the targeted compositions, in particular the common spinels. Ideally, the chosen technology should allow composition changes without complex process reconfiguration. The capability to introduce and precisely tune dopants within the process is likewise beneficial for further optimization of established material systems.

The previously discussed difficulty of forming uniform, continuous layers with line-of-sight methods must be addressed with particular attention. Sharp features on interconnect components, which face severe corrosive fluxes during SOC operation, and which are located close to the cell, should be protected as effectively as possible. Preservation of fine structures and overall geometry is critical for thin-sheet, application-relevant designs. This directs interest towards coating methods with low thermal and mechanical loads to avoid damage potentially observable with thermal spraying. With cell areas trending larger to enhance stack performance, coating approaches must scale to planar parts of several hundred cm^2 while maintaining high reproducibility and stable quality in industrial production chains. Methods limited to laboratory scale, very small formats, or single-piece deposition are therefore excluded from consideration.

While continuous coverage in critical zones is essential, the primary requirement is a coherent, dense (or closed-porous) layer whose protection is evident not to be defined by maximized thickness.[96,124,151,153] The resulting objective is to produce thin and still high-quality coatings, also to reduce material use. In view of industrial deployment, processes with high deposition efficiencies and low energy demand should be prioritized.

Effective, geometry-independent masking and de-masking on real components is another aspect not to be neglected. This should be feasible without elaborate steps. For pre-coated thin sheets, such as those from Alleima, potential interactions between glass-ceramic sealants and the protective coatings in the joining zone must be considered. For techniques targeting near-net-shape parts, adjacent masks prior to deposition are conceivable that self-remove in later steps, for example during heat treatments.

Thermal processing must be compatible with the stack process chain, including joining and general operation. Designing the coating route for integration into the thermal schedule can streamline the overall manufacturing process.

Considering these points highlights a group of methods with a common core: deposition from a liquid medium. Continuous and permanent wetting of the component can enable high material efficiency and coverage of complex structures under mild conditions, such as room temperature and negligible mechanical loads.

As one route, sol-gel dip-coating is a classical method for highly homogeneous, thin layers in the lower nanometer range, widely used for ceramic functional films, for example in electronic components.[154] Although the high coating quality is attractive, the limited thickness and often demanding processing limit its relevance for interconnect protection.[155]

A different picture arises for liquid-based methods that leverage the electrical conductivity of the substrate, letting it serve as a deposition electrode. Two sub-routes can be distinguished: solution-based and suspension-based. Solution-based methods correspond to electroplating or electrolytic deposition (ELD), where metallic films condense from a precursor solution under a defined potential. Specific layer compositions require careful tuning of bath and process parameters, which also allows targeted adjustment of coating properties. Oxidic films are formed after deposition via suitable heat treatments. For interconnect protection, electroplating has a noticeable laboratory and demonstrator-scale literature base with promising results, especially for common Mn-Co spinels.[156–158]

However, this approach faces hurdles. Bath definition is inherently complex, and controlling phase transformation with associated stress evolution during subsequent high-temperature treatment is challenging. Electrolytes typically comprise an aqueous solution of the main salt (e.g., nitrate, borate, or citrate of the metal to be plated), a supporting salt, a pH buffer agent, complexing agents, and further additives.[159] Precise definition of the solution and process parameters, such as current density, deposition time, and bath temperature, is essential for high coating quality. Varying composition and co-depositing complex, accurate chemistries therefore remain difficult.[159]

Against this background, depositing the target stoichiometry directly from a suspension via electrically driven transport is particularly attractive. The corresponding deposition technique is named electrophoretic deposition (EPD). EPD is used at large scale in various application domains and industries, as especially for bio-medical purposes.[160,161] It is flexible with respect to component geometry, surface structuring, and coating materials. Consequently, this work investigates EPD as a promising method and examines it in detail in the following section.

2.4. Electrophoretic Deposition (EPD)

EPD offers highly flexible applicability with respect to suitable materials, their combinations, and substrate architectures. Conductive substrates of various types and forms can be used, including flat sheets from bulk materials as well as meshes, foams, or comparable structures. If the substrate is not intrinsically conductive, conductivity can be

provided by depositing conductive thin films such as Pt or C, for example via PVD techniques like sputtering.[162]

A wide portfolio of material classes is accessible. While this work focuses on oxide-ceramic layers, particularly spinels, other oxides of relevance in the SOC context such as perovskites and fluorites can also be deposited, same as non-oxide ceramics.[162,163] EPD further enables the deposition of fine metallic particles and metal oxides/hydroxides, multicomponent systems and composites, polymers and organic particles, and carbon-based materials. As noted, a major application field is the biomedical sector, including deposition of bioactive glasses, hydroxyapatite, and even biological species such as proteins.[161–164]

Given the focus on oxide-ceramic protection layers, the following concentrates on mechanisms and parameters most relevant in this context, while the fundamental principles remain transferable to other applications. Therefore, this chapter introduces the fundamentals required to understand the operation of EPD, covering the deposition mechanism, key influencing factors in practice, and options for process control with regards to the production of thin ceramic coatings. An overview of EPD for SOC interconnect coatings then consolidates the current state of the field. The relevant process window is derived by comparing parameters reported in existing studies, which forms the baseline for this work. Particularly valuable reviews summarizing EPD fundamentals – including relevant mechanisms, applications, and kinetic considerations – were authored by Besra and Liu[162] and by Ferrari and Moreno[163], and serve as key references for the following sections.

2.4.1. Fundamental principles and mechanisms

The EPD method is based on field-induced transport of surface-charged particles through a liquid medium (suspension medium or electrolyte) towards the electrode to be coated. Electrophoretic transport requires an interfacial potential drop across the solid-liquid interface (electric double layer), which results in a certain electrophoretic mobility and particle drift in an applied field.

Surface charges in suspensions commonly arise from interactions of the particles with a polar medium, particularly water. In water, surface charging can result from (i) protonation/deprotonation of amphoteric surface hydroxyl groups (≡MOH), (ii) specific adsorption of electrolyte ions, and (iii) lattice defects/isomorphic substitution. For ceramic particles, the dominant mechanism is often acid-base charging of surface hydroxyls: $\equiv MOH + H^+ \rightleftharpoons \equiv MOH_2^+$ and $\equiv MOH + OH^- \rightleftharpoons \equiv MO^-$, leading to a strong pH dependence.[162,165]

Ions involved in surface charging are attracted to or repelled from the colloid depending on polarity, leading to the formation of an electric double layer. Its structure and the potential profile with distance from the particle surface are shown in Figure 15.

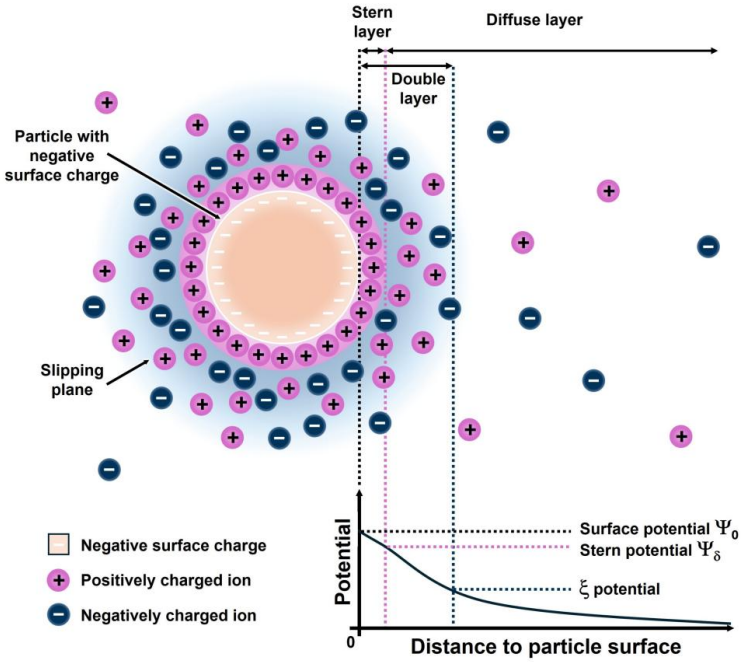

Figure 15: Schematic depiction of the electric double layer forming around a negatively charged colloid and the evolution of decreasing potential along the distance to the particle surface, including the charged surface, Stern layer, slipping plane and remaining diffuse layer or counter ions. Own illustration derived from[166].

The commonly used description is the Stern model as modified by Graham.[167,168] It defines a hypothetical layer, the Stern layer, where hydrated counterions reside closest to the surface. Remaining counterions populate the more distant diffuse layer. Interparticle interactions can be rationalized by the Derjaguin-Landau-Verwey-Overbeek (DLVO) theory, which describes colloidal stability as the balance between van der Waals attraction and electrostatic repulsion arising from overlap of the electrical double layers.

The experimentally accessible electrokinetic descriptor is the zeta potential (ζ), defined at the shear/slipping plane relative to the bulk electrolyte (as indicated in Figure 15).[169] ζ is strongly affected by pH and ionic strength (via surface charge regulation and electrostatic screening/Debye length), which is important for colloidal stability and interparticle interactions. It also determines electrical mobility and thus the velocity of colloids through the electrolyte. The strong pH dependency in aqueous media involves a specific pH, the isoelectric point (IEP), where the net potential vanishes and purely electrostatic stabilization is minimal. Operation close to the IEP is therefore typically avoided to obtain stable, electrophoretically depositable suspensions.[162]

For colloids suspended in a non-aqueous liquid, double-layer formation often requires additives that adsorb in ionic form on particle surfaces to enable material transport

between electrodes. A common surface-charge enhancer for ceramic colloids is I_2. Typical non-aqueous electrolytes include organic solvents such as ethanol, acetone, or isopropanol, as well as their mixtures.[162]

In acetone-I_2 systems, surface charging is frequently attributed to iodine-induced solvent reactions (often requiring trace water) that generate H^+ and I^-. Protonation of particle surfaces yields positive ζ and thus cathodic deposition.[162]

Stabilization of suspensions preventing agglomeration and sedimentation of dispersed particles can be achieved by different mechanisms. Beyond DLVO, additional physical interaction mechanisms such as steric stabilization and structural (solvation) forces are particularly useful. These effects become relevant, beyond particles simply dispersed in the liquid medium, when hydrophilic macromolecules with high molecular weight adsorb or bind to the surfaces and interact. The effective range is governed by the thickness and conformation of the adsorbed/grafted layer and is typically on the order of several nanometers (or more), depending on polymer architecture and solvent quality.[162]

Generating ceramic layers on conductive substrates by EPD can be described as a four-stage process, starting with colloid dispersion and surface charging, followed by electrophoretic transport and particle deposition. A schematic of the sequence is shown in Figure 16.

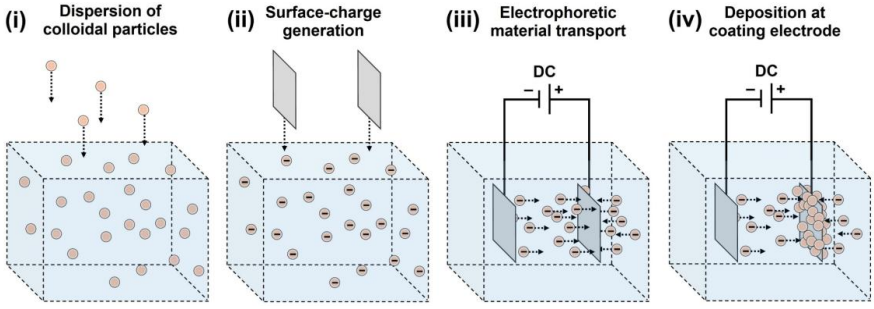

Figure 16: Process sequence of EPD, depicted for flat substrates: (i) dispersion of colloidal particles, (ii) surface charge built-up, (iii) electrophoretic material transport, and (iv) deposition at coating electrode. Own schematic after[170].

After deposition and drying, the ceramic layers constitute relatively fragile powder beds with only electrostatic and steric adhesion. Thermal post-treatment is required to obtain continuous, solid, and adhesive coatings.[162] As with other particle-based, low-temperature coating methods, including WPS and other processes in SOC cell manufacturing, suitable sintering steps must be designed.

With appropriate tuning of the deposition process and subsequent heat treatments, EPD can yield ceramic coatings with defined microstructural properties and thicknesses from around or even below one up to roughly 100 µm.[162] The specific levers for tailoring EPD coating characteristics and the underlying relationships are addressed in the next subsection.

2.4.2. Key parameters and process control

Decisive parameters for producing ceramic layers on the substrate span the entire process chain and comprise both material- and process-related factors. On the materials side, the particles, their interaction with the electrolyte, and the substrate must be considered. The individual influence factors can be summarized by the Hamaker equation[171], which describes the deposited mass m (g) on a substrate:

$$m = C_s \mu S E t \tag{2.9}$$

where C_s (g·cm^{-3}) is the solid load in the suspension, μ (cm^2·s^{-1}·V^{-1}) the electrophoretic mobility of the particles, S (cm^2) the coated area, E (V·cm^{-1}) the applied electric field, and t (s) the deposition time. The electric field results simplified as a quotient of potential drop and electrode distance. The electrophoretic mobility is a quantity that depends on the particles and the electrolyte and can be calculated as:

$$\mu = \frac{\varepsilon \zeta}{\eta} = \frac{\nu}{E} \tag{2.10}$$

Here, ε (F·m^{-1}) is the dielectric constant of the electrolyte, η (Pa·s) its dynamic viscosity, ζ (mV) is the Zeta-potential and ν (m·s^{-1}) the particle velocity, which is directly related to electrophoretic mobility via the applied electric field.

The linear relationship in Equation 2.9, which implies straightforward control of deposition in terms of deposited mass, and thus thickness, is highly relevant in practice and can serve as a basis for process design in typical applications. However, the validity of this idealized description generally holds for short deposition times with approximately constant conditions and small coating thicknesses. Extending the mathematical description to include additional aspects is useful, in particular particle adhesion behavior and suspension depletion during deposition.

Sarkar and Nicholson[165] contributed to these descriptions and first introduced the "sticking factor" $f \leq 1$ (with $f = 1$ for ideal coating efficiency) to quantify deposition efficiency by accounting only for particles that actually deposit. For the Hamaker equation, the following simplified expression for the deposition rate is obtained for infinitesimally small times, neglecting depletion:

$$\frac{dm}{dt} = f C_s \mu S E \tag{2.11}$$

The depletion of the suspension, already within a single coating pass, becomes non-negligible for longer or practical deposition times and especially when reusing suspensions. The deposited mass and the solid load can then be described as:

$$m = V(C_{s,0} - C_s) = \frac{m_0}{C_{s,0}}(C_{s,0} - C_s) \tag{2.12}$$

where V (cm^3) is the suspension volume, $C_{s,0}$ (g·cm^{-3}) the initial solid load, and m_0 (g) the total particle mass in the initial suspension. These quantities are related by:

$$C_{s,0} = \frac{m_0}{V_0} \tag{2.13}$$

Thus, for Equation 2.12:

$$C_s = C_{s,0}\left(1 - \frac{m}{m_0}\right) \tag{2.14}$$

Combining Equations 2.14 and 2.11 yields:

$$\frac{d}{dt}\left(\frac{m}{m_0}\right) = \frac{1}{\tau}\left(1 - \frac{m}{m_0}\right) \tag{2.15}$$

Here, τ (s) is defined as the characteristic timescale and is given by:

$$\tau = \frac{V}{f\mu SE} \tag{2.16}$$

Assuming a stable suspension without mass loss by sedimentation – which means depletion only by deposition – and an initial condition of $m(0) = 0$ at $t = 0$, the solution to Equation 2.15 is:

$$m = m_0(1 - \mathrm{e}^{-t/\tau}) \tag{2.17}$$

This approach is widely accepted in the literature to describe the deposited mass while accounting for changes in suspension concentration. For short time intervals, this description reduces to the Hamaker equation (Eq. 2.9).

Another aspect with strong influence on ongoing layer build-up, and one that depends markedly on the material systems and various suspension and process parameters, is the effect of the growing deposit itself. The conductivity or resistance of this layer relative to the electrical characteristics of the suspension is critical here and was incorporated by Sarkar and Nicholson into their model.[165] They considered deposition at constant potential with a deposit conductivity lower than that of the suspension. The effect of varying resistances on the electric field acting on the suspension is described as:

$$E = \frac{\Delta U}{L + \delta((\rho_s/\rho_d) - 1)} \tag{2.18}$$

where ΔU (V) is the potential drop between the electrodes and L (cm) their separation. The resistivities of the suspension and the deposit are ρ_s and ρ_d (Ω·cm), respectively, and the deposit thickness is δ (cm), further defined as:

$$\delta = \frac{V_d}{S} = \frac{m/C_d}{S} \tag{2.19}$$

In this simple relation, V_d (cm^3) is the deposit volume and C_d (g·cm^{-3}) the deposit density. Combining Equations 2.18 and 2.19 gives:

$$E = \frac{\Delta U}{L + R'm} \tag{2.20}$$

with R' (cm·g^{-1}) as a material- and system-specific constant defined as:

$$R' = \frac{(\rho_s/\rho_d) - 1}{C_d S} \tag{2.21}$$

To obtain a general expression, Equations 2.11, 2.12, and 2.18 are combined, resulting in:

$$\frac{d}{dt}\left(\frac{m}{m_0}\right) = k'\left(1 - \frac{m}{m_0}\right) \tag{2.22}$$

where k' is the "kinetics parameter," defined as:

$$k' = \frac{f\mu S}{V} \tag{2.23}$$

Solving Equation 2.22 with the same boundary conditions as for Equation 2.15 yields the general expression for deposition kinetics:

$$R'm(t) + (R'm_0 + L)\ln\left(\frac{m_0 - m(t)}{m_0}\right) + k'\Delta\psi t = 0 \tag{2.24}$$

This approach reduces to Equation 2.17 when similar resistive contributions from suspension and deposit are expected ($\rho_s = \rho_d$). Hence, under potentiostatic deposition of thin layers, at short deposition times, and assuming stable, non-sedimenting suspensions within the EPD process, the simplified Hamaker equation remains valid. There are, however, further theoretical and experimental considerations that extend deposition kinetics to additional factors and conditions. For example, Sarkar and Nicholson[165], later extended by Anné et al.[172], incorporated highly concentrated suspensions (particle mass fractions > 0.2) to create thick deposits, and included galvanostatic or constant-current conditions, which were later supported experimentally by Ma and Cheng[173]. Further additions to the Sarkar-Nicholson model are provided in the work of Biesheuvel and Verweij[174], who proposed extensions to non-planar, e.g., cylindrical, geometries. For the application case addressed in this work, and as broadly accepted in practice, the model derived above – especially the simplest form of the Hamaker equation – is adequate and forms the basis for iterative process optimization.

When classifying the influencing factors relevant for practical EPD coatings beyond the purely theoretical-kinetic considerations – these factors are implicitly reflected in the above quantities – it is useful to group them into pre-processing, the deposition process itself, and post-processing. Within these groups, several levers are available to tailor layer formation and the resulting coating properties. Table 2 provides an overview of these aspects, separated into the three named process sections.

Table 2: Overview on key parameter fields relevant within the preparation of ceramic coatings via EPD, dividing into pre-processing, the deposition process itself and post-processing.

Pre-processing (suspension)	Deposition process	Post-processing
Primary particles	Potential/current	Drying
Medium	Signal	Mechanical treatment
Additives	Duration	Thermal treatment
Powder/suspension treatment	Substrate	
	Electrode(s)	

An itemized breakdown of the parameter fields, their influences, and corresponding levers to adjust the deposition process and the resulting coatings is given below.

Pre-processing (suspension)

Setting up the deposition begins with selecting the starting materials – primary particles, medium, and possible additives – and processing them into a suspension. This preparation establishes the basis for a well-aligned EPD process and for homogeneous, reproducible coatings. Careful matching of the constituents to the process is essential for high coating quality.

Primary particles

The choice of primary particles is the most influential factor for final coating properties, since the chemical composition defines layer chemistry, and surface chemistry governs deposition behavior. Targeted control of particle size and size distribution, morphology, and specific surface area enables tuning of accessible surface charge in the electrolyte and thus, via the mobility μ, the deposition rate. For very small particle sizes in the nanometer range, a slowdown of deposition kinetics is observed.[175] Increased agglomeration tendency under insufficient dispersion and higher suspension viscosity η (cf. Eq. 2.10) contribute to this effect. Nanopowders can yield highly homogeneous and dense thin layers[176], although the high green density further slows deposition kinetics. For larger particle diameters, the risk of sedimentation must be considered with respect to suspension stability.

Beyond narrow, monomodal distributions, broader PSDs and targeted powder mixing can raise green packing density. For SOC interconnect protective coatings, Ajdys et al. showed that bimodal PSDs increase the green density of Mn-Co spinel coatings and, after heat treatment, lead to greater densification and improved protectivity.[177] Moreover, particle shape can be influential. While platelets or needles can be used to engineer specific microstructures, a study by Laska and Bartmański[176] indicates that spherical particles are advantageous for homogeneous, adherent coatings with dense microstructures.

The solid load C_s is a key factor for suspension control and reproducible results (cf. Eqs. 2.12–2.14). It largely sets the required deposition time and thus the practicality of the process for industrial implementation. Low C_s can support especially uniform deposition

but result in low rates. Higher C_s accelerates deposition, yet highly loaded suspensions tend towards inhomogeneity due to turbulence and coagulation, and increased viscosity inhibits mobility (cf. Eq. 2.10). A constant solid load can be maintained by continuously feeding powder during deposition.

Medium

The second major factor is the medium, i.e., the fluid electrolyte. By enabling surface charging, it determines electrophoretic mobility and thus the kinetics. It acts via viscosity, dielectric permittivity, and the resulting zeta potential (cf. Eq. 2.10). Choosing between polar media (notably water) and non-polar organic solvents decides whether surface charges form intrinsically or require charge enhancers.

Organic media offer several advantages over aqueous electrolytes. Lower conductivities and higher dielectric constants can enable more effective deposition[162,178], and water electrolysis at the electrodes – and associated bubble entrapment – can be suppressed[179]. Literature however shows that adding organic solvent and using moderate voltages (below or around 50 V) can also sufficiently suppress electrolysis to achieve continuous layers, e.g.[180–182]. Non-aqueous media dry faster, which helps to avoid flow patterns and improves green-layer quality. In practice, water is often mixed with organic solvents such as ethanol to avoid charge enhancers while still obtaining good coating quality. This can also mitigate the stronger tendency for sedimentation and agglomeration seen in aqueous systems, although purely organic suspensions typically show higher stability and deposition rates.[162,179] Adjusting the medium also enables setting a suitable pH to avoid the IEP and to establish stable suspensions. In purely aqueous and mixed aqueous-organic media, zeta potentials around 30 mV are established as a stability criterion, whereas in purely organic media, lower thresholds (typically around 20 mV) are commonly adapted due thinner double layers and corresponding lower dielectric constants.[162]

Additives

Additives can stabilize suspensions and the dried layers. As discussed, surface-charge enhancers are common to ensure dispersion and mobility in nonpolar solvents. I_2 as standard is acting via the formation of protons and I^- ions[183,184] (see Section 2.4.1), although organic agents such as poly(diallyldimethylammonium chloride) (PDDA)[185] are also used. Typical dosages are below 1 $g \cdot l^{-1}$, and precise control is important to avoid defects such as cracks or inhomogeneities due to excessive ionic strength.[186] Polymers such as polyethylenimine can function as binders that co-deposit to form a wetting matrix. They are, however, less typical in EPD.[162,164] Binders may reduce defects and improve adhesion and handling, yet excessive amounts can slow and unevenly shape layer formation, since polar chain ends begin to dominate deposition and particle capture becomes insufficient.[187] A restrained use is preferable, and steric stabilization after drying is often sufficient, rendering polymers obsolete.

Powder and suspension treatments

Beyond composition and proportions, treatment of the powders and the mixed suspension is critical for reproducible quality. Mechanical methods such as mortar milling, grinding, and sieving tailor morphology and particle size. Powder washing can help to control surface chemistry and reduce impurities.[162] Suspension handling targets stability and homogeneity to prevent agglomeration or sedimentation before and during deposition and to ensure uniform particle distribution. Stirring and ultrasonication are common, prior to or even during deposition.

Deposition process

Starting from a well-tuned, stable suspension, the deposition process offers multiple levers, spanning operating parameters and modes as well as substrate and electrode design.

Potential and current

As discussed theoretically, kinetics can be controlled via voltage or current. Galvanostatic (constant-current) and potentiostatic (constant-voltage) operation show distinct characteristics, with voltage control being most common. Figure 17a and b sketch characteristic deposition curves for different modes and for different voltages under potentiostatic control, respectively.

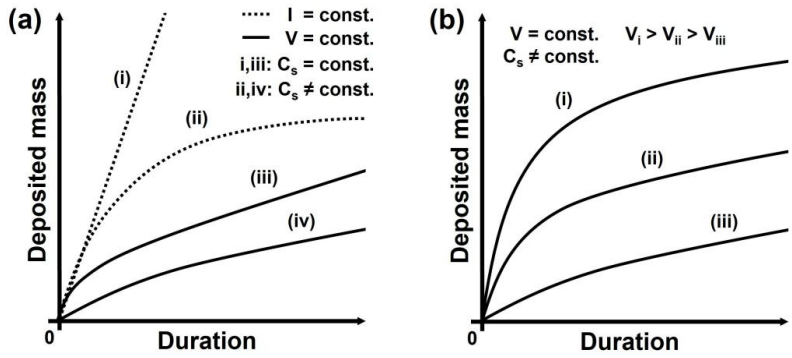

Figure 17: Schematic deposition curves for different parameter sets of EPD; (a) presenting galvanostatic (i,iii) and potentiostatic (ii,iv) operation at constant (i,ii) and decreasing (iii,iv) solid load, own graphic schematized after[188], and (b) presenting potentiostatic operation at decreasing solid load with different voltages ($V_i > V_{ii} > V_{iii}$), own graphic schematized after[189].

With current control, especially when continuously feeding powder, a near-linear deposition can be achieved, allowing direct mapping from time to deposited mass. For practicality, voltage control is typically used.[162]

Signal

While constant DC voltage is most widespread, pulsed potentials and oriented AC fields can address specific requirements. For aqueous EPD, Besra et al. showed that DC

operation with millisecond pulse durations suppresses pore formation compared to constant current.[190,191]

For AC potentials, longer unidirectional pulses are required to maintain directed transport. This can facilitate infiltration of porous substrates by continuously loading pores without early blockage at the outer surface, since material is alternately deposited and stripped. Several studies demonstrated this for protective coatings in porous metal substrates for MSCs.[118,192]

Duration

Depending on suspension and process parameters that set the kinetics, early times remain approximately linear, whereas at longer times the deposition rate flattens (cf. Figure 17b). At extended durations, possible loss of suspension stability must be considered. Otherwise, especially within the validity of the Hamaker relation, deposition time is an effective handle to set deposited mass and thus thickness, which is also common practice.[162]

Substrate

Substrate design and condition significantly influence coating quality and the process itself. Uniform electron supply and removal must be ensured to obtain uniform layers. Metallic substrates, as used here, offer ideal conditions. Poorly conducting or multiphase substrates such as cermets pose greater challenges. Surface roughness is relevant and can promote defects if in the same range as the targeted thickness.

In addition to flat substrates, geometries with higher specific surface area, such as meshes and foams, are applicable. Since macroscopic area enters linearly in the deposited mass, thickness control via the Hamaker equation remains feasible. However, distributing the deposit over larger specific area reduces local thickness and must be accounted for in process design. EPD is also suitable for substrates with macroscopic structuring on the order of the electrode spacing, including classical interconnect flow-field geometries. Local variations in deposition conditions, such as gradients in field strength or local depletion, shape the layer. Achieving uniform, continuous layers here becomes more complex and hinges on electrode design, which in general offers substantial scope for optimization in EPD.

Electrodes

Electrode-related aspects determine deposition kinetics and can be adjusted in practice to optimize results. Electrodes must be chemically stable under the applied potential and in sometimes corrosive electrolytes. Various geometries are possible depending on the substrate, and adapting to more complex forms can enable coating of bodies such as tubes or spheres.

Key factors beyond outer shape include electrode size relative to the active coated area, spacing to the substrate, and configuration, e.g., single counter-electrode or multiple, and

symmetric opposed plates for planar setups. All directly influence the local electric field, producing a coupled design space. Computational and empirical approaches can support optimized electrode design.

Post-processing

While deposition sets the basis for integer and uniform layers, subsequent handling of the initially fragile and non-densified particle networks is decisive to avoid defects and for the final microstructure and properties. Immediate drying after deposition, any potential mechanical treatment, and especially the thermal processing must be considered.

Drying

Drying of the powder load on the substrate is governed by material factors such as medium type and volatility, particle morphology and size (thus green density), and layer thickness. It is a sensitive step where irreversible defects can form, including flow patterns from mass re-distribution, pores, or cracks, which may persist through later treatments. Drying is therefore not negligible and should proceed under stable conditions to prevent avoidable drying-induced stresses and defects.

Mechanical treatment

Mechanical consolidation by applying pressure prior to sintering can be considered to increase green density and improve densification. Due to the limited robustness of green layers and the limitation to specific surface geometries, this approach however is laborious and is only rarely discussed in the literature.[193] Typically, consolidation is achieved by optimizing powder and deposition parameters and, especially, by appropriate thermal processing.

Thermal treatments

As outlined in Section 2.1.3 for other particle-based manufacturing steps in SOC production, heat treatment is integral to the ceramic process chain and decisive for functional coating properties. Different sintering techniques and parameters influence microstructure formation and ensure layer integrity without classic defects such as cracks or delamination. Matching temperature, heating and cooling rates, and dwell times is essential, particularly under complex stress states arising from constrained sintering of thin films on dissimilar substrates. Atmosphere selection is another key factor. Multistep "reactive" sintering, first under reducing conditions and subsequently under oxidizing conditions in air, is commonly employed for spinels to promote densification, as noted earlier.

2.4.3. Application of EPD for SOC interconnect coatings

EPD was recognized at an early stage by the SOC community as an effective method to produce uniform functional layers in the few-micrometer range and has been explored for various purposes. The first studies by Ishihara et al. in the early 1990s targeted optimization of YSZ electrolytes and LSM air electrodes.[183,194,195] Around the turn of the

millennium, Zhitomirsky and Petric extended applications to Ni-YSZ cermets and, already then, to corrosion protection layers based on GDC.[196,197]

While EPD never became the standard for the primary functional layers in SOCs – where tape casting, screen printing, and PVD have been established – it has been continuously pursued for interconnect protective coatings.[23,25] Studies addressed diverse aspects including material systems, parameter optimization, and performance indicators. Most investigations remained at laboratory scale on coupons of a few square centimeters, yet they covered a wide range of materials and combinations.

On the steel side, in addition to studies focusing on state-of-the-art interconnect steels such as Crofer22APU (e.g.[193,198,199]) and Crofer22H (e.g.[200–202]) – which are also used here as standard substrates – several works aimed to qualify lower-cost commercial alloys. The ferritic stainless-steel grades AISI430 (e.g.[105,200,203]) and AISI441 (e.g.[199,200,204]) were investigated as well.

Regarding coating materials, the literature reflects the broader field of interconnect coatings, spanning perovskites[205,206] from earlier studies and composites[207], and, most prominently and currently most widespread, spinels[208]. For EPD coatings, Mn-Co spinels with various stoichiometries[180,200] and dopant additions[198,199,203] have been the primary focus. The Mn-Cu spinel family[115,120,209] has also been examined, as well as other spinel systems such as Mn-Ni[210] and Ni-Fe[211]. Individual studies demonstrate that more complex compositions can be formed via *in-situ* co-deposition.[181,182,212]

Beyond single-layer EPD coatings, combined approaches with other methods have occasionally been explored. Examples include coupling with electrolytic deposition[213], magnetron sputtering[214], and dip-coating[215] to enhance electrical and protective properties. Nevertheless, single-layer EPD remains the most widely studied route. Considering industrial implementability and cost efficiency, multi-step hybrids, even when offering slight performance advantages, are not preferred.

Accordingly, the focus here is on the state of single-step EPD coatings. A review by Zanchi et al. published in 2021 surveyed the literature and outlined a process window for potentiostatic DC-EPD of relevant spinels on ferritic stainless steels.[208] Incorporating this base and more recent studies, Table 3 provides an overview of typical boundary conditions for the preparation of EPD coatings along the previously outlined process sections and serves as orientation for this work.

Table 3: Overview on selected key parameters within the EPD process, as used in relevant literature on interconnect protective spinel coatings, divided after pre-processing, the deposition process and post-processing.

	Parameter	Range / specification	Ref.
Pre-processing	Particle size (d50)	60 nm–~1 µm	208,216
	Solid load	7.9–39.4 g·l^{-1}	200,217
	Medium	Ethanol, ethanol/distilled water, ethanol/acetone, ethanol/isopropanol	180,193,216,217
	I_2 concentration	None or 0.15–1.09 g·l^{-1}	119,216
	Powder treatment	Roll milling, ball milling	177,217
	Suspension treatment	Stirring, ultrasonication	102,118
Deposition process	Potential	5–140 V	180,203
	Duration	5 s–10 min	180,203
	Substrate treatment	Cleaning in acetone and/or ethanol in ultrasonic bath	198,218
	Electrode distance	10 or 15 mm	182,200
	Electrode constellation	2 or 3 electrode setup	118,213
Post-processing	Reduction temperature	800–1100°C	203,212
	Reduction time	2–24 h	119,201
	H_2 content at reduction	2–9 vol%	202,217
	Oxidation temperature	750–1100°C	180,203
	Oxidation time	1–100 h	216,219

*Data derived from relevant literature sources, the parameter-set might not be exhaustive.

To evaluate suitability of EPD coatings as protective coatings for interconnects, various performance indicators are used. In general, suppression of steel corrosion – indicated by mass gain and Cr-oxide scale growth – and the maintenance of low ASR values serve as the principal metrics.[208] Chromium retention is also assessed in a few studies via measured Cr evaporation.[151,220] Because the analytical techniques are not standardized and differ in procedural parameters and equipment, direct comparison of reported results is limited.

To sidestep the general comparability issue in the literature, Reddy et al. recently conducted a comprehensive comparison of coating systems.[122] Under representative SOFC conditions on Crofer22APU substrates, the study included the Jülich MCF-APS coating and the commercial Co-Ce PVD coating from Alleima, and within other coating systems also several EPD coatings. Three Mn-spinel-based coatings deposited exclusively by EPD were examined, all previously characterized in detail: a stoichiometric Mn-Co spinel $MnCo_2O_4$ (MnCo-EPD)[151,200], an Fe- and Cu-doped Mn-Co spinel $Mn_{1.2}Co_{1.2}Fe_{0.3}Cu_{0.3}O_4$ (MCF-Cu-EPD)[221,222], and a Cu-Mn spinel $CuMn_{1.8}O_4$ (MnCu-EPD)[199,209,219]. Coating thicknesses were comparable at about 15 µm. Figure 18 summarizes *ex-situ*-determined ASR after 3000 h in air at 800°C and cumulative Cr evaporation after 1000 h.

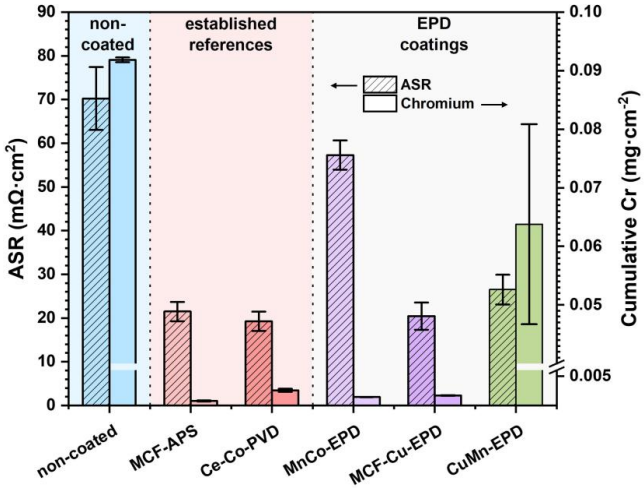

Figure 18: Own depiction of the key results from the experimental comparison of different coating systems applied to Crofer22APU specimen, after exposure in air at 800°C, performed by Reddy et al., including *ex-situ* ASR values (after 3000 h exposure) and cumulative Cr evaporation (after 1000 h, except for the uncoated specimen, exposed for 500 h).[122]

The established systems – Jülich's MCF-APS and Alleima's Ce-Co-PVD – showed strong suppression of oxidation-related ASR increase and of Cr evaporation, the latter reduced by roughly two orders of magnitude relative to the uncoated reference, especially pronounced by MCF-APS. Effective suppression of Cr volatilization was also demonstrated for Mn-Co-spinel EPD coatings, whereas the Cu-Mn spinel showed only little reduction compared to bare steel (order of magnitude remains), and pronounced scatter. With respect to electrical resistance dominated by oxide scale formation, Fe- and Cu-doped Mn-Co spinel EPD coatings were competitive, showing major improvement over the undoped spinel and acceptable values for the Cu-Mn spinel. Overall, the study provides a solid indication that EPD can yield effective spinel protective coatings, while highlighting the importance of doping. As discussed in Section 2.3.1, this is particularly relevant for Mn-Cu-based spinels and appears critical for effective Cr retention and cell protection.

Against this background, the Basu group refined their initial $CuMn_{1.8}O_4$ composition through targeted Ni doping, proposing $CuMn_{1.8}Ni_{2.0}O_4$ with improved properties and good suitability for EPD in several recent studies.[117,118] This supports the view that EPD is at an advanced and promising stage for interconnect coatings.

EPD has also been demonstrated beyond small coupon formats. In two studies within the group around Smeacetto, coatings were scaled to real component size.[223,224] SOFC stack tests conducted in this context already indicated protection and functionality of the deposited Mn-Co spinel layers, and potential for other system designs could be estimated. The limited scope of the reported results, however, does not resolve potential scaling challenges, particularly when using aqueous suspensions. Moreover, development of

component-scale coatings for existing stack concepts is case-specific, influenced not only by suspension and material system but also by geometry and by adjacent steps in stack assembly, especially thermal processing.

This raises an underrepresented question in the literature regarding integration of EPD coatings into manufacturing flows, considering typical thermal process chains, classical geometries such as gas-distributor structures, and compatibility with adjacent components. Systematic comparison with alternative coating methods is likewise important. Given the lacking economic competitiveness of SOCs versus other hydrogen technologies and broader ecological factors, continued cost reduction and improved sustainability are essential in designing coating processes.

2.5. Cost reduction and sustainability perspective

It is crucial to capture hurdles and potentials for SOCs with respect to economic and ecological aspects – i.e., broader sustainability – systemically and to develop targeted optimization strategies. The following adopts a generally applicable perspective while reflecting the Jülich research context. On the one hand, detailed formulations and process configurations – especially those needed for explicit accounting – are often proprietary in industrial settings. On the other hand, the Jülich SOC research aims to deliver system-level solutions of industrial relevance. After outlining the role of the interconnect within this question and developing possible strategies, a concise overview of a suitable evaluation framework is provided: the life cycle assessment (LCA).

2.5.1. Economical and ecological relevance of interconnects

When positioning SOCs against other green-hydrogen technologies, a substantial gap in competitiveness remains. Although unique features such as reversible operation and high efficiencies under combined heat and power may have strong impact, estimations on green hydrogen costs (though studies differ, dependant on specific assumptions and boundary conditions) still see SOEC far behind the relevant alternatives. A perspective study within the EA Greenhouse Gas R&D Programme estimates the levelized costs of hydrogen in 2030 for SOEC at 58 €·kg^{-1} whereas PEM electrolysis and alkaline electrolysis are placed at 36 and 31 €·kg^{-1}, respectively.[225] Comprehensive LCA studies on SOCs, as highlighted in a review by Salim et al., reflect the substantial potential of SOCs as a clean hydrogen technology compared to alternatives, both in ecological terms and in economic potential when effectively deployed.[226] At the same time, manufacturing remains a financial hurdle, and establishing industrial production chains is a key lever for unlocking potential and achieving economic competitiveness.

Harboe et al. developed a manufacturing cost model[11] for two Jülich stack concepts and, along the production chain, calculated significant cost savings with increasing annual output. Raising production from 1 MW/y to 25 MW/y improved overall direct cost

efficiency by a factor of 2 or 3–4, depending on stack design.[11] The concepts differ primarily in interconnect designs and manufacturing routes. The first is based on comparatively thick steel parts, milled from bulk, and the second integrates hydro-formed thin-sheet steel parts. The bulk-based concept resembles the previously introduced type F10 but employs larger cells (20 cm rather than 10 cm edge length) and is denoted F'''20. The thin-sheet concept, termed CS^V, is the latest in a stack line designed for straightforward manufacturing and material savings with a focus on industrialization. A particularly strong reduction of total cost with higher production volumes is likewise expected for the CS^V design. A schematic of this stack type is shown in Figure 19.

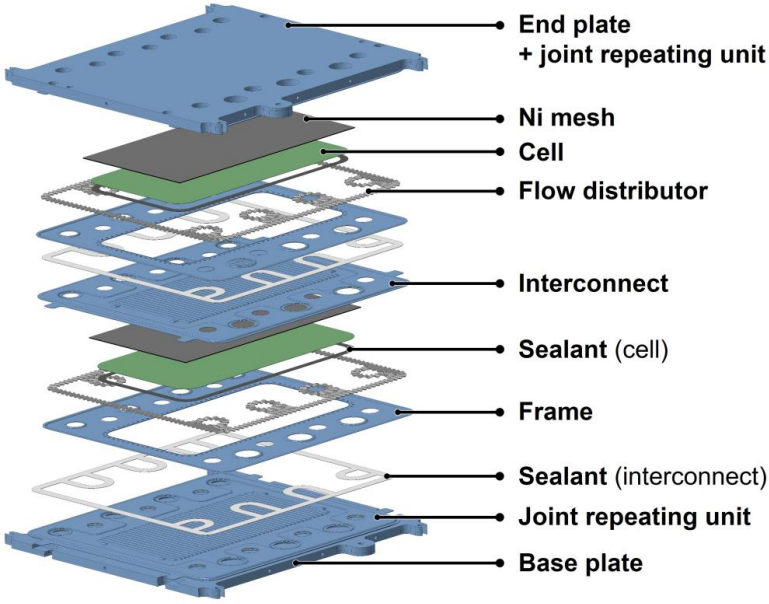

Figure 19: Technical drawing of a Jülich four-layer CS^V-type SOC stack, incorporating two joint and two exploded repeating units. Drawing provided by W. A. Mertens (FZJ-ITE).

The study of Harboe et al. provides cost estimates and breakdowns for several annual volumes and differentiates material and component contributions to total mass, followed by a material-cost breakdown. The latter depends on production volume and associated material pricing. While data relevance may be constrained by geopolitical developments and customs policies, the study still offers a solid basis for identifying cost and resource saving potentials and is an important foundation for this work. An overview of key results, highlighting differences between and within the stack concepts, is given in Figure 20.

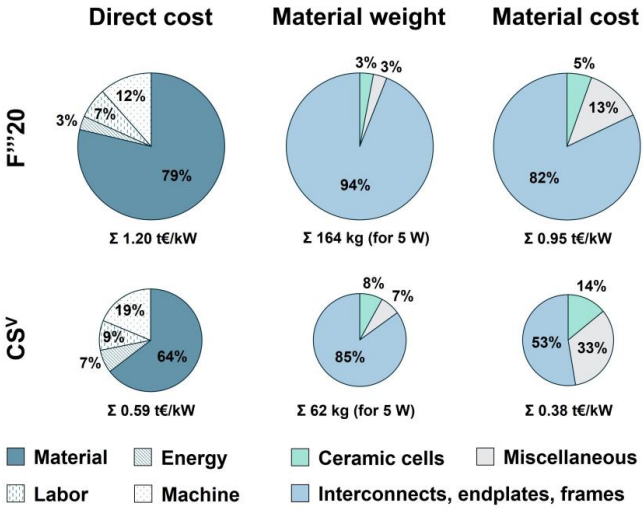

Figure 20: Own depiction of relevant findings in Harboe et al.'s manufacturing cost model, highlighting differences and shares in direct costs, material weights, and material costs, comparing the Jülich stack concepts F'''20 and CS^{V}, assuming an annual manufacturing volume of 25 MW. The circles' areal ratio within one category reflects the total differences between F'''20 and CS^{V}. Data derived and/or calculated from[11].

Overall, the study clearly indicates that switching to a lightweight stack concept yields substantial savings in total costs and, even more, in material use and material costs, with the latter two reduced by over 60%. Closely related is the dominant share of material in total cost, which decreases when shifting the concept. Analysis of material fractions and associated costs shows that, for comparable cell concepts, this is driven by the significant reduction of stainless steel, representing major potential for both SOC compatibility and resource footprint. Indeed, replacing ceramic interconnects with metallic ones has already provided a meaningful step through lower material cost and simpler processing. However, Harboe et al. additionally identify the transition from specific Crofer grades to commercial standard steels as a key additional lever.[11]

Progress has also been made in recycling SOC stacks at end-of-use (EoU) or end-of-life (EoL), offering credible potential for cost and resource efficiency. After Sarner et al.[227] outlined options for different SOC types with focus on FESCs, further studies followed[228–232] with concrete technological approaches to individual components. In a comprehensive study[233], Kaiser et al. combined several routes and showed how open-loop and closed-loop processes could recover material constituents, including functional layers subdivided into perovskites, fluorites, etc., with recovery rates largely above 90% and constitutional purities often beyond 98%.

For the largest mass fraction from a resource perspective, stainless steel parts, promising results were also obtained. Recent studies by Lastam et al. on the recycling of interconnect steels from EoU/EoL stacks via pyrometallurgical processing demonstrated

markedly increased material efficiency over the lifetime.[234,235] For example, Crofer22APU EoU stack components became directly recoverable after acid pickling through pyrometallurgical processing into a common steel grade (AISI304) with yields above 95%.[235]

Nonetheless, re- and down-cycling are only one pillar of more sustainable and resource-efficient SOC stacks. Material savings and the use of widely available compositions, rather than dedicated specialty grades, should be central goals. Component and stack design for re-use and recoverability can be emphasized further. In all cases, interconnects play a key role, making it worthwhile to develop specific strategies for them.

2.5.2. Strategies towards cost reduction and sustainability

Based on the aspects outlined in Section 2.3.3 for interconnect coating methods and the relationships presented in Section 2.5.1, several core approaches can be distilled to better realize the economical and ecological potential of the components. These approaches define the guiding framework of this work. The intent is to maintain general applicability, while starting from the current Jülich standard – APS-MCF coatings on F10 or F'''20 interconnects (or comparable), manufactured from bulk Crofer22APU steel. The strategy of this work follows three core directions:

(i) **Thinner interconnects:** Switching from heavy-weight designs, machined from bulk material to shaped, sheet-based light-weight designs accompanied by the selection of suitable, non-destructive coating methods.

(ii) **Thinner coatings:** Reducing coating thicknesses while guaranteeing high uniformity and integrity standards by establishing efficient and reliable coating approaches.

(iii) **Alternative materials:** Enabling the use of commercial stainless-steel grades and Co-free coating compositions by introducing highly effective and flexible deposition methods.

With the transition towards thin-sheet interconnect designs, replacing the Jülich standard APS route becomes a focal point. The previously introduced suspension-based techniques WPS and EPD step forward as suitable processes. As a highly flexible non-line-of-sight method, EPD is regarded as particularly promising for typical, demanding interconnect geometries. For alternative material concepts and combinations, the widely used ferritic stainless steel AISI430 is of interest, while the family of Cu-Mn spinels, especially in doped form with Fe or Ni, appears essential for coatings.

System-level LCA of stacks has already helped to identify key levers to improve sustainability. As stainless-steel components are expected to become thinner and impact decreases, their coatings and the associated technologies move further into focus.

Comparative assessment of relevant coating technologies is therefore an important step to select suitable methods on a foundation that goes beyond purely technical criteria.

2.5.3. Life cycle assessment (LCA) of coating technologies

The environmental life cycle assessment, usually abbreviated LCA, is an essential – though not exclusive – component of a broader life cycle sustainability assessment (LCSA).[236] While the social life cycle assessment (S-LCA) addresses the social dimension and life cycle costing (LCC) the economic dimension, the (environmental) LCA captures the overall ecological impacts of a product, an isolated process, or a human activity.[236,237] It considers the entire value chain, from raw material extraction through manufacturing and use to end-of-life disposal. In this way, LCA serves as a robust environmental management instrument, with initial implications for social and economic aspects as well.[237]

LCA is highly effective for comparing products or processes and for making decisions on a solid basis regarding potential environmental trade-offs. It reveals how problematic influences propagate across process steps, media, or locations and offers options to address them.[237] The procedure is standardized by the International Organization for Standardization (ISO) [238] and comprises four main phases:

(i) **Defining goal and scope:** Research question, system boundaries and functional unit (quantified term for the product system's performance) are set precisely.

(ii) **Compiling inventory:** Relevant material and energy inputs as well as environmental releases (life cycle inventory (LCI) analysis) are collected.

(iii) **Evaluating impacts:** Potential environmental impacts that are associated with inputs and emissions (life cycle impact assessment (LCIA)) are calculated.

(iv) **Interpreting results:** Output data is discussed and put into perspective in order to derive recommendation for actions.[237]

Following this scheme, one or more comparative assessments can be carried out for the case at hand. It is important to ensure transparency of both the underlying data and the related uncertainties, to document them openly, and to regard LCA as iterative rather than linear. A single quantitative "winner" needs not always to emerge; articulating qualitative differences can be equally valuable.[237]

For coatings and coating technologies for interconnects, the LCA procedure concretely entails, first, defining the intended targets – e.g., comparison of different technologies or materials with/without considering interconnect material or manufacturing – and establishing starting assumptions, such as scaling effects. Next is identifying suitable databases (e.g., at EU level EcoInvent) and determining energy and material flow data (e.g., ceramic powder, electricity) as well as releases (e.g., CO_2, direct/indirect), consistent with the predefined assumptions. On this basis, impacts for the considered categories are

calculated according to the models and boundary conditions, for example climate change potential, acidification, or resource consumption. Finally, results are organized and compared by category to derive a well-founded evaluation of environmental suitability, for instance oriented towards minimal consumption of critical raw materials or greenhouse-gas emissions.

While social and economic implications (e.g., from energy use and critical raw materials with problematic value chains such as Co) can already be inferred, explicit S-LCAs and LCCs are often useful to support robust decisions. Coupling LCA with a technical evaluation – here, coating performance or protectivity – can be particularly effective. This way, enhanced protective performance can be paired with resource-efficient production, laying the groundwork for more sustainable interconnects – and, in turn, for thinner components and more cost-effective steels.

3. Methodology

This chapter introduces the materials selected for this work, the experimental approaches, characterization techniques and their fundamentals, and the performance evaluations conducted. Beyond the previous theoretical foundations, it conveys practice-relevant procedures and metrics and provides a structured overview of the experiments. The scope spans material selection, deposition methods and thermal post-treatments, a set of exposure tests and performance measurements, and, finally, the transfer of developments to relevant component geometries and sizes, including an ecological assessment of the coating routes.

3.1. Materials

This section presents the materials used in the experimental work and their role in the study design. It lists the steel grades and formats selected from the literature base outlined above, as well as the spinel coating materials.

3.1.1. Ferritic stainless steels

The steel set includes tailor-made grades designed for SOC service and conventional ferritic stainless steels that are widely discussed in research and relevant for industrial use. As tailored steels, the established types Crofer22APU and Crofer22H have been selected, displaying the state-of-the-art materials, with regards to their performance characteristics and long-term stability (details in Section 2.1.6).[239,36] Crofer22H features enhanced mechanical properties, particularly improved creep resistance, due to the precipitation of intermetallic Laves phases[53,240] and is consequently of particular interest for thin-sheet applications. As these are increasingly required by modern lightweight interconnect designs, as for the Jülich CS^{V} stack type (see Section 2.5.1, esp. Figure 19), Crofer22H is considered with attention here. The earlier developed and still widely established Crofer22APU serves as the base material for the Jülich F"'20 and F10 stack types (see Sections 2.1.4, esp. Figure 6, and 2.5.1) and is treated as a relevant benchmark in this study.

Within the pathway of implementing conventional, less expensive grades, AISI430 was selected because it combines sufficient chromium content with suitable thermo-mechanical properties and is frequently reported as candidates in the literature (details in Section 2.1.6). The compositions of all three steels, together with their CTE values up to 800°C, are summarized in Table 4. Another highly promising conventional grade, AISI441, was partially included in the investigations in NOUVEAU as well. As provision of thin sheets for suspension-based coating applications was not possible for the project partner, however, investigations were limited to few-millimeter stock material for thermal spray coatings and bare sheets. The results are included in D. Vakhrameev's dissertation[241].

Table 4: Chemical composition and CTE (up to 800°C) for the steel grades, used in this work: Crofer22APU, Crofer22H, and AISI430.[242–244]

		Crofer22APU		Crofer22H		AISI430	
	Unit	min	max	min	max	min	max
Fe	–	Bal.	Bal.	Bal.	Bal.	Bal.	Bal.
Cr	wt%	20	24	20	24	16	18
C	wt%		0.3		0.3		0.08
N	wt%	–	–		0.04	–	–
S	wt%		0.02		0.006	0.015	0.03
Mn	wt%	0.30	0.80		0.80		1.00
Si	wt%		0.50	0.10	0.60		1.00
Ti	wt%	0.03	0.20	0.02	0.20	–	–
W	wt%	–	–	1.0	3.0	–	–
Nb	wt%	–	–	0.20	1.0	–	–
Cu	wt%		0.50		0.50	–	–
P	wt%		0.05		0.50		0.04
Ni	wt%	–	–		0.50	–	–
Al	wt%		0.50		0.1	–	–
La	wt%	0.04	0.20	0.04	0.20	–	–
CTE	10^{-6} K^{-1}		11.9		11.8		12

*Values as derived from manufacturers data sheets; actual compositions could deviate.

These grades were used for coating development, characterization, and testing, for scale-up to full-size components, and for reference measurements in the uncoated state. Several sample formats were therefore employed and described in the respective sections. In principle, rolled sheets were pre-cut to formats suitable for the coating procedures by mechanical and/or laser cutting. Sheet thicknesses were 300 and 500 µm for suspension-based coatings and 2 mm for thermal-spray coatings on flat sheets. Structured samples were taken from real stack components and therefore retained the actual thicknesses. Specific surface preparations required by each coating process are provided in the corresponding sections.

3.1.2. Spinel compositions

In this work, both a state-of-the-art composition with well-known functional properties and long-term stability and alternative, sustainability-oriented compositions were employed. At first, as the state-of-the-art composition, $MnCo_{1.9}Fe_{0.1}O_4$ (MCF) was chosen as it has been established at Forschungszentrum Jülich and beyond as a benchmark material for interconnect coatings both in laboratory-scale studies using different deposition techniques and in long-term stack tests exceeding 30,000 h (details in Section 2.3.1).[107,110–112,148] Therefore, in this work, MCF served as the reference composition.

As cobalt-free alternatives, two compositions were selected based on reports from literature and Kiefer's PhD research[106]. Within the Mn-Cu spinel family – the most promising Co-free group – $CuMn_{1.9}Fe_{0.1}O_4$ (CMF) and $CuMn_{1.8}Ni_{0.2}O_4$ (CMN) were chosen, as proposed by Kiefer and by the group around Basu, respectively (details in Section 2.3.1). These candidates were selected for closer evaluation as protective coatings. For CMF, interconnect-coating-relevant data are largely limited to Kiefer's work and several subsequent studies.[106,115,116] In contrast, Basu and co-workers conducted comprehensive investigations and demonstrated successful application of Mn-Cu spinel coatings by EPD. This technique – as also central here – was first adapted for such coatings by Huang et al. in 2008 and has been advanced continuously since then.[209] As noted above, follow-up studies of the Basu group indicated that Ni additions to basic Cu-Mn spinel improve stability and conductivity and facilitate processing by EPD, with 0.2 molar Ni identified as optimal. Therefore, $CuMn_{1.8}Ni_{0.2}O_4$ was also selected here.[117–121]

The three coating compositions – MCF, CMF, and CMN – were sourced from three suppliers. Commercial MCF and CMF powders were obtained from H.C. Starck (Selb, Germany) and KCeracell (Pyeongtaek, South Korea), respectively, while CMN powder was synthesized within the project NOUVEAU by Marion Technologies (Verniolle, France). Prior to implementation into coating development, the powders were proven for thermo-mechanical stability (further explained in Section 3.6.3). In general, powder preparation for the coating processes and the corresponding characterization are described in Sections 3.2, 3.3, and 3.6, respectively.

3.2. Established coating processes in Jülich

This chapter provides an overview of the methodologies and specifications of the coating techniques established at Forschungszentrum Jülich – APS and WPS – with special focus on the application of MCF coatings.

These coatings were employed in this work and, for the first time, were compared side by side through parallel investigations under comparable conditions. Building on the theoretical foundations of both technologies outlined in Section 2.3.2, the practically relevant procedures, process parameters, and equipment are described.

3.2.1. Atmospheric Plasma Spraying (APS)

The MCF-APS coating type, established and successively developed at Forschungszentrum Jülich since 2007, represents a state-of-the-art reference for interconnect coatings in SOC research.[245,246] The APS methodology used in this study follows the optimized process already implemented in numerous stack runs, demonstrating excellent functionality and suitability for long-term operation.[110–112] The coatings were applied using a Triplex Pro 210 gun within a multi-coat facility (manufacturer: Oerlikon Metco, Wohlen, Switzerland) operating with Ar/He as the primary plasma gases and

employing a standard powder feeding system. The MCF feedstock was a monomodal spinel powder (d_{50} ≈ 27 μm, basic characterization in Figure 21), ensuring stable flowability during spraying. Further technical details and information on the working principle of the coatings can be found elsewhere.[147,148] It is worth noting that MCF-APS coatings for all Jülich stack components are now applied by an external industrial partner, underscoring industrial scalability.

Due to the reduction-re-oxidation effect – arising from reducing conditions in the plasma torch and oxidizing conditions during stack assembly prior to operation – which leads to densification, no additional thermal post-treatment is necessary (see Section 2.3.2).[148] Consequently, MCF-APS coatings can be implemented in the as-coated state, in contrast to suspension-based coatings.

In this work, APS coatings were applied to 5 × 5 cm^2 sheets that were sand-blasted beforehand to remove surface impurities and increase adhesion. Coatings were deposited single-sided on sheets of Crofer22H, AISI430, and AISI441 (the latter exclusively treated in the dissertation of D. Vakhrameev[241]) clamped at the edges in sample holders and oriented vertically to the spray direction. Coated sheets were then laser-cut into 20 × 10 mm^2 specimens for basic characterization and subsequent exposures with follow-up testing (further details in Sections 3.6 and 3.7).

3.2.2. Wet Powder Spraying (WPS)

The establishment of the WPS technique, as in principle employed in this work, is based on the remarkable 100 kh stack run, initially using the basic Mn spinel.[60,247] Based on the more recently established MCF composition adapted from APS coatings, Wolff et al. developed an MCF-WPS coating and reported favorable microstructures and protective properties in 2024.[107] The coating process applied in the present work follows the methodology proposed by Wolff et al., using an ethanol-based suspension system containing organic binder and appropriate plasticizers, namely ethoxylated alcohol, polyvinyl acetate and triethylene glycol, to ensure particle stabilization. The suspension was homogenized via ball milling on a roller bench prior to spraying to achieve a uniform distribution of the MCF powder. The initial powder showed substantially smaller particle sizes than for the APS process (d_{50} ≈ 1.0 μm, basic characterization in Figure 21), to ensure continuous flow in the tube system and uniform atomization in the nozzle. Further details on the suspension composition and processing, as well as the deposition process itself can be found elsewhere[107].

A contrast of the specific powders required for APS versus WPS is shown by the morphological analyses (via secondary electron microscopy (SEM), utilizing secondary electron (SE) detection) and particle size distributions (PSD; via laser diffraction) in Figure 21. Further details on the powder characterization and the techniques employed are provided later in Section 3.6.

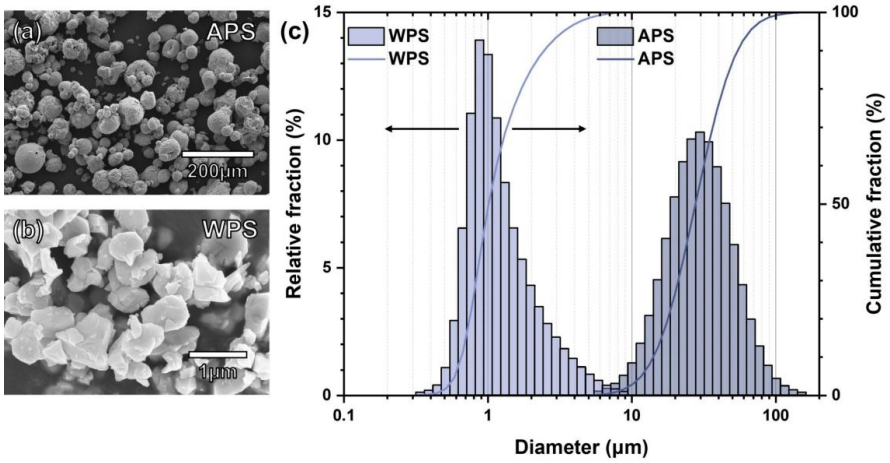

Figure 21: SEM-SE images of MCF powders, as used for (a) APS and (b) WPS coatings, and (c) particle size distribution of both powders. Powders as received (APS from H.C. Starck, and WPS from KCeracell).

Unlike APS coatings, the initial, loosely deposited state of WPS coatings require subsequent heat treatment to achieve stability and the desired properties, thereby removing residual organic components and sintering the deposited powder to a continuous, dense layer. In this work, selecting an appropriate thermal treatment protocol – single-step or multi-step/reactive sintering (see Sections 2.3.2 and 2.4) – is crucial for achieving favorable microstructures and is aligned with key findings from the later developed EPD coatings. The respective protocols under consideration are presented in Section 3.4, with the aim to include the final densification step in the re-oxidation treatment during stack joining.

By integrating densification of the WPS coatings into the stack-assembly process, an additional high-temperature oxidation treatment of the entire stack components can be omitted. This is critical because certain uncoated regions of the interconnects – needed for electrical contacting to the fuel electrode and for sealing at the outer area of the stack – must remain free of corrosion. The combined approach of coating densification and stack assembly ensures protective functionality while preventing unwanted oxidation of uncoated, functional areas.

In this work, WPS coatings were applied to 25 × 25 mm^2 sheets that were cleaned by ultrasonication in ethanol beforehand (details as in Section 3.3) to remove manufacturing contaminants. Coatings were applied single-sided and double-sided to Crofer22H and AISI430 sheets placed on the spraying table and oriented vertically to the spray direction. Three layers were deposited to achieve sufficient thickness and homogeneity. Coated specimens were either investigated in the initial format or laser-cut into 20 × 10 mm^2 samples for subsequent exposures and testing after thermal treatments (further details in Sections 3.6 and 3.7).

3.3. EPD process development and optimization

EPD is the coating method identified as especially well-suited for developing next-generation coatings for SOC interconnects, for reasons outlined in Sections 2.3.3 and 2.4.3. It is therefore central to this work. Building on the literature, coatings based on EPD were developed for use in Jülich SOC stacks and systems, first employing the established reference material MCF. After assessing cobalt-free alternatives for suitability, the method was transferred to the most promising Co-free composition.

In principle, various organic solvents, such as ethanol, acetone, and isopropanol, as well as their mixtures, are commonly used as suspension media (see Section 2.4.3, esp. Table 3) and could be adapted here as well. To facilitate material transport and suspension stabilization however, the addition of surface charge enhancers, typically iodine (I_2), is required.[248] Thus, additionally, suspension systems incorporating water alongside organic solvents have been established, as the inherent polarity of water induces surface charge formation, eliminating the need for charge-enhancing additives. Numerous studies employing aqueous systems are methodologically based on the process first described by Smeacetto et al. (2015)[180], which utilizes a water-ethanol medium.[102,181,182,212]

The above-mentioned procedure[180] serves as the foundation for the EPD coatings developed in this work and was further optimized for the specific powders used. A suspension medium comprising 60 vol.% ethanol and 40 vol.% deionized water was employed. After adding the powder to the medium, the suspension was stirred for 30 min, followed by 30 min of ultrasonic treatment (Sonorex Digitec, manufacturer: Bandelin, Berlin, Germany), with manual stirring for 1 min every 5 min, for stabilization. To enable multiple uses of the suspension for coating several samples, reconditioning was carried out by subjecting the suspension to 10 min of ultrasonic treatment along with 1 min of manual stirring immediately before deposition. During deposition, the suspension remained static.

In the EPD setup, substrates were positioned parallel to the counter electrodes in a three-electrode configuration and electrically connected using alligator clips. The three-electrode configuration was chosen to enable homogeneous deposition and the option to produce symmetrically double-side coated samples when required. Counter electrodes made of Crofer22APU were placed 1.5 cm from the substrate on either side and were always matched in area to the sample. Voltage was supplied using a three-channel laboratory power supply, type 2230-30-1 (manufacturer: Keithley Instruments, Solon, Ohio, USA). A photograph of the setup, here implementing flat sheets of 25 × 25 mm^2, in a fume hood is shown in Figure 22.

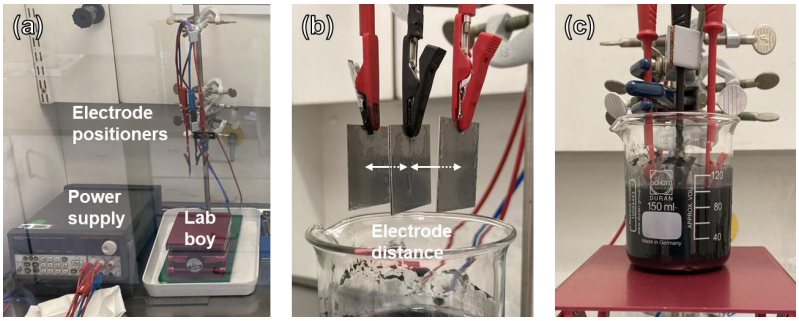

Figure 22: Photographs of the three-electrode EPD setup, as used for laboratory-scale samples, here implementing 25 × 25 mm²-sized sheets, using 100 ml of suspension; (a) full setup in the fume hood, (b) electrode constellation before the deposition process, and (c) electrodes in the container during deposition.

In preliminary trials, guided by parameter ranges reported in the literature (see Table 3), several factors were fixed for practicality, including electrode configuration and spacing, and the suspension medium. In accordance with safety guidance for open setups and to avoid excessively long deposition times that would be impractical in industry, fixed values were set for potential or field strength and for the solid load. For all deposition studies reported here, these were set to 40 V and 40 g·l^{-1}, respectively. In all coating studies, independent of sample type and suspension composition, the specimens were cleaned in ethanol in an ultrasonic bath for 30 min prior to deposition.

With the suspension and process parameters defined, the deposition studies focused on optimizing particle size and morphology, and on narrowing suitable deposition times, and thereby achievable coating thickness ranges.

3.3.1. Suspension and deposition parameter screening

To optimize coating quality, particle size distributions and deposition times were varied systematically while keeping all other conditions constant. Powders with defined milling states were assessed for their deposition behavior as a function of deposition time and characterized in the green state. The goal was to maximize green-layer integrity as a starting point for subsequent densification during heat treatment and to limit the amplification or spread of any pre-existing defects.

Powder modification was performed in a planetary ball mill (Pulverisette 7, manufacturer: Fritsch GmbH, Idar-Oberstein, Germany) to approach monomodal particle size distributions. Milling time served as the key lever for particle characteristics. The MCF feedstock powder (the same as used for WPS coatings) was milled in ethanol using 1 mm YSZ balls at 500 rpm. For each run, 10 g powder, 100 g milling balls, and 25 ml ethanol were used. Powders after 30, 45, and 60 min milling, as well as the unmilled one, were employed in deposition trials. Each powder was examined for morphology (SEM), particle size

distribution (laser diffraction), and specific surface area (gas adsorption). Details of the measurement techniques and their principles are provided later in Section 3.6.

Deposition times were varied across series in response to the resulting thicknesses and defect patterns, covering 15, 30, 45, 60, 90, and 120 s. All deposition studies used 25 × 25 mm^2 Crofer22APU sheets coated on one side by placing two identical specimens back-to-back in the symmetric three-electrode setup. Coating quality and its evolution across the series were compared to select a parameter set for further development of the MCF-EPD coatings.

3.3.2. Coating quality assessment

Qualitative assessment after deposition and drying was conducted by optical inspection of the coating surfaces. The primary focus was set on integrity, that is, continuity and the absence of cracks, blisters, and other through-thickness defects that can originate during deposition or drying and may worsen during thermal treatment or operation. Homogeneity and surface planarity were also evaluated, as pronounced waviness could promote cracking and eventual failure.

Laser scanning confocal microscopy (LSCM, hereafter mostly named laser microscopy) served as the main method for qualitative assessment at characteristic positions across the coating area. The square samples were examined at the center and near the edge region, approximately 1 mm from the side, to capture possible edge effects from locally varying deposition conditions and to ensure robust comparison across the deposition series. Methodological details are summarized later in Section 3.6.

After optimizing parameters for the MCF composition, the procedure was transferred to the selected Cu-Mn spinel powder. The most suitable mechanical treatment was applied, and an identically designed deposition study was carried out. Coating quality assessment followed the same approach for all compositions.

Beyond surface quality in the green state, the mass of deposited material provided key information. Deposition rates per area were derived as a function of deposition time to track efficiency and kinetics. These data also enabled estimations on thickness and gave indications of suspension depletion. For this purpose, gravimetric characterization was performed along the deposition series and evaluated accordingly.

3.3.3. Deposition yield and suspension recycling

To determine deposition rates and quantify suspension depletion from deposited mass, the powder mass on each substrate was weighed at each deposition time and normalized to area. Plotting mass versus time yielded deposition curves for direct comparison. The ratio of deposited mass per run to the total particle mass present in the suspension volume was used to evaluate process effectiveness and to monitor the change in solid load. Based on these results, the allowable number of successive coatings from a single

suspension was limited by a maximum 5% reduction of solid load relative to the initial state. These detailed studies of deposition behavior were carried out for the reference material MCF.

Given the significant quantity of non-deposited material remaining in EPD suspensions in general, options for recovery were examined to improve process sustainability. The straightforward route is recovery by drying and reconditioning of the residual suspension, which was investigated here. Post-deposition suspensions were dried in an oven and then analyzed for possible secondary phases formed during EPD, either due to the applied potential or reaction with evolved hydrogen. Phase stability was checked by X-ray diffraction (XRD). The dried residues were gently re-mortared and characterized by laser scattering for particle size distribution. For comparison with the residual fraction and with the initial suspension, the deposited fraction was also examined. Therefore, coatings were detached from substrates using ethanol and ultrasonication, followed by the same characterization workflow.

3.4. Post-deposition thermal treatments

After EPD and subsequent drying, EPD coatings are present in a non-densified state. Appropriate thermal treatments are therefore required to achieve densification, ensure adhesion to the underlying steel substrate, and generate a coherent layer with closed porosity, capable of effectively blocking inward or outward migrating O- and Cr-species.

At the same time, the thermal treatments are intended to be compatible with the thermal process chain of SOC stack fabrication. Each additional heat treatment step represents a hurdle in terms of scalability and cost, and partial coating of interconnect components requires careful consideration of uncoated areas. As noted earlier, the exposure of uncoated surfaces to oxidizing atmospheres must be avoided, as this would compromise the integrity of the interconnect and the functionality of contacting areas such as Ni meshes spot-welded on the fuel side.

To minimize such risks, in this work, the final densification of the coatings was targeted to occur *in-situ* during the stack-assembly step or early operation.

3.4.1. Stack assembly procedure

At Forschungszentrum Jülich, the established stack assembly procedure involves a 100 h joining step at 850°C, designed to ensure crystallization and toughening of the glass sealant (see Section 2.1.4).[249] This process is preceded by a three-step heating program applied at 2 K·min^{-1}, with intermediate dwells at 350°C and 550°C, to enable gradual binder removal of the screen-printed glass seal and to ensure uniform heating of the components. During this joining step, the interconnects are exposed to air on the coating side, while argon gas is supplied on the opposite side, minimizing oxidation of the uncoated steel surface. A schematic of the joining procedure is shown in Figure 23a.

While the currently established APS-MCF coatings can be integrated into the stack without additional heat treatment, literature reports indicate that suspension-based spinel coatings benefit from two-step treatments including a preliminary reduction step, as already introduced as reactive sintering. In this mechanism, partial reduction of the spinel and the transient presence of metallic phases enhance diffusion-driven sintering, leading to denser coatings with closed porosity and favorable electrical properties.[124,151,250] Therefore, in this work, the influence of such a reduction step was systematically assessed.

3.4.2. Sintering strategies

Next to direct oxidation, two different reduction programs were carried out for 2 h in Ar/2.9% H_2, with heating and cooling rates of 5 K·min^{-1}, at 900°C or 1000°C, respectively. These were followed by the oxidation step, representing the stack joining procedure, resulting in three distinct programs: a single-step oxidation (S0), reduction at 900°C followed by oxidation (R1/S1), and reduction at 1000°C followed by oxidation (R2/S2). The selection of these programs was based on the established work by Wolff et al. on wet powder spraying of MCF[107] and the comprehensive review by Zanchi et al. on EPD for interconnect coatings[208]. Even though, in real stack-assembly procedures, the heat-up phase includes several dwell stages, for basic characterization (microstructural and phase analyses, see Section 3.4.3), a simplified oxidation program was used, applying a continuous heating rate of 5 K·min^{-1}. After deposition and prior to heat treatment, all coatings were air-dried for at least 1 h. An overview on the applied thermal protocols, reported here in detail, is illustrated in Figure 23b and further provided in Table 5.

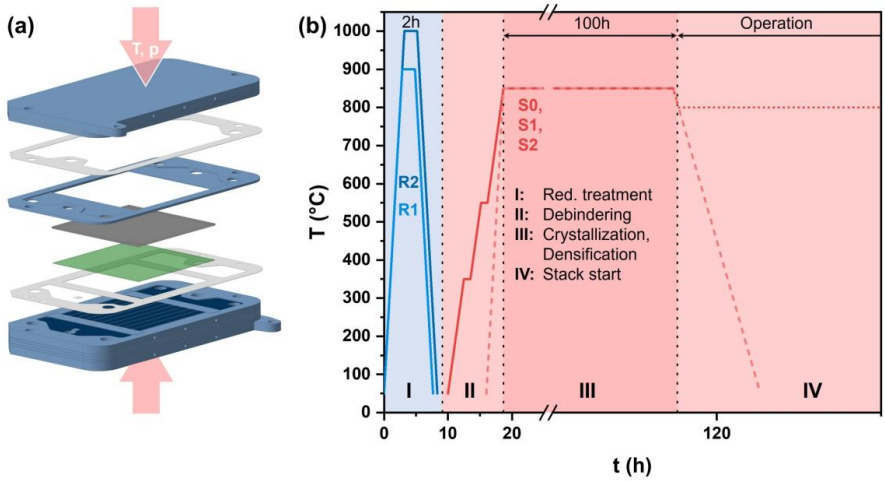

Figure 23: (a) Schematic of the stack-assembly procedure, featuring a Jülich F10 stack, and (b) heat-treatment curves and thermal history of a common Jülich stack run, including 100 h stack assembly and operation at 800°C.

Table 5: Heat-treatment protocols applied to the EPD-coated steel substrates, further characterized and discussed in this thesis. Additionally investigated treatments include longer reduction, shorter oxidation and higher oxidizing temperatures.

	Reduction		Oxidation	
Program	**T_{Red} (°C)**	**t_{Red} (h)**	**T_{Ox} (°C)**	**t_{Ox} (h)**
S0	–	–	850	100
S1	900	2	850	100
S2	1000	2	850	100

*Heating and cooling rates +/−5 K·min^{-1}.

Beyond the discussed protocols, additional strategies were screened, including extended reduction (10 h), shortened oxidation (10 h), and higher oxidation temperatures (1000°C). Owing to limited practicality, misalignment with system boundaries, and unfavorable side effects, these variants are not treated in detail here. To enable an initial assessment of the thermal treatments, coated substrates were examined at characteristic stages of the thermal process chain using microstructural and phase analyses.

3.4.3. Microstructure and phase evolution

To assess the changes in the coatings and coated substrates along the processing steps investigated in this work, analyses were conducted at the specific stages with respect to phase formation by XRD and to microstructures and elemental distributions by SEM and energy-dispersive X-ray spectroscopy (EDS). These investigations provide qualitative insight into the structure, integrity, and stability of the coating types, as well as their interaction with the steel substrate throughout the thermal treatment sequence and their compatibility with the established SOC stack-assembly procedures.

The thermal treatment study and corresponding analyses were again performed on single-side coated Crofer22APU coupons of 25 mm × 25 mm. Samples were investigated in the as-coated state, after the two reduction treatments (R1 and R2), and after the subsequent oxidation steps (S0, S1, and S2). In the XRD analyses, all performed at room temperature, the starting powders were additionally included as reference.

Microstructural analysis was carried out on surfaces and metallographic cross-sections to evaluate the continuity, density, and overall quality of the coatings, as well as their elemental distribution. Imaging was performed analogously to powder characterization utilizing SE and backscattered electron (BSE) detection to visualize structural features and phase variations, respectively. Complementary EDS analysis was applied to characterize elemental distributions across the relevant processing states. Closer details on the characterization methods and their principles are provided in Section 3.6.

Where appropriate, SEM micrographs of the EPD coatings were evaluated quantitatively by image analysis. Shrinkage was determined at the characteristic processing stages from metallographic cross-sections, and porosity was quantified both in cross-section

(bulk) and in plan view (surface). For each analysis, at least three equivalent fields of view were evaluated at distinct, representative locations per specimen type. For thickness/shrinkage on cross-sections, five equidistant measurements were taken within each image. Porosity was obtained by grayscale segmentation with a fixed threshold applied within each specimen group, using the Fiji image-analysis platform (open-source distribution of ImageJ). Gaussian error propagation was applied to the computed shrinkage values to quantify the propagation of measurement uncertainties.

3.5. Mid-term exposure tests

To meaningfully assess the performance of protective coatings and coated steel sheets, exposures under operation-relevant conditions – coupled with accompanying *in-situ* or subsequent *ex-situ* tests – are indispensable. While target stack lifetimes can reach up to 80,000 h, substantially shorter exposures on the order of hundreds to a few thousand hours are well established for gauging typical degradation phenomena and their mitigation.[251] Accordingly, this work conducted exposure campaigns under representative SOC air-side conditions. Across several studies, the developed EPD coatings were benchmarked against established MCF-APS and MCF-WPS systems and compared among themselves.

Beyond qualitative and quantitative evaluation of corrosion behavior for coated and uncoated steel substrates – and the associated evolution of electrical properties via ASR, which was assessed comparatively across coating types – chromium retention was examined specifically for the newly developed EPD coatings. This chapter details the specimen types used in each campaign, the test sequences, and the linked characterization strategies.

3.5.1. Exposed specimen types

Depending on the intended conclusions, workflow, and experimental constraints at the respective test sites – as well as limitations imposed by the coating techniques – different specimen formats were employed. Exposure series were carried out both at Forschungszentrum Jülich (IMD-1, within the project NOUVEAU) and at Chalmers University of Technology (Department of Chemistry and Chemical Engineering, within a bilateral collaboration). Each institution uses a dedicated specimen design and fixture concept, which in turn also shapes the interpretability of the resulting data.

At Forschungszentrum Jülich, rectangular coupons of 20 × 10 mm^2 with a 2.5 mm hole were used, enabling placing on an Al_2O_3 tube inside the furnace. After coating and, where applicable, thermal treatment, specimens were laser-cut from the parent sheets. For MCF-APS, coatings were applied to 2 mm thick 5 × 5 cm^2 sheets and the coupons were extracted in the as-coated state (see Figure 24a). Owing to the comparatively high sheet thickness, coatings were applied single-side, since no appreciable asymmetry effects were expected during high-temperature exposure. Coatings were produced analogously on

Crofer22H and AISI430, as well as AISI441, discussed solely in D. Vakhrameev's dissertation[241].

The same coupon format was used for MCF-WPS and for the various EPD-coated samples. To avoid thermo-mechanically driven deformation during exposure – given the thinner sheet thicknesses (500 µm) used for suspension-based coatings – specimens were coated on both sides. Parent substrates were 25 × 25 mm² sheets (see Figure 24b). The steel grades employed were Crofer22H and AISI430.

In addition to the Jülich format, EPD coatings – prepared in parallel with the thermal-treatment study (see Section 3.4) – were deposited on a special specimen design provided by Chalmers University of Technology. Although the two-sided Jülich coupons are largely covered by the coating and laser cutting has only a very local impact on coating quality, the uncoated cutting edges are not entirely negligible, particularly when assessing processes reflected by small mass changes across the entire coupon area (oxidation-related mass gain, chromium-evaporation-related mass loss; cf. Section 2.2).

For this purpose, at Chalmers University of Technology, a special sample design was created to minimize the influence of uncoated areas. Using this geometry, more than 99.8% of the total specimen surface was coated by preparing perforated coupons (15 mm × 17 mm) within a larger supporting frame (~5 cm × 10 cm). Each coupon was connected to the frame by two 1 mm bridges (see Figure 24c). This configuration enabled reliable electrical contacting of every specimen, allowing all ten coupons to be coated simultaneously under identical conditions. Coating preparation for this format required a suspension amount of 400 ml. Thermal treatments were carried out with the coupons still embedded in the frame. Specimens were detached afterwards to minimize handling-related edge damage. For samples subjected to direct oxidation without a prior reduction step (S0), an additional one-hour stabilization at 850°C in air was introduced to secure sufficient layer adhesion before detaching and exposure.

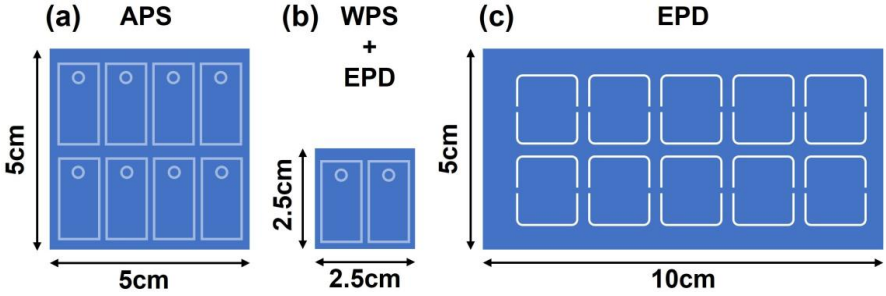

Figure 24: Schematic illustration of substrate formats, as used for coating application and cutting of specimen for exposure tests; (a) format type for APS coatings and (b) for WPS and EPD coatings, both implementing laser-cuttings of 20 × 10 mm² lateral size and a 2.5 mm hole for sample mounting in the furnace (FZJ-IMD-1); (c) perforated sheet format, enabling manual detachment of 15 × 17 mm² coupons within a supporting frame (Chalmers University of Technology).

Unlike the Jülich format, specimen positioning in the furnace was not achieved by hanging but by upright fixation in a narrow slit of an Al_2O_3 block (see later in Figure 29b). Within the comparative EPD coating study, specimens prepared in the Chalmers format were restricted to Crofer22APU as the substrate material. Multiple exposure series were designed to target different evaluation criteria and degradation phenomena, differing in sequence and especially in exposure durations. A concise overview follows.

3.5.2. Aging protocols and test conditions

Real stack atmospheres include dual-atmosphere situations and spatially varying flow rates and gas compositions, which may introduce specific challenges for the interconnect. Nevertheless, the primary focus typically lies on air-side degradation mechanisms that manifest under standard oxygen partial pressures and temperatures, often with defined humidity (see Section 2.2). Restricting tests to a simulated air-electrode atmosphere – with controlled pO_2 and pH_2O and, where applicable, regulated flow, but also including static air – therefore remains common practice. The exposure studies in this work fall into two main groups:

(i) **Assembly-/start-up-oriented series (Chalmers):** A qualitative and quantitative comparison among the developed EPD coatings with emphasis on effects during stack assembly and operation start. The protocol mirrored the multi-step assembly phase with a 100 h hold at 850°C, followed by 400 h at 800°C. The goal was to determine whether EPD-coated components can be integrated into the stack before final densification – i.e., whether *in-situ* oxidation during stack joining is feasible – without incurring adverse side effects, especially the evaporation of critical amounts of volatile chromium species.

(ii) **Mid-term benchmarking series (Jülich):** A qualitative comparison across coating systems (MCF-APS, MCF-WPS, and the most promising EPD variants) over extended durations up to 3000 h. Exposures were performed at 800°C – a widely established condition – using the Jülich specimen format, targeting mid-term effects relevant to stack operation.

Chromium evaporation was monitored continuously (methodological details in Section 3.6.5). Other measurements were conducted discontinuously – either by temporarily removing specimens during exposure or by post-exposure testing. The following section summarizes the measurement techniques applied at intermediate intervals or at end-of-test. Equipment-specific details for the exposure setups are given in Section 3.6.

3.5.3. Post-exposure characterization

To evaluate key performance markers of the coating systems – and their time evolution as a measure of protective effect – specimens were systematically withdrawn at

defined intervals and at the end of each campaign for analysis. In both study lines, two metrics were central: oxidation of the steel, quantified via mass-gain measurements, and electrical performance, quantified via ASR. In the Jülich series, microstructural evolution was additionally assessed, focusing on oxide-scale formation, potential secondary phases, coating integrity, and related aspects, and was correlated with the complementary measurements. In the Chalmers series, an additional workflow quantified volatile chromium species.

Table 6 compiles the exposed specimen sets, precise exposure conditions, and time schedule of the campaigns. Details on the methodology and instrumentation for each characterization technique are provided in Section 3.6.

Table 6: Framework of the two exposure studies, included in this work, highlighting sample specifications, exposure conditions and characterization measures and frequency.

	Exposure study i (Chalmers)	**Exposure study ii** (Jülich)
Coating types	EPD (S0, S1, S2)	APS, WPS, EPD, none
Substrate materials	Crofer22APU	Crofer22H, AISI430, AISI441
Substrate type	Chalmers-type (17 × 15 mm^2)	Jülich-type (20 × 10 mm^2)
Temperature	850°C 800°C	850°C
Duration (total)	100 h 400 h	3000 h
Atmosphere	Ambient air + 3% H_2O	Ambient air
Characterization	Chromium evaporation, mass-gain, *ex-situ* ASR	Cross-sections (SEM, EDS), mass-gain, *ex-situ* ASR
Sequences	100 h, 200 h, 500 h	300 h, 3000 h

*Mass-gain measurements within the Jülich studies included additional sequences; 18 data points were received approximately every 170 h. AISI441 only investigated in D. Vakhrameev's dissertation[241].

Beyond the specimen types, exposure conditions, and methods summarized here, the Jülich study also included complementary investigations – e.g., higher-temperature "accelerated testing," additional intermediate exposure times, and further analytical techniques such as glow discharge optical emission spectroscopy (GD-OES) and electron backscatter diffraction (EBSD). This more in-depth assessment of corrosion behavior for coated and uncoated ferritic stainless steels was conducted by D. Vakhrameev and is documented in his dissertation[241]. The investigations reported here, together with the Chalmers study, though, form a robust basis for selecting a suitable coating system.

Ensuring comparability and reproducibility – across coated and uncoated specimens as well as baseline materials – is essential for drawing meaningful conclusions.

3.6. Material and coating characterization

This section outlines the key characterization methods employed in this work, briefly introducing their underlying principles and essential technical details. The content moves from baseline analyses of the starting materials to structural investigations of both

established and newly developed coatings, and concludes with the performance metrics utilized in the exposure studies.

3.6.1. Particle analysis

A solid understanding of the powder characteristics is pivotal for process control in powder-based ceramic coating routes – both for selecting suitable manufacturing parameters and for achieving high reproducibility. Two quantitative descriptors are especially important: the particle size distribution and the specific surface area (SSA) normalized to powder mass. Standard methods to determine these are laser diffraction and gas adsorption, respectively.

Particle size distribution

Laser diffraction leverages the interaction of a broadened laser beam with a dispersed particulate ensemble in either a liquid or gaseous medium. The detected scattering angle is inversely related to particle size. In addition to scattering, refraction and diffraction contribute to the measured signal. While ideal spheres produce circular diffraction patterns, real particle morphologies yield irregular yet point-symmetric patterns.

Data evaluation can follow either the Fraunhofer or the Mie model. Fraunhofer analysis assumes opaque particles and considers only diffraction phenomena. The optical constants (refractive index) of the material are therefore not required and the approach is appropriate for sufficiently large particles. As particle size approaches the laser wavelength and morphology departs from sphericity, refraction, multiple reflection, absorption, and emission become non-negligible. In such cases, the optical properties must be known and Mie theory should be used to obtain meaningful results. If Mie analysis is necessary but the exact optical constants are unknown, a sufficiently accurate numerical approximation can be achieved by using two different laser wavelengths in parallel. Primary particles can be measured by deagglomerating dilute suspensions with ultrasound. It must be noted, however, that this does not quantify the agglomeration state, nor does it break pre-formed aggregates.[252]

Within this work, PSD measurements were conducted with a laser diffraction particle size analyzer (LA-950V2, manufacturer: Horiba, Kyoto, Japan) operating at 405 nm and 650 nm laser wavelengths. Given the fine particle sizes of the commercial powders from KCeracell as well as the powder provided by Marion Technologies (before and after ball milling) Mie theory was applied for evaluation, assuming a refractive index of 2. The commercial powder from H.C. Starck was, due to the large particle sizes, analyzed using the Fraunhofer theory.

Specific surface area

The mass-specific surface area can be obtained from the amount of gas adsorbed onto the powder surface. The Brunauer-Emmett-Teller (BET) method is widely used for this purpose. It assumes multilayer physisorption with distinct adsorption capacities per layer

and an equilibrium between layers, neglecting interactions among adsorbed layers.[253] Practically, adsorption isotherms (adsorbed amount vs. gas pressure in the mixture) are recorded at controlled temperature. A typical BET isotherm exhibits a steep initial increase due to monolayer formation at low relative pressures and tends toward a plateau as multilayers develop and the surface saturates. A linear segment of the BET plot is then selected to calculate the specific surface area A_S according to Equation 3.1:

$$A_S = \frac{n_m L \sigma_m}{m} \tag{3.1}$$

where n_m is the monolayer capacity, L is Avogadro's constant (6.022×10^{23} mol^{-1}), σ_m is the molecular cross-sectional area, and m is the adsorbent mass.[254] In this work, SSA was determined from N_2 adsorption isotherms ($\sigma_m = 0.162$ nm^2) using an areameter (type AREA-mat, manufacturer: Jung Instruments, Viersen, Germany) and applying Equation 3.1.

Beyond quantitative metrics, qualitative assessment of powder morphology and condition is also important. Accordingly, representative morphology inspections – aligned with the microstructural investigations of coatings at key points in the thermal process chain and after exposures – were carried out.

3.6.2. Microstructure and morphology

Microscopic techniques were employed for both powders and coated specimens across the various sample formats, targeting surface features and, in particular, polished cross-sections. For non-destructive surface topography, a laser scanning confocal microscope was used. This was applied primarily during the development of EPD green films to assess as-deposited layer integrity and uniformity (see Section 4.1.2).

For higher-resolution analyses of topography, morphology, and phase contrast, scanning electron microscopy was utilized and complemented by energy-dispersive X-ray spectroscopy (EDS) for elemental mapping and spot analyses. SEM/EDS served two roles in this work: first, the qualitative assessment of powder morphology; second, the comparative characterization of the coating systems throughout the thermal-treatment studies and after exposures, using both surface views and metallographically prepared cross-sections.

Laser scanning confocal microscope

Laser scanning confocal microscopes are indispensable tools in the life sciences and are increasingly adopted in materials research. They function as high-resolution optical microscopes – operating in transmission or reflection – with a "pseudo-infinite" depth of field, and they also serve as non-contact optical profilometers. Coupled to an external spectrometer, LSCMs can further enable Raman spectroscopy. The required instrumentation is comparatively straightforward: no special sample preparation, no

electrical contacting, and no vacuum environment are needed. Measurements are contactless and performed in air.[255]

LSCMs utilize collimated laser light as a point illumination source, focused onto the sample. The reflected or transmitted light is directed through a pinhole to a point detector. The pinhole defines a second crossover focal point and serves as a wide-angle spatial filter. If scattered light does not pass the pinhole, the spot is out of focus. Light that passes is typically split into different wavelengths via filters and dichroic mirrors and is then detected by photomultiplier tubes (PMTs). Imaging of larger areas is enabled by lateral scanning of the beam with mirrors driven by piezoelectric actuators, and height resolution is achieved by stacking multiple images taken at distinct focal positions. A schematic illustration of the concept and working principle of an LSCM is shown in Figure 25a.[255]

In this work, topographic analyses were performed using a VK-X160K device (manufacturer: Keyence Corp., Osaka, Japan). Primarily flat samples were investigated – EPD-coated specimens in the green state – and structured samples were also characterized by exploiting the large depth of field, for example flow-field structures (see Section 3.7). While laser microscopy provided an effective, low-barrier method for mid-range resolution at mesoscopic scales, electron microscopy was used for finer scales such as the morphology of fine powders and microstructural features.

Scanning electron microscope

As many relevant features – particle shapes, grain-boundary networks, pores as well as oxide scales – start in the upper nanometer to lower micrometer range, the wavelengths used in light microscopy no longer provide adequate resolution. Shorter electron wavelengths are required. Across electron-microscopy modalities, the common basis is the emission of electrons by thermionic or field emitters, their acceleration in high vacuum towards the specimen, and the analysis of electron-matter interactions.[256]

The scanning electron microscope, being the microscope type used in this work, probes near-surface regions through electron-surface interactions. Information is therefore restricted to the specimen surface, in contrast to transmission electron microscopy (TEM), which interrogates electron-transparent lamellae and can resolve crystal structures and atomic-scale defects. While SEM offers a lower ultimate resolution than TEM, its instrumentation and specimen preparation are far less demanding, making SEM a highly effective and often sufficient method for routine and comparative studies.[256]

After emission, electrons are accelerated by an electric field and focused by electromagnetic lenses and scan coils to scan the surface, analogous in concept to LSCM scanning. A schematic of the instrument layout and operating principle is shown in Figure 25b.

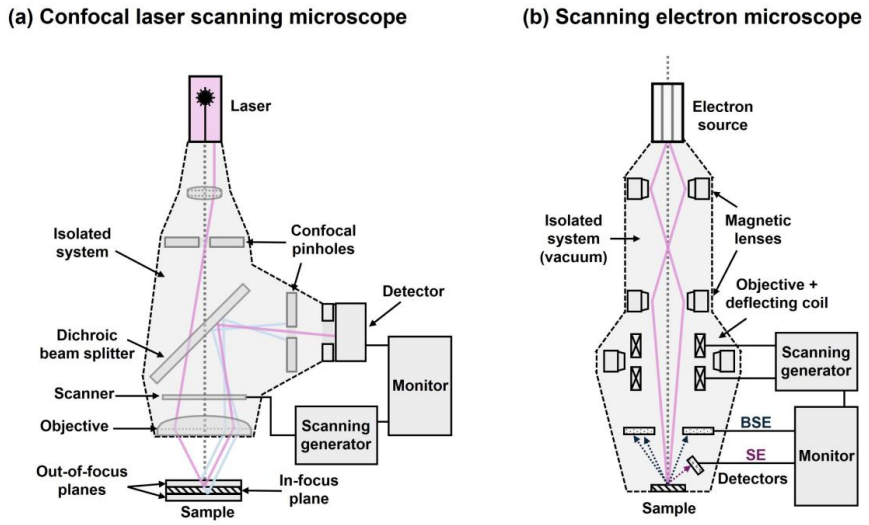

Figure 25: Schematic depiction of the microscope configurations, utilized for morphological and elemental analysis: (a) Laser scanning confocal microscope, and (b) scanning electron microscope. Own illustrations, derived from[255,257].

By evaluating the various interaction mechanisms of primary electrons with the specimen material, different kinds of information can be obtained. Elastically backscattered electrons (BSEs) originate from deeper interaction volumes and are more intense for high-atomic-number elements, producing bright regions and enabling material (compositional) contrast. Secondary electrons, with only a few eV energy, escape from the top nanometres and thus emphasize surface topography.[256]

Element-specific X-ray emission generated under the focused electron beam enables compositional analysis. Each element produces characteristic lines that correspond to electronic transitions. Detection and assignment of this radiation is performed by energy-dispersive X-ray spectroscopy (EDS). Point analyses, line scans, and area maps (mappings) are possible. Schematics of the interaction volume and the mechanisms behind BSE, SE, and EDS signals in SEM are provided in Figure 26a and Figure 26b, respectively.

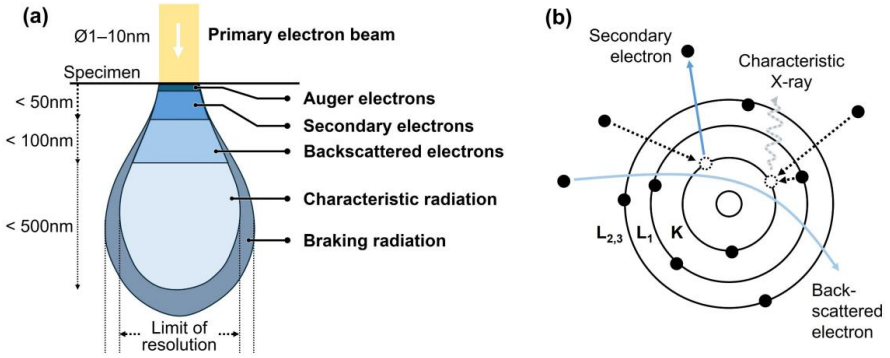

Figure 26: Schematics for SEM characterization: (a) excitation volume, and (b) atomistic mechanisms for secondary electron emission, electron backscattering, and characteristic X-ray emission. Own illustration after[257].

In this work, multiple instruments were employed. Lower-magnification overview images (combined SE and BSE) were acquired on a tabletop SEM TM3000 (manufacturer: Hitachi High-Technologies Corp., Tokyo, Japan) with a thermionic electron source. For higher-resolution work outside the exposure study, a GeminiSEM 450 and an Ultra 55 (manufacturer: Zeiss, Oberkochen, Germany) equipped with field-emission sources were used. SE and BSE detection were applied, and for powders an in-lens detector was selected to achieve high topographic fidelity at low accelerating voltages. EDS analyses used an ULTIMAX170 detector (manufacturer: Oxford Instruments, Abingdon, United Kingdom). SEM/EDS characterizations during the exposure study were performed on a Merlin SEM (manufacturer: Zeiss, Oberkochen, Germany) with a field-emission source and integrated detectors (BSE, SE, EDS).

Specimens for SEM/EDS were coated with a thin Pt layer by sputtering to ensure adequate surface conductivity, suppress charging, and improve image quality. Powders were dispersed on conductive carbon tape to provide electrical contact and adhesion in vacuum. For surface imaging of coated coupons, samples were fixed to carbon tape from the rear and additionally bridged with a thin adhesive Cu strip. Complementary metallographic cross-sections were prepared by embedding in epoxy followed by automated multi-step grinding and polishing. Prior to embedding, oxidized samples were partially Ni-electroplated to minimize coating damage during preparation and to enhance contrast in microstructural analysis. After polishing, Cu stripes were applied accordingly.

Beyond microstructure and elemental analysis by SEM/EDS – which already implies information about present compounds – the explicit determination of crystalline phases is essential. This is relevant for assessing starting materials, deposited coatings, and their evolution during processing.

3.6.3. Phase analysis

For identifying the phases present in powders and consolidated bodies, X-ray diffraction is the established technique of choice. XRD serves both to determine lattice parameters or interplanar spacings in known crystalline materials and to identify – qualitatively, and to a limited extent quantitatively – the crystalline phases in unknown or mixed samples. The method exploits the elastic interaction of X-rays with the long-range ordered structure of the specimen. Reflected, diffracted beams generate constructive interference, described by Bragg's law:

$$n\,\lambda = 2\,d\,\sin(\theta) \tag{3.2}$$

where n is the order of interference (natural number), λ the X-ray wavelength, d the interplanar spacing, and θ the diffraction angle. In practice, different instrumental geometries are used. A widely adopted arrangement keeps the sample fixed while the incident beam and the detector move in concert, known as the θ-2θ configuration, which is also employed in this work and is shown schematically in Figure 27a. Additionally, a schematic of the interaction between the incident beam and the crystal lattice, including the relevant quantities, is shown in Figure 27b.[258]

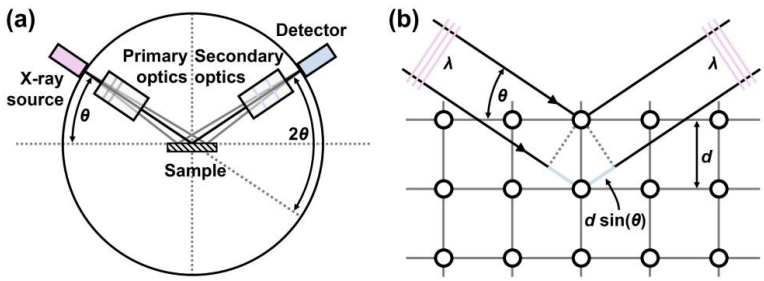

Figure 27: Schematics of (a) θ-2θ configuration, and (b) X-ray scattering in a crystal after Bragg. λ: X-ray wavelength, θ: diffraction angle, d: interplanar spacing. Own illustrations derived from[258].

In an XRD measurement, the intensity of the diffracted beam is recorded as a function of the scattering angle. Phase attribution relies on reference patterns from single-crystal or highly pure polycrystalline standards. This enables qualitative identification of phases in mixed samples; with Rietveld refinement, and when only a few phases are present, semi-quantitative to quantitative estimates of phase fractions are also possible. As interatomic distances are probed, the chosen wavelength must be of the same order of magnitude. The effective information depth is limited to several micrometers, which constrains conclusions to the near-surface region for grazing-incidence geometries and to the irradiated volume for conventional powder scans. Moreover, a phase must exceed a minimum abundance to generate a detectable peak. Amorphous fractions cannot be identified, and peak overlap may complicate assignments.[258]

In this work, XRD measurements were performed on two instruments depending on the objective. Standard analyses were conducted on a Bruker D4 Endeavour diffractometer (manufacturer: Bruker AXS, Karlsruhe, Germany) equipped with a LynxEye 1D detector, using monochromatic Cu Kα radiation. Patterns were collected over a 2θ range from 10° to 80° with a step size of 0.92° and a counting time of 0.75 s per step. These measurements were carried out on powders (affixed to glass carriers using adhesive tape) and on flat samples (coated coupons).

In addition, *in-situ* high-temperature XRD (HT-XRD) in ambient air was employed to assess the thermo-structural behavior of the spinels MCF, CMF, and CMN considered as coating materials. Measurements were performed between 25–1000°C and evaluated via the evolution of characteristic reflections. In this way temperature-dependent phase compositions under SOC-relevant conditions were obtained.

HT-XRD was carried out on a Malvern Panalytical Empyrean powder diffractometer (manufacturer: Malvern Panalytical, Malvern, United Kingdom) equipped with a HTK1200N heating chamber (manufacturer: Anton Paar GmbH, Graz Austria). Individual diffraction patterns were recorded every 100°C during heating and cooling. Heating and cooling rates were 5 $K \cdot min^{-1}$. The dwell and measurement times were 2 min and 52 min, respectively, using a 2θ range from 10° to 90°, an angular step size of 0.026°, and a counting time of 250 s per step on a 255-channel linear detector. Data processing for both room-temperature and HT-XRD measurements was performed using HighScore Plus.

3.6.4. Electrical characterization

Beyond the methods described above – which were central for screening materials, optimizing coating routes, and qualitatively assessing protectivity – quantitative performance markers are often decisive for evaluating durability and protection. In this study, the key metrics were electrical properties (ASR), chromium evaporation (Cr release/retention), and oxidation kinetics (mass gain), each described in the following sections.

As one of the most critical aspects for assessing the suitability of interconnect coatings for stack operation, the ASR of coated steel substrates under SOC-relevant conditions was investigated. Though *in-situ* ASR characterizations in literature can be found, aiming to display the evolution of electrical performance over exposure duration, this work focussed on *ex-situ* characterization after exposure. As the contacting itself, usually applying continuous noble metal layers on the coating area to be measured, can create a severely different testing atmosphere than present in a stack, a significant impact on the measurement can often not be neglected. Also, ASR tends to show a continuous evolution for stable coatings, due to the key underlying mechanism of oxide scale growth. Therefore, measurements were conducted after exposure, re-arranging the exposure conditions during the measurements.

Samples, resulting from both exposure studies (Chalmers (i) and Jülich (ii)) were included in the ASR investigations, which were all performed at 800°C in atmospheric air. In the Chalmers study (i.e., the simulated stack joining and start-up phase), the distinct comparison between the EPD coatings after 500 h exposure provided focused insight into the transient losses that the interconnect may exhibit after the microstructure of the coating has stabilized and the stack has run into operational equilibrium. The samples from the Jülich-study, where MCF-APS-coated substrates served as reference which the most promising EPD-coated samples were benchmarked to, were characterized to have a meaningful comparison across the systems in a relevant exposure duration and to compare to literature.

Measurements were performed in a tube furnace with contact to platinum wires and platinum meshes. Prior to measurement, both sides of each sample were sputtered with a thin gold layer, using a sputter coater, with a mask defining the contacting area. Due to the different specimen sizes across the exposure studies, the Chalmers samples received 10 × 10 mm^2 contact area, while the Jülich samples received an 8 × 8 mm^2. After sputtering, gold paste (M-9875, manufacturer: METALOR Technologies, Marin, Switzerland) was applied to the sputtered region. After drying, the contact layer was solidified by sintering at 800°C for 1 h. The resistance was measured after stabilizing the temperature in the furnace at 800°C for 30 min, using a 4-wire, 2-point configuration. A Keithley source-meter unit of type 2400 (manufacturer: Keithley Instruments, Solon, Ohio, USA) was used for the measurements, with the applied current density set to 100 $mA{\cdot}cm^{-2}$. Eight resistance readings were taken every 8 minutes and averaged. More details on the ASR measurement method are provided elsewhere[259]. A schematic depiction of the sample preparation process and measurement setup is provided in Figure 28a and b, respectively.

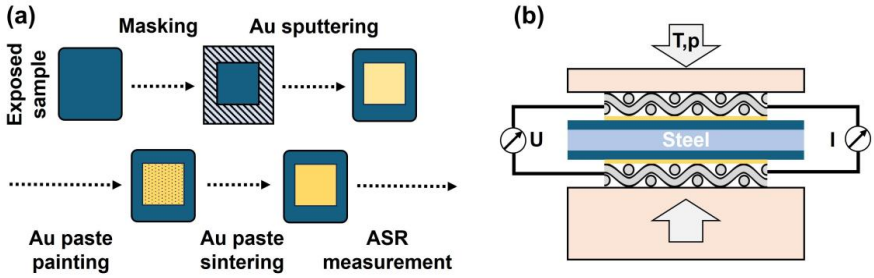

Figure 28: Sample preparation and mounting as used at Chalmers University of Technology for ASR characterization; Schematic illustration of (a) the Au contacting procedure for exposed coupons, and (b) the electrical circuit in the 4-wire, 2-point configuration.

As the majority of the steel sheets used in the ASR study were coated on both sides (or non-coated steel sheets), whereas in real stack operation protection is applied only on the air-side, the evaluated ASR values were normalized to the contacted area and corrected by a factor of 0.5. Only the single-side coated APS-samples were not in need of a mathematical

correction but underwent a backside grinding step for oxide-scale removal before sputtering and painting. Potential oxide scale formation below the contact during the short duration of the measurement was initially neglected.

3.6.5. Chromium evaporation and retention

Besides the electrical performance, a key metric for evaluating the protective performance of interconnect coatings is the quantification of chromium evaporation under SOC-relevant conditions. Therefore, coatings were exposed to a defined thermal treatment profile – comprising the simulated stack assembly procedure with the multi-step heating ramp (see Section 3.4.2, esp. Figure 23b), followed by 400 h of simulated SOC operation at 800°C – to determine the cumulative release of volatile chromium species.

The exposures, limited to EPD-coated substrates (details on the investigated coating and specimen types in Section 3.5), were conducted using the established denuder technique in a tubular furnace under continuous gas flow. To replicate the oxidizing, cathode-side atmosphere in SOFC stacks, humidified air containing 3% H_2O was employed. A porous SiC flow restrictor was mounted upstream of the samples to homogenize the gas distribution and minimize natural convection and backflow. The total flow rate was set to 6000 sml·min^{-1}, ensuring a flow-independent regime inside the reactor. Samples were placed on an alumina holder aligned with the direction of the flow.

At least three coupons of each type were subjected to each exposure, using a single-zone furnace for the continuous runs. Chromium evaporation was measured *in-situ* according to the denuder method originally introduced by Froitzheim et al.[260] The vapor stream leaving the reactor passed through denuder tubes coated with Na_2CO_3, where volatile chromium species were trapped via the reaction shown in Equation (3.3):

$$Na_2CO_3\,(s) + CrO_2\,(OH)_2(g) \rightarrow Na_2CrO_4\,(s) + CO_2\,(g) \qquad (3.3)$$

Denuder tubes were exchanged at regular intervals without interrupting the experiment. The removed tubes were leached with water, and the resulting solutions were analyzed using an Evolution 60S spectrometer (manufacturer: Thermo Scientific, Schwerte, Germany) to obtain the time-resolved chromium evaporation rates. Measurement points were defined after 100 h to represent stack assembly, and further after 200 h and 500 h to capture early operation stages. A schematic of the experimental setup, as used at Chalmers University of Technology, is illustrated in Figure 29.

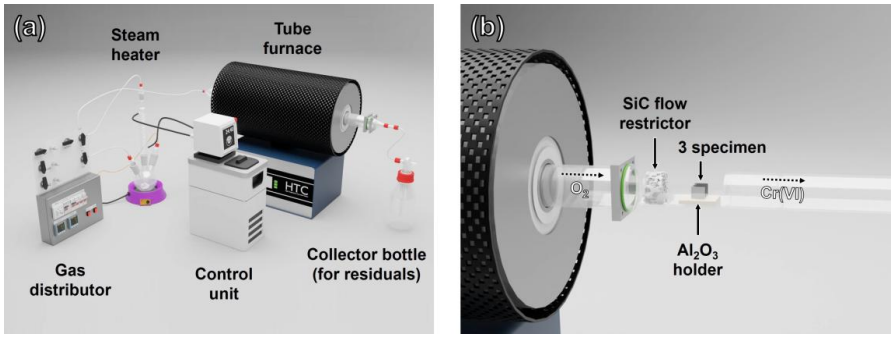

Figure 29: Experimental setup for denuder technique measurements to determine Cr evaporation at high-temperature exposure with continuous and controlled oxidant flow rate, as proposed by Froitzheim et al.[260] (a) Overview and (b) detailed schematic of sample chamber. Initial schematic created and provided by T. Krogsgaard (Chalmers University of Technology, Gothenburg, Sweden).

3.6.6. Oxidation kinetics (mass gain)

Mass-based measurements serve not only as indicators of released species, but also as meaningful probes of mass-uptake-driven material changes. In particular, quantifying the mass gain associated with steel oxidation is a robust way to assess coating protectivity and corrosion resistance, which is the approach also used in this work.

Mass gain is a commonly used indicator of the oxidation kinetics of interconnect steels and the corrosion protection provided by different coating types. In this work, the cumulative mass increase and its evolution were determined during the exposures. In contrast to the chromium evaporation tests, the determination of mass gain was performed as a discontinuous process. In principle, a similar procedure was conducted across the Chalmers and Jülich exposure studies. Several samples were exposed simultaneously, while specimens were removed at defined time intervals. The mass gain was calculated from the difference in sample weights recorded at the respective intervals. For each data point, a minimum of three (Chalmers) or two (Jülich) samples per sample type were temporarily taken out. Each removal step required cooling to room temperature, subsequent weighing, and reheating to the operating temperature.

In the Chalmers series, which focused on the different EPD coatings, the same equipment and the same discontinuous procedure were used as for the chromium-evaporation analyses (see Section 3.6.5). Measurements were carried out in two phases over a total of 500 h at 850°C and 800°C. In contrast to the Jülich study, to isolate the contribution of steel oxidation beneath the coatings – i.e., the growth of the Cr_2O_3/$(Mn,Cr)_3O_4$ oxide scale by oxygen incorporation – the data were corrected by subtracting the previously quantified mass of volatilized chromium species. The resulting value is referred to as the "corrected mass gain". For the pre-reduced samples, an additional contribution to the mass gain arises from re-oxidation of the coatings back into the spinel

phase. This contribution was calculated from the reaction stoichiometry and the expected coating mass, and it was included as a separate correction (details in Section 4.3.2).

The Jülich exposure study was conducted under static atmospheric conditions at 800°C in ambient air. Since the measurements did not account for the amount of volatilized chromium species and the laser-cut specimens had uncoated edge regions that were exposed to the corrosive atmosphere, the results carry non-negligible limitations. Nevertheless, the series provides an important comparison between the coating systems, particularly due to the substantial total exposure time of 3000 h.

Taken together, these measurements usefully complement the individual exposure studies and performance metrics. Building on the successful development of novel coatings, they enable a well-founded comparison of the systems. While the transfer of existing coatings to component and stack level has already been demonstrated – WPS[107], as well as APS as long-standing Jülich standard[110–112] – this transition remains a decisive step for EPD coatings to prove their suitability beyond small-format specimens and to establish their applicability in real systems. This aspect was also investigated in the present work.

3.7. Real component demonstration for EPD coatings

Exploiting the promise of EPD for interconnect protective coatings ultimately requires moving beyond flat, small coupons to real geometries and component scales. This entails adapting equipment where necessary and accounting for additional boundary conditions when implementing the approach at stack level. Alongside compatibility with conventional gas-distribution structures – rib-channel patterns or corrugated designs – chemical compatibility can be critical, with the glass sealant emerging as a key consideration. While sealants are typically not in direct contact with the protective coating when handled correctly, this interface may nonetheless offer an interesting lever for optimization and will be briefly examined first.

3.7.1. Glass-sealant compatibility

In case of feasibility to directly apply the glass sealant onto the coating this could enable full-surface coating of the interconnects without the need for masking and thereby streamline the overall EPD processing. Furthermore, this approach could completely avoid the occurrence of uncoated zones, for example between the coating edge and the glass sealant (cf. Figure 30a). Even if the sealant must be joined on bare steel for adhesive reasons, a transition zone could still be realized provided coating and glass are sufficiently compatible. Therefore, small-scale compatibility tests were conducted.

These tests aimed to provide insight into the chemical and thermo-mechanical stability of the glass-coating interface, with particular emphasis on potential stresses arising from differences in thermal expansion due to phase precipitation. In addition, the experiments were designed to assess possible interdiffusion effects, which could impair the

electrical insulation function of the glass sealant and thereby risk short-circuits within the stack. These investigations were carried out on basis of chemical compositions only and could be extended to electrical measurements in case of critical component formation.

As noted in Section 2.1.4, the established sealing solution at Forschungszentrum Jülich is a composite sealant based on a Ca-Ba-silicate glass with YSZ fibers as filler material. In this work, according to the standard processing route, sealant was employed in the form of screen-printed green foils (further details on the sealant system can be found elsewhere[34,35]). Circular blanks of 18 mm diameter were punched from the green foils and applied to the coated side of single-side EPD-coated 25 mm × 25 mm Crofer22H coupons. The investigations were conducted, implementing all coating types within the thermal treatment study (see Section 3.4.2), though the focus lays on the most promising types from the previous results. Each sample was counter-faced with an uncoated Crofer22H coupon of identical dimensions. The gap thickness was defined by pre-sintered YSZ spacers with a thickness of 150 µm. Joining was performed following the multi-step procedure described in Section 3.4.1, under air atmosphere and with a joining load of 200 g. A schematic depiction of the testing procedure is shown in Figure 30b.

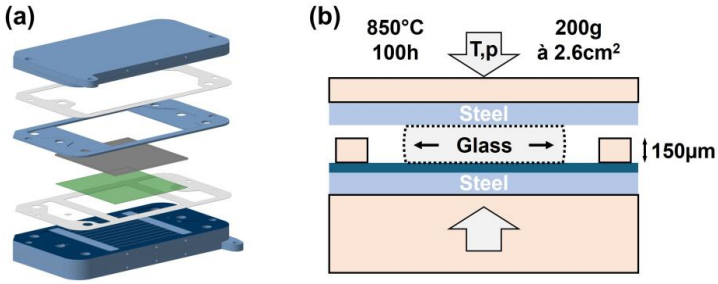

Figure 30: Direct application of glass sealant on EPD-coated interconnect steel; (a) Drawing of four-layer F10 stack with fully coated interconnects (inlay sheets uncoated), and (b) schematic of glass-sealant compatibility tests, as conducted by S.-M. Groß-Barsnick (FZJ-ITE). Drawing provided by W. A. Mertens (FZJ-ITE).

The joined assemblies were evaluated by preparing cross-sections, analogous to the procedure used for single coupons (see Section 3.6.2). Subsequent characterization comprised SEM imaging and EDS analysis, including line scans across representative regions of the interaction zone at the center of the joint. Imaging was carried out using a Gemini 1 Sigma 300 VP SEM (manufacturer: Zeiss, Oberkochen, Germany).

While the interplay between glass sealant and coating is a forward-looking topic, it remains a side consideration and has so far been avoided in practice by masking the steel components prior to coating to prevent interaction of the materials. Of central importance, however, is the transferability of the coating method to those structures that must be protected in the stack itself.

3.7.2. Flow-field structures

As the flow fields face direct contact with the air-electrode and are also exposed to aggressive atmospheric conditions, they are especially critical areas for the application of protective coatings. At the same time, the complex geometries of flow fields, often including sharp edges and steep flanks, pose significant challenges to achieving continuous and defect-free coverage. Demonstrating the suitability of EPD for such application-relevant geometries is therefore of particular importance.

To address this, EPD coatings were deposited onto representative flow-field sections and assessed with respect to their continuity, integrity, and microstructural quality in characteristic regions of the structures. Therefore, in this work, the two different interconnect types, reflecting the designs currently relevant to SOC research at Forschungszentrum Jülich and that were introduced earlier, were selected.

The first is the interconnect from the long-established F10 stack design (see Figure 6), which continues to serve as the reference system for stack testing and is supported by decades of operational data. Its rib-channel geometry, with sharp rib edges directly in touch with the air-side contacting, provides an especially challenging case for assessing EPD coating performance. F10 interconnects are manufactured by milling from bulk Crofer22APU material, resulting in heavy and material-intensive components (cf. Figure 20) clearly directing its application towards laboratory testing.

In addition, the more recently developed interconnect type belonging to the CS^{V} design (see Figure 19) was considered. This design, based on hydroformed thin sheets of Crofer22H, is of broader industrial interest due to its lightweight and resource-efficient construction. As coating such components by APS is problematic, due to the higher susceptibility of the thin walls to deformation under the mechanical and thermal loads of thermal spraying, EPD is of special interest here (see Sections 2.3.3 and 2.4).

Representative cut-outs of 25 mm × 25 mm from the flow fields of both interconnect types (F10 and CS^{V}) were prepared. These samples were integrated into the deposition setup in the same manner as flat substrates, with the electrode spacing adjusted to match the mid-height of the structures. For the structured specimen, deposition time was increased by +33%, accounting for their increased surface area compared to the flat counter electrodes. Photographs of the two interconnect types, as well as an F10 cut-out integrated into the setup, are shown in Figure 31.

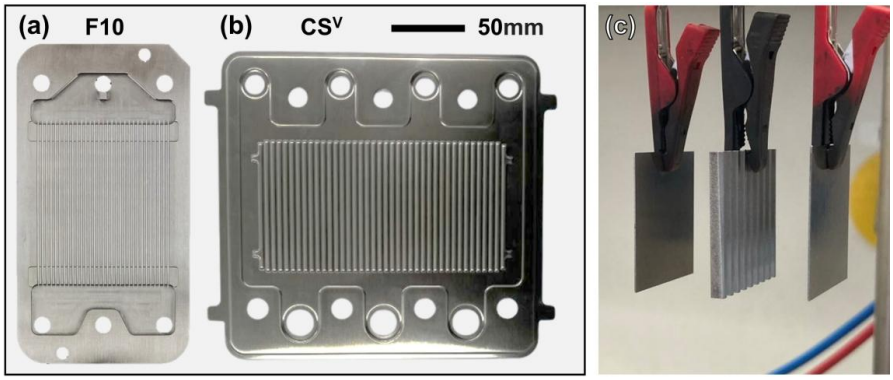

Figure 31: Investigation of characteristic flow-field structures of Jülich interconnect components; Photographs of (a) the Jülich F10-type interconnect, (b) a CS^V interconnect sheet, and (c) a representative F10 flow-field cut-out, as integrated into the EPD setup.

The investigations focused on the coating variant identified in the preceding studies as the most suitable candidate. Characterization followed the same procedures as for flat substrates, employing SEM imaging of embedded cross-sections (cf. Section 3.6.2). Stitched overview images were generated from multiple micrographs, and additional detailed views were recorded in characteristic structural areas for direct comparison with APS and WPS. Building on the small-format investigations, adapting to real-component scale was the next logical step, and key for stack and system integration.

3.7.3. Full-size interconnects and stack integration

Transferring the EPD coatings developed on small, flat coupons to stack components requires scaling the equipment and tuning the processing workflow. Much of the methodology optimized for small samples can be retained, but certain adjustments are necessary. The suspension composition, applied voltage, electrode spacing and configuration, deposition time, post-deposition drying, and the optimized thermal protocol are transferable. Changes are needed for the suspension volume, electrode dimensions, and the mechanical setup, including positioning and fixation of electrodes and components.

Additional hurdles emerged during upscaling that were not apparent on the smallest formats and had to be addressed to achieve adequate coating quality. These issues, and their mitigation, are discussed later in the Results.

Although the cassette-based CS^V stack design is more relevant for industrial deployment, a stack test with EPD-coated interconnect sheets in this concept would currently offer only limited interpretability due to a small comparison basis and remaining challenges for stable, reproducible operation. The technology transfer was therefore focused on the established F10 model, which provides a broader basis in comparison with past stack runs. For scaling, a stand-alone EPD rig was designed with support from the IMD-2 in-

house workshop (with substantial contribution by C. Gebhart, J. Müller and E. Sucuoglu). The system can be adapted to multiple large component formats.

Voltage supply followed the small-format setup and employed a Keithley three-channel laboratory power supply, type 2230-30-1. Suspension preparation was likewise analogous but scaled to a working volume of 2 l using a high-density polyethylene (HD-PE) container and a large ultrasonic bath. The ultrasonic bath was of type Sonorex Super RK 1028 (manufacturer: Bandelin, Berlin, Germany). A photograph of the upscaled apparatus is provided in the Supporting Information (cf. SI 3). Assistance in the conduction of the full-size component coating runs was provided by F. Gallo (Politecnico di Torino).

Coating quality on full-size components was first assessed in the green state using a laser microscope. To demonstrate protective functionality under realistic conditions and to verify seamless integration into the thermal process chain, a four-layer SOFC stack was assembled. While a central ambition of this work is to enable cost-effective, more sustainable stacks by utilizing conventional steels, Crofer22APU was selected here to maintain comparability with established stack runs. An earlier cell standard was also adopted: FESCs with a Ni-YSZ fuel-electrode/electrolyte system, and a GDC barrier layer, employing the previously established LSM on the air side, instead of newer materials.

Although LSC/LSCF are the more recent and better-performing air electrodes for efficient, durable stacks, LSM was selected as the appropriate choice for evaluating the protective action of the new EPD interconnect coating. Any detrimental impact of volatile chromium species manifests faster and more strongly with LSM than with the newer air electrodes. Stack assembly was conducted at ITE, guided by A. Cramer, while the test itself was run at Institute of Energy Technologies (IET-1), conducted by U. de Haart. The stack was operated at 800°C SOFC mode, which imposes demanding conditions for interconnect-related degradation due to the high air-side humidity.

Over a total operating time of 3000 h – combined with periodic electrochemical characterization (electrochemical impedance spectroscopy, EIS, every 1000 h) and post-test microscopic and chemical analyses – the functionality of the developed coatings was assessed. The goal was to conclude the technical evaluation of the EPD coatings and evaluate whether they are a plausible alternative to, or even an improvement over, the established benchmark from a functional standpoint. The assessment does not end at the purely technical level, however.

3.8. Life Cycle Assessment (LCA)

Following the extensive technical investigations of the coating systems and the demonstration of the newly developed EPD coatings for integration at stack level, it is essential to broaden the perspective beyond purely technical criteria. To extend the evaluation of the coating systems – and the decision basis for future stack manufacturing in Jülich and beyond – by the ecological dimension, a comprehensive life cycle assessment was carried out for the APS, WPS, and EPD coatings. For EPD, the assessed route reflects the process configuration that delivered the best technical performance. The optimized heat-treatment schedule was likewise assumed for both EPD and WPS. The comparison was based on coatings using the reference material MCF, applied to a single, representative Jülich interconnect component.

This section provides a structured overview of the process chains for the three coating methods, the analysis methodology and data acquisition, and finally the subsequent impact assessment. First, the defined scope and key assumptions used at Forschungszentrum Jülich (IMD-2) are outlined. The section then details the assessment carried out within the collaboration in the project NOUVEAU at IMDEA Energy (Móstoles, Spain) by K. El Jardali, V. Feyzi and D. Iribarren.

3.8.1. Goal, scope and system boundaries

The goal of this LCA study is to characterize and compare the environmental performance of the three discussed coating techniques for SOC interconnects: APS, WPS, and EPD. Moreover, the study aimed to identify the corresponding environmental hotspots where improvements should be focused for future large-scale application and technology commercialization. In focus were green-house gas emission, consumption of raw materials and energy, and acidification. In order to facilitate the comparison of the environmental profiles, the functional unit was defined as 175 cm^2 of coated area, which corresponds to a typical pilot-scale SOC stack interconnect size – similarly suiting for the previously introduced interconnect types F10 and CS^V. The coating plant was assumed to be located in Germany.

The detailed analysis was focusing processes directly related to producing the coatings and to subsequent steps required to make the component ready for use. A brief assessment on the substrate provision, including steel casting, rolling and hydroforming to the final shape was also conducted, though primarily to define the impact share of coating preparation in contrast to the production of the interconnect itself. The incorporated interconnect design was the CS^V type. A breakdown and side-by-side comparison of the process chains for the three methods – which also served as the roadmap for data collection – is shown in Figure 32.

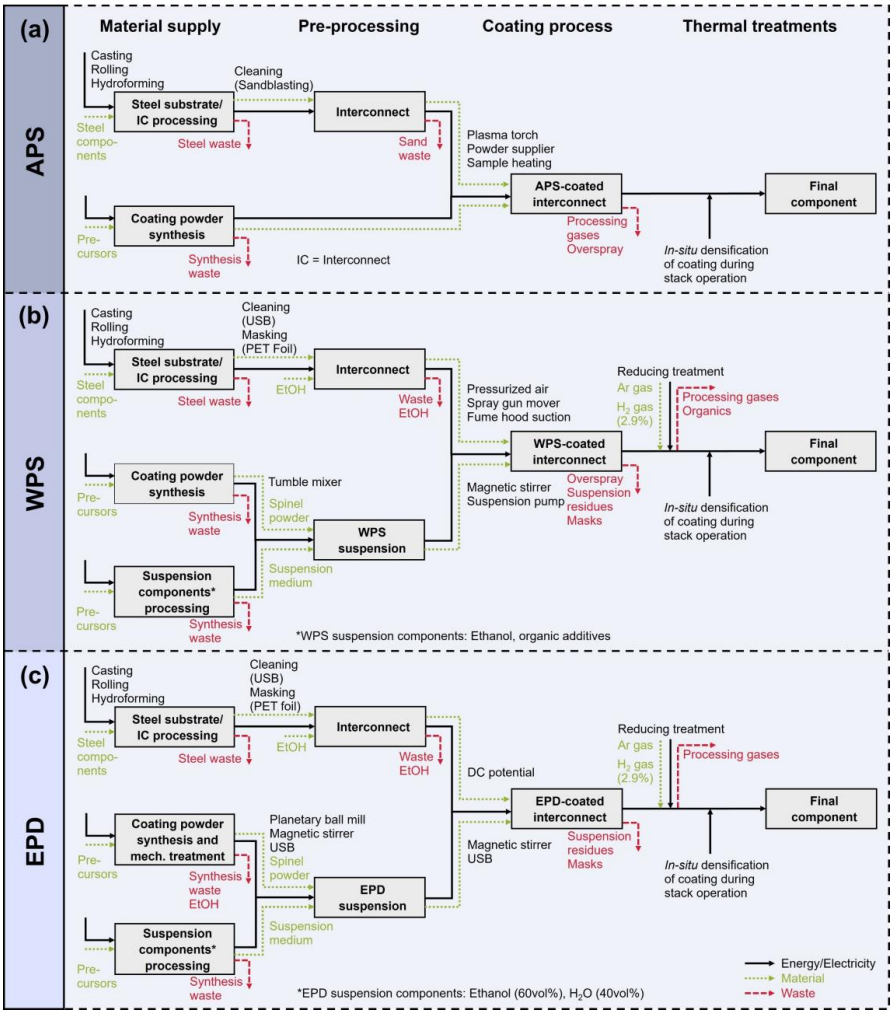

Figure 32: Flowcharts of the coating processes investigated: (a) APS, (b) WPS, and (c) EPD, with process-relevant positions disaggregated by energy, material, and waste flows.

3.8.2. Inventory data acquisition and impact assessment

The coating systems under study encompass raw material acquisition, coating powder production and the preparation of coating suspensions, including mask preparation and the final steps for heat treatment of the coated substrates. The involved processes and streams can be attributed to foreground and background in the impact assessment. A schematic, including the key positions in the foreground and background of the three coating systems, which were involved in the assessment is provided in Figure 33.

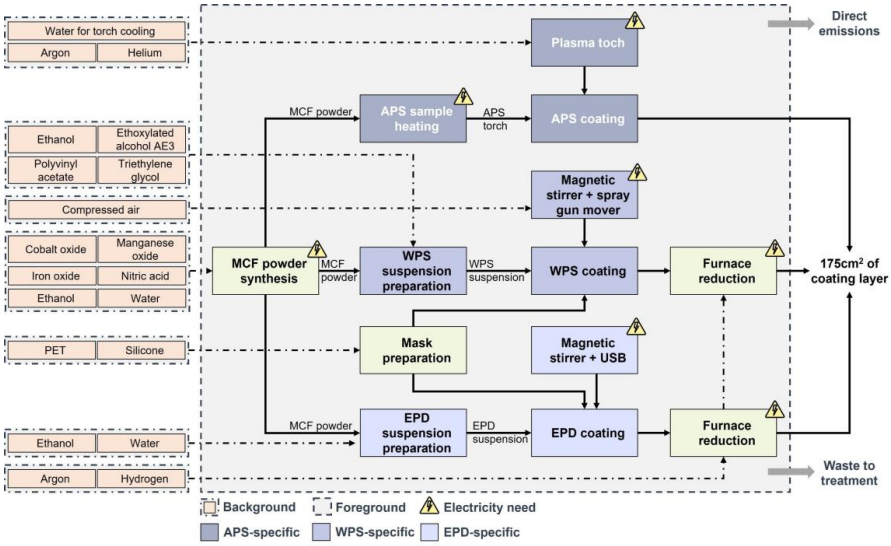

Figure 33: Schematic of the foreground and background processes and streams within the three coating systems under investigation. Overview based on contributions of K. El Jardali, V. Feyzi and D. Iribarren (IMDEA Energy).

Data on mass and energy flows for the processes within the foreground system (Figure 33) were based on the experimental work explained in Sections 3.2–3.4, supplemented by literature data and adapted to industrial application as explained below. The synthesis of MCF powder for the three coating methods was based on the work of El Jardali et al.[261] For APS, the powder is heated and fed into a plasma torch and then coated on a substrate. Unlike APS, WPS and EPD follow a similar coating approach that involves suspension synthesis, mask preparation, coating processes coupled with magnetic stirring and treatment in an ultrasonic bath (USB), and finally furnace reduction. Materials and energy consumption data for USB cleaning and EPD coating were adjusted by considering periodic replacement of the USB fluid and EPD suspension solvents. It was assumed that ethanol used for USB cleaning is changed after six hours of continuous use, while the suspension solvent (ethanol + deionized water) is renewed after every ten coating cycles in the EPD process.

For WPS, an overspray of 50% in continuous operation was assumed according to masking and the prevention of edge effects, while losses in the tube and container system were neglected. For APS, a total spraying efficiency of not more than 25% was assumed, due to comparably high overspray rates of 50% and further a powder sticking ratio of another 50%.

Electricity consumption in each system was calculated according to the power of the involved machines and their utilization time for each processing step. Machine power data were received, employing a conventional home power meter during representative coating runs in the individual procedures (WPS and EPD) or were available in the coating protocols

(APS). Continuous electrical furnaces were considered for the reduction of the coated substrates in the WPS and EPD process. The electricity consumption in the reduction furnaces was estimated based on the adjusted conveyor speed, heating and cooling rate, reduction temperature and time, and the furnace dimension.[262] Finally, inventory data for background processes such as waste management and chemicals production were retrieved from the ecoinvent database.[263]

The established inventories were implemented in the software SimaPro® for the subsequent environmental characterization of each coating system. Environmental Footprint 3.1 was used as the environmental characterization method following the recommendations of the European Commission.[264] In particular, four environmental indicators were evaluated: the carbon footprint of each coating technique (i.e., climate change, in kg CO_2 eq), acidification (mol H^+ eq), use of fossil resources (MJ), and use of minerals and metals (kg Sb eq).

4. Results and Discussion

The following sections present and interpret the results, with the aim of supporting decisions within future stack development. Starting with material stability evaluation, the development of EPD coatings is passed, culminating in the evaluation of the thermal-treatment studies. Building on a cross-comparison of coating systems – EPD vs. WPS and APS – together with exposure studies and associated performance metrics, the applicability of the newly developed EPD coatings at stack level is evaluated. Finally, the technical assessment is complemented by the LCA results to provide a complete picture.

4.1. Spinel evaluation and EPD process development

For EPD coating development, phase stability of the preselected compositions under application-relevant thermal and atmospheric conditions is the key decision criterion. Coating development for the selected compositions – within the parameter space defined beforehand – proceeded through mechanical powder conditioning, deposition time studies, and green-state characterization. The essential outcomes of these investigations are summarized below.

4.1.1. Phase stability of spinels

HT-XRD data were recorded from room temperature to 1000°C in 100°C steps. The diffractograms were interpolated as normalized intensities across the temperature interval and plotted for comparison. The resulting maps for MCF, CMF, and CMN are shown in Figure 34, Figure 35 and Figure 36, respectively.

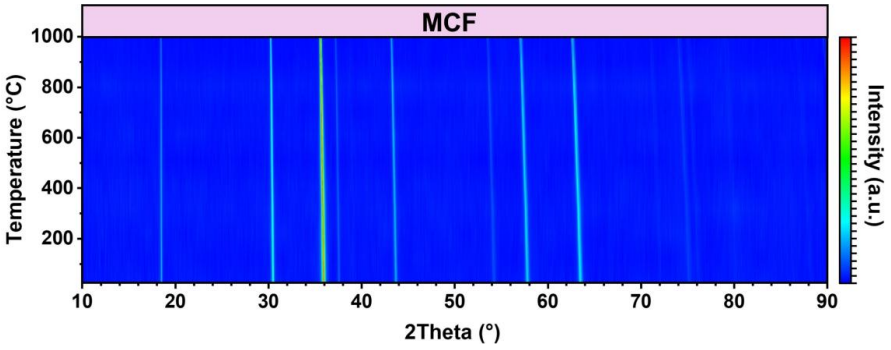

Figure 34: Interpolated HT-XRD curves for MCF powder, measured from RT to 1000°C in ambient air. Normalized intensity scale as provided in the plot. Measurement conducted by Y. J. Sohn (FZJ-IMD-2).

For MCF, the continuity of the significant peaks and their linear shift over the full temperature range indicate a single-phase spinel and a linear thermal expansion (see Figure 34).

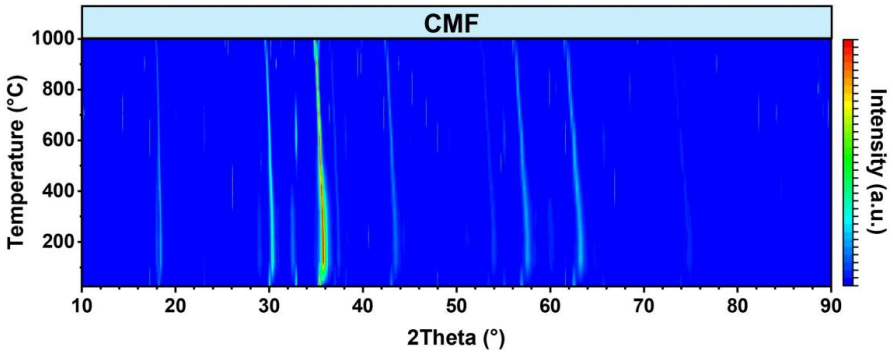

Figure 35: Interpolated HT-XRD curves for CMF powder, measured from RT to 1000°C in ambient air. Normalized intensity scale as provided in the plot. Measurement conducted by Y. J. Sohn (FZJ-IMD-2).

For the cobalt-free CMF, the intensity maps already indicate that the material is not consistently present as a cubic spinel over the measured range but occurs in a multiphase state with varying compositions and fractions (see Figure 35). Rietveld refinements of individual diffractograms enabled estimates of the phase fractions. The phases detected within the respective temperature windows and their calculated shares are listed in Table 7.

Table 7: Phase types and fractions, present in the CMF spinel powder during heat-up to 1000°C in air, determined via HT-XRD and Rietveld refinement. Measurement and evaluation conducted by Y. J. Sohn (FZJ-IMD-2).

	$CuMn_2O_4$	Mn_3O_4	Mn_2O_3	$CuFeO_2$
T (°C)	Cubic	Tetragonal	Cubic	Orthorhombic
25	67%	33%	–	–
100	68%	32%	–	–
200	68%	32%	–	–
300	69%	31%	–	–
400	79%	21%	–	–
500	95%	–	5%	–
600	79%	–	21%	–
700	86%	–	14%	–
800	100%	–	–	–
900	100%	–	–	–
1000	80%	–	–	20%

The refinements reveal several phase transformations and evolving phase ratios across the interval. Such changes can cause altered thermomechanical properties and stress generation. During measurement, this manifested in decomposition and pronounced cracking, in contrast to the uniformly sintering MCF powder. In comparison with MCF, CMF therefore suggests problematic thermomechanical behavior for interconnect coatings under thermal cycling when constrained by the steel substrate, with expected losses in adhesion, mechanical stability, and overall layer integrity. Similar observations have been reported for undoped and doped Mn-Cu spinels[117], and even studies that consider CMF workable note multiphase formation and related implications.[115,116] Due to this unfavorable

behavior, CMF was not pursued further, and attention shifted to the alternative CMN composition.

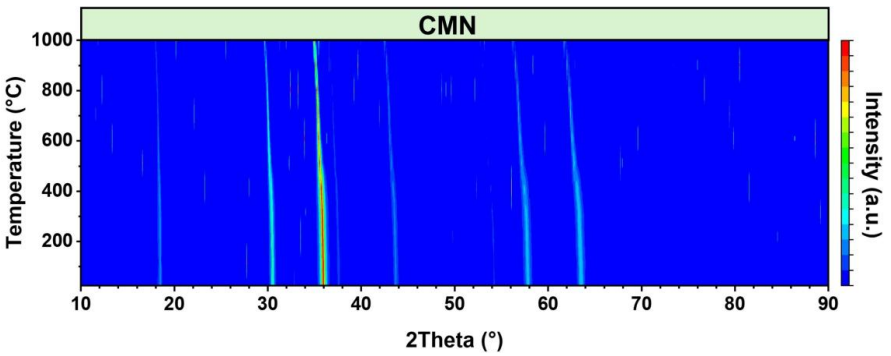

Figure 36: Interpolated HT-XRD curves for CMN powder, measured from RT to 1000°C in ambient air. Normalized intensity scale as provided in the plot. Measurement conducted by Y. J. Sohn (FZJ-IMD-2).

For CMN, the analysis likewise indicates the presence of secondary phases during the run (see Figure 36), yet these are less pronounced and do not lead to material break-up. The powder shows shape-stable sintering. Identification and quantification via Rietveld refinement yielded the distribution summarized in Table 8.

Table 8: Phase types and fractions, present in the CMN spinel powder during heat-up to 1000°C in air, determined via HT-XRD and Rietveld refinement. Measurement and evaluation conducted by Y. J. Sohn (FZJ-IMD-2).

	$CuMn_2O_4$	Mn_3O_4	Mn_2O_3	$CuMnO_2$
T (°C)	Cubic	Tetragonal	Cubic	Rhombohedral
25	88%	12%	–	–
100	88%	12%	–	–
200	87%	13%	–	–
300	88%	12%	–	–
400	88%	12%	–	–
500	98%	–	2%	–
600	97%	–	3%	–
700	99%	–	1%	–
800	100%	–	–	–
900	100%	–	–	–
1000	77%	–	–	23%

The Ni-doped Cu-Mn spinel is thus multiphase, especially at lower temperatures, with secondary phases similar in type to Fe-doped variant but at considerably lower levels. The reduced fraction of (especially non-cubic) secondary phases likely contributes to the more uniform sintering observed. Although CMN exhibits lower phase stability than the established MCF, prior reports point to promising suitability – particularly for EPD as deposition method[117,121,219] – thus the composition was included for coating development and benchmarking against MCF. Assessment of suitability therefore proceeded via the

quality of EPD-derived green layers, the ability to densify through appropriate thermal treatments, and the application-relevant tests. Process development for EPD started with the reference MCF powder.

4.1.2. EPD parameter optimization and deposition quality

As a starting point for developing the EPD coatings, powder properties were systematically adjusted by mechanical processing. The outcome of the milling study on the as-received MCF powder is presented in terms of particle size distributions, characteristic metrics (d10, d50, d90, and SSA), and qualitative SEM observations. A side-by-side comparison for milling durations of 30, 45, and 60 min against the non-milled state is shown in Figure 37.

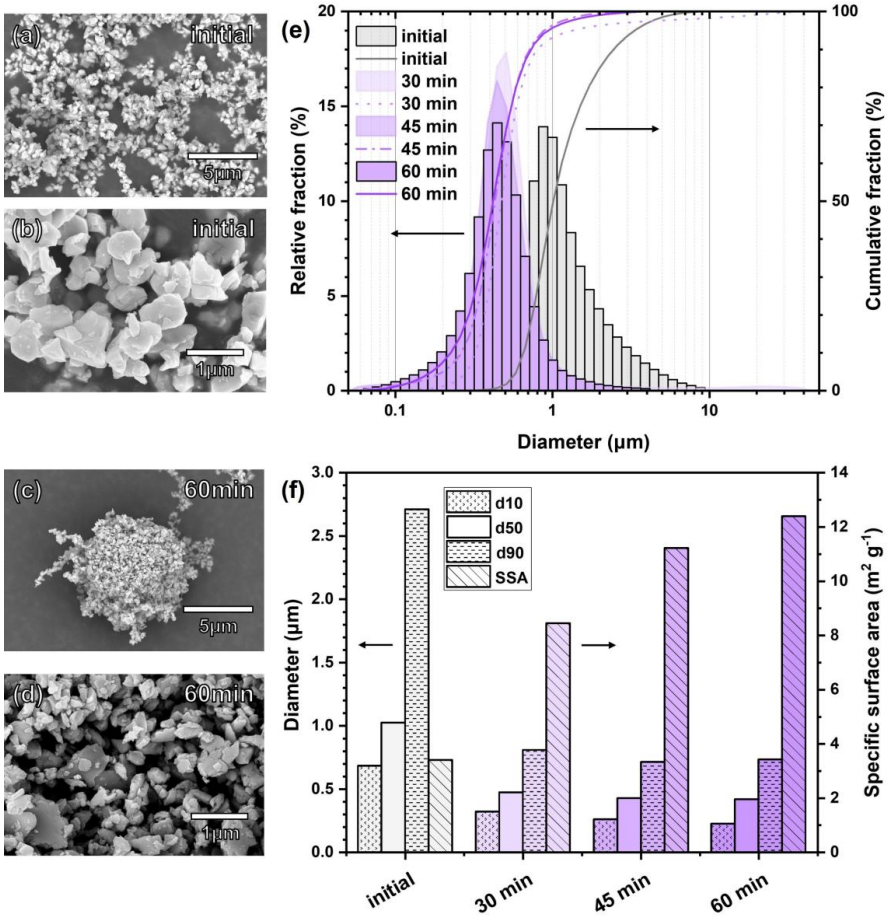

Figure 37: Ball-milling study (0, 30, 45 and 60 min milling time) of MCF powder; SEM images of (a,b) initial powder and (c,d) 60 min ball-milled powder, (e) PSDs, and (f) key numbers, including d10, d50 and d90, and SSA of all powders.

Milling preserved the monomodal PSD (with slight agglomeration after drying, most apparent at 30 min) while roughly halving the characteristic particle sizes. With respect to the median size (see Figure 37f, d50), only minor changes occurred beyond 30 min, whereas a key effect of milling is the progressive breakup of aggregates (compare the d90 values in Figure 37f). The SSA increased more markedly and reached about 12.4 $m^2 \cdot g^{-1}$ after 60 min, which is roughly three times the initial value. Particle morphology changed only marginally during milling, and the powder remained composed of rounded, slightly plate-like particles (compare Figure 37c/d with a/b). Visible agglomerates in Figure 37c can be dispersed by brief manual mortaring and/or ultrasonication.

Based on these conditioned powders and the baseline parameters identified in preliminary trials (details in Section 3.3), EPD deposition studies were performed and evaluated with a focus on deposition behavior and deposition rates, which were then related to the characteristic powder properties. With the *as-received* powder and the chosen suspension and deposition parameters (as well as in broader preliminary screening), no deposition could be achieved. This motivated an increase in electrophoretic mobility through systematic SSA enhancement and particle size reduction to enable deposition at all. The mechanical conditioning step then enabled deposition for the 30, 45, and 60 min milled powders.

The deposition curves for suspensions containing the 30, 45, and 60 min milled powders are shown in Figure 38a. The corresponding deposition rates are plotted in Figure 38b against d50 and SSA. Where deposition proceeded slowly, the time window was extended in separate runs and showed a consistent continuation of the trends (e.g., for 30 min up to 480 s). For comparability of the data presented here – and to reflect practical constraints in an industrial setting – the plotted interval is limited to 120 s.

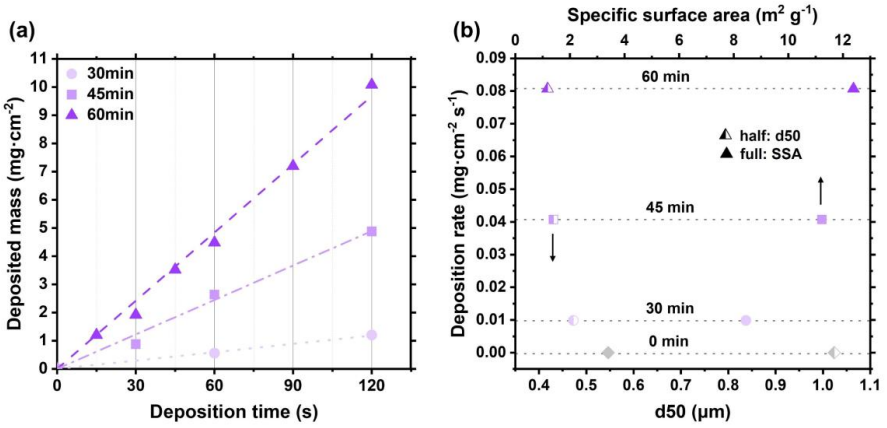

Figure 38: EPD deposition-time study with MCF powders after 30, 45 and 60 min milling treatment; (a) deposition mass curves over time, and (b) extracted deposition rate over d50 and SSA.

The data reveals an approximately linear mass/time relation within this window. Given near-constant deposition conditions – fixed potential, relatively short times, and a solid load that changes only marginally due to its magnitude – the simplified Hamaker regime (Eq. 2.10) is assumed to apply. Under continuous deposition, this permits direct control of the resulting coating thickness via time. Plotting the linearly fitted deposition rates against d50 and SSA confirms and quantifies the link between powder characteristics and deposition behavior. The results indicate that SSA has a strong influence on the rate, while also suggesting a threshold in particle size below which deposition becomes feasible – hence, the milling step itself is pivotal. At the same time, the available dataset does not support a single, unambiguous mathematical relation between these variables.

The observed overall trend is plausibly linked to improved wetting of the powder and a higher density of transport-enabling ions at the particle surface, which increases electrophoretic mobility. That deposition became possible only after milling appears as an activation step. This activation may originate from nanoscale changes in particle morphology, surface topography or stress states, which could in principle be probed by advanced microscopy. As a direct, related metric, the zeta potential – widely used in the field – could be tracked versus powder conditioning. However, mixed aqueous/organic media bring certain difficulties for reliable claims, and kinetic modelling and mechanism decoding were out of scope here. The aim was to develop functional coatings; thus, an engineering-oriented route was pursued. Accordingly, qualitative assessment of green layers formed the next step in the process, where clear differences between deposition series emerged.

Milling the as-received powder for 30 min enabled electrophoretic transport, yet deposition remained strongly inhomogeneous. Pronounced edge-to-center differences appeared: Particles nucleated at the substrate edges first and only gradually advanced inward with longer deposition times, leaving the major area uncoated (cf. SI 4). This points to an insufficient population of electrophoretically active particles, combined with locally elevated electric fields at the edges – the typical “dog-bone” effect. Beyond the limitations for industrial adaptation, long deposition times also challenge suspension stability, which in this workflow relied on ultrasonication and stirring immediately before coating and was time-limited.

Extending the milling time to 45 min produced continuous, full-area coatings under the given conditions. At moderate deposition times below one minute, shallow inhomogeneities remained visible in laser microscopy and levelled out only at longer times (cf. SI 5). Edge cracks appeared once deposition exceeded about 2 min and were weaker in the center. These defects are consistent with drying stresses, which are amplified at the faster-drying edges and where thickness is slightly higher. For 45 min milled powder, sufficiently homogeneous coatings without deep defects such as cracks were feasible at

intermediate deposition times. Nonetheless, shortening deposition time is desirable – not only for economic reasons but also to better preserve suspension stability during the run.

For the one-hour milled MCF powder, continuous coatings formed across the entire area within the investigated time window. Representative laser microscope images at multiple magnifications for edge and center regions are shown in Figure 39.

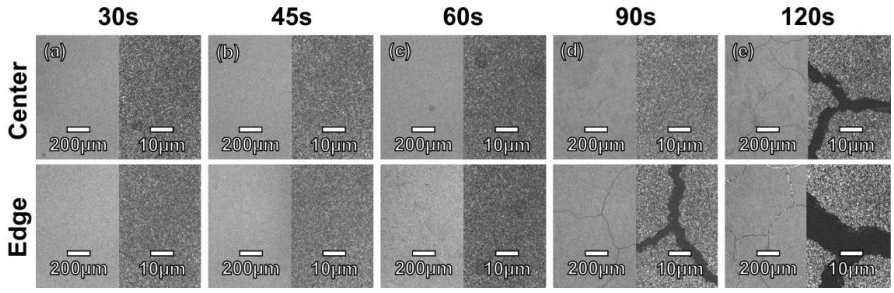

Figure 39: Laser microscopy images of coating surfaces received during the EPD deposition study, using 60 min ball milled MCF powder, after (a) 30, (b) 45, (c) 60, (d) 90, and (e) 120 s. Micrographs display the center (top row) and edge (bottom row) of the coatings.

Even at short times, deposition proceeded without the earlier inhomogeneities. From about 90 s onward, edge cracks developed and grew with longer times, extending inward and increasing in vertical and lateral extent. With increasing time, occasional agglomerate deposition was also observed, attributed to agglomerates formed during powder drying after milling or within the suspension. From about 60 s, slight edge waviness became noticeable as well.

Additional tests with longer milling times were carried out. These showed increasing agglomeration tendencies, unevenness from overly rapid and turbulent deposition, and earlier crack formation (see SI 6). Further intensification of mechanical conditioning was therefore not prioritized.

Balancing homogeneous, integral coatings with practical deposition times, a one-hour milling duration was identified for the MCF powder. A deposition time of 45 s was selected as the working point. In the standard configuration – 100 ml suspension and two 25 × 25 mm^2 faces coated in a single run – the suspension with an initial solids mass of 4 g was depleted by about 44 mg per pass, i.e., roughly 1%. Based on the initially defined criterion, five coating runs from the same suspension without reconditioning were considered acceptable.

Based on comparative characterizations of the starting powder, the powder deposited via the optimized process, and the powder remaining in suspension, additional insight was gained into which particle fractions were deposited versus left behind. The dataset combined material detached from at least ten coated substrates – stripped in ethanol using an ultrasonic bath and subsequently dried – with a minimum of 500 ml of dried residual

suspensions. The corresponding PSDs and characteristic powder metrics are contrasted in Figure 40a and b, respectively.

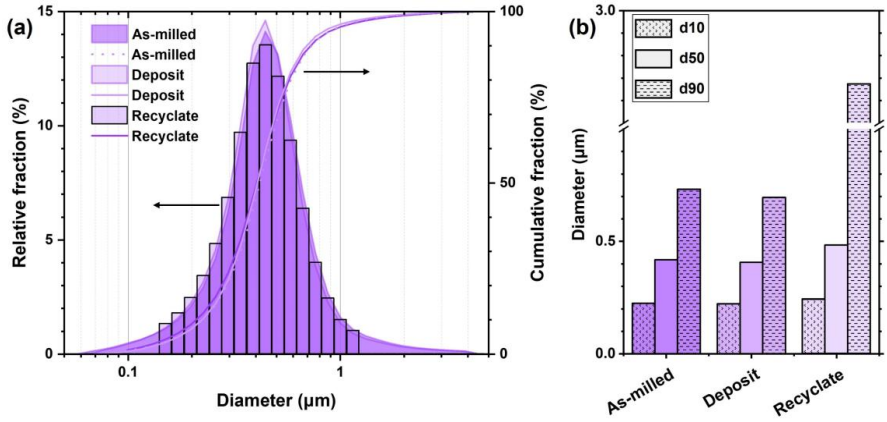

Figure 40: Powder characterization over EPD process, employing 1 h ball-milled MCF powder, reflecting the suspended, deposited and remaining powder fractions for 45 s deposition time; (a) Cumulative and relative PSDs, and (b) d10, d50 and d90 values.

The analyses indicate that the developed EPD process does not selectively harvest only the finest fraction but approximately deposits the full breadth of the particle population. Only a very small proportion of the largest particles or agglomerates may remain undeployed. The measured impact on the d90 value is barely resolvable (see Figure 40b). For the powder recovered by drying the suspensions, a slight shift towards larger particle sizes is evident – most visibly in d90 – yet mild post-conditioning via low-energy milling or mortar grinding is expected to restore full reusability. This expectation is supported by the observed depositability across the entire PSD, which argues against depleting the fine fraction. In sum, the process demonstrated near-complete utilization of the input powders and, thus, high material efficiency – an aspect of relevance for industrial implementation.

The process route defined for MCF to produce EPD green layers of high quality then served as the basis for transferring the approach to the cobalt-free alternative CMN. Powder characteristics for CMN – prepared identically to MCF – are shown by SEM together with the measured PSD in Figure 41, contrasted against the mechanically conditioned MCF reference.

Using the milling protocol optimized for the MCF feedstock, the initially partly agglomerated/aggregated CMN powder reached very similar particle morphologies and a closely matching PSD. The corresponding d10, d50, and d90 values, together with SSAs, are listed in Table 9.

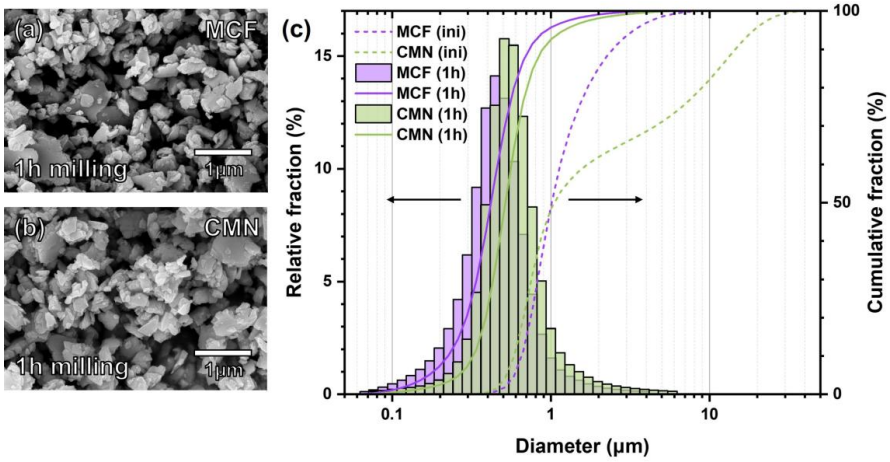

Figure 41: SEM-SE images of (a) MCF and (b) CMN powders after 1 hour milling treatment, and (c) PSD of milled powders with untreated (initial) powders as reference.

Table 9: Powder characteristics of MCF and CMN powder as prepared for this study; Values for d10, d50 and d90, as well as mass-specific surface area.

Composition	Abbrev.	d10 (µm)	d50 (µm)	d90 (µm)	SSA ($m^2 \cdot g^{-1}$)
$MnCo_{1.9}Fe_{0.1}O_4$	MCF	0.23	0.42	0.73	12.39
$CuMn_{1.8}Ni_{0.2}O_4$	CMN	0.32	0.52	0.89	10.39

*Gentle manual mortaring after ball milling to de-agglomerate the dried powder.

Overall, both powders exhibited strongly similar properties after identical treatment, in particular monomodal PSDs. CMN remained marginally coarser and showed a slightly lower SSA. It was therefore processed analogously in the EPD workflow without additional adjustments.

Also, during deposition of the milled CMN powder, the behavior closely mirrored that of MCF. Homogeneous, continuous layers formed, with a 45 s CMN deposition reaching 3.4 $mg \cdot cm^{-2}$ (versus 3.5 $mg \cdot cm^{-2}$ for the corresponding MCF layer). Despite the slightly coarser CMN powder, the deposition response was essentially the same, underscoring the complexity of EPD kinetics and the interplay of several factors. Beyond small morphological differences, the slightly lower density and the altered surface chemistry associated with composition likely contribute. Laser-microscope images from the CMN deposition series, acquired in full analogy to the MCF study, are shown in Figure 42.

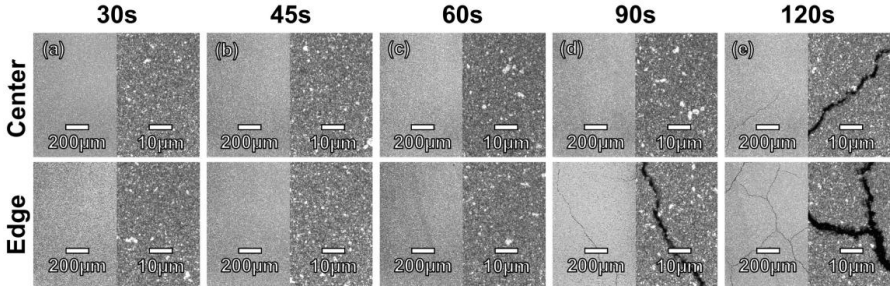

Figure 42: Laser microscopy images of coating surfaces received during the EPD deposition study, using 60 min ball milled CMN powder, after (a) 30, (b) 45, (c) 60, (d) 90, and (e) 120 s. Micrographs display the center (top row) and edge (bottom row) of the coatings.

The outcome confirms the close parity in deposition behavior and layer formation and supports adopting the full parameter set from the MCF reference (cf. Figure 39). With EPD layers optimized in the green state and a standardized process window established, attention could turn to developing thermal treatment schedules for densification and targeted microstructural tailoring. The results and interpretation of the MCF- and CMN-EPD heat-treatment study are presented in the following chapter.

4.2. Thermal treatment study on EPD coatings

With the EPD coatings optimized in the green state and deposited on Crofer22APU substrates, the systematically defined thermal treatment schedules (S0–S2; see Section 3.4.2, Table 5) were applied to achieve maximum densification and, ultimately, the most favorable microstructure for performance. All coatings examined initially showed a coherent appearance without macroscopic defects such as spallation or cracking.

The characterization of microstructures along the specific steps of the thermal treatment sequence, as well as the associated phase evolution, was performed to qualitatively assess the integrity and structural condition of the coatings and to gain an understanding of the underlying transformations.

4.2.1. Phase evolution during reduction and oxidation

The comparison first focuses on the reference material, MCF. Phase development is traced from the powder to the deposited layer (as-coated), through the optional reduction steps, and finally to the oxidizing sintering in air, simulating stack joining. A comparison of XRD surface analyses for the MCF coating group is shown in Figure 43.

The diffractograms at first confirmed the presence of the spinel phase after deposition, while additional Fe peaks were attributed to the signal of the underlying steel substrate due to the limited thickness of the non-densified EPD coating. For both reduction treatments (R1 and R2), the presence of Mn in its simple oxide form (MnO) and the occurrence of Co and Fe in metallic states were identified. Following the oxidizing heat

treatment simulating the stack assembly, the original spinel phase was restored for all three programs (S0, S1, and S2), regardless of the preceding thermal history.

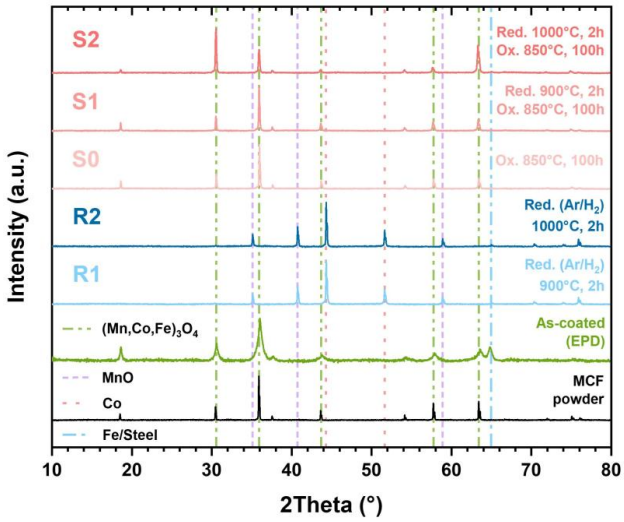

Figure 43: XRD of MCF-EPD coatings in the specific states: as-coated, after the reduction steps R1 and R2, and after the according (re-)oxidation steps S0, S1 and S2. The diffractograms include max. the five most significant peaks of each phase. The results indicate the partial reduction of the spinel to metal phase (Co + Fe) and MnO.

For the group of CMN coatings, an analogous comparison of XRD surface analyses is presented in Figure 44.

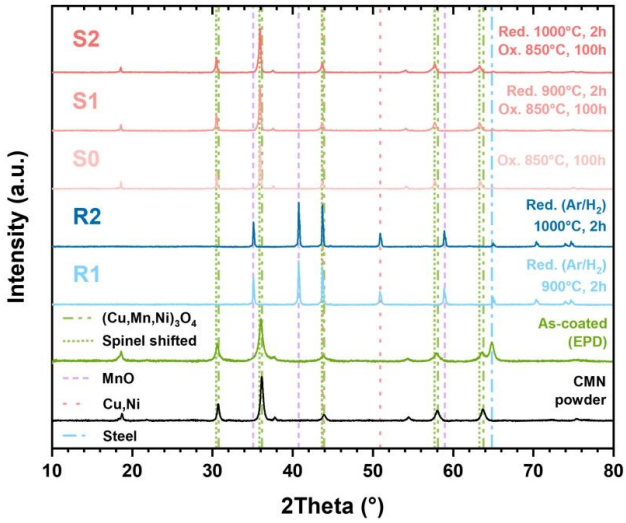

Figure 44: XRD of CMN-EPD coatings in the specific states: as-coated, after the reduction steps R1 and R2, and after the according (re-)oxidation steps S0, S1 and S2. The diffractograms include max. the five most significant peaks of each phase. The results indicate the partial reduction of the spinel to metal phase (Cu + Ni) and MnO. A slight peak shift of the spinel phase towards lower 2θ angles is observed after (re-)oxidation.

Comparable to the analyses of the MCF coatings, the CMN samples exhibited similar general tendencies, but with several decisive differences. The diffractograms confirmed the presence of the spinel phase after deposition, with an additional Fe peak again attributed to the steel substrate due to the low coating thickness. After reduction (R1 and R2), the diffraction patterns indicated the presence of metallic Cu and Ni phases alongside MnO. Following the oxidizing treatments, all three sample types were re-converted into the original spinel structure. However, in contrast to MCF, all three oxidized CMN coatings showed a systematic shift of the characteristic spinel peaks towards lower 2θ angles, suggesting a slight compositional change relative to the initial state. The incomplete transformation into metallic phases and MnO, observed for both MCF and CMN, is consistent with the limited reducing potential of the chosen conditions, by means of remaining O_2 partial pressure and H_2 concentrations of a few vol.%, and aligns with reports on reactive sintering and partial reduction in similar systems.[203,250,265]

Further insight into structural changes, the spatial arrangement of emerging phases, and overall coating uniformity at each processing stage is provided by microstructural analyses. The corresponding results – SEM and EDS examinations of surfaces and cross-sections, complemented in parts by quantitative assessments of key microstructural metrics – are presented and interpreted in the next section.

4.2.2. Microstructural evolution during thermal treatments

For MCF, cross-sectional analysis revealed adhering, coherent, and intact coatings in all investigated stages without the formation of cracks or comparable defects, considering both surfaces and cross-sections. A detailed microstructural comparison of coated Crofer22APU substrates in the as-coated state and after simulated stack joining is provided in Figure 45. The results of the complementary quantitative image analysis along the thermal treatment schedules, including the evolution of shrinkage and porosities (bulk and surface-accessible) are later presented in Figure 49.

For the direct oxidizing sintering route, a slight reduction in coating thickness accompanied by residual open porosity, reaching the coating surface, was observed (cf. Figure 45c/d). At the same time, the development of a distinct chromium oxide scale exceeding 1 µm in thickness became visible, with only the directly adjacent region of the MCF coating of comparable thickness appearing consistently dense (cf. Figure 45d). The overall low shrinkage, as well as the marginal particle coalescence with remaining open porosity results from the limited sinterability of the loosely bound powder compact after deposition. The concurrent growth of a chromia scale below the thin, continuous bottom part of the coating is explained by the strongly facilitated inward migration of oxygen through the open porosity during the simulated assembly step. While the spinel phase remains stable, the microstructure of MCF-S0 – with its open porosity – already

compromises the protective function in terms of both corrosion resistance and chromium retention.

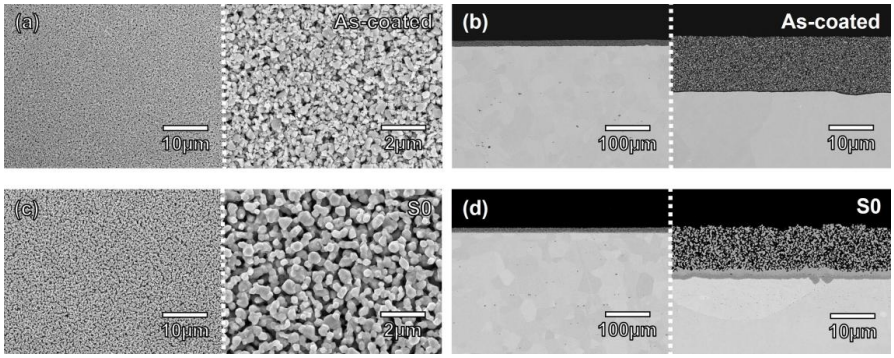

Figure 45: SEM images of MCF-EPD coated Crofer22APU substrates, as surfaces and cross-sections (a,b) in the as-coated state, and (c,d) after the simulated stack-assembly step (S0). Topography images via SE and crosscuts via BSE detection.

The additionally employed two-step treatments aimed to enable stronger densification and closed porosity. Analogous comparisons, featuring the reduction treatments at 900°C (R1) and 1000°C (R2) as well as the corresponding oxidation treatments (S1 and S2) during the subsequent assembly step are provided in Figure 46 and Figure 47, respectively. The quantified assessment is again provided in Figure 49.

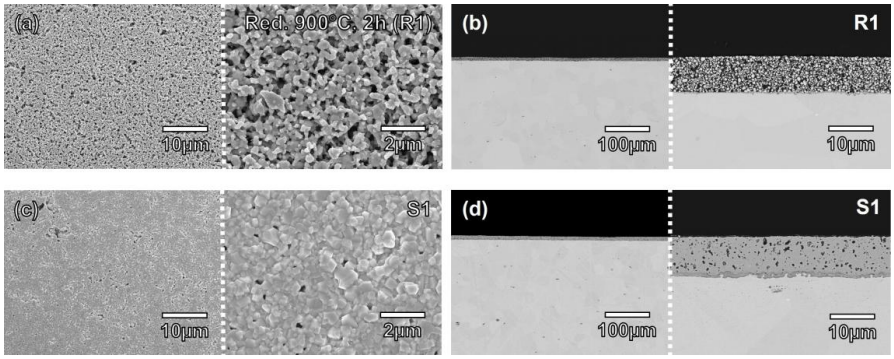

Figure 46: SEM images of MCF-EPD coated Crofer22APU substrates, as surfaces and cross-sections (a,b) after 2 h reducing treatment at 900°C (R1), and (c,d) after subsequent simulated stack-assembly (S1). Topography images via SE and crosscuts via BSE detection.

In the reduced states, a pronounced decrease in coating thickness was observed, with R2 showing particularly strong shrinkage to less than half of the initial thickness and a correspondingly reduced porosity. The multiphase nature of these states, as indicated by the XRD analysis (cf. Figure 43), was also evident in SEM images, specifically the cross-sections (cf. Figure 46b and Figure 47b).

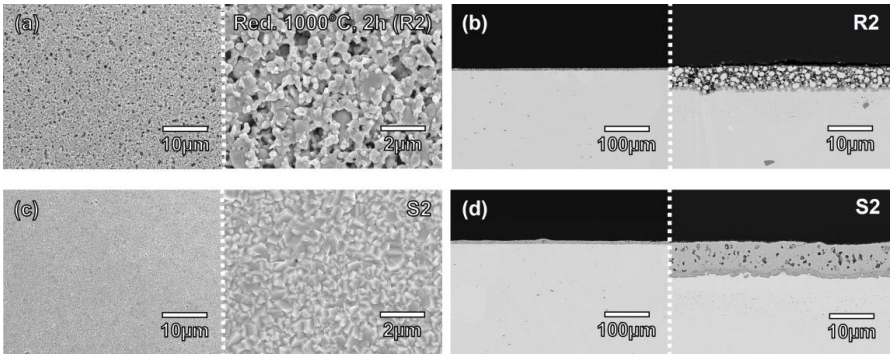

Figure 47: SEM images of MCF-EPD coated Crofer22APU substrates, as surfaces and cross-sections (a,b) after 2 h reducing treatment at 1000°C (R2), and (c,d) after subsequent simulated stack-assembly (S2). Topography images via SE and crosscuts via BSE detection.

Additional insight into the distribution of phases and elements across the different stages was provided by detailed EDS mappings, exemplified for the two-step treatment R2/S2 in Figure 48.

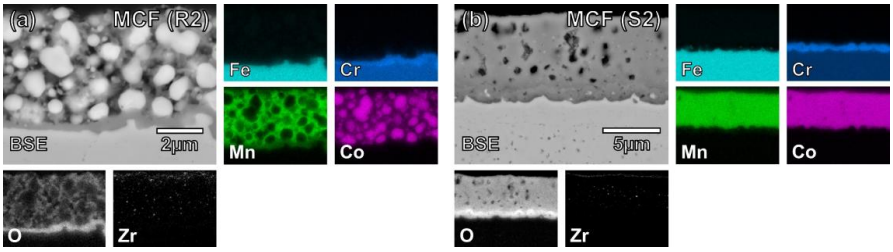

Figure 48: Cross-sectional EDS mappings of MCF-EPD coatings after (a) R2 treatment (2 h reduction at 1000°C) and (b) after the subsequent oxidation (100 h oxidation at 850°C) accounting to the overall treatment S2. The elemental analyses reveal a pronounced localization of Cr within the chromia scale. Detected traces of Zr can be attributed to impurities in the commercial powder.

The EDS results indicate that the metallic phase (Co + Fe) was embedded as spherical particles within an MnO matrix, with R2 showing substantially larger metallic particles than R1. The detected shrinkage during reduction is clearly linked to oxygen release and the enhanced diffusivity of the metallic phases formed. The accompanying reduction in pore fraction, more pronounced at the higher reduction temperature (R2 compared to R1), is attributed to this mechanism and to the agglomeration of metallic particles, driven by temperature-enhanced diffusion.

After the final oxidizing step, the previously reduced samples exhibited an increase in coating thickness compared to their respective reduced states, with the effect being substantially more pronounced for S2 compared to S1. This is due to the stronger coagulation of metal particles, resulting in thinner coatings in the reduced state. As diffusion-driven reorganization within the strongly segregated R2 layers is limited, the formation of highly dense coatings during re-oxidation is hindered. Therefore, re-oxidation

results in a strong re-growth in coating thickness for R2/S2, whereas the effect for R1/S1 remains within the limits of the propagated uncertainty. Although the overall appearance of the coatings is uniform, slight irregularities result in rather high error values in the Gaussian uncertainty propagation for relative changes (see Figure 49a). Despite the uncertainties, both two-step treatments clearly show a significantly stronger shrinkage (cf. Figure 49a), in contrast to the single-step protocol.

Further considering the cross-sections, both two-step treatments resulted in closed porosity, with S2 showing fewer but slightly enlarged pores compared to S1 (cf. Figure 46d and Figure 47d). With respect to the surface-attaching porosity, indicated in the topographical images (cf. Figure 46c and Figure 47c), a clear decrease was observed when comparing the two-step treated coatings – most pronounced for R2/S2 – with the single-step treatment (S0). Though bulk porosity appears rather equal across the two-step treatments, the surface porosity was determined to be one order of magnitude lower for S2 than for S1 (cf. Figure 49b).

The uniform layer characteristics with closed porosity after the two-step treatments are attributable to the homogeneous re-incorporation of oxygen into an already densified structure. The slightly higher degree of densification in the S2 protocol stems from the more compact microstructure resulting from the preceding high-temperature reduction. As a result, MCF coatings subjected to the two-step thermal treatments exhibit a more favorable property profile, while the nearly fully dense top layer obtained for S2 especially indicates a promising barrier character.

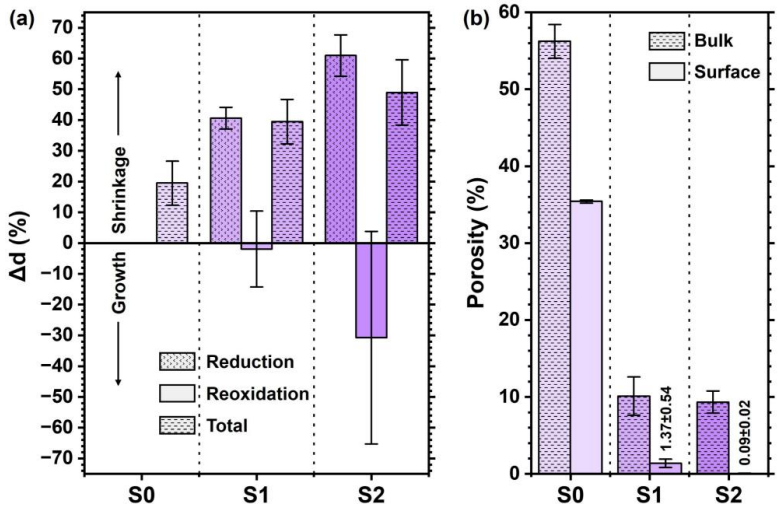

Figure 49: Quantitative image analysis of MCF-EPD coatings over the characteristic stages, highlighting the systematic differences in microstructural evolution over the thermal treatment schedules S0–S2; (a) shrinkages, including propagated uncertainties within the corresponding step, and (b) porosities in the bulk and with surface accessibility.

For CMN, complementary to the laser microscopical surface characterization, cross-sectional SEM analysis further demonstrated that the identical processing route, as established for the MCF powder, covering powder preparation and deposition, enabled the fabrication of similarly uniform green layers. CMN coatings in the as-deposited state appeared continuous and free of visible defects, with thicknesses in the range of 10–15 µm. The SEM comparison of the coatings in the as-coated state and after the simulated assembly step, analogous to the MCF coatings, is provided in Figure 50.

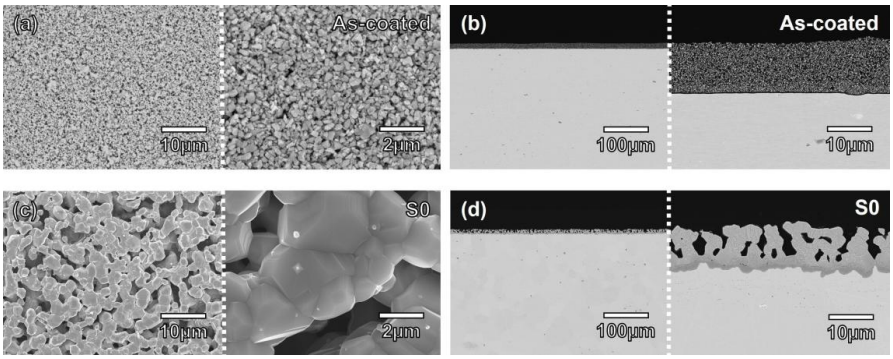

Figure 50: SEM images of CMN-EPD coated Crofer22APU substrates, as surfaces and cross-sections (a,b) in the as-coated state, and (c,d) after the simulated stack-assembly step (S0). Topography images via SE and crosscuts via BSE detection.

After direct oxidizing treatment, the coatings retained a porous morphology with pore channels partially extending through the entire thickness (cf. Figure 50d). Compared to the equivalent MCF coatings, the CMN samples exhibited a noticeably coarser microstructure combined with a slightly more pronounced thickness reduction. For CMN-S0, the stronger redistribution of material compared to MCF reflects the effect of Cu on the sinterability of Mn-based spinels and the overall higher sintering activity of Cu-Mn spinels.[117,120,266,267] Nevertheless, the formation of a porous structure with pore channels spanning the entire coating thickness is again a direct consequence of the low initial density of the EPD coatings. This microstructure does not provide favorable conditions for blocking inward oxygen migration or volatile chromia release.

Again, the employment of a pre-reduction aimed to tackle the inadequate microstructural properties and to enable the formation of uniform, dense coatings. Comparative SEM images, including R1 and R2 reduction, as well as the corresponding oxidation treatments S1 and S2 are shown in Figure 51 and Figure 52, respectively.

After both reduction programs, the CMN coatings again showed pronounced shrinkage, accompanied by the formation of spherical metallic Cu and Ni particles embedded within a MnO matrix (EDS provided in Figure 53). In R2, the metallic features appeared distinctly coarser compared to R1, combined with the occurrence of isolated large

pores in some instances spanning major parts of the coating thickness (compare Figure 51b and Figure 52b).

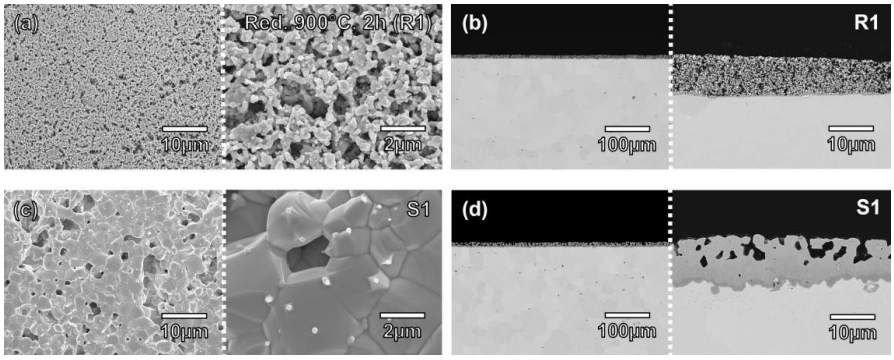

Figure 51: SEM images of CMN-EPD coated Crofer22APU substrates, as surfaces and cross-sections (a,b) after 2 h reducing treatment at 900°C (R1), and (c,d) after subsequent simulated stack-assembly (S1). Topography images via SE and crosscuts via BSE detection.

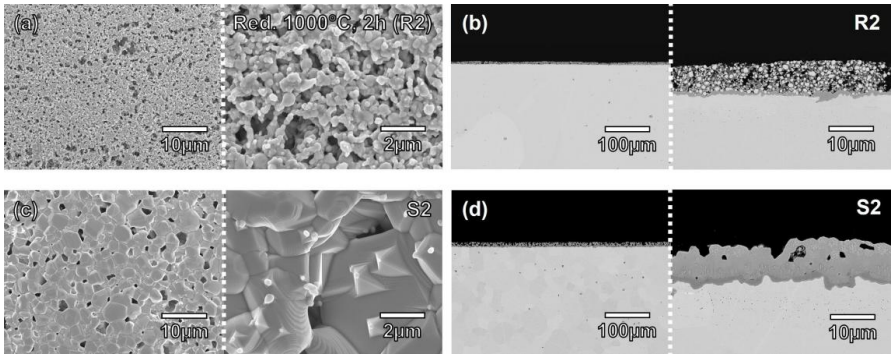

Figure 52: SEM images of CMN-EPD coated Crofer22APU substrates, as surfaces and cross-sections (a,b) after 2 h reducing treatment at 1000°C (R2), and (c,d) after subsequent simulated stack-assembly (S2). Topography images via SE and crosscuts via BSE detection.

After the simulated stack assembly, the pre-reduced coatings displayed a reduced thickness compared to the as-deposited state but with slight re-thickening relative to the reduced condition (compare Figure 51d and Figure 52d). The strongest shrinkage with the lowest residual porosity was again associated with protocol S2. Nevertheless, in comparison to MCF, the residual porosity in CMN exhibited a different morphology, with a particularly surface-accessible distribution combined with a continuous, dense base layer of several micrometers adjacent to the substrate.

The reduced contribution of re-oxidation to densification in CMN relative to MCF is related to the higher Mn content of the base spinel ($CuMn_2O_4$ vs. $MnCo_2O_4$; later discussed for the re-oxidation-related mass gain, see Section 4.3.2, Eqs. 4.1 and 4.2). Combined with the intrinsic tendency of Cu-Mn spinels towards particle agglomeration,

this results in coarse microstructures after re-oxidation, consistent with the grain coarsening also observed after direct oxidation of CMN.

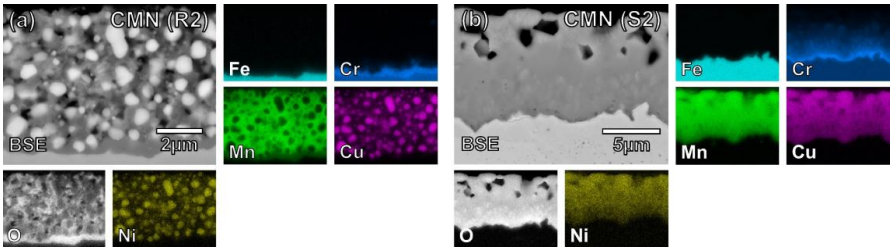

Figure 53: Cross-sectional EDS mappings of MCF-EPD coatings after (a) R2 treatment (2 h reduction at 1000°C) and (b) after the subsequent oxidation (100 h oxidation at 850°C) accounting to the overall treatment S2. The elemental analyses reveal an extensive Cr spreading throughout the coating.

The formation of a chromia scale was detected for all CMN specimens, though the steel-coating interface appeared less regular than for MCF. The EDS mappings (comparing Figure 53 and Figure 48) highlight the pronounced difference in chromium distribution between the two spinel types after simulated joining. While for MCF, chromium was clearly confined to the chromia scale at the steel-coating interface, CMN in contrast exhibited a far-reaching chromium penetration, extending into surface-accessible porosity. This was further accompanied by a concurrent depletion of the spinel phase, most evident in the Ni and Cu signals. It aligns well with the systematic shift of the spinel peaks observed in the phase analysis, which likely originates from the incorporation of chromium into the spinel lattice, resulting in the formation of a partially substituted $(Cu,Mn,Ni,Cr)_3O_4$ spinel. This allows the conclusion of accelerated diffusion processes and reflects the known tendency of Cu-Mn spinels to permit chromium transport and trapping.[122,219,268] Such behavior already raises fundamental concerns regarding the protective effectiveness of CMN-based coatings over long-term operation.

The irregular interface observed between CMN coatings and the steel substrate after the assembly step is also likely a result of the strong sintering activity of the spinel and its interaction with steel components, particularly chromium. This is a further critical aspect in terms of thermo-mechanical stability. Due to substantial non-uniformity and irregularities across the CMN-EPD coatings, no reliable quantitative data processing was possible, thus the evaluation remained on a rather qualitative level. Nevertheless, a solid estimation considering the relevant microstructural characteristics could be made on the given base.

Taken together, the qualitative structural analysis across the selected thermal treatments and the integration of the assembly step highlight the superior suitability of the established MCF composition and the benefits of two-step thermal treatments. For CMN, by contrast, the results raise the question of whether coatings of this composition – or Cu-Mn spinels more generally – can be integrated into existing thermal processes such as the

100 h assembly step, or whether lower joining temperatures and/or shorter dwell times are essential to avoid significant degradation during assembly itself and to achieve beneficial microstructural properties. A more detailed picture of how the thermal treatment protocols – and the resulting structural features – affect coating performance should be obtained from the investigations carried out within the exposure series.

4.3. Exposure study on EPD coatings (Chalmers)

The characterizations conducted within the Chalmers exposure study jointly serve two aims: To identify the most suitable EPD coating and corresponding thermal process route, and to assess the general integrability of these coatings at stack level from both materials and processing perspectives. The findings on phenomena during stack assembly and the first hundreds of operating hours (total of 500 h) provide the basis for selecting the EPD variants carried forward into the longer exposure campaign (3000 h). They are also central for choosing an appropriate thermal route for the parallel MCF-WPS investigations. A detailed breakdown and discussion of chromium evaporation, mass gain and the underlying kinetics, as well as the electrical characterization, are presented in this section.

4.3.1. Cr evaporation during in-situ coating densification

The spectrometrically evaluated chromium evaporation data, collected continuously during exposure, are summarized for the six investigated coating types with measurement points at 100 h (simulated assembly) and at 200 h and 500 h (simulated stack start). As a reference for uncoated Crofer22APU steel, data from a study by Reddy et al.[122] were included. Although the referenced study employed a constant exposure at 800°C, while the present work involves an initial 100 h joining step at 850°C, the comparable measurement methodology and identical denuder setup provide a suitable basis for comparison. Moreover, the slightly milder conditions in the reference study ensure that no artificial improvement of the present results is implied. The chromium release rates of the six coating types, compared with the uncoated reference, are presented in Figure 54a, while Figure 54b shows the isolated data set for the MCF coatings.

Across all exposure conditions, the application of protective coatings resulted in a substantial reduction of chromium volatilization. However, two distinct groups emerged, separated by coating composition. The MCF coatings consistently reduced chromium evaporation by a factor of 10–20 compared to CMN and by approximately a factor of 30 compared to the uncoated steel. Within both groups, the two-step treatment including pre-reduction at 1000°C (S2) provided the lowest evaporation rate. For MCF, the other two treatments (S1 and S0) yielded slightly higher cumulative release but remained close to each other. In contrast, for CMN the 900°C pre-reduction route (S1) deviated towards significantly higher values.

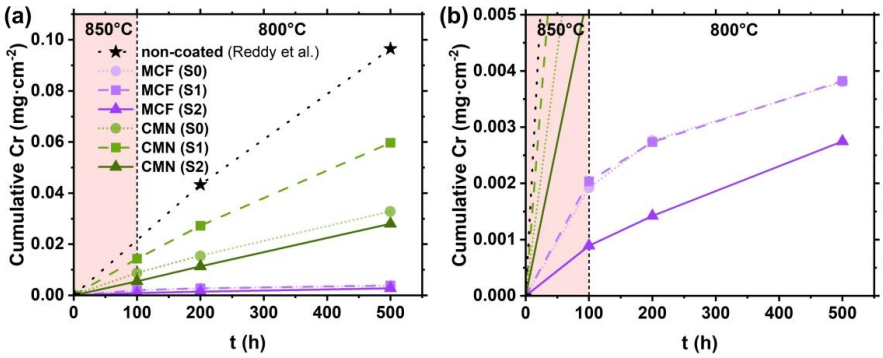

Figure 54: Cumulative Cr evaporation curves for all coating types (a) and in detail for MCF samples (b), in contrast to non-coated Crofer22APU substrates (reference).

Thereby, the results reinforce the tendencies already indicated by the structural analyses. The markedly better chromium retention of the MCF coatings compared to the CMN coatings – partially only providing minor improvements over the uncoated reference – underlines the excellent protectivity of MCF against chromium poisoning of the air electrode. The visible flattening of the Cr evaporation can be attributed to the slightly elevated temperatures and microstructural evolution during the simulated stack-assembly phase.[46,122]

The distinctly lower chromium release measured for the MCF samples subjected to pre-reduction at 1000°C (R2) can likely be linked to the slightly higher densification, in particular the formation of a denser and more continuous top layer (compare Figure 46d and Figure 47d, and further Figure 49). The nearly identical behavior of the S0 and S1 types suggests that residual open porosity remains in these coatings, facilitating the outward diffusion of volatile chromium species. Nevertheless, the absolute chromium evaporation rates of all MCF coatings are on a very low level, in line with favorable values reported in the literature.[46,122] In contrast, the substantially poorer chromium retention of the CMN-coated substrates is consistent with the chromium penetration observed after stack assembly in the microstructural analysis. The nearly identical results of CMN-S0 and CMN-S2, together with only a marginal advantage of the two-step treatment, indicate that the limited chromium retention of CMN under the present conditions is dominated by intrinsic material properties rather than by the specific microstructure formed. The disproportionately poor performance of CMN-S1, however, likely points to quality issues in this specimen group. Since all coupons were coated in one batch and cut from the same carrier plate, the occurrence of critical defects such as cracks due to unnoticed process deviations cannot be excluded. Based on the structural results presented in Section 4.2, the degradation of CMN-S1 cannot be sufficiently explained by microstructural arguments alone.

4.3.2. Mass-gain curves during stack start

As complementary characterization, the discontinuously determined mass gain rates should provide further insight into the protective functionality of the coating types and the relation of blocking inward and outward migrating species. Accordingly, the mass gain data is presented and discussed in this section.

The mass gains of the six coating types were determined discontinuously by repeated removal, weighing, and reinsertion of the samples during the 500 h exposure. Analogous to the chromium evaporation data, the results were processed and plotted, as shown in Figure 55a. As concurrent mass loss due to evaporating chromium influences the measured data, a correction, employing the corresponding masses from Section 4.3.1 was performed and is provided in Figure 55b.

From the phase analyses in Section 4.2.1 it is evident that during the assembly step, coatings subjected to pre-reduction undergo a complete re-oxidation to the spinel phase. This transformation is necessarily associated with a mass increase due to oxygen incorporation into the coating. The contributions of this re-oxidation to the total mass gain are governed by the spinel stoichiometry and therefore differ between the two compositions, as outlined by the following reactions (Eqs. 4.1 and 4.2):

$$1.0\ MnO + 1.9\ Co + 0.1\ Fe + 1.5\ O_2 \rightarrow 1\ MnCo_{1.9}Fe_{0.1}O_4 \quad (4.1)$$

$$1.8\ MnO + 1.0\ Cu + 0.2\ Ni + 1.1\ O_2 \rightarrow 1\ CuMn_{1.8}Ni_{0.2}O_4 \quad (4.2)$$

Based on these stoichiometries, the expected re-oxidation-induced mass increases relative to the reduced state amount to +25.5% for MCF and +23.3% for CMN. Combined with the determined average coating masses, these contributions formed the basis for the applied corrections to the measured mass gain curves. The doubly corrected data are presented in Figure 55c. In order to fully exclude the oxidation effects during the assembly phase, which enables a clearer perspective on the trends after the initial stack start, an additional correction of the curves was performed by only subtracting the 100 h value. In this case, once again, the study by Reddy et al.[122] was used as a reference for uncoated Crofer22APU steel. Since no value was reported for 500 h in that study, the measurement point at 1000 h was considered, which however continues the trend evident up to 200 h. The corresponding curves are presented in Figure 55d.

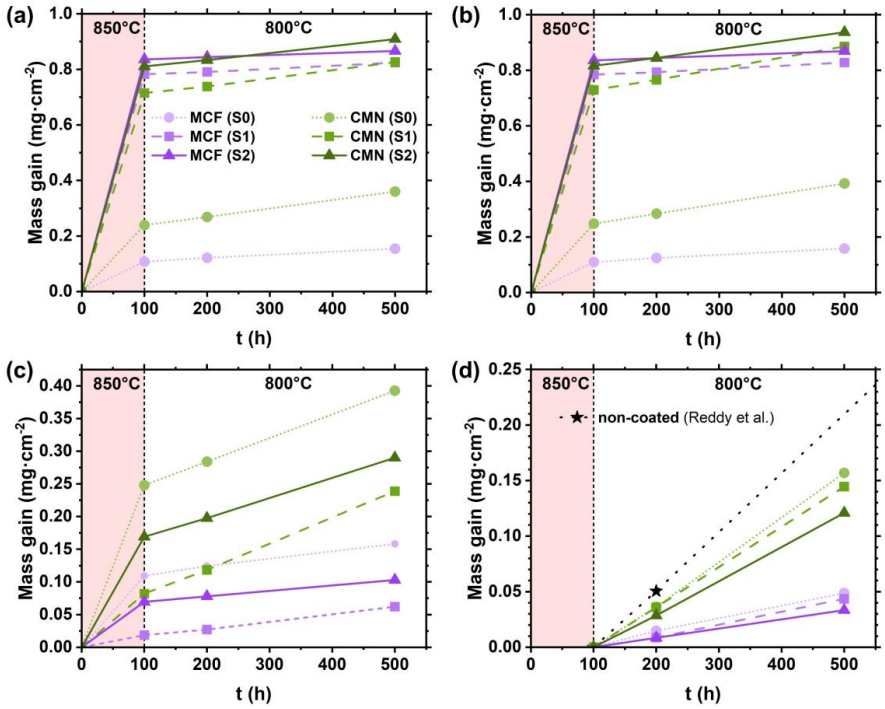

Figure 55: Mass gains of EPD-coated and non-coated Crofer22APU substrates (reference): (a) without corrections, (b) after correction for Cr evaporation, (c) after subtraction of the re-oxidation contribution of the spinel coating, and (d) with chromium-evaporation-related correction and subtraction the cumulated mass-gain after the assembly phase.

The plots in Figure 55 (a, b) show a continuous increase in mass gain relative to the initial state for all coated samples, with a pronounced flattening of the curves after the first 100 h. Due to the substantially lower amount of evaporating Cr in the MCF samples, the impact of the related correction on the curves is nearly negligible, in contrast to CMN. When additionally the calculated re-oxidation contributions for the S1 and S2 types are subtracted (cf. Figure 55c), the effect of re-oxidation-induced curve flattening is substantially reduced, and the overall trends during the exposure duration reflect the same separation already observed in the chromium evaporation results: the group of MCF coatings consistently exhibits lower mass gain compared to the CMN group. Particularly after the simulated assembly step, the MCF coatings show systematically lower increases in the mass gain curves. Within both groups, MCF and CMN, the lowest mass gain rates during continued exposure after assembly are observed for the S2 samples, i.e., after pre-reduction at 1000°C.

During the exposure period following the initial 100 h, a decrease in the slope of the cumulative mass gain is evident for all coated sample types in comparison with the uncoated reference, observable in Figure 55d. Moreover, a clear separation between the curves,

determined by material and treatments becomes visible in this depiction. Additionally, it should be noted again that the reference data for uncoated Crofer22APU were obtained under slightly milder conditions in the comparative study[122], and this must be considered when interpreting the overall dataset.

The separation of the pre-reduced specimens (S1 and S2) from the oxidized specimens (S0) that is visible in the non-corrected (Figure 55a) and chromium-corrected curves (Figure 55b) is directly attributable to the re-oxidation of the coatings. After applying the second correction, accounting for both chromium evaporation and the calculated mass gain from re-oxidation, the trends converge with the findings from the evaporation tests: The MCF group over the duration of the exposure exhibits lower mass-gain rates than the CMN group, while the uncoated reference (Figure 55d) shows the highest values. This confirms the superior protectivity of MCF.

For both spinels, the lowest mass-gain rates after the first 100 h of exposure were observed for the R2 condition. For MCF this can again be attributed to the denser top layer (cf. Figure 47c), which strongly slows the inward migration of oxygen. For CMN, the effect may be caused by the combined action of a slightly denser top layer (cf. Figure 52c) and the comparatively thick and continuous bottom layer adjacent to the substrate.

For all estimations, based on the calculated re-oxidation effect, the robustness of the double-corrected curves must, however, be considered with caution. Small variations in the actual coating mass can introduce errors into the re-oxidation correction, which is based on averaged values. This mainly affects the interpretation within the assembly phase, while the longer-term trends during subsequent operation remain unaffected and still provide a reliable picture. Further, it must be noted that the processes occurring during the one-hour fixation treatment of the samples exposed in air solely were not included in the data. This introduces a minor underestimation of mass gain and chromium release but does not affect the overall trends.

Overall, despite minor limitations in comparability and data robustness, the trend, previously observed in the Cr-evaporation tests, carries through: Under the conditions relevant to stack joining and start-up, the reference composition MCF provides distinctly better protection than the alternative CMN. The previously indicated advantage of a two-step thermal treatment – especially with a 1000°C reduction step – was likewise reinforced. As an important performance marker, partially linked to steel corrosion, the next section briefly addresses the results of the electrical resistance characterization.

4.3.3. Electrical performance after stack start-up

The area-specific resistances, measured *ex-situ* after 500 h total exposure time including simulated stack assembly and the first 400 h of stack operation, are compared in Figure 56.

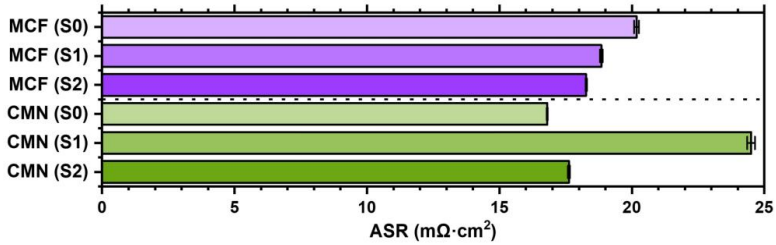

Figure 56: *Ex-situ*-measured ASR values of MCF- and CMN-EPD coated Crofer22APU substrates after 100 h exposure at 850°C and additional 400 h at 800°C in wet air.

The measurements showed values consistently around or below 20 mΩ·cm², with a slight tendency of the CMN-coated samples towards lower values. Only the CMN-S1 type deviated from this trend, displaying an increased ASR of about 25 mΩ·cm², in line with the observations from the preceding exposure-related investigations.

While the variation between individual measurements of a given sample was minimal, the uncertainties related to possible differences in the contact configuration (e.g. caused by the manual application of the Au paste) are assumed to be more significant. Therefore, a precise differentiation within the investigated sample groups is not meaningful, whereas comparisons with literature data and general expectations remain more relevant.

In general, ASR values around or below 20 mΩ·cm² after 500 h are fully acceptable for stack operation. With respect to the aim of maintaining interconnect-related ASR contributions below 50 mΩ·cm², all coating types clearly remain within the target range even after exposure to harsh joining conditions and several hundred hours at 800°C. Only the CMN-S1 samples show slightly elevated values, consistent with their inferior performance in the complementary degradation metrics. Interestingly, the generally stronger degradation observed for CMN in terms of oxidation is not reflected in uniformly higher ASR values. This may result only to a minor extent from the intrinsically higher electrical conductivity of CMN compared to MCF, and more likely from improved contacting effects, for instance due to the larger interfacial area between the Au contact layer and the porous CMN coatings. Such effects could partly compensate for degradation-related losses.

The exposure study, together with the embedded performance tests, focusing on stack joining and start-up, provided a general assessment of the developed EPD coatings – their functionality as well as the integration of the thermal process into existing workflows. This established a solid basis for further evaluation and yielded guidance on suitable heat treatments which is also transferable to the current WPS coatings. Clear benefits emerged for a two-step schedule that achieves stronger densification and closed porosity of the coating by introducing a reducing pre-treatment prior to the subsequent oxidizing sintering step, which can be integrated into the stack-assembly procedure. In line with this, an improvement in protective performance was demonstrated, with the two-hour reduction at

1000°C (R2) standing out as the most promising option. Although the established reference material MCF already indicated superior suitability over the CMN alternative under the present conditions, the Co-free variant should not be discarded at this stage and will be further examined.

Building on these insights, the longer-term exposure study was pursued to assess coating functionality in application-relevant time scales and to set a fundament for the selection of next-generation coating systems. Therefore, a direct comparison with the established concepts is included.

4.4. Exposure study on different coating systems (Jülich)

Whereas the study in Section 4.3 highlighted the processes associated with stack joining and start-up – and their implications for interconnect coatings and vice versa – the focus now shifts to steady, mid-term operation. In addition to the previously developed EPD coatings, the scope is broadened to include the Jülich standard MCF-APS coating and an MCF-WPS coating employing a newly selected heat-treatment schedule. Beyond Crofer-type specialty steels, results for the commercial stainless steel AISI430 are presented as well. A qualitative comparison of the morphological features of the three central coating types – APS, WPS, and EPD – in the initial state is followed by the 3000 h exposure campaign. In close analogy to the prior study, the program comprises comparative assessment of microstructural evolution, evaluation of oxidation kinetics, and finally again resistance measurements as a key indicator of functional performance.

4.4.1. Comparison of APS, WPS and EPD in initial state

To place the three coating techniques in a meaningful comparison and to enable robust statements about differences in the resulting layers and their suitability as interconnect protective coatings, the investigations were pursued under best-possible baseline conditions. Accordingly, the initial comparison used the most established and extensively characterized material combination: An MCF coating on Crofer22H steel substrate. With an eye to integration into the stack manufacturing workflow, coatings were assessed both before stack assembly and after the assembly protocol. For EPD, the two-step thermal treatment S2 identified as most promising in Section 4.3 – i.e., including a pre-reduction at 1000°C – was applied and, in parallel, transferred to the WPS coating. By contrasting the coating systems in their initial state, the groundwork is laid for the subsequent, analogous evaluation in the exposure study: First, by confirming that each method can produce continuous, defect-free layers, and second, by illustrating that WPS can be processed similarly to EPD – as assumed due to the similarity in the starting powders and coating thickness, in contrast to the APS reference.

The investigation of the coatings' microstructural evolution during stack assembly by means of metallographic cross sections of coated steel substrates provides insights into

coating densification and structural characteristics in the final component, i.e., the coated interconnect. Cross-sectional SEM images at the relevant processing stages – after deposition (APS) or reductive treatment (WPS, EPD), as well as after the assembly protocol – are contrasted in Figure 57.

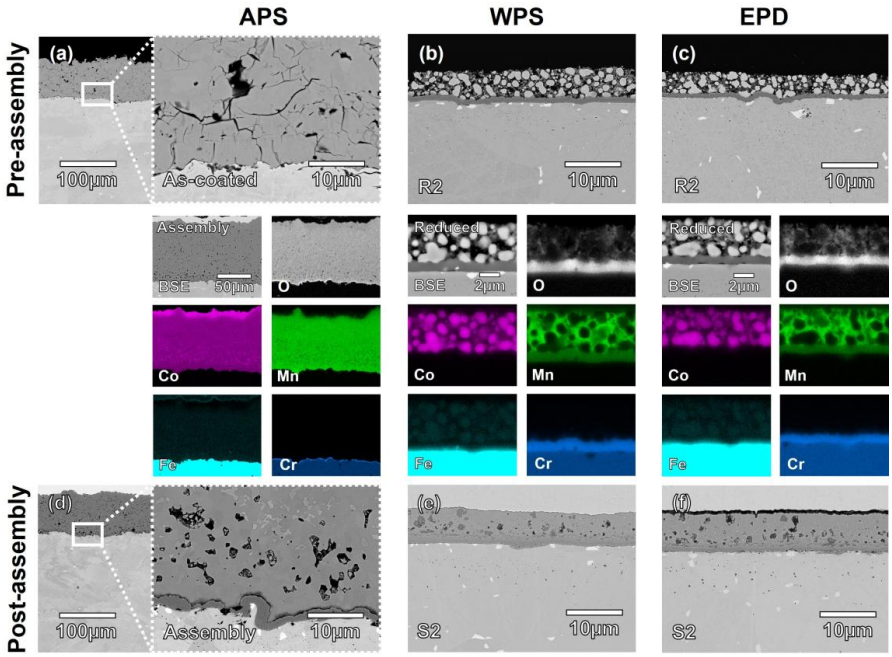

Figure 57: SEM images of cross sections highlighting the relevant processing states of the three MCF coating – (a,d) APS, (b,e) WPS and (c,f) EPD – on flat Crofer22H substrates. Reduction of WPS and EPD coatings at 1000°C for 2 h in Ar/2.9% H_2 (R2) and simulated assembly step at 850°C for 100 h in air (S2). Fe signals enhanced by +50% to visualize the localization of Fe within the coating.

From these micrographs it becomes evident that – consistent with earlier results – coherent, well-adhering layers can be obtained for EPD, as well as for WPS with the analogous two-step heat treatment, and APS, through deposition followed by the respective thermal steps. Moreover, continuity and closed porosity is achieved for all three coating types after the re-oxidizing stack-assembly step.

In the case of the APS process, cracks formed during deposition under reducing conditions are locally healed by a phase transformation of the MCF material from the rock-salt structure into the spinel phase during re-oxidation, thereby leading to a closed porosity (cf. Figure 57a/d). In contrast, the enhanced sinterability and densification during subsequent re-oxidation, promoted by the partially reduced state after the reductive pre-treatment, was observed for the WPS coating in an identical extent as already known for the EPD coatings (cf. Figure 57b/e and c/f). This (re-)affirms the possibility of "reactive sintering" the WPS coatings, present with a similar structure and thickness as the EPD

coatings, and further highlights the comparable characteristics of the suspension-based coating types.

Not only do WPS and EPD coatings show a multi-phase constitution during thermal processing, but the APS coating also exhibits the presence of several phases, though only after the assembly procedure. As stated above and in Section 2.3.2, the phase transformation from $(Mn,Co,Fe)_1O_1$ to $(Mn,Co,Fe)_3O_4$ initially occurs in areas of microcracks, inducing self-healing through volume expansion. As this blocks oxygen pathways through the coating, the further transformation of the bulk material into the spinel phase proceeds via solid-state processes. Due to the large coating thicknesses limiting the kinetics, the full phase transformation of the entire layer exceeds the assembly time of 100 hours. During this transition, a temporary top layer dominated by the Co_3O_4 phase forms, as indicated by EDS analysis (cf. Figure 57a/d), which can later fully re-incorporate into the $(Mn,Co,Fe)_3O_4$ phase. Though the process is not complete after assembly, the resulting dense microstructure already provides the required protection against the uncontrolled migration of gaseous oxygen and chromium species at the start of operation. A detailed description of the thermodynamic processes and microstructural development of the MCF-APS coating is reported by Grünwald et al.[148]

The examination of the coating types in their initial state reveals pronounced differences in overall appearance – most notably the coating thickness, which in APS exceeds that of WPS and EPD by more than an order of magnitude – highlighting the separation into the APS reference process and the suspension-based techniques WPS and EPD.

These differences could be characterized and described in greater detail; however, this is not within the scope of this work. In-depth analysis of similar systems can be found in various works cited above. Importantly, these variations are not crucial to prove the suitability of the coating types for application as interconnect protective coatings. Rather, it is far more critical – besides adaptability to relevant geometries – to demonstrate the protective functionality of the coatings under air-side operating conditions. The latter will be addressed in the second exposure study, together with the subsequent and accompanying characterizations.

4.4.2. Microstructural changes over 3000 hours

Before contrasting the three coating techniques across the full exposure window, the focus first narrows to the newly developed EPD coatings and their internal comparison. In addition to MCF, the alternative composition CMN is examined. Guided by the 500 h exposure results, the set of thermal routes is reduced. Given the generally weaker protection for the single-step oxidative sintering route and the beneficial effect of a prior reduction step for anchoring the layer on the substrate, solely protocols with reduction are considered here, i.e., S1 and S2.

Beyond coated Crofer22H coupons, coatings on AISI430 are included, along with a reference to uncoated sheets. Microstructural examinations are presented after an initial exposure segment (300 h) and after completion of the campaign (3000 h). Comparable, wide-ranging investigations were also conducted for WPS coatings; these extend beyond the scope of this work and are detailed in the dissertation of D. Vakhrameev[241].

Starting with the established pairing of MCF on Crofer22H, a comparison of EPD and the uncoated reference is provided. All samples remained macroscopically intact, with no significant defects such as spallation or macro-cracks. Comparative SEM and EDS analyses were therefore carried out. Representative cross-sections after 300 h and 3000 h are compiled in Figure 58.

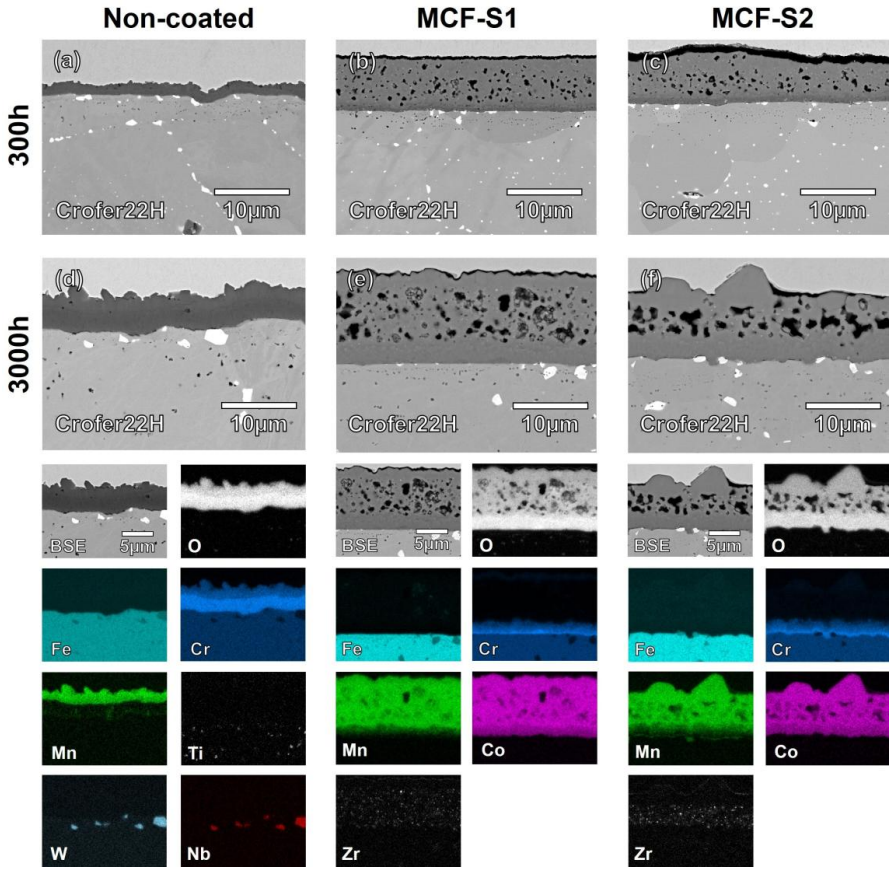

Figure 58: SEM images (and complementary EDS mappings) of Crofer22H substrates after 300 and 3000 h exposure at 800°C in air. (a,d) Bare and MCF-EPD-coated steel after (b,e) S1 and (c,f) S2 treatment as cross sections highlighting the individual oxide-scale formation and Cr localization. W and Nb indicate Laves phases, and Ti corresponds to TiO precipitates, both characteristics of Crofer22H.

The results first confirm the stable and uniformly developed thermally grown oxide (TGO) on Crofer22H – both for the uncoated reference and beneath the EPD coatings – in the form of a bilayer scale. The characteristic compound of a lower Cr_2O_3 layer topped by a $(Mn,Cr)_3O_4$ layer is pronounced for the uncoated sample (Figure 58d), and it is likewise evident in the Mn and Cr signals for the MCF-EPD-coated samples after both S1 and S2. At the same time, there is a marked suppression of oxide-scale growth, most notably of the ASR-dominating Cr_2O_3 sub-layer, which appears similarly thin for S1 and S2 – around or below ~1 μm.

While this effect primarily reflects the favorable intrinsic properties of the Mn-Co spinel with respect to coating continuity and partial density, a contribution from the reactive-element effect (see Section 2.1.6) is also plausible, stemming from the trace yet highly uniform distribution of Zr.[56] This cannot be confirmed here, as verifying the hypothesis would require high-resolution TEM to localize Zr within the scale or coating.

Across the two treatment types, the slight microstructural coarsening already noted in the initial state appears to persist, with S2 showing a marginally stronger tendency. For both S1 and S2, coarsening progresses between 300 h and 3000 h. Together with the growing TGO, this can be misread as coating thickening.

Beyond the beneficial impact on the near-surface oxidation kinetics of the steel, the MCF-EPD coatings also influence the subsurface microstructure. Both grain growth and the coalescence of characteristic TiO_2 precipitates and Laves phases are more constrained compared with the uncoated steel, where such evolution would be expected to alter the intentionally tuned mechanical properties.

Overall – despite minor differences between S1 and S2 and the diffusion-driven, thermally induced changes relative to the as-deposited state – the developed MCF-EPD coatings provide excellent protection over mid-term exposures. This conclusion, for now, is based on microstructural evidence and pertains to Crofer22H as a representative tailor-made steel with an intrinsically optimized property profile.

In analogy to Crofer22H, the conventional ferritic stainless steel AISI430 was included. While it oxidized stably during the first 300 h, longer exposures (clearly after 3000 h) led to macroscopically visible oxide-scale spallation. By contrast, the coated sheets remained intact throughout, without macroscopic irregularities. The microstructural evolution is shown in Figure 59 in direct analogy to the Crofer22H case. For the uncoated reference, a location with an intact TGO is presented. Since irregular corrosion in uncoated steels is not the focus here, a depiction of spallation effects is provided in the Supporting Information (see SI 7).

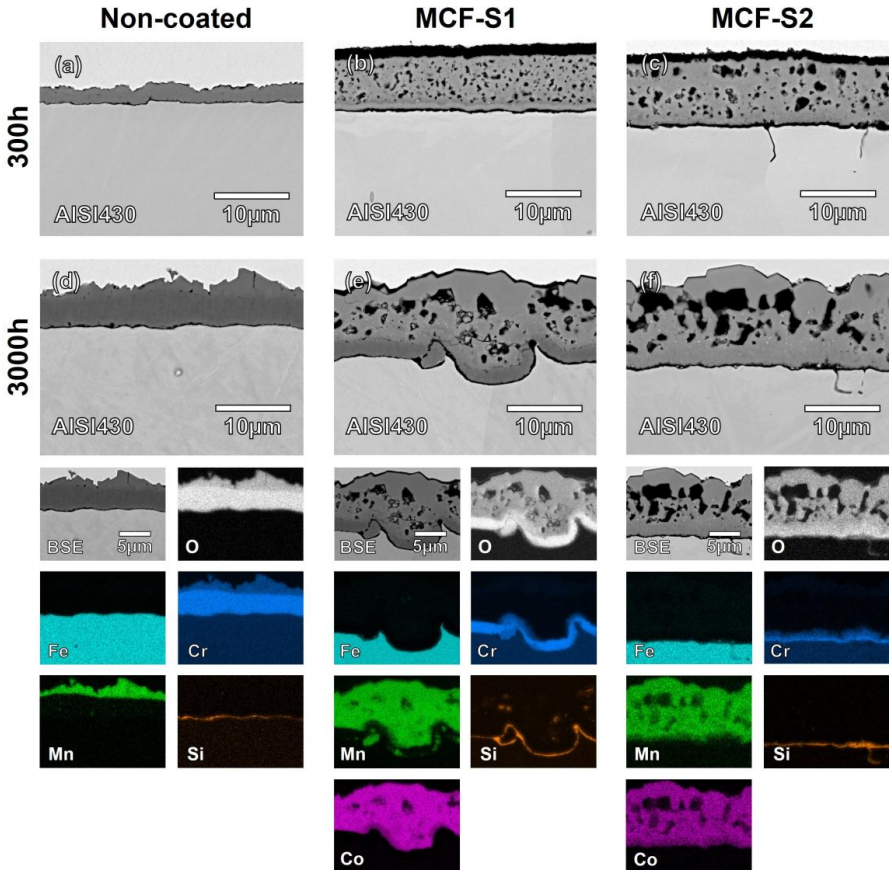

Figure 59: SEM images (and complementary EDS mappings) of AISI430 substrates after 300 and 3000 h exposure at 800°C in air. (a,d) Bare and MCF-EPD-coated steel after (b,e) S1 and (c,f) S2 treatment as cross sections highlighting the individual oxide-scale formation and Cr localization. The Si signal indicates the formation of a continuous SiO_2 layer for all three specimen types.

Beyond stabilizing the oxide scale and controlling overall oxidation kinetics, the MCF-EPD-coated AISI430 coupons also showed a clear suppression of the growth of the characteristic bilayer Cr-oxide scale. The differences between S1 and S2 appear more pronounced here than for Crofer steel. As before, S2 exhibited more evident pore coarsening. However, the Cr-oxide scale that developed under S2 is much more clearly bilayered, with a strongly constrained inner Cr_2O_3 sublayer, whereas S1 formed a thicker scale dominated by Cr_2O_3. In addition to these compositional differences, the scale morphologies diverge: S1 showed an uneven, wavy TGO and interface, while S2 was approximately planar.

The previously discussed risk of forming a SiO_2 sub-scale at the steel/Cr-oxide interface due to manufacturing residues is also observed for AISI430, and the MCF coatings did not fully suppress it. Because the coatings could not completely block oxygen ingress

and as Si oxidizes at lower pO_2 than Cr, the effect persists. Variations in SiO_2 sub-scale thickness between S1 and S2, and even within a single specimen, are likely driven by local differences in composition, oxygen diffusivity, and especially the interface roughness that partially developed. Several studies[175,269] – also including Mn-Co spinel coatings – report the absence of SiO_2 sub-scales in certain cases. By contrast, Reddy et al. show in a more recent study[46] that even the highly effective Ce-Co-PVD coatings can develop a continuous SiO_2 layer after 3000 h, with a strong impact on electrical properties. For conventional grades such as AISI430, which are not tailored to SOC interconnect requirements and for which impurity levels of Si and Al are not tightly controlled in production, pronounced differences between manufacturers and batches must be expected. Elevated Si levels can therefore drive continuous SiO_2 formation and explain divergent outcomes across studies.

The pronounced coarsening of porosity and the distinct differences in Cr-oxide development can be linked back to features established in the initial state. On the one hand, the initially coarser porosity in S2 tends to coarsen further by diffusion. On the other hand, the denser top layer may reduce oxygen ingress, which in turn affects oxidation kinetics at the TGO/steel interface.

A detailed analysis of kinetics for each scenario, including precise conclusions about local corrugation at the TGO/steel interface or anomalies in the SiO_2 sub-scale (for S2, see Figure 59c,f), is beyond the scope here. For an in-depth treatment, see the dissertation by D. Vakhrameev[241]. In general, the observations for MCF-EPD coatings already indicate strong protection on Crofer22H, suggesting a favorable impact on overall performance. For AISI430, a noticeable mitigation of uncontrolled Cr-oxide growth is also evident – especially for S2 – but complete suppression of a potentially severe SiO_2 sub-scale is not achieved. Crucially, the MCF coatings nonetheless enable stable, controlled oxidation without spallation. Additional insight into suitability follows from quantifying oxidation impact in the ASR characterizations.

For the CMN coatings included in direct analogy to MCF, all types remained stable over 3000 h on both Crofer22H and AISI430 substrates. A comparison of cross sections for Crofer22H is provided in Figure 60.

Comparable to the MCF counterparts, the CMN-EPD coatings also exhibited moderate microstructural coarsening – also visible, in the evolution of characteristic precipitates in the steel. Already after 300 h, and more distinctly after 3000 h, pronounced irregularities in layer thickness formed – for both the spinel coating and the underlying TGO – with a wavy, nonplanar interface for S1 and S2. While the CMN coatings continued to compact during exposure, the already extensive chromium diffusion through the coating observed after assembly (cf. Figure 53) clearly persisted.

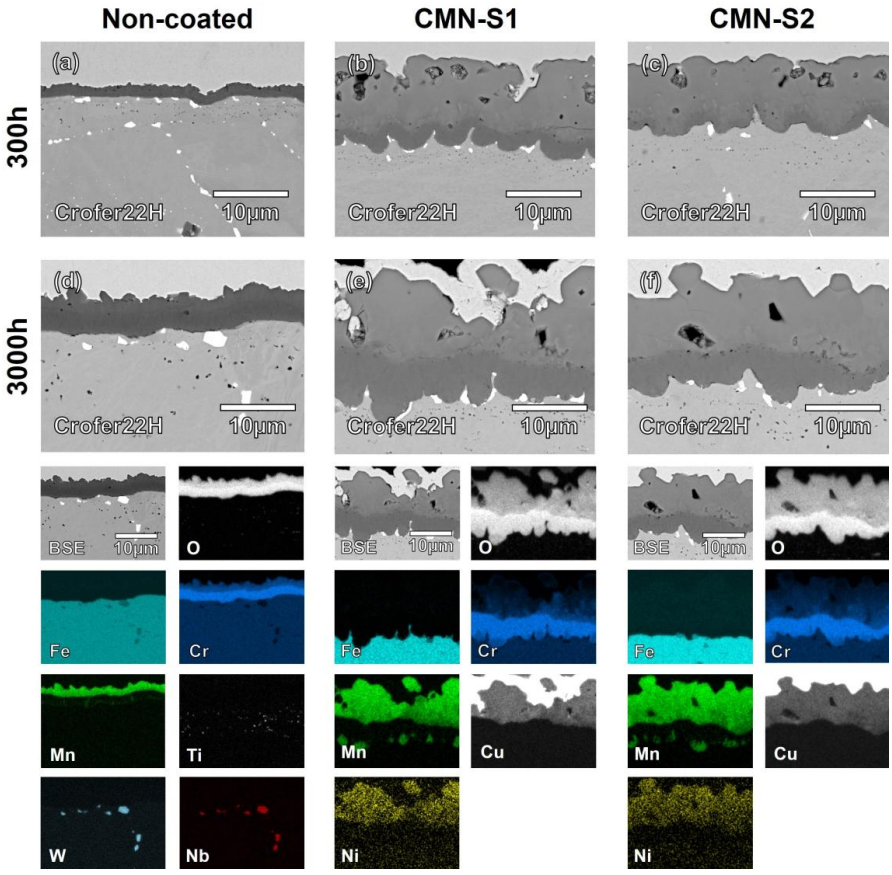

Figure 60: SEM images (and complementary EDS mappings) of Crofer22H substrates after 300 and 3000 h exposure at 800°C in air. (a,d) Bare and CMN-EPD-coated steel after (b,e) S1 and (c,f) S2 treatment as cross sections highlighting the individual oxide-scale formation and Cr localization. Cu was used as coating protection during embedding, resulting in strong contrast in the corresponding signal.

The Cr-oxide scales beneath the coatings appear even thicker than in the uncoated reference, consistent with outward corrosion and suggestive of a chromium "draw-out" mechanism driven through the layer. Beyond the already problematic conditions for chromium retention (evident within the first hundreds of hours), these findings further underscore fundamental limitations of the CMN-EPD coatings with respect to corrosion resistance and electrical performance.

The analogous comparison for CMN-EPD coatings on conventional AISI430 is presented in Figure 61.

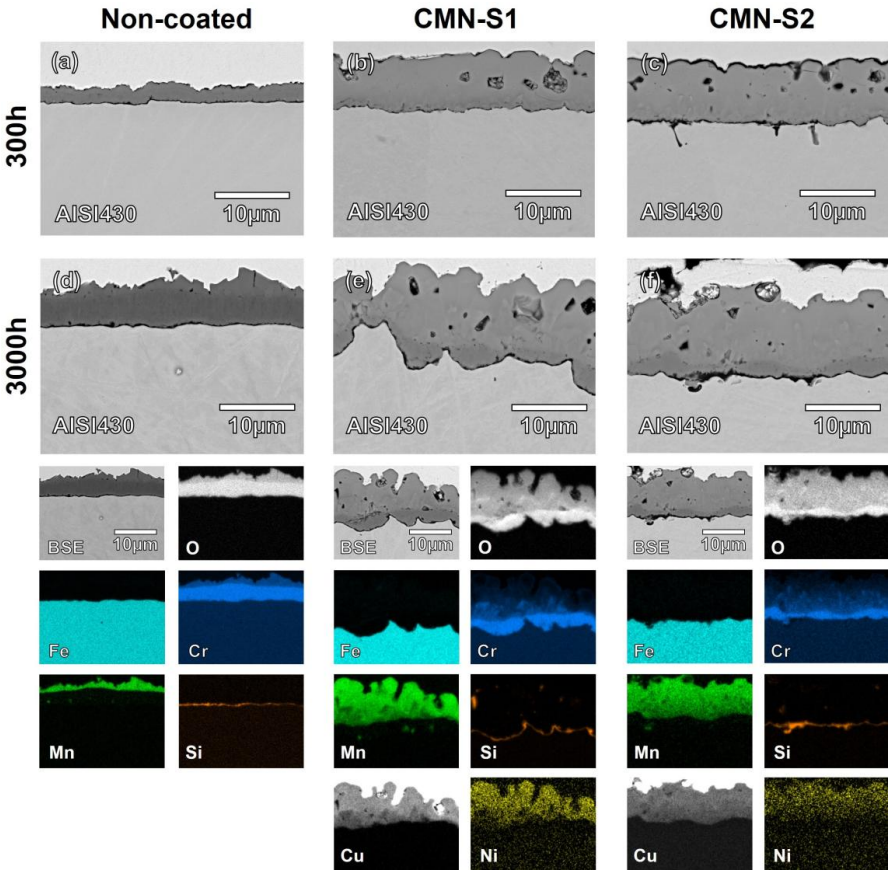

Figure 61: SEM images (and complementary EDS mappings) of AISI430 substrates after 300 and 3000 h exposure at 800°C in air. (a) Bare and CMN-EPD-coated steel after (b) S1 and (c) S2 treatment as cross sections highlighting the individual oxide-scale formation and Cr localization. The Si signal indicates the formation of a continuous SiO_2 layer for all three specimen types. Cu was used as coating protection during embedding, resulting in strong contrast in the corresponding signal.

While the CMN-EPD coatings on the conventional substrate exhibited microstructures comparable to their counterparts on Crofer22H, the TGO/substrate interface again reflected the trend already observed for MCF with respect to thermal treatment: For S2, the chromium-oxide scale was substantially thinner than in the reference and S1 cases. Observed here as well, chromium transport throughout the entire coating was evident, and the formation of a continuous SiO_2 sub-scale could not be prevented. This behavior is consistent with the preceding analyses – especially those performed during the thermal-treatment study – and further underscores the limited suitability of this material for SOC interconnect applications.

Within the comparison MCF versus CMN, the established Mn-Co spinel demonstrated superior performance, and the two-step thermal treatment S2 proved

advantageous for suppressing Cr_2O_3 scale growth (particularly on AISI430). By contrast, the Co-free composition delivered markedly reduced corrosion protection – up to and including an apparent enhancement of TGO growth – and promoted extensive chromium distribution across the entire coating, whereas for MCF chromium remained distinctly localized within the TGO.

Finally, the benchmark MCF-APS system is contrasted with comparable WPS and EPD coatings. In line with the above findings, Crofer22H served as the substrate and the suspension-based coatings were processed using S2, i.e., a 1000°C pre-reduction. SEM/EDS analyses at relevant magnifications over the exposure period, analogous to the detailed EPD study, are presented in Figure 62.

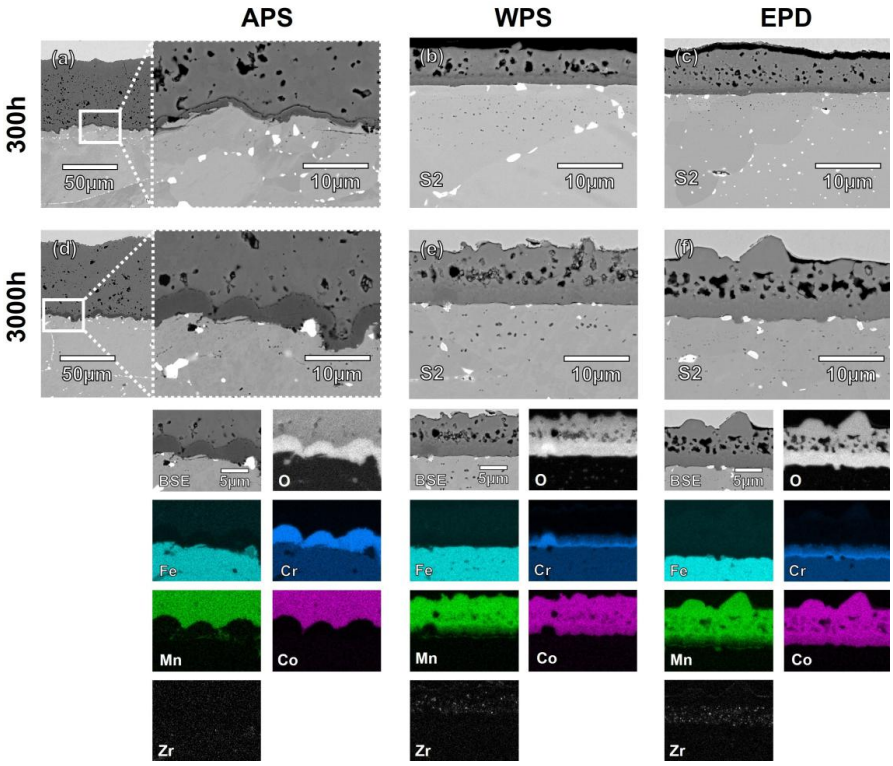

Figure 62: SEM images and EDS mappings of Crofer22H substrates after 300 and 3000 h exposure at 800°C in air. (a,d) APS-, (b,e) WPS- and (c,f) EPD-coated steel as cross sections highlighting the oxide-scale formation below the MCF coatings.

In the direct comparison of the three methods, the strong similarity between the suspension-based approaches became evident once more. Beyond the structural commonalities already highlighted in the initial state, their corrosion behavior proved closely aligned, with both showing effective suppression of TGO growth and localized chromium within the oxide scale for WPS as well. Zr accumulation was also detected in the

WPS coating, as with the EPD coating, a beneficial influence on corrosion behavior is conceivable but would require targeted verification (see reactive element effect, Section 2.1.6). These features were not observed for the APS coating, which also differed in several other respects.

Whereas a largely single-layer Cr_2O_3 scale beneath the MCF-APS coating was already apparent after assembly (see Figure 57), this tendency intensified during subsequent exposure. An uneven TGO/substrate interface and a generally non-uniform TGO developed over time. Although APS still reduced oxide-scale growth compared with uncoated Crofer22H (see Figure 58), the newer suspension-based WPS and EPD coatings provided a clearly stronger protectivity. Despite the expected blocking of migrating oxygen via the self-healing mechanism in APS – especially at large thicknesses around 100 µm – residual microcracks and occasional macrocracks (see SI 8) likely contributed to the relatively lower corrosion protection of APS compared with the suspension-based variants. Given that the APS system has demonstrated robust long-term stack performance[110–112], these findings point to considerable potential for the newer coatings, even at much smaller thicknesses. Additional insight into oxidation behavior follows from the mass-gain curves of the specimen types investigated.

4.4.3. Oxidation kinetics

Within the gravimetric characterization of corrosion behavior, double-side coated (and fully uncoated) specimens in the Jülich 20 × 10 mm² format (cf. Figure 24) were assessed, using Crofer22H and AISI430 as substrate materials. In addition to the uncoated references, the previously discussed two-step thermally treated EPD coatings were investigated alongside their MCF-WPS counterparts. The corresponding curves over 3000 h of exposure for Crofer22H and AISI430 are shown in Figure 63.

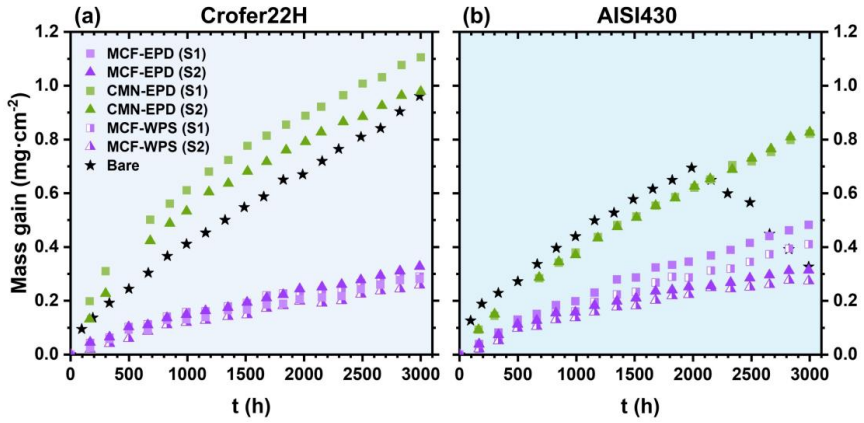

Figure 63: Mass gains of EPD- and WPS-coated and non-coated steel coupons over 3000 h exposure in air, employing (a) Crofer22H and (b) AISI430 as substrates. Exposures and weighing study conducted at FZJ-IMD-1 by D. Vakhrameev and D. Naumenko.

Across all curves, the oxidation kinetics generally follow a parabolic trend – more or less pronounced depending on the case – while oxide-scale spallation for uncoated AISI430 is indicated by an abrupt onset and continued decrease in mass (cf. Figure 63b). In broad terms, the mass-gain results align well with the preceding microstructural analyses and further reinforce steel-dependent differences between the thermal schedules. The effect of coating material (MCF vs. CMN, in the direct comparison within EPD coatings) also appears strongly substrate-specific: For Crofer22H, an increased oxygen uptake was even observed for CMN-coated samples relative to the uncoated reference (see also Figure 63). However, the trajectory of the curves suggests that at longer exposure times a beneficial trend – particularly for CMN-S2 – may emerge.

Comparing equivalent EPD and WPS coatings reveals a relatively small, not perfectly consistent pattern across thermal schedule and substrate: WPS exhibits slightly lower mass gain in the direct comparisons of counterparts. Exceptionally the combination Crofer22H/MCF-S1 shows nearly identical behavior for WPS and EPD. Minor differences in thickness or microstructure may cause this behavior. A more detailed discussion of these trends and their causes could enable further optimization but is beyond the scope of this work. For an in-depth treatment (including additional steels for APS and WPS as well as EBSD and GD-OES analyses), see the dissertation by D. Vakhrameev[241].

Overall, the coatings again yield stable, parabolic corrosion behavior. They substantiate the functionality of suspension-based approaches and reconfirm the superiority of MCF – preferably with the 1000°C pre-reduction (R2/S2). With respect to implications for electrical performance, *ex-situ* ASR measurements were conducted after the defined exposure intervals and are discussed in the following section.

4.4.4. Electrical characterization and degradation

Complementary to the microstructural and mass-gain analyses, again *ex-situ* ASR measurements after prolonged exposure serve as a direct indicator of interconnect protection and component functionality over time. The results for uncoated coupons and for coupons coated with MCF-APS and the selected MCF/CMN-EPD variants are shown separately for Crofer22H and AISI430 in Figure 64a and b, respectively.

Across all specimen types, higher ASR values were recorded after longer exposure, reflecting ageing via steel oxidation. Though where protection was most effective, the ASR increase remained minimal (cf. Figure 64a). Within the Crofer22H group, the particularly small rise observed for the MCF-EPD coatings is consistent with the strong suppression of TGO growth and yields the lowest overall resistances, on the order of ~15 $m\Omega \cdot cm^2$ (cf. Figure 20, Reddy et al.[122]), i.e., roughly a threefold reduction relative to the uncoated reference.

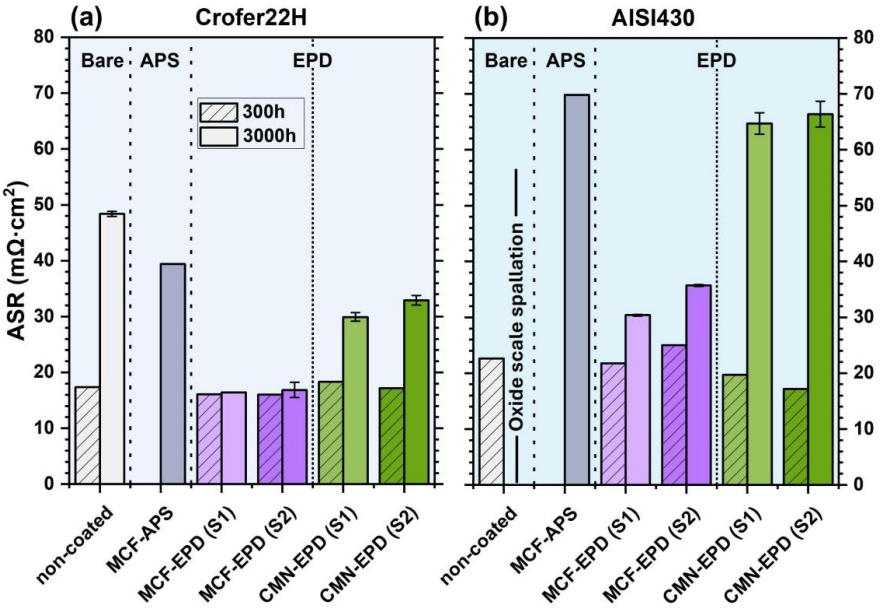

Figure 64: *Ex-situ* ASR values for steel coupons exposed for 300 and 3000 h in air at 800°C. Bare steel and APS-coatings as reference, compared to the developed and selected two-step treated EPD-coating based on MCF and CMN, employing (a) Crofer22H and (b) AISI430 as substrates.

In contrast to the comparison by Reddy et al., high ASR values were measured here for APS-coated coupons, which agrees with the observed oxide-scale thicknesses. While some contribution from backside oxidation during measurement cannot be ruled out (backside oxide was removed and temporary protection relied on sputtered/painted Au), the short measurement duration and robust gold contact suggest this effect is secondary. Slight differences in atmospheric conditions against the Reddy study may also contribute, yet it is unlikely they do fully explain the discrepancy.

For CMN-EPD coatings, higher ASR values – on both Crofer22H and AISI430 – track with the increased oxygen uptake and thicker Cr_2O_3 scales relative to MCF. The clear ASR reduction for CMN on Crofer22H compared with the uncoated reference likely reflects a countervailing effect, such as an enlarged effective interface area caused by a more corrugated TGO/steel interface. A similar interplay may explain why MCF-EPD on AISI430 yielded lower ASR for the S1 schedule, even though its Cr_2O_3 layer was significantly thicker than for S2 (cf. Figure 64b). For AISI430, the roughened steel surface can also locally reduce the average SiO_2 sub-scale thickness – presumably a dominant contributor to ASR.

A weak but consistent pattern emerged for the EPD coatings across both steels: after 3000 h, S2 produced slightly higher ASR than S1 for both spinels. For MCF this continues the trend already visible at 300 h, whereas for CMN the short-term trend reverses at longer

times. Three substrate- and coating-dependent processes likely compete and shift in relative weight: (i) thickness of the dominant oxide layer, (ii) specific area of the TGO/steel interface, and (iii) pore distribution – and thus effective area – within the coating.

A next step could involve quantitative image-based metrics for these factors and correlation with ASR to resolve their individual contributions. That analysis lies beyond the scope here. Even from the qualitative perspective, firm conclusions emerge on coating methods, materials, and substrates, and avenues for further optimization become clear. Among the newly developed coatings, MCF – consistent with its established status, when combined with the tailor-made Crofer22H – delivers excellent performance, whereas the Co-free alternative CMN does not provide adequate protection or low resistance at 800°C under the conditions studied. The results align well with the shorter EPD-focused exposure study and complement it effectively.

Regarding the conventional steel, the comprehensive assessment indicates that MCF-EPD (and likely MCF-WPS) can provide notable corrosion protection. Nonetheless, impurity-driven SiO_2 sub-scale formation remains a limiting factor for long-term operation, making this composition a less favorable choice for durable systems. Considering protection and structural traits on small, flat substrates, WPS and EPD exhibit broadly similar suitability profiles. Ultimately, however, integration into existing manufacturing and stack architectures is decisive – an aspect addressed next, together with a side-by-side evaluation of APS, WPS, and EPD in that context.

4.5. Integration and compatibility aspects for EPD coatings

Building on the preceding chapters, there is substantial potential to integrate the developed EPD coatings into the manufacturing of SOC interconnects and their implementation in stacks and systems. Beyond the thermal process control – treated in detail in Section 4.2 and shown to be highly compatible with stack workflows, particularly for the two-step schedules – two further aspects are critical here: compatibility with adjacent components and applicability to relevant geometries. This section addresses both points and, in comparison with the competing WPS and APS concepts, concludes the technical evaluation by transferring the coatings to full interconnect parts and integrating them into a stack test.

Across the previous results, the two-step heat treatments emerged as especially beneficial from multiple angles. Given its pronounced chromium retention, the focus in the following will be on schedule S2. As a starting point for the final part of the technical assessment, the compatibility of EPD coatings with the glass sealant was examined.

4.5.1. Glass sealant compatibility

The interaction of glass sealant with the spinel coatings was evaluated based on cross-sectional SEM imaging and EDS analyses, here exemplarily for MCF and CMN coatings processed via protocol R2/S2, i.e., coatings reduced at 1000°C prior to sealing. Comparative micrographs with line scans at representative positions in the center of the joining zone are shown for MCF and CMN in Figure 65a and b, respectively, whereas larger area analyses (EDS mappings) to support the findings are presented in Figure 66a, and b, respectively.

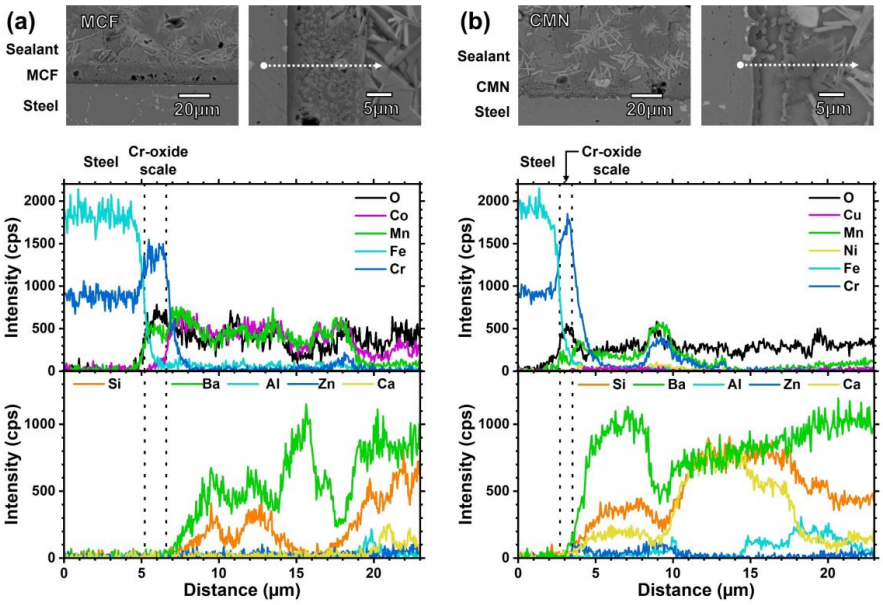

Figure 65: SEM images and corresponding EDS line scans of glass sealant-coating composites: glass sealant applied to (a) MCF and (b) CMN coatings after R2 treatment, followed by crystallization for 100 h at 850°C in air.

Cross-sections revealed extensive infiltration of the glass sealant into both coating types. In both cases, largely dense composite layers formed, with only localized residual porosity remaining in the MCF sample. Moreover, the microstructure of the MCF coating resembled the morphology obtained under free sintering, with a comparable thickness.

In contrast, the CMN coating exhibited a pronounced alteration in both microstructure and thickness compared to its reference state after air sintering without contact to the glass. A significant reduction in coating thickness by approximately 50% was observed, and the resulting composite was characterized by a largely displaced coating core with only a remaining bottom and top layer enclosing infiltrated glass. In both cases, the bonding between the glass and the EPD coatings occurred coherently, without evidence of delamination, cracking, or related defects.

Line scans confirmed the infiltration of glass components into the MCF coating, with elements such as Si, Ca, Ba, and Zn detected within the layer. The infiltrated zone did not

show the typical crystallization of the glass matrix and maintained amorphous with precipitates formed within the coating, while typical feldspathoid reinforcement fibers, here indicated by Al, were only present outside the coating. For the CMN sample, similar infiltration of glass constituents into the former coating zone was observed. However, at the same time, the principal spinel components showed a markedly different behavior: their presence within the original coating was diminished, and redistribution into the glass sealant was evident. In particular, Cu no longer showed a clear localization near the steel substrate but was instead dissolved and irregularly precipitated throughout the glass matrix. For MCF, only a minor diffusion of Co into the adjacent glass phase was detectable.

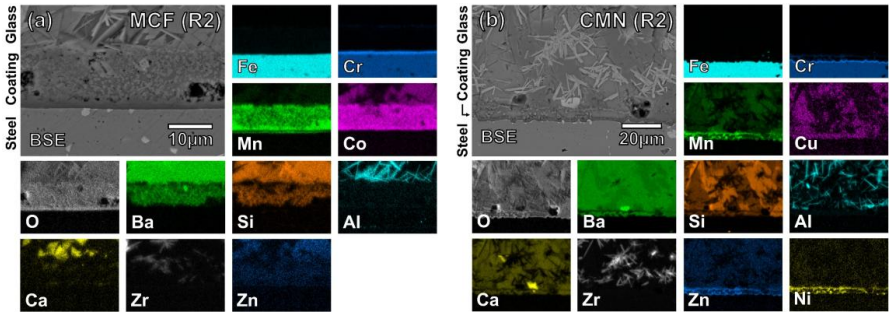

Figure 66: Crosscutting EDS mappings of MCF- and CMN-coated Crofer22H coupons with applied glass-sealant after pre-reduction (R2) and joining cycle.

The EDS mappings further support the patterns observed in the line scans, while explicitly highlighting the extend of Cu spreading in the glass, observed for the CMN case. A further distinction between the two coating systems, most evident in the line scans, concerned the localization of Cr. For the MCF sample, a coherent Cr-rich oxide layer adjacent to the steel substrate was present, similar to that observed under other thermal treatments, with only a weak Cr enrichment near the outer surface of the coating. In the CMN case, an additional continuous Cr-rich layer formed above the remnants of the former EPD coating, accompanied by a pronounced Mn signal, while the oxide layer at the substrate remained comparable in morphology.

Overall, the formation of a dense composite without the occurrence of defects such as cracks or delamination during direct joining indicates that the selected MCF and CMN coatings are thermo-mechanically feasible. However, the pronounced interaction observed within the CMN sample, including the expansive dissolution of the coating into the glass, represents a potentially severe issue under SOC operating conditions. While the present investigation cannot fully assess how the interfacial interaction might evolve over time or whether stress-induced defects could eventually lead to leakage, a major risk arises from the diffusion of metallic copper. The extensive Cu penetration, facilitated by its high reactivity and diffusivity and by the large active surface area of metallic Cu present at the onset of the

joining process, could critically impair the electrical insulation of the glass sealant and may even cause short-circuiting during stack operation.

In contrast, the morphological stability of MCF coatings during joining, accompanied by the formation of a dense, continuous composite layer, is highly beneficial. The absence of significant diffusion of conductive species into the glass sealant suggests that reliable electrical insulation can be maintained. Nevertheless, further investigations of insulation performance, gas tightness, mechanical durability, and long-term coating-glass interactions remain essential before drawing final conclusions on stack-level applicability.

As next to the chemical and thermo-mechanical compatibility the coating application on real flow-field structures is a crucial step towards implementation on stack level, this is presented in the next section. Due to the outperformance of MCF over CMN in the various investigated aspects, the focus from now on lies on MCF coatings with R2/S2 treatment.

4.5.2. Flow-field coverage: Suitability of EPD

During transfer of the EPD coatings to F10-type specimens (rib-channel geometry), machining grooves proved problematic: they manifested as cracks in the as-coated state and persisted through thermal treatment. This was resolved by lightly polishing the surface, which enabled the formation of uniform layers (see Supporting Information SI 9). For the CS^V interconnect type (corrugated design), no additional pre-treatment was required prior to deposition. Cross-sections of the two prepared substrate types with MCF-S2 coatings are shown in Figure 67 (F10 type) and Figure 68 (CS^V type), whereas characteristic zones of each geometry were analyzed in detail.

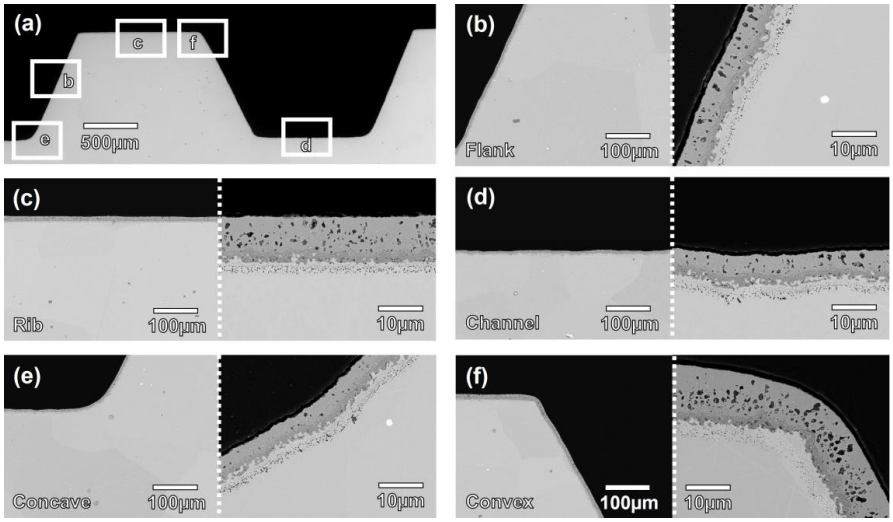

Figure 67: MCF-EPD coating applied on rib-channel-type flow-field structure, cut out of F10 interconnect, heat-treated with two-step protocol S2. Stitched overview (a), and detailed images in characteristic areas along the structural unit (b–f).

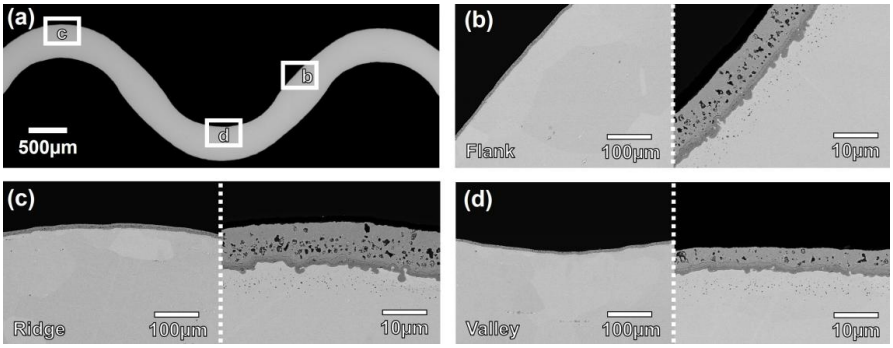

Figure 68: MCF-EPD coating on wave-type flow-field structure, cut out of CS-type interconnect, heat-treated with two-step protocol S2. (a) Stitched overview, and (b–d) detailed images in characteristic areas along the structural unit.

For both substrate types, the coatings exhibited continuous and coherent layers throughout all regions without evidence of defects such as cracks or delamination. Across both geometries, variations in coating thickness were observed depending on the specific position within the structural unit. In the rib-channel and corrugated structures, increased coating thicknesses were detected on the ridges (cf. Figure 67c and Figure 68c), which gradually decreased along the flanks (cf. Figure 67b and Figure 68b) and reached their lowest values in the valleys (cf. Figure 67d and Figure 68d). The variation in thickness spanned a factor of two or more. Notably, even in areas characterized by pronounced differences in surface-to-volume ratio and complex stress states during thermal treatment – particularly the convex and concave zones of the F10 structure (cf. Figure 67e and Figure 67f) – the coatings remained continuous and coherent, without the formation of defects.

The overall coating thicknesses on the structured substrates ranged slightly below and above those obtained on flat substrates. The microstructures closely resembled those of flat samples, with a general tendency towards increased layer thickness. In all regions of the structured substrates, the coatings displayed the characteristic closed porosity typical of the two-step S2 treatment on flat coupons.

The results clearly indicate the general suitability of EPD for geometries relevant to SOC interconnects. Comparable performance is further expected for alternative designs based on sheet forming or bulk machining, including localized features such as dimples. The advantages of EPD, as a suspension-based, non-line-of-sight technique capable of producing continuous and homogeneous coatings across all characteristic zones of the structures, are underlined. The excellent coating quality at sharp edges (cf. Figure 67e and Figure 67f) and the absence of stress-induced cracking or delamination are particularly positive, as these regions are highly prone to mechanical stress during thermal cycling.[270]

The observed thickness variations along the profile are attributable to several factors. The reduced coating thicknesses in recessed zones are primarily related to the larger effective electrode distance and the locally lower surface-to-volume ratio, which in turn lead to

weaker electric fields and local suspension depletion. This variation is not necessarily detrimental, provided that a continuous and sufficiently dense coating is maintained in all areas. Moreover, the preferential thickening at elevated features and sharp edges is advantageous, since these zones are in direct contact with the air electrode and thus demand the highest level of protection, considering especially Cr volatilization.

Overall, these findings confirm the suitability of EPD as a coating method and demonstrate the compatibility of the developed MCF coatings with the applied thermal treatment for relevant interconnect structures. Considering the investigations of different thermal processing routes together with the performance indicators, this provides a robust foundation for transferring the approach to real stack components and for subsequent long-term testing under system-relevant conditions.

Since this work also aims to benchmark the investigated methods with respect to their technical suitability for applying interconnect protective coatings on relevant components, at first the EPD results are contrasted with the APS and WPS counterparts in the next subsection. The basis for this comparison is the more established – and structurally more demanding – F10 interconnect geometry.

4.5.3. Flow-field coverage: EPD vs APS and WPS

For an initial, rough comparison of coating quality with respect to areal coverage and the absence of macroscale defects, surface characterization was performed via laser microscopy. Stitched images assembled from nine tiles, spanning at least one structural repeat unit, are shown for the three MCF coatings – APS, WPS, and EPD – in Figure 69. More detailed insight into critical regions is provided next by SEM cross-sections.

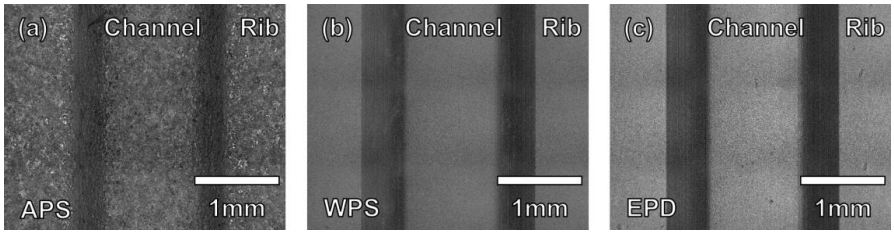

Figure 69: Stitched laser microscopy images of rib-channel structures coated by (a) APS, (b) WPS, and (c) EPD. Samples in the state prior to SOC stack integration.

From the LSCM images taken in the state relevant for stack assembly – as-coated for APS and reduced (R2) for WPS and EPD – continuous, full-area coverage is evident for all methods, though differences emerge. For APS, the uneven surface finish stems from the previously shown coarse, crack-containing structure after spraying (cf. Figure 57a). For WPS and EPD, the much lower layer thickness yields flatter topography with smaller fluctuations. However, WPS shows slight inhomogeneities along rib flanks compared to EPD. In plan view, all three techniques demonstrate the ability to form continuous coatings.

The precise morphology at critical sites – flanks and edges – was then clarified in the cross-sectional view. Corresponding images, analogous to those previously shown for MCF-EPD (cf. Figure 67), are provided for APS in Figure 70 and for WPS in Figure 71, both in the post-assembly condition.

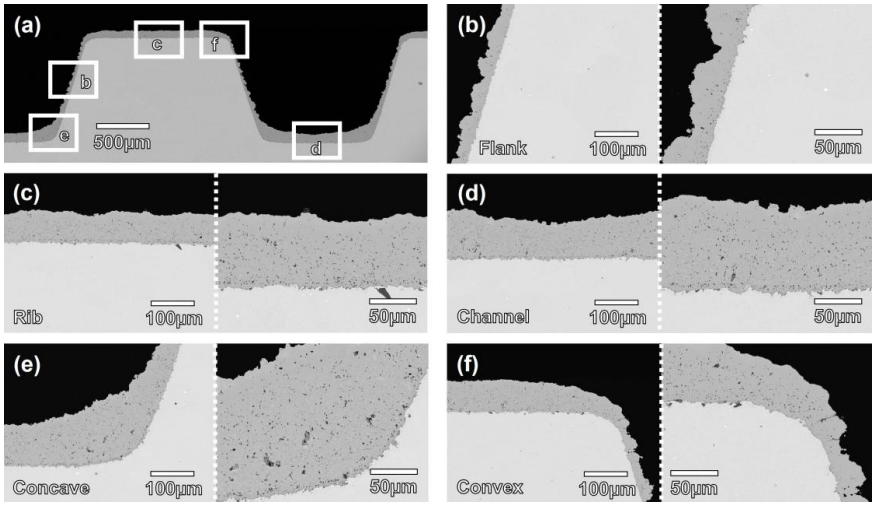

Figure 70: MCF-APS coating applied on rib-channel-type flow-field structure, cut out of F10 interconnect, after simulated assembly. (a) Stitched overview, and (b–f) detailed images in characteristic areas along the structural unit.

For the MCF-APS coating on the rib-channel structure, cross-sections of flat segments, ribs, and channels (cf. Figure 70c,d) reveal a morphology comparable to fully flat coupons (cf. Figure 57d), but with approximately 1.5× higher thickness in the channels. The coating is particularly thick in the concave transitions from channel to flank (cf. Figure 70e), while the thinnest and most irregular coverage occurs at convex edges and especially along the flanks. These irregularities can be attributed to the expected line-of-sight effect of APS, which – despite prior sandblasting – leads to weaker adhesion and material accumulation in recessed zones and a "build-up" in the transitions.

Although the beneficial, characteristic APS microstructure observed on flat substrates is present across all areas here, incipient cracking appears at mechanically critical convex edges. Despite edge rounding by sandblasting, these cracks are likely thermally induced. The APS coating is overall very thick relative to the EPD variant, yet the strongly non-uniform flank coverage (which represents a substantial fraction of the exposed surface) necessitates a certain minimum thickness to ensure complete protection everywhere. It should be noted that, unlike the EPD and WPS samples used for direct comparison, the APS sample, stemming from archival stock, employed an older interconnect type with slightly steeper flanks (compare Figure 70b and Figure 67b). Nonetheless, the impact is considered minor, and the line-of-sight effect remains a key constraint for APS and a challenge for optimizing towards lower coating thicknesses.

Also, for WPS, a line-of-sight tendency exists during particle delivery to the substrate. However, due to much lower particle velocities and forces, and a different spray orientation relative to gravity, the overall outcome differs significantly. The contrasts become clear in the characteristic regions within a structural repeat unit (cf. Figure 71).

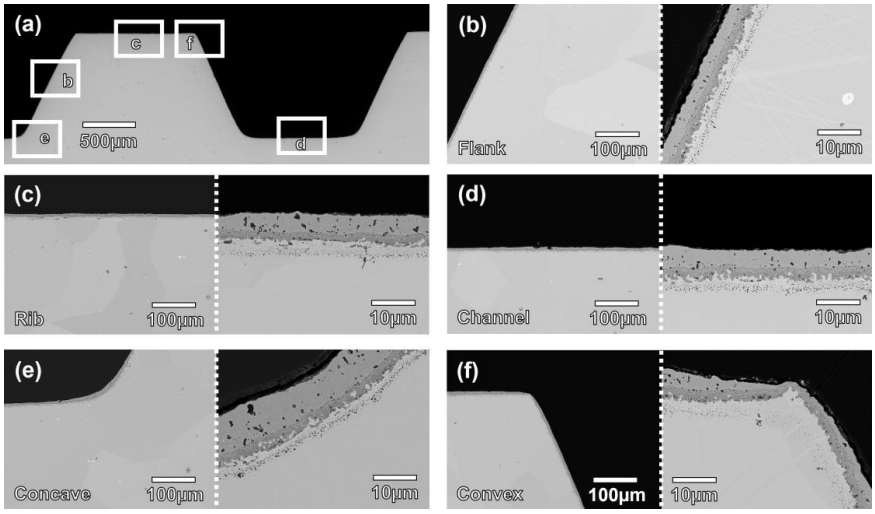

Figure 71: MCF-WPS coating applied on rib-channel-type flow-field structure, cut out of F10 interconnect, heat-treated with two-step protocol S2. (a) Stitched overview, and (b–f) detailed images in characteristic areas along the structural unit. Spraying-related defect visible in (d).

For the MCF-WPS coating on the F-type flow-field, the resulting microstructure closely matches that on flat coupons. A thickness increase caused by particle accumulation during spraying appears in the concave channel-to-flank transition, comparable to APS (cf. Figure 71e). In channels and on ribs, layer thicknesses are approximately the same – lower than APS and comparable to EPD – yet slightly reduced relative to flat samples. Compared to APS, this confirms the weaker impingement forces and the reduced tendency to displace particles into channels during deposition. Along the flanks, WPS yields thinner but highly uniform layers, roughly half the thickness found on ribs and in channels.

A particularly critical feature of WPS emerges at convex edges. Here, the coating thins dramatically, in places approaching complete loss of coverage (cf. Figure 71f), leaving the TGO as the primary barrier. Part of the difference relative to the EPD counterpart (cf. Figure 67f) stems from the sharper, unpolished edge geometry used for the WPS specimen. Nevertheless, the pronounced thinning is most plausibly driven by post-deposition flow of the liquid suspension prior to final drying. Incremental improvement may be achievable through targeted surface finishing of the component or by tuning suspension chemistry to enhance shape stability during drying. The potential absence of coating at highly exposed zones – with high surface-to-volume ratio and elevated susceptibility to chromium

depletion and breakaway corrosion – requires special attention and must be reflected in the overall assessment.

In summary, each of the three methods produces a characteristic coverage pattern with direct implications for corrosion protection under SOC operation. While especially the APS coatings remain a proven, sufficiently performing solution in stack service, the distinct advantages of the newly developed EPD coating are evident. This sets the stage for transferring EPD to full-size interconnect components.

4.5.4. Stack integration and functional demonstration for EPD

As part of scaling the developed MCF-EPD coatings, the suspension volume was increased from the laboratory 100 ml scale to a 2 l scale. Using the previously employed ethanol-water system, inhomogeneities emerged during deposition and drying – most obviously detectable on flat, trial substrates at full interconnect size (shown in the Supplementary Information SI 10).

Alternative suspension-preparation routes – such as extended ultrasonication or the use of an Ultra-Turrax for enhanced stabilization – did not resolve these issues. Additional approaches could conceivably enable uniform deposition with the aqueous system on real components. A related up-scaling study by Sabato et al. (2021) reported coating of comparable parts using a very similar suspension system[224], yet provided no overview of macroscopic coating uniformity and only microstructural characterizations of relatively small regions.

Because the primary objective here was to demonstrate the feasibility of EPD for SOC stack-level application – not necessarily to preserve the aqueous medium at this step – the process was shifted, within a master's thesis, to a non-aqueous, fully organic system to remove water-related challenges. Candidate media, additives, and concentrations were screened based on literature guidance and preliminary trials at Politecnico di Torino (at Prof. F. Smeacetto, within the group GLANCE (Glasses, Ceramics and Composites)). The detailed study conducted by M. Siviji within a master's thesis[271] is not considered here. Its development pathway mirrored the approach taken for the aqueous route.

The most promising coating results – while largely retaining the original process parameters – were obtained with an ethanol-acetone system supplemented with iodine as a surface-charge enhancer for the MCF powder. The solid load of the 60 min milled powder was reduced to 20 $g \cdot l^{-1}$, and the water in the original suspension was replaced 1:1 by acetone. Iodine addition during suspension preparation was set to 0.5 $g \cdot l^{-1}$. Maintaining the three-electrode setup and a 1.5 cm electrode spacing, deposition on flat components was performed, as established, for 45 s. The previously identified two-step thermal schedule S2 (pre-reduction at 1000°C) was applied to the coatings.

To benchmark functionality against the original aqueous method, a short exposure of 300 h at 800°C in static air (analogous to the Jülich exposure study) was conducted. An

overview of the microstructural evolution across the characteristic processing stages is shown as SEM cross-sections in Figure 72, with EDS mappings after 300 h exposure provided in Figure 73 to assess corrosion resistance and chromium localization.

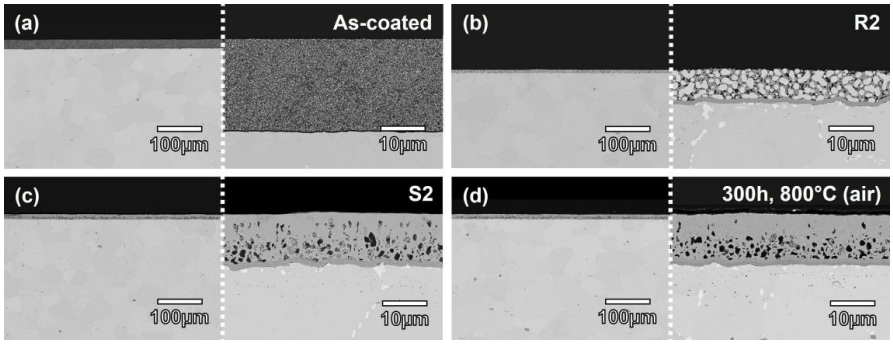

Figure 72: MCF-EPD-coated Crofer22H substrates, produced by employing the acetone-ethanol-based suspension system, (a–c) at the relevant thermal process stages, and (d) after additional 300 h exposure at 800°C in air. Samples prepared by M. Siviji.

Cross-sections show that the new ethanol-acetone route yields continuous, uniform, and adherent coatings that remain stable through the selected thermal schedule and the short-term exposure. The microstructural evolution closely matches that of the initially developed aqueous route (cf. Figure 45 and Figure 47). Phase separation and agglomeration during reduction (cf. Figure 72b), as well as the formation of closed porosity with a dense top layer during oxidation (cf. Figure 72d), do not appear to be substantially affected by the change in suspension system.

A noticeable difference is the larger coating thickness, particularly visible in the as-coated state. Though, improved particle stabilization and altered drying behavior in the fully organic suspension likely broaden the process window for high coating quality, which could be exploited to achieve lower thicknesses. In this study, the parameters established from the green-state assessment were maintained.

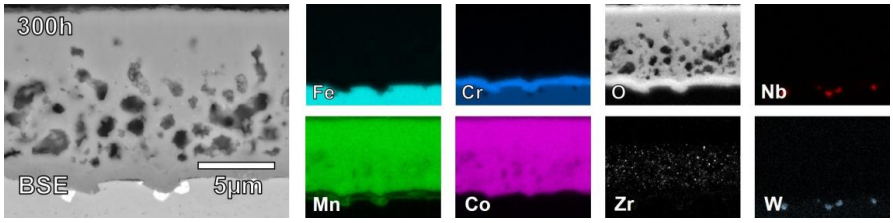

Figure 73: Cross-sectional EDS mapping of MCF-EPD coating on Crofer22H, achieved through the fully organic route. Coating underwent S2 treatment and 300 h oxidizing exposure at 800°C. The elemental analyses reveal a pronounced localization of Cr within the chromia scale. Zr belongs to trace level from powder manufacturing, and Nb and W to Laves-phase precipitation.

Beyond the preserved stability and adhesion after 300 h exposure, chromium localization in the TGO was again clearly observed, with contributions from both Cr_2O_3

and spinel $(Mn,Cr)_3O_4$ indicated. Zirconium was likewise detected, concentrated in the lower, more porous portion of the coating.

These findings support good transferability of the EPD methodology to the organic system. To assess applicability to relevant geometries, deposition on an F-type cut-out was repeated and stability under short-term exposure was evaluated. Representative SEM cross-sections of an S2-treated sample after 300 h at 800°C in air are shown in Figure 74.

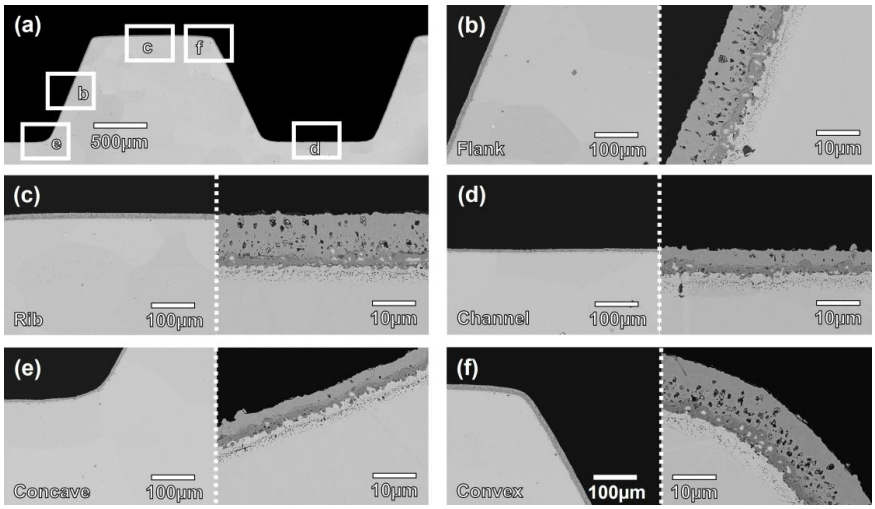

Figure 74: MCF-EPD coating applied on rib-channel-type flow-field structure, cut out of F10 interconnect, heat-treated with two-step protocol S2 and exposed for 300 h at 800°C in air; EPD procedure based on ethanol-acetone suspension system. (a) Stitched overview, and (b–f) detailed images in characteristic areas along the structural unit.

The fully organic route again produced a microstructure closely comparable to that of the aqueous route, with coherent layers across all regions and the characteristic features of the coating. The layer-thickness variation across the structural repeat unit matched previous observations (cf. Figure 67). Stability during short-term exposure – adhesion and integrity – was likewise maintained. Minor differences in the TGO reflect the substrate choice (Crofer22APU for the F-type and Crofer22H for the flat specimen).

Based on the successful transfer of the EPD methodology to the fully organic system at small scale, the process was scaled to full F10-type interconnects. With the new route, the targeted homogeneous coating quality was achieved without macroscopic defects or flaws detectable via laser microscope. Because the final verification of direct glass-sealant joining on the coating (with respect to gas tightness and electrical insulation) was not yet completed, masking was used as in the current standard. After verifying the four components selected for stack testing following the reduction step, Ni meshes were spot-welded on the fuel side and the stack was assembled stepwise with glass sealants, frames, and cells. Photographs of representative components in the as-coated and reduced states – i.e., prior to assembly – are

provided in Figure 75a and b, respectively. Figure 75c shows the assembled four-layer SOFC stack on the test rig with connected measurement wires.

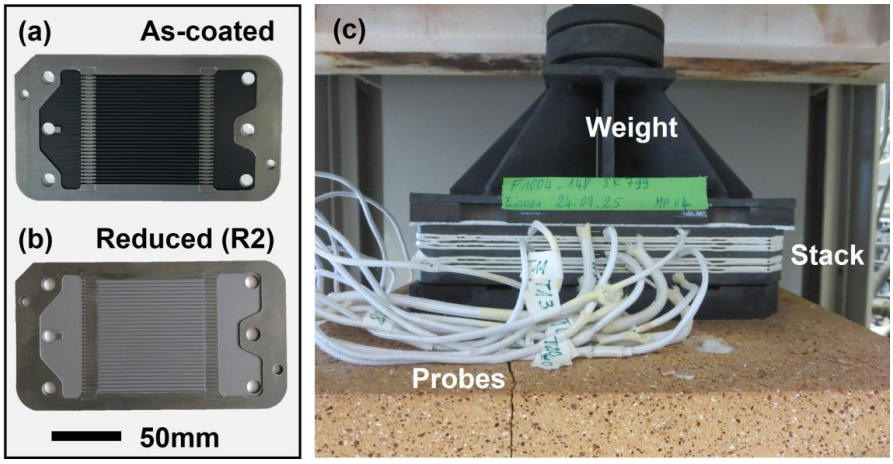

Figure 75: Depiction of MCF-EPD-coated F10 interconnects (a) as-coated, and (b) after pre-reduction before stack assembly; (c) assembled four-layer stack as inserted into the testing rig. Stack arrangement by A. Cramer (FZJ-ITE), and stack supervision and photo provision by U. de Haart (FZJ-IET-1).

After arranging all layers, the stack was joined following the standard procedure and operated at 800°C under typical SOFC conditions at 0.7 A·cm^{-2}. By finalizing this thesis, the stack run was not completed. Consequently, the post-test characterization – critical for assessing coating protectivity with respect to steel corrosion and air-electrode poisoning – remained pending. Nevertheless, the initial i/v curve recorded at start-up indicates fundamental stack functionality. This curve is shown in Figure 76.

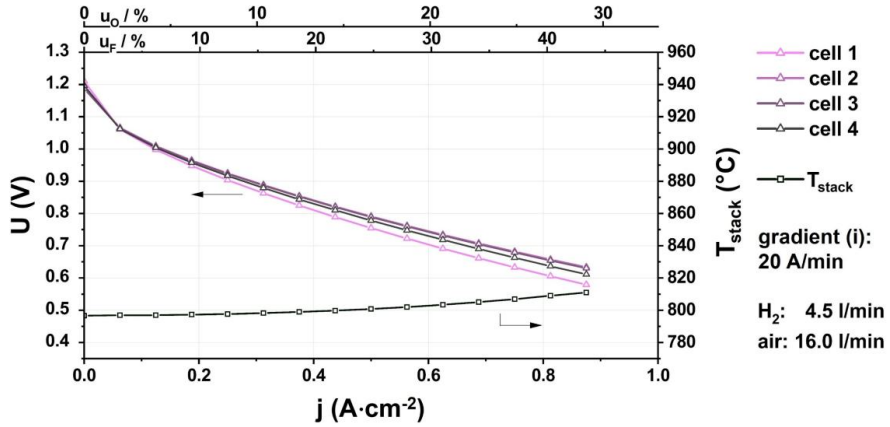

Figure 76: Initial i/v curve of the four-layer F10 SOFC stack with MCF-EPD-coated interconnects, running at 800°C and 0.7 A·cm^{-2}. T_{stack} determined in stack center; measured value at stack start 797°C. Data evaluation and provision by U. de Haart (FZJ-IET-1).

The initial polarization curve confirms basic stack operability, including reliable contacting across all layers and stable operation throughout the tested current-density range. Differences in performance between the individual cells (cell 1–4) are within typical variation for a four-layer stack. Outer positions (1 and 4) commonly show slightly lower voltages than the inner cells (2 and 3) due to less uniform thermal conditions and flow distributions.

At 0.7 A·cm^{-2} the measured voltage of ~0.7 V indicates comparatively modest performance. Current Jülich reference stacks equipped with LSC air electrodes and LSCF contact layers typically exceed 0.9 V at the same load. The observed gap is not attributable to the interconnect coatings per se but is primarily linked to the intrinsically lower power capability of the cell set used here, which employs an LSM air electrode with an LCC10 contact layer. The specific contribution of the EPD coating to performance cannot be isolated from the polarization curve alone. Its protective function will be assessed primarily in the post-test analysis focused on steel oxidation and chromium poisoning of the air electrode.

Crucially, stack-level functionality with the newly developed EPD coatings has been demonstrated. The next step is to place these results alongside APS and WPS in the sustainability assessment to draw a complete picture.

4.6. Life cycle and sustainability evaluation

Building on the working assumption – supported by the preceding technical investigations – that APS, WPS, and EPD are each capable of producing effective interconnect coatings, the detailed LCA complements this view with an environmental perspective. This section first summarizes the process-chain data on relevant energy as well as material consumptions and then presents and contextualizes the key outcomes of the assessment.

4.6.1. Process data, material and energy demands

The data collected across the individual process steps (cf. Figure 32 and Figure 33) – measured values and database-derived numbers – were normalized to a representative coated area of 175 cm^2 using the assumptions and conversions outlined in Section 3.8. The corresponding inventory data are presented in Table 10. It should be noted that the values per functional unit except for electricity consumption, could remain valid under equivalent assumptions regardless of production scale. It must also be noted that the EPD process examined here was based on the widely focused aqueous suspension system, which has since been replaced by the fully organic medium. However, the aqueous route remains the long-term target and, given the high degree of recyclability within the EPD workflow, the overall impact of this change is expected to be comparatively small.

Table 10: Main inventory data of the coating systems APS, WPS and EPD (values for 175 cm² of coated area). Data provided by K. El Jardali, V. Feyzi and D. Iribarren (IMDEA Energy).

Input from technosphere	Value	Unit	Output	Value	Unit
Atmospheric plasma spraying (APS)					
Helium	1.213	g	Product coated area	175	cm^2
Argon	109.5	g	Waste paint to treatment	20.7	g
MCF powder	27.50	g	Waste sand to treatment	81.9	g
Electricity	1.360	kW·h	Direct argon emission	109	g
			Direct helium emission	1.2	g
Wet powder spraying (WPS)					
Ethanol	9.660	g	Product coated area	175	cm^2
Ethoxylated alcohol (AE3)	0.046	g	Waste paint to treatment	1.45	g
Polyvinyl acetate	0.028	g	Wastewater to treatment	234	g
Triethylene glycol	0.469	g	Direct argon emission	156.6	g
Argon	159.6	g	Direct ethanol emission	9.4	g
Compressed air	9.770	l			
Hydrogen, gaseous	0.241	g			
Polyethylene terephthalate	0.002	g			
Silicone	0.002	g			
MCF powder	0.936	g			
Electricity	1.799	kW·h			
Electrophoretic deposition (EPD)					
Ethanol	0.943	g	Product coated area	175	cm^2
Water, deionized	0.801	kg	Wastewater to treatment	234	g
Argon	159.6	g	Direct argon emission	155.9	g
Hydrogen	0.241	g	Direct ethanol emission	0.855	g
MCF powder	0.490	g			
Polyethylene terephthalate	0.002	g			
Silicone	0.002	g			
Electricity	1.786	kW·h			

*Equal thermal pre-treatment (R.2) included for WPS and EPD.

The collected data were processed in SimaPro® at IMDEA Energy according to the defined model to derive the target metrics. The results are presented and discussed below.

4.6.2. LCA results on APS, WPS and EPD

The environmental characterization results for each coating system facilitate the identification of the environmental hotspots and possible areas of improvement in relation to each coating technique. In absolute numbers, the results are presented in Figure 78 and enable direct comparison between the techniques. For an improved distinction within an individual technique, highlighting the specific hotspots, Figure 79 presents the share percentage of each process to the potential environmental impacts. In this regard, the MCF

powder, argon, and electricity were identified as the three environmental hotspots for the three assessed coating methods. Processes with low contribution (under 5%) to the assessed environmental indicators were grouped under the category "Rest".

The manufacturing of the steel component – here explicitly the lightweight CS^V interconnect – was assessed across the same impact categories as the coating methods. A detailed breakdown of the interconnect production is not the focus and is therefore omitted. To contextualize the relative contributions of the steel part versus the applied coatings, a side-by-side comparison of their shares in the four impact categories was conducted. A normalized (100%) graphical breakdown is presented in Figure 77.

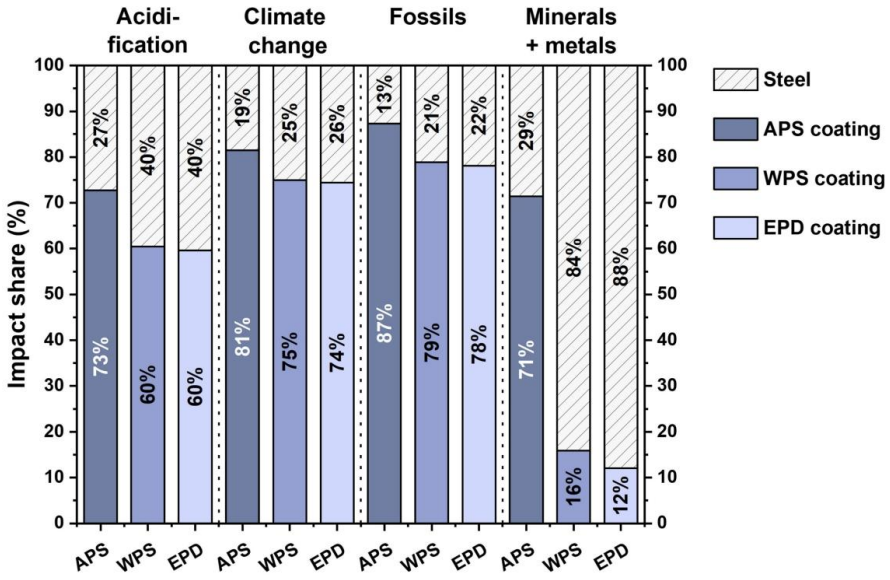

Figure 77: Impact shares of coating and steel component contribution, divided for the three techniques APS, WPS and EPD into the four main categories (i) acidification, (ii) climate change, (iii) resource use/fossils, and (iv) resource use/minerals and metals; Calculation based on the sheet-based CS^V interconnect type.

It could be clearly derived that the magnitude of the total environmental impacts of the coating processes in relation to the steel component suggests the importance of including coating-related impacts besides those of the substrate when coated materials are involved in LCA studies. So far, the data also suggest the importance of further progress in coating science and technology with special regards to the environmental implications.[263] While the coating contribution varies across categories, there is a clear decrease – most notably for minerals and metals consumption – when moving from the APS reference to the suspension-based WPS and EPD routes. More granular levers can be identified in the detailed breakdowns for each coating technology, as shown in Figure 78 and Figure 79.

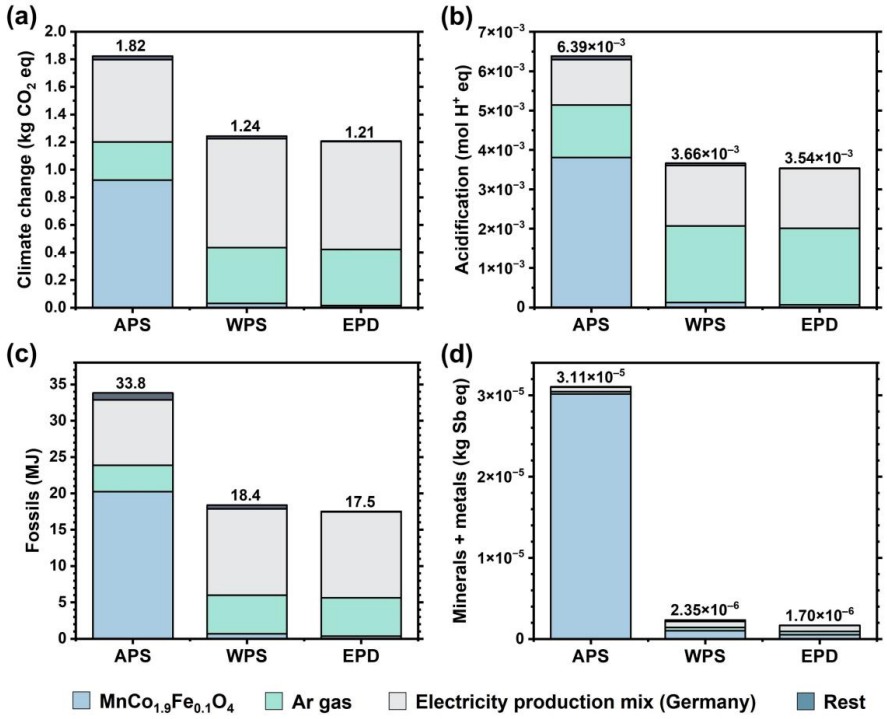

Figure 78: Results of LCA analysis of coating methods APS, WPS and EPD, separated into the specific impact factors of (a) climate change, (b) acidification, (c) use of fossil resources, and (d) use of minerals and metals; absolute impact per method split up for the specific contributions. Data provided by K. El Jardali, V. Feyzi and D. Iribarren (IMDEA Energy).

As shown in Figure 78, APS would involve the worst environmental performance among the three coating techniques in the four indicators under study. According to Figure 79 the unfavorable performance of APS would be closely linked to its demand for MCF powder as it dominates every indicator with contribution percentages higher than 50%. Notably, MCF's impact would reach a maximum contribution of 97% for the use of minerals and metals. These effects could be mitigated with continuous research for the APS coating technique in terms of material efficiency and by advancements to reduce critical raw materials in protective coatings for metals.

For WPS and EPD, the environmental profiles were found to be similar, with a slightly better performance for EPD in all four indicators. In these two techniques, argon and electricity were generally found to play a more dominant role than MCF. This is linked to the fact that the amounts of MCF powder used in WPS and EPD are much lower than in the APS case (Table 10). The higher MCF consumption in APS is associated with the higher thickness of the coating layer (one order of magnitude more than in the other two techniques) and the lower coating efficiency due to direct over-spraying and powder falling while sprayed over the substrate.

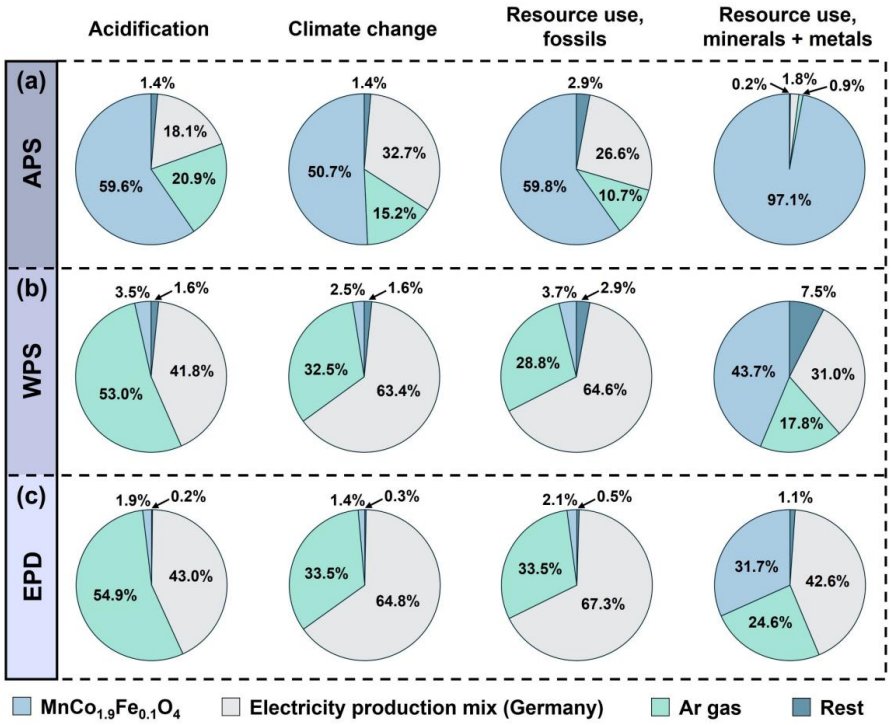

Figure 79: Results of LCA analysis of coating methods (a) APS, (b) WPS and (c) EPD, separated into the specific impact factors of climate change, acidification, use of fossil resources, and use of minerals and metals; impact per method split up for the relative fractions of the specific contributions. Data provided by K. El Jardali, V. Feyzi and D. Iribarren (IMDEA Energy).

Continuous development and innovations are necessary to achieve better performance and reduce the reported environmental impacts. For the reference APS, reducing the amount of powder consumption and/or changing its composition should be pursued. Efforts to recycle the undeposited powder – pending feasibility studies – could significantly improve process efficiency and substantially influence the assessment outcomes.

For WPS and EPD, optimization of synthesis processes and steps could lower energy consumption leading to a more favorable environmental profile and wider industrial use. Additionally, adjustments on operational parameters (as reducing temperature and dwell time) or alternative energy sources could also contribute to impact reduction. Moreover, further research and experimental work on replacing argon with nitrogen could be pursued, as this substitution could significantly improve environmental performance across all indicators.[263]

All in all, the LCA results indicate that EPD, followed by WPS, is the most environmentally friendly coating method among the three assessed ones in this work, whereas further efforts should be directed towards increasing material efficiency in APS.

Optimizing the energy-intensive process of reduction for WPS and EPD could notably lower the system energy consumption and its associated impacts. Looking ahead, the increased integration of renewable energy sources into electricity production mixes and advancements in coating technology are expected to enhance the environmental performance of these processes. In this sense, LCA studies should be regularly updated to reflect emerging innovations and improvements concerning the three identified environmental hotspots. So far however, the presented results complement the technical assessment above in a proper manner, enabling a well-founded classification of the coating solutions in a combined technical and environmental assessment.

4.7. Comprehensive ranking of coating technologies

To conclude, the results from the technical and environmental assessments are contrasted once more before the work is summarized. A visualization of the comprehensive comparison of MCF-based coatings is provided in Figure 80.

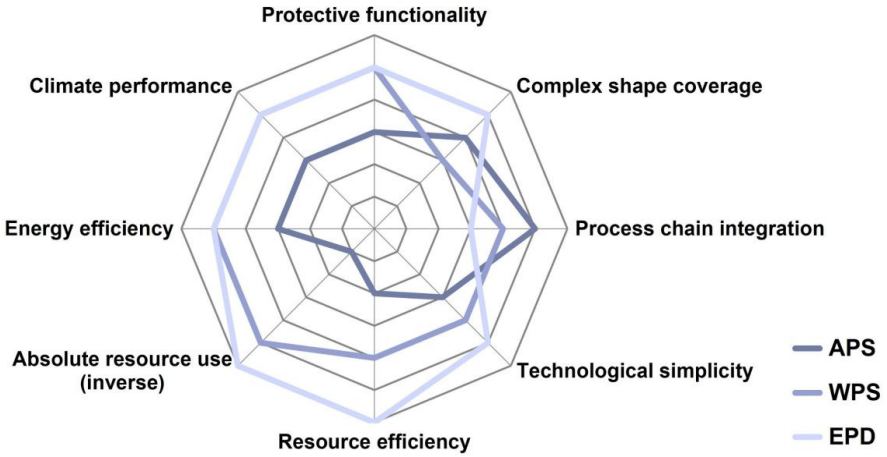

Figure 80: Superposition of APS, WPS and EPD in terms of eight relevant categories for the functionality- and sustainability-driven choice of coating technologies for SOC interconnects, derived from the technical and LCA analyses within this work.

Fundamentally, all three methods – APS, WPS, and EPD – can produce continuous coatings of the target composition, the Mn-Co spinel $MnCo_{1.9}Fe_{0.1}O_4$, on application-relevant steel structures for SOC interconnect components. With respect to coating quality on complex, sharp-edged flow-field geometries, decisive differences were nevertheless identified. For APS and WPS, a pronounced line-of-sight effect was observed. In WPS this appeared as poorly wetted rib edges. In APS continuous coverage in the most critical zones, such as flanks, could be ensured only by applying comparably large layer thicknesses on the planar segments. EPD, in contrast, yielded a distinctly different picture, with continuous

and sufficiently thick coatings, especially in these critical regions near the cell unit, and with overall uniform layer characteristics.

In terms of protective function – limiting TGO growth and localizing chromium to prevent outward migration – all three methods improved performance compared with uncoated steel. Counterintuitively, the weakest protection was found for the thickest, thermally sprayed APS layers, while the thinner, suspension-based coatings showed very strong protective effects.

APS offers a clear process advantage because the coatings are operation-ready immediately after deposition and the components can be integrated directly into the stack. WPS and EPD require a reductive heat treatment, which entails additional consumption of argon and electricity and therefore has non-negligible environmental implications (see Figure 79). At the same time, solid optimization potential was identified. For EPD, an additional powder-preparation step must be considered, which increases process-chain complexity. Though, this can likely be mitigated in future optimization, for example by using finer, synthesized powders in industrial implementation.

Conversely, the more complex equipment required for APS is a significant limitation relative to the suspension-based routes. EPD stands out for its simple and flexible setup.

Because APS layers are on the order of 100 µm – roughly an order of magnitude thicker than WPS and EPD – material demand is substantially higher. Beyond thickness, overspray in the spray-based methods is a major constraint on resource efficiency, with APS again performing the weakest. Relative to APS, the EPD route achieved about a 40-fold reduction in total coating-material consumption. By depositing from a liquid medium and by broadly recovering non-deposited powder, EPD enables near loss-free material utilization under ideal conditions and thus emerged as the most resource-efficient option.

Across the further environmental impact categories considered, EPD – and to a very similar extent WPS – showed comparatively low burdens. Overall, the suspension-based methods are clearly competitive with the established APS benchmark. Moreover, specific and decisive advantages were demonstrated for the newly developed EPD route. For future stack concepts that emphasize thin and deformation-sensitive interconnect designs, demanding flow-field geometries, and especially the environmental dimension, EPD should therefore be prioritized, with WPS as a secondary option.

5. Conclusions and Outlook

Across this work, the groundwork for a more sustainable design of SOC technology was pursued with the interconnect as the central lever. This chapter revisits the strategies followed, the core findings and limitations, and outlines how these can be addressed next, together with forward-looking research questions and recommended paths.

5.1. Summary of key findings

Building on the literature, the interconnect emerged as a major contributor to the current competitiveness gap between SOCs and co-existing hydrogen technologies, both in materials demand and cost. From this starting point, three strategy pillars were defined towards economical and ecological optimization: Moving to thin-sheet interconnects that require coating routes able to create protectivity without inducing substrate damage, reducing coating thickness while keeping integrity and adhesion, and substituting materials towards conventional stainless steels and Co-free coating compositions.

Guided by these key strategies, electrophoretic deposition (EPD) was selected as a particularly promising method and was developed systematically against a state-of-the-art technology atmospheric plasma spraying (APS) and the established wet powder spraying (WPS) route in Jülich. The first objective was to enable uniform, homogeneous, thin coatings using the Jülich reference spinel $MnCo_{1.9}Fe_{0.1}O_4$ (MCF) on steel substrates, initially employing Crofer-type specialty steels. After optimizing powder properties and a water-ethanol suspension route to achieve high green-layer quality, the process was transferred to a cobalt-free alternative. Based on stability considerations, the Ni-doped Cu-Mn spinel $CuMn_{1.8}Ni_{0.2}O_4$ (CMN) was selected and deposited analogously.

A thermal-treatment study then targeted microstructural optimization with the specific aim of integrating the final oxidizing sintering into the stack-assembly step at 850°C for 100 h. In addition to single-step oxidation, two two-step "reactive sintering" schedules with a preceding reduction at 900°C and 1000°C were investigated. XRD confirmed spinel formation after the full thermal chain across all types, and reactive sintering generally promoted densification. While MCF developed favorable microstructures, CMN already showed limitations, including steel oxidation during treatment and chromium transport through the coating rather than localization in the thermally grown oxide (TGO) scale.

Stack integrability was also assessed via performance indicators that are central to coating function. Cr evaporation was used to gauge air-electrode protection, mass gain to quantify steel oxidation, and ASR to capture electrical behavior. In an exposure campaign that emulated the 100 h of stack joining followed by 400 h at 800°C, simulating stack start-up, all six coating types achieved suitable ASR values at or below roughly 20 $m\Omega \cdot cm^2$, yet with clear differences in protection. All coatings reduced Cr evaporation, although only

marginally for CMN, which simultaneously showed higher oxidation-related mass gain. MCF performed substantially better overall, with the 1000°C reduction standing out.

A second study extended exposure up to 3000 h and compared selected two-step EPD coatings with MCF-APS and MCF-WPS. Within EPD, MCF again outperformed CMN, while WPS and EPD behaved very similar. Relative to APS, corrosion protection was markedly more effective. For Crofer22H this translated into more than a twofold reduction in ASR compared with APS and about a threefold reduction relative to uncoated steel, with stable values below roughly 20 $m\Omega \cdot cm^2$, which is competitive with the literature. As a conventional alternative, AISI430 was also assessed. MCF coatings helped stabilizing and controlling TGO growth on this steel type, yet they could not suppress the formation of a continuous insulating SiO_2 sub-scale caused by Si contamination, which resulted in substantially poorer electrical performance than on Crofer22H. Within the scope of this study, the pairing of MCF with Crofer steels emerged as best performing overall.

To further assess stack integration, compatibility with the glass sealant was examined. CMN showed pronounced decomposition and redistribution into the glass, indicating a durability risk for insulation. In contrast, MCF formed a dense compound without extensive interdiffusion or decomposition, which indicates that direct sealing on the coating is feasible and could significantly simplify manufacturing.

When transferring to rib-channel gas distributor structures, EPD displayed a pronounced advantage over APS and WPS. The absence of the line-of-sight limitation enabled full-surface and largely uniform coverage even at very low thickness, while preserving the favorable microstructural traits observed on flat coupons. The methodology was then scaled to full interconnect size. After minor process adjustments, components for a four-layer SOFC stack were coated with MCF, pre-reduced at 1000°C, and oxidized *in-situ*. Initial i/v curves confirmed basic stack operability across all layers. A full post-test analysis will determine the coatings' protective performance in detail.

Finally, a comprehensive LCA extended the selection criteria beyond technical performance. Suspension-based WPS and EPD showed clear advantages in categories such as acidification and climate impact, with EPD offering a particularly strong benefit in resource demand through an approximately forty-fold reduction in minerals and metals consumption relative to APS. This advantage stems from much lower layer thickness and near-lossless powder utilization.

Taken together, the newly established EPD route proved not only competitive but, in many respects, superior to the APS benchmark, and broadly aligned with WPS while offering decisive advantages in coverage and resource efficiency.

5.2. Limitations of this work

In addition to the progress established in this thesis, it also delineates open questions and targeted next steps towards robust industrial implementation. While the EPD route was successfully advanced to deliver effective protective coatings, the approach remained largely engineering-driven. A more fundamental, system-level exploration would likely reveal additional performance reserves. This would entail a broader and more systematic screening of deposition parameters, designed to map interactions among powder characteristics, suspension chemistry, electrokinetics, and thermal schedules in a way that goes beyond locally optimized conditions.

The focus on a limited set of coating compositions is another constraint. Other systems that are, in principle, viable – such as Fe-Ni spinels or related families – could compete with the MCF reference. For CMN and other Cu-Mn spinels, application at milder operating conditions, for example in intermediate-temperature SOCs around 650°C, could be the more plausible use case. The steel set was also narrowed. Although this work contrasted Crofer-type specialty steels with AISI430 as a conventional option, other studies point towards promise in further commercial grades such as AISI441. This alloy performed more favorably in the parallel doctoral research of D. Vakhrameev[241] and may mitigate the Si-driven sub-scale formation that limited AISI430 here.

A further limitation lies in the up-scaling step. To overcome water-related inhomogeneities at large suspension volumes, the process was shifted from an aqueous to a fully organic medium. On the long run, however, an aqueous system remains the preferred direction for sustainability and safety. This final step was not pushed to completion in the present work.

The LCA, which clearly favored the suspension-based routes – especially EPD – also needs to be read alongside improvement levers on the APS side that were out of scope here. Resource efficiency in APS could benefit from overspray recovery and from more advanced robot movement, improving deposition efficiency in critical geometries. Similar trajectory optimizations apply to WPS. Such measures would further enable thinner coatings with lower materials demand, partially narrowing today's environmental gap, as seen for APS. These points motivate targeted follow-ups, while the next section concentrates on EPD-specific steps towards large-scale implementation and focusing the sustainability perspective.

5.3. Outlook on large-scale implementation

The immediate priority is the full analysis of the ongoing stack test. This should couple electrochemical performance and degradation analysis – through impedance spectroscopy and i/v characterization over time – with post-test microstructural and chemical investigations to localize losses and assign them to mechanisms. A subsequent

validation run with an updated cell concept is advisable. Also, ideally an additional run employing thin-sheet interconnects could be meaningful to further reflect the intended design direction.

Process optimization at component scale should continue with a view towards resource-efficient manufacturing. The objective is to realize the aqueous suspension system for large parts while retaining the deposition quality achieved with the organic medium. To enable full-surface coating and direct glass sealing on the coating, dedicated campaigns should verify electrical insulation and leak tightness through resistance and gas-permeability testing, complemented by quantitative assessments of mechanical robustness of the sealed joint.

On the materials side, conventional steels remain a key avenue. AISI441 is a primary candidate, although batch-to-batch screening is deliberate due to variations in Si and Al that control sub-scale formation. For coatings, Cu-Mn spinels should be continued in study – at minimum for intermediate-temperature or proton-conducting SOCs where CMN may again be attractive – while widening the search towards other cobalt-free compositions.

Finally, the LCA highlights remaining room for improvement in EPD. The reduction step weighs heavily through electricity and Ar consumption. Future work should examine shorter reductions with higher ramp rates and, critically, the substitution of Ar by N_2 as the inert carrier. These measures point towards an EPD process that is not only technically compelling but also more sustainable at industrial scale.

Thus, it has shown that even after this work a broad palette of demand but also potential for optimization persists in the frame of developing sustainability-driven solutions for the interconnect component, and besides several tackled ones, new research questions arose. Nonetheless, decisive approaches were mapped, offering a substantial contribution to enhance both economical competitiveness and ecological impact of the interconnect and the overall SOC technology – within Forschungszentrum Jülich and beyond.

References

1. Team GW. Trends in CO2 - NOAA Global Monitoring Laboratory [Internet]. [cited 2026 Feb 10]. Available from: https://gml.noaa.gov/ccgg/trends/global.html
2. Intergovernmental Panel On Climate Change (Ipcc). Climate Change 2021 – The Physical Science Basis: Working Group I Contribution to the Sixth Assessment Report of the Intergovernmental Panel on Climate Change [Internet]. 1st ed. Cambridge University Press; 2023 [cited 2026 Feb 10]. Available from: https://www.cambridge.org/core/product/identifier/9781009157896/type/book doi:10.1017/9781009157896
3. Intergovernmental Panel On Climate Change (Ipcc). Climate Change 2022 – Impacts, Adaptation and Vulnerability: Working Group II Contribution to the Sixth Assessment Report of the Intergovernmental Panel on Climate Change [Internet]. Cambridge University Press; 2023 Jun [cited 2026 Mar 25]. Available from: https://www.cambridge.org/core/product/identifier/9781009325844/type/book doi:10.1017/9781009325844
4. United Nations. Report of the United Nations Conference on Environment and Development [Internet]. New York: United Nations; 1993 [cited 2026 Mar 25]. p. Annex 1. Available from: https://documents.un.org/doc/undoc/gen/n92/836/55/pdf/n9283655.pdf
5. Intergovernmental Panel On Climate Change (Ipcc). Global Warming of 1.5°C: IPCC Special Report on Impacts of Global Warming of 1.5°C above Pre-industrial Levels in Context of Strengthening Response to Climate Change, Sustainable Development, and Efforts to Eradicate Poverty [Internet]. Cambridge University Press; 2022 Jun [cited 2026 Mar 25]. Available from: https://www.cambridge.org/core/product/identifier/9781009157940/type/book doi:10.1017/9781009157940
6. Umweltbundesamt. Energiebedingte Emissionen von Klimagasen und Luftschadstoffen [Internet]. 2025 [cited 2026 Mar 25]. Available from: https://www.umweltbundesamt.de/daten/energie/energiebedingte-emissionen
7. Overland I, Juraev J, Vakulchuk R. Are renewable energy sources more evenly distributed than fossil fuels? Renew Energy. 2022 Nov 1;200:379–86. doi:10.1016/j.renene.2022.09.046
8. Rau GH, Willauer HD, Ren ZJ. The global potential for converting renewable electricity to negative-CO2-emissions hydrogen. Nat Clim Change. 2018 Jul;8(7):621–5. doi:10.1038/s41558-018-0203-0
9. IEA. Global Hydrogen Review 2025 [Internet]. Paris: IEA; 2025. Available from: https://www.iea.org/reports/global-hydrogen-review-2025
10. Hauch A, Küngas R, Blennow P, Hansen AB, Hansen JB, Mathiesen BV, et al. Recent advances in solid oxide cell technology for electrolysis. Science. 2020 Oct 9;370(6513):eaba6118. doi:10.1126/science.aba6118
11. Harboe S, Schreiber A, Margaritis N, Blum L, Guillon O, Menzler NH. Manufacturing cost model for planar 5 kWel SOFC stacks at Forschungszentrum Jülich. Int J Hydrog Energy. 2020 Mar;45(15):8015–30. doi:10.1016/j.ijhydene.2020.01.082

12. Hao Y, Zhu R, Cao H, Liu Z, Ran R, Yang G. A Mini-Review on Mitigating Degradation of Metallic Interconnects in Solid Oxide Cell Stack Systems: Advances, Challenges, and Solutions. Energy Fuels. 2025 Sep 22. doi:10.1021/acs.energyfuels.5c03611
13. Winter M, Brodd RJ. What Are Batteries, Fuel Cells, and Supercapacitors? Chem Rev. 2004 Oct 1;104(10):4245–70. doi:10.1021/cr020730k
14. Pastore LM, Sgaramella A, Bruno G, Lo Basso G, De Santoli L. Coupling high-temperature electrolysis and industrial waste heat for on-site green hydrogen production: energy, economic and environmental analysis. Int J Hydrog Energy. 2025 May;126:87–98. doi:10.1016/j.ijhydene.2025.04.069
15. Duan C, Huang J, Sullivan N, O'Hayre R. Proton-conducting oxides for energy conversion and storage. Appl Phys Rev. 2020 Mar 1;7(1):011314. doi:10.1063/1.5135319
16. Wolf SE, Winterhalder FE, Vibhu V, De Haart LGJ (Bert), Guillon O, Eichel RA, et al. Solid oxide electrolysis cells – current material development and industrial application. J Mater Chem A. 2023;11(34):17977–8028. doi:10.1039/D3TA02161K
17. Guillon O. Advanced Ceramics for Energy Conversion and Storage. Elsevier; 2019. 750 p.
18. McPhail SJ, Kiviaho J, Conti B. The Yellow Pages of SOFC Technology, International Status of SOFC deployment 2017 [Implementing Agreement Advanced Fuel Cells]. IEA; 2017. Implementing Agreement Advanced Fuel Cells Annex 32 – SOFC.
19. Yamamoto O. Solid oxide fuel cells: fundamental aspects and prospects. Electrochimica Acta. 2000 May;45(15–16):2423–35. doi:10.1016/S0013-4686(00)00330-3
20. Kaur P, Singh K. Review of perovskite-structure related cathode materials for solid oxide fuel cells. Ceram Int. 2020 Apr;46(5):5521–35. doi:10.1016/j.ceramint.2019.11.066
21. Menzler NH, Schäfer D, Kruse N, Peters R, Kunz F. Solid Oxide Cells for Hydrogen Generation and Usage: From Materials to Systems. In: Ceramic forum international. 2023.
22. Tucker MC. Progress in metal-supported solid oxide electrolysis cells: A review. Int J Hydrog Energy. 2020 Sep;45(46):24203–18. doi:10.1016/j.ijhydene.2020.06.300
23. Menzler NH, Tietz F, Uhlenbruck S, Buchkremer HP, Stöver D. Materials and manufacturing technologies for solid oxide fuel cells. J Mater Sci. 2010 Jun 1;45(12):3109–35. doi:10.1007/s10853-010-4279-9
24. Tietz F, Fu Q, Haanappel VAC, Mai A, Menzler NH, Uhlenbruck S. Materials Development for Advanced Planar Solid Oxide Fuel Cells. Int J Appl Ceram Technol. 2007 Oct;4(5):436–45. doi:10.1111/j.1744-7402.2007.02156.x
25. Zakaria Z, Awang Mat Z, Abu Hassan SH, Boon Kar Y. A review of solid oxide fuel cell component fabrication methods toward lowering temperature. Int J Energy Res. 2020;44(2):594–611. doi:10.1002/er.4907
26. Ramler DJ, Mücke R, Lenser C, Guillon O, Menzler NH. Influence of powder characteristics on the rheology of ceria-based screen-printing pastes for solid oxide cell applications. J Eur Ceram Soc. 2025 Dec;45(15):117570. doi:10.1016/j.jeurceramsoc.2025.117570

27. Salmang H, Scholze H. Sintern. In: Telle R, editor. Keramik. Berlin, Heidelberg: Springer; 2007. p. 313–80. doi:10.1007/978-3-540-49469-0_4
28. Al-Qudsi A, Kammler M, Bouguecha A, Bonk C, Behrens BA. Comparison between different numerical models of densification during solid-state sintering of pure aluminium powder. Prod Eng. 2015 Feb 1;9. doi:10.1007/s11740-014-0574-7
29. Pederson LR, Singh P, Zhou XD. Application of vacuum deposition methods to solid oxide fuel cells. Vacuum. 2006 Aug;80(10):1066–83. doi:10.1016/j.vacuum.2006.01.072
30. Mattox DM. Handbook of Physical Vapor Deposition (PVD) Processing. William Andrew; 2010. 793 p.
31. Pan Y, Wang J, Lu Z, Wang R, Xu Z. A review on the application of magnetron sputtering technologies for solid oxide fuel cell in reduction of the operating temperature. Int J Hydrog Energy. 2024 Jan;50:1179–93. doi:10.1016/j.ijhydene.2023.10.143
32. Pierson HO. Handbook of Chemical Vapor Deposition: Principles, Technology and Applications. William Andrew; 1999. 507 p.
33. Singh K, Walia T. Review on silicate and borosilicate-based glass sealants and their interaction with components of solid oxide fuel cell. Int J Energy Res. 2021;45(15):20559–82. doi:10.1002/er.7161
34. Gross SM, Federmann D, Remmel J, Pap M. Reinforced composite sealants for solid oxide fuel cell applications. J Power Sources. 2011 Sep;196(17):7338–42. doi:10.1016/j.jpowsour.2011.02.002
35. Federmann D, Groß-Barsnick SM, Zerfass HR, Forschungszentrum Jülich GmbH. Method for producing a solder glass green seal. EP2 991 942B1, 2017.
36. Mah JCW, Muchtar A, Somalu MR, Ghazali MJ. Metallic interconnects for solid oxide fuel cell: A review on protective coating and deposition techniques. Int J Hydrog Energy. 2017 Apr;42(14):9219–29. doi:10.1016/j.ijhydene.2016.03.195
37. Wu J, Liu X. Recent Development of SOFC Metallic Interconnect. J Mater Sci Technol. 2010 Apr;26(4):293–305. doi:10.1016/S1005-0302(10)60049-7
38. Fergus JW. Metallic interconnects for solid oxide fuel cells. Mater Sci Eng A. 2005 Apr;397(1–2):271–83. doi:10.1016/j.msea.2005.02.047
39. Sakai N, Yokokawa H, Horita T, Yamaji K. Lanthanum Chromite-Based Interconnects as Key Materials for SOFC Stack Development. Int J Appl Ceram Technol. 2004;1(1):23–30. doi:10.1111/j.1744-7402.2004.tb00151.x
40. Fergus J. Lanthanum chromite-based materials for solid oxide fuel cell interconnects. Solid State Ion. 2004 Jun;171(1–2):1–15. doi:10.1016/j.ssi.2004.04.010
41. Kofstad P. High temperature corrosion. London ; New York : New York, NY, USA: Elsevier Applied Science ; Sole distributor in the USA and Canada, Elsevier Science Pub. Co; 1988. 558 p.
42. Wagner C. Beitrag zur Theorie des Anlaufvorgangs. Z Für Phys Chem. 1933 Feb 1;21B(1):25–41. doi:10.1515/zpch-1933-2105
43. Young DJ. High Temperature Oxidation and Corrosion of Metals. Elsevier; 2008. 593 p.

44. Samsonov GV. Electrical and Magnetic Properties. In: The Oxide Handbook. Boston, MA: Springer US; 1973. p. 263–319.
45. Badwal S, Deller R, Foger K, Ramprakash Y, Zhang J. Interaction between chromia forming alloy interconnects and air electrode of solid oxide fuel cells. Solid State Ion. 1997 Aug 2;99(3–4):297–310. doi:10.1016/S0167-2738(97)00247-6
46. Reddy MJ, Chausson TE, Svensson JE, Froitzheim J. 11–23% Cr steels for solid oxide fuel cell interconnect applications at 800 °C – How the coating determines oxidation kinetics. Int J Hydrog Energy. 2023 Apr;48(34):12893–904. doi:10.1016/j.ijhydene.2022.11.326
47. Yang Z, Hardy JS, Walker MS, Xia G, Simner SP, Stevenson JW. Structure and Conductivity of Thermally Grown Scales on Ferritic Fe-Cr-Mn Steel for SOFC Interconnect Applications. J Electrochem Soc. 2004 Oct 7;151(11):A1825. doi:10.1149/1.1797031
48. Holappa L, Conejo AN. Chapter 1.7 – Secondary Steelmaking. In: Treatise on Process Metallurgy [Internet]. Elsevier; 2024 [cited 2026 Feb 12]. p. 267–301. Available from: https://www.sciencedirect.com/science/chapter/edited-volume/abs/pii/B9780323853736000338 doi:10.1016/B978-0-323-85373-6.00033-8
49. Jablonski PD, Cowen CJ, Sears JS. Exploration of alloy 441 chemistry for solid oxide fuel cell interconnect application. J Power Sources. 2010 Feb;195(3):813–20. doi:10.1016/j.jpowsour.2009.08.023
50. Quadakkers WJ, Piron-Abellan J, Shemet V, Singheiser L. Metallic interconnectors for solid oxide fuel cells – a review. Mater High Temp. 2003 Jan;20(2):115–27. doi:10.1179/mht.2003.015
51. Froitzheim J, Meier GH, Niewolak L, Ennis PJ, Hattendorf H, Singheiser L, et al. Development of high strength ferritic steel for interconnect application in SOFCs. J Power Sources. 2008 Mar;178(1):163–73. doi:10.1016/j.jpowsour.2007.12.028
52. Douglass DL, Armijo JS. The influence of manganese and silicon on the oxidation behavior of Co-20Cr. Oxid Met. 1971 Mar 1;3(2):185–202. doi:10.1007/BF00603486
53. Hsiao ZW, Kuhn B, Chen D, Singheiser L, Kuo JC, Lin DY. Characterization of Laves phase in Crofer 22 H stainless steel. Micron. 2015 Jul;74:59–64. doi:10.1016/j.micron.2015.04.007
54. Froitzheim J. Ferritic steel interconnectors and their interactions with Ni base anodes in solid oxide fuel cells (SOFC). [Aachen]: RWTH Aachen University; 2008.
55. Whittle DP, Stringer J. Improvements in high temperature oxidation resistance by additions of reactive elements or oxide dispersions. Philos Trans R Soc Lond Ser Math Phys Sci. 1980 Feb 7;295(1413):309–29. doi:10.1098/rsta.1980.0124
56. Pint BA. Experimental observations in support of the dynamic-segregation theory to explain the reactive-element effect. Oxid Met. 1996 Feb;45(1–2):1–37. doi:10.1007/BF01046818
57. Hou PY, Stringer J. The effect of reactive element additions on the selective oxidation, growth and adhesion of chromia scales. Mater Sci Eng A. 1995 Nov 1;202(1):1–10. doi:10.1016/0921-5093(95)09798-8
58. Quadakkers WJ, Holzbrecher H, Briefs KG, Beske H. The Effect of Yttria Dispersions on the Growth Mechanisms and Morphology of Chromia and Alumina Scales. In: Lang

E, editor. The Role of Active Elements in the Oxidation Behaviour of High Temperature Metals and Alloys [Internet]. Dordrecht: Springer Netherlands; 1989 [cited 2026 Mar 20]. p. 155–73. Available from: https://doi.org/10.1007/978-94-009-1147-5_11 doi:10.1007/978-94-009-1147-5_11

59. Przybylski K, Garratt-Reed AJ, Yurek GJ. Grain Boundary Segregation of Yttrium in Chromia Scales. J Electrochem Soc. 1988 Feb 1;135(2):509. doi:10.1149/1.2095646
60. Menzler NH, Sebold D, Sohn YJ, Zischke S. Post-test characterization of a solid oxide fuel cell after more than 10 years of stack testing. J Power Sources. 2020 Dec;478:228770. doi:10.1016/j.jpowsour.2020.228770
61. Chou JT, Inoue Y, Kawabata T, Matsuda J, Taniguchi S, Sasaki K. Mechanism of SrZrO3 Formation at GDC/YSZ Interface of SOFC Cathode. J Electrochem Soc. 2018 Aug 21;165(11):F959. doi:10.1149/2.0551811jes
62. Mogensen MB, Chen M, Frandsen HL, Graves C, Hauch A, Hendriksen PV, et al. Ni migration in solid oxide cell electrodes: Review and revised hypothesis. Fuel Cells. 2021;21(5):415–29. doi:10.1002/fuce.202100072
63. Wachsman ED, Lee KT. Lowering the Temperature of Solid Oxide Fuel Cells. Science. 2011 Nov 18;334(6058):935–9. doi:10.1126/science.1204090
64. Gunduz KO, Reddy M, Chyrkin A, Froitzheim J. The Dual Atmosphere Effect - 20+ Years of Research. ECS Meet Abstr. 2025 Nov 24;MA2025-03(1):452–452. doi:10.1149/MA2025-031452mtgabs
65. Yang Z, Walker MS, Singh P, Stevenson JW. Anomalous Corrosion Behavior of Stainless Steels under SOFC Interconnect Exposure Conditions. Electrochem Solid-State Lett. 2003;6(10):B35. doi:10.1149/1.1603012
66. Zhao Y, Fergus JW. Oxidation of Alloys 430 and 441 in SOFC Dual Atmospheres: Effects of Flow Rate and Humidity. J Electrochem Soc. 2012;159(3):C109–13. doi:10.1149/2.013203jes
67. Rufner J, Gannon P, White P, Deibert M, Teintze S, Smith R, et al. Oxidation behavior of stainless steel 430 and 441 at 800°C in single (air/air) and dual atmosphere (air/hydrogen) exposures. Int J Hydrog Energy. 2008 Feb;33(4):1392–8. doi:10.1016/j.ijhydene.2007.12.067
68. Skilbred AWB, Haugsrud R. The effect of dual atmosphere conditions on the corrosion of Sandvik Sanergy HT. Int J Hydrog Energy. 2012 May;37(9):8095–101. doi:10.1016/j.ijhydene.2011.10.096
69. Skilbred AWB, Haugsrud R. The Effect of Water Vapour on the Corrosion of Sandvik Sanergy HT Under Dual Atmosphere Conditions. Oxid Met. 2013 Jun;79(5–6):639–54. doi:10.1007/s11085-012-9313-7
70. Ardigo MR, Popa I, Combemale L, Chevalier S, Herbst F, Girardon P. Dual atmosphere study of the K41X stainless steel for interconnect application in high temperature water vapour electrolysis. Int J Hydrog Energy. 2015 Apr;40(15):5305–12. doi:10.1016/j.ijhydene.2015.01.116
71. Kurokawa H. Oxidation behavior of Fe–16Cr alloy interconnect for SOFC under hydrogen potential gradient. Solid State Ion. 2004 Mar 15;168(1–2):13–21. doi:10.1016/j.ssi.2004.02.008

72. Alnegren P, Sattari M, Svensson JE, Froitzheim J. Temperature dependence of corrosion of ferritic stainless steel in dual atmosphere at 600–800 °C. J Power Sources. 2018 Jul;392:129–38. doi:10.1016/j.jpowsour.2018.04.088
73. Gunduz KO, Chyrkin A, Goebel C, Hansen L, Hjorth O, Svensson JE, et al. The effect of hydrogen on the breakdown of the protective oxide scale in solid oxide fuel cell interconnects. Corros Sci. 2021 Feb;179:109112. doi:10.1016/j.corsci.2020.109112
74. Holcomb GR, Ziomek-Moroz M, Cramer SD, Covino BS, Bullard SJ. Dual-Environment Effects on the Oxidation of Metallic Interconnects. J Mater Eng Perform. 2006 Aug 1;15(4):404–9. doi:10.1361/105994906X117198
75. Horita T. Chromium poisoning for prolonged lifetime of electrodes in solid oxide fuel cells - Review. Ceram Int. 2021 Mar;47(6):7293–306. doi:10.1016/j.ceramint.2020.11.082
76. Caplan D, Cohen M. The Volatilization of Chromium Oxide. J Electrochem Soc. 1961 May 1;108(5):438. doi:10.1149/1.2428106
77. Wachsman ED, Oh D, Armstrong E, Jung DW, Kan C. Mechanistic Understanding of Cr Poisoning on La0.6Sr0.4Co0.2Fe0.8O3-δ (LSCF). ECS Trans. 2009 Sep 25;25(2):2871–9. doi:10.1149/1.3205852
78. Opila EJ, Myers DL, Jacobson NS, Nielsen IMB, Johnson DF, Olminsky JK, et al. Theoretical and Experimental Investigation of the Thermochemistry of CrO_2 $(OH)_2$ (g). J Phys Chem A. 2007 Mar 1;111(10):1971–80. doi:10.1021/jp0647380
79. Ebbinghaus BB. Thermodynamics of gas phase chromium species: The chromium oxides, the chromium oxyhydroxides, and volatility calculations in waste incineration processes. Combust Flame. 1993 Apr 1;93(1):119–37. doi:10.1016/0010-2180(93)90087-J
80. Fergus J. Effect of cathode and electrolyte transport properties on chromium poisoning in solid oxide fuel cells. Int J Hydrog Energy. 2007 Nov;32(16):3664–71. doi:10.1016/j.ijhydene.2006.08.005
81. Kindelmann M, Guillon O, Mayer J, Menzler NH. Atomic-scale insights into air electrode degradation after 10 years of fuel cell stack operation. J Mater Chem A. 2025;13(40):34306–15. doi:10.1039/D5TA03917G
82. Tedmon CS. The Effect of Oxide Volatilization on the Oxidation Kinetics of Cr and Fe-Cr Alloys. J Electrochem Soc. 1966 Aug 1;113(8):766. doi:10.1149/1.2424115
83. Pujilaksono B, Jonsson T, Halvarsson M, Panas I, Svensson JE, Johansson LG. Paralinear Oxidation of Chromium in O2 + H2O Environment at 600–700 °C. Oxid Met. 2008 Oct 1;70(3):163–88. doi:10.1007/s11085-008-9114-1
84. Konysheva E, Seeling U, Besmehn A, Singheiser L, Hilpert K. Chromium vaporization of the ferritic steel Crofer22APU and ODS Cr5Fe1Y2O3 alloy. J Mater Sci. 2007 Jul 1;42(14):5778–84. doi:10.1007/s10853-006-1194-1
85. Stanislowski M, Froitzheim J, Niewolak L, Quadakkers WJ, Hilpert K, Markus T, et al. Reduction of chromium vaporization from SOFC interconnectors by highly effective coatings. J Power Sources. 2007 Feb;164(2):578–89. doi:10.1016/j.jpowsour.2006.08.013
86. Materials Project [Internet]. [cited 2026 Mar 22]. Materials Project. Available from: https://next-gen.materialsproject.org/materials

87. Fontana S, Amendola R, Chevalier S, Piccardo P, Caboche G, Viviani M, et al. Metallic interconnects for SOFC: Characterisation of corrosion resistance and conductivity evaluation at operating temperature of differently coated alloys. J Power Sources. 2007 Sep;171(2):652–62. doi:10.1016/j.jpowsour.2007.06.255
88. Alman D, Jablonski P. Effect of minor elements and a Ce surface treatment on the oxidation behavior of an Fe–22Cr–0.5Mn (Crofer 22 APU) ferritic stainless steel. Int J Hydrog Energy. 2007 Nov;32(16):3743–53. doi:10.1016/j.ijhydene.2006.08.032
89. Chevalier S, Valot C, Bonnet G, Colson JC, Larpin JP. The reactive element effect on thermally grown chromia scale residual stress. Mater Sci Eng A. 2003 Feb;343(1–2):257–64. doi:10.1016/S0921-5093(02)00359-3
90. Fontana S, Chevalier S, Caboche G. Metallic Interconnects for Solid Oxide Fuel Cell: Performance of Reactive Element Oxide Coating During 10, 20 and 30 Months Exposure. Oxid Met. 2012 Dec 1;78(5):307–28. doi:10.1007/s11085-012-9308-4
91. Grolig JG, Froitzheim J, Svensson JE. Effect of Cerium on the Electrical Properties of a Cobalt Conversion Coating for Solid Oxide Fuel Cell Interconnects – A Study Using Impedance Spectroscopy. Electrochimica Acta. 2015 Dec;184:301–7. doi:10.1016/j.electacta.2015.10.111
92. Gillot B, Legros R, Metz R, Rousset A. Electrical conductivity of copper and nickel manganites in relation with the simultaneous presence of Mn3+ and Mn4+ ions on octahedral sites of the spinel structure. Solid State Ion. 1992 Mar;51(1–2):7–9. doi:10.1016/0167-2738(92)90337-O
93. Huang K, Hou PY, Goodenough JB. Reduced area specific resistance for iron-based metallic interconnects by surface oxide coatings. Mater Res Bull. 2001 Jan;36(1–2):81–95. doi:10.1016/S0025-5408(01)00506-2
94. Petric A, Ling H. Electrical Conductivity and Thermal Expansion of Spinels at Elevated Temperatures. J Am Ceram Soc. 2007 May;90(5):1515–20. doi:10.1111/j.1551-2916.2007.01522.x
95. Navrotsky A, Kleppa OJ. The thermodynamics of cation distributions in simple spinels. J Inorg Nucl Chem. 1967 Nov;29(11):2701–14. doi:10.1016/0022-1902(67)80008-3
96. Goebel C, Fefekos AG, Svensson JE, Froitzheim J. Does the conductivity of interconnect coatings matter for solid oxide fuel cell applications? J Power Sources. 2018 Apr;383:110–4. doi:10.1016/j.jpowsour.2018.02.060
97. Hosseini SN, Karimzadeh F, Enayati MH, Sammes NM. Oxidation and electrical behavior of CuFe2O4 spinel coated Crofer 22 APU stainless steel for SOFC interconnect application. Solid State Ion. 2016 Jun 1;289:95–105. doi:10.1016/j.ssi.2016.02.015
98. Bi ZH, Zhu JH, Batey JL. CoFe2O4 spinel protection coating thermally converted from the electroplated Co–Fe alloy for solid oxide fuel cell interconnect application. J Power Sources. 2010 Jun 1;195(11):3605–11. doi:10.1016/j.jpowsour.2009.12.011
99. Reddy MJ, Goebel C, Valot A, Kiebach R, Svensson JE, Frandsen HL, et al. Comparison of Ce/Co and Ce/FeNi coatings for interconnects in solid oxide electrolysis. Int J Hydrog Energy. 2026 Jan 23;203:152996. doi:10.1016/j.ijhydene.2025.152996

100. Zhu JH, Chesson DA, Yu YT. Review—(Mn,Co)$_3$ O$_4$ -Based Spinels for SOFC Interconnect Coating Application. J Electrochem Soc. 2021 Nov 1;168(11):114519. doi:10.1149/1945-7111/ac3a29
101. Froitzheim J, Canovic S, Nikumaa M, Sachitanand R, Johansson LG, Svensson JE. Long term study of Cr evaporation and high temperature corrosion behaviour of Co coated ferritic steel for solid oxide fuel cell interconnects. J Power Sources. 2012 Dec;220:217–27. doi:10.1016/j.jpowsour.2012.06.092
102. Molin S, Sabato AG, Bindi M, Leone P, Cempura G, Salvo M, et al. Microstructural and electrical characterization of Mn-Co spinel protective coatings for solid oxide cell interconnects. J Eur Ceram Soc. 2017 Dec;37(15):4781–91. doi:10.1016/j.jeurceramsoc.2017.07.011
103. Wang B, Li K, Liu J, Zhang T, Yang T, Zhang N. Promoting electric conductivity of MnCo spinel coating by doping transition metals (Cu, Fe) or rare-earth elements (La, Y) for solid oxide fuel cell interconnect. Int J Hydrog Energy. 2024 Apr;61:216–25. doi:10.1016/j.ijhydene.2024.02.198
104. Yang Z, Xia G, Nie Z, Templeton J, Stevenson JW. Ce-Modified (Mn,Co)[sub 3]O[sub 4] Spinel Coatings on Ferritic Stainless Steels for SOFC Interconnect Applications. Electrochem Solid-State Lett. 2008;11(8):B140. doi:10.1149/1.2929066
105. Qiao WQ, Li YW, Zhang YS, Wang MH, Li K, Li ZJ, et al. Cu- and Ce-doped MnCo2O4 spinel coatings on ferrite interconnects by electrophoretic deposition. Mater Today Commun. 2024 Mar;38:108061. doi:10.1016/j.mtcomm.2024.108061
106. Kiefer T. Entwicklung neuer Schutz- und Kontaktierungsschichten für Hochtemperatur-Brennstoffzellen. Jülich; 2008. 138 p. (Schriften des Forschungszentrums Jülich Reihe Energie & Umwelt; Bd. 3).
107. Wolff M, Schwiers A, Wilkner K, Sebold D, Menzler NH. Wet powder spraying – A versatile and highly effective technique for the application of spinel-type protective coatings on SOC interconnects. J Power Sources. 2024 Feb;592:233931. doi:10.1016/j.jpowsour.2023.233931
108. Montero X, Tietz F, Sebold D, Buchkremer HP, Ringuede A, Cassir M, et al. MnCo1.9Fe0.1O4 spinel protection layer on commercial ferritic steels for interconnect applications in solid oxide fuel cells. J Power Sources. 2008 Sep;184(1):172–9. doi:10.1016/j.jpowsour.2008.05.081
109. Trebbels R, Markus T, Singheiser L. Reduction of Chromium Evaporation with Manganese-based Coatings. ECS Trans. 2009 Sep 25;25(2):1417–22. doi:10.1149/1.3205673
110. Blum L, Packbier U, Vinke IC, De Haart LGJ. Long-Term Testing of SOFC Stacks at Forschungszentrum Jülich. Fuel Cells. 2013 Aug;13(4):646–53. doi:10.1002/fuce.201200151
111. Blum L, de Haart LGJ, Malzbender J, Margaritis N, Menzler NH. Anode-Supported Solid Oxide Fuel Cell Achieves 70 000 Hours of Continuous Operation. Energy Technol. 2016 Aug;4(8):939–42. doi:10.1002/ente.201600114
112. Menzler NH, Sebold D, Guillon O. Post-test characterization of a solid oxide fuel cell stack operated for more than 30,000 hours: The cell. J Power Sources. 2018 Jan;374:69–76. doi:10.1016/j.jpowsour.2017.11.025

113. Tkaczyk AH, Bartl A, Amato A, Lapkovskis V, Petranikova M. Sustainability evaluation of essential critical raw materials: cobalt, niobium, tungsten and rare earth elements. J Phys Appl Phys. 2018 May 23;51(20):203001. doi:10.1088/1361-6463/aaba99
114. Lèbre É, Stringer M, Svobodova K, Owen JR, Kemp D, Côte C, et al. The social and environmental complexities of extracting energy transition metals. Nat Commun. 2020 Sep 24;11(1):4823. doi:10.1038/s41467-020-18661-9
115. Łazor M, Naumovich Y, Ajdys L, Yaremchenko A, Żurawska A, Wiecińska P. Functional properties of CuMn1.9Fe0.1O4-based coatings deposited on Crofer 22 APU steel exposed to selected pre-oxidation conditions. Int J Hydrog Energy. 2025 Apr;120:613–27. doi:10.1016/j.ijhydene.2025.03.242
116. Ignaczak J, Bik M, Jamroz J, Górnicka K, Drewniak A, Karczewski J, et al. Development and evaluation of interconnect protective coatings based on commercial Mn1.9CuFe0.1O4 spinel powder. J Eur Ceram Soc. 2025 Jul;45(7):117259. doi:10.1016/j.jeurceramsoc.2025.117259
117. Basu SN, Zhu Z, Mulligan JR, Pal UB, Gopalan S, Hussain AM, et al. Electrophoretically Deposited Protective Cu-Mn and Mn-Co Spinel Coatings for Solid Oxide Fuel Cell Interconnects. In: ECS Transactions, 111. Boston, USA; 2023. p. 2233–42.
118. Suo K, Zhu Z, Mulligan JR, Gopalan S, Pal UB, Hussain AM, et al. Processing and performance of protective Ni-doped Cu Mn spinel interconnect coatings. Int J Refract Met Hard Mater. 2025 Jan;126:106947. doi:10.1016/j.ijrmhm.2024.106947
119. Sun Z, Gopalan S, Pal UB, Basu SN. Electrophoretically Deposited Copper Manganese Spinel Coatings for Prevention of Chromium Poisoning in Solid Oxide Fuel Cells. In: Wang T, Chen X, Guillen DP, Zhang L, Sun Z, Wang C, et al., editors. Energy Technology 2019. Cham: Springer International Publishing; 2019. p. 265–72.
120. Zhu Z, Darl-Uzu C, Pal U, Gopalan S, Hussain AM, Dale N, et al. Comparison of Cu–Mn and Mn–Co spinel coatings for solid oxide fuel cell interconnects. Int J Hydrog Energy. 2022 Oct;47(87):36953–63. doi:10.1016/j.ijhydene.2022.08.239
121. Zhu Z, Sun Z, Gopalan S, Pal UB, Hussain AM, Dale N, et al. Effects of Ni-Doping in CuMn2O4 Spinel Coatings for Interconnects in Solid Oxide Fuel Cells. JOM. 2025 Feb 1;77(2):719–28. doi:10.1007/s11837-024-06900-z
122. Reddy MJ, Kamecki B, Talic B, Zanchi E, Smeacetto F, Hardy JS, et al. Experimental review of the performances of protective coatings for interconnects in solid oxide fuel cells. J Power Sources. 2023 Jun;568:232831. doi:10.1016/j.jpowsour.2023.232831
123. Jin Y, Sheng J, Hao G, Guo M, Hao W, Yang Z, et al. Highly dense (Mn,Co)3O4 spinel protective coating derived from Mn–Co metal precursors for SOFC interconnect applications. Int J Hydrog Energy. 2022 Apr;47(29):13960–8. doi:10.1016/j.ijhydene.2022.02.129
124. Lee SI, Hong J, Kim H, Son JW, Lee JH, Kim BK, et al. Highly Dense Mn-Co Spinel Coating for Protection of Metallic Interconnect of Solid Oxide Fuel Cells. J Electrochem Soc. 2014;161(14):F1389–94. doi:10.1149/2.0541414jes
125. Żurawska A, Naumovich Y, Ajdys L, Kosiorek M, Wierzbicki M, Skrzypkiewicz M, et al. Toward Cobalt-Free SOC Stacks: Comparative Study of (Mn,Cu,Fe)3O4 vs.

(Mn,Co)2O4 Spinels as Protective Coatings for SOFC Interconnects. Energies. 2025 Dec 19;19(1). doi:10.3390/en19010011

126. Vaßen R, Kaßner H, Stuke A, Hauler F, Hathiramani D, Stöver D. Advanced thermal spray technologies for applications in energy systems. Surf Coat Technol. 2008 Jun;202(18):4432–7. doi:10.1016/j.surfcoat.2008.04.022
127. Gannon P, Deibert M, White P, Smith R, Chen H, Priyantha W, et al. Advanced PVD protective coatings for SOFC interconnects. Int J Hydrog Energy. 2008 Jul;33(14):3991–4000. doi:10.1016/j.ijhydene.2007.12.009
128. Bernuy-Lopez C, Bexell U, Stenstrom M, Norrby N, Westlinder J. The Time for Industrialization Has Come: A Pre-Coated Solution for the GW Scale. ECS Trans. 2021 Jul 9;103(1):1803–8. doi:10.1149/10301.1803ecst
129. Norrby N, Li S, Stenström M, Westlinder J. The Effect of Nominal Ce Thickness on Ce/Co Coated AISI 441 Steel after >9 Years of Box Furnace Exposures at 800 °C. ECS Meet Abstr. 2025 Nov 24;MA2025-03(1):455. doi:10.1149/MA2025-031455mtgabs
130. Li S, Norrby N, Stenström M, Westlinder J. The Effect of Substrate Steel on Oxidation Behavior of Ce/Co-Coated SOFC Interconnects after Long-Term Furnace Exposures. ECS Meet Abstr. 2025 Nov 24;MA2025-03(1):473. doi:10.1149/MA2025-031473mtgabs
131. Grolig JG, Froitzheim J, Svensson JE. Coated stainless steel 441 as interconnect material for solid oxide fuel cells: Oxidation performance and chromium evaporation. J Power Sources. 2014 Feb;248:1007–13. doi:10.1016/j.jpowsour.2013.08.089
132. Canovic S, Froitzheim J, Sachitanand R, Nikumaa M, Halvarsson M, Johansson LG, et al. Oxidation of Co- and Ce-nanocoated FeCr steels: A microstructural investigation. Surf Coat Technol. 2013 Jan;215:62–74. doi:10.1016/j.surfcoat.2012.08.096
133. Reddy MJ, Svensson JE, Froitzheim J. Reevaluating the Cr Evaporation Characteristics of Ce/Co Coatings for Interconnect Applications. ECS Trans. 2021 Jul 9;103(1):1899–905. doi:10.1149/10301.1899ecst
134. Goebel C, Berger R, Bernuy-Lopez C, Westlinder J, Svensson JE, Froitzheim J. Long-term (4 year) degradation behavior of coated stainless steel 441 used for solid oxide fuel cell interconnect applications. J Power Sources. 2020 Feb;449:227480. doi:10.1016/j.jpowsour.2019.227480
135. Falk-Windisch H, Sattari M, Svensson JE, Froitzheim J. Chromium vaporization from mechanically deformed pre-coated interconnects in Solid Oxide Fuel Cells. J Power Sources. 2015 Nov;297:217–23. doi:10.1016/j.jpowsour.2015.07.085
136. Website Alleima [Internet]. 2026 [cited 2026 Mar 24]. Available from: https://www.alleima.com/en/products/coated-strip-steel/sanergy-ht/
137. Blum L, Fang Q, Groß-Barsnick SM, de Haart LGJ (Bert), Malzbender J, Menzler NH, et al. Long-term operation of solid oxide fuel cells and preliminary findings on accelerated testing. Int J Hydrog Energy. 2020 Mar;45(15):8955–64. doi:10.1016/j.ijhydene.2020.01.074
138. Fauchais PL, Heberlein JVR, Boulos MI. Thermal Spray Fundamentals: From Powder to Part [Internet]. Boston, MA: Springer US; 2014 [cited 2025 Apr 22]. Available from: https://link.springer.com/10.1007/978-0-387-68991-3 doi:10.1007/978-0-387-68991-3

139. Swain BK, Mohapatra SS, Pattanaik A, Samal SK, Bhuyan SK, Barik K, et al. Sensitivity of Process Parameters in Atmospheric Plasma Spray Coating. J Therm Spray Eng. 2018;1(1):1–6. doi:10.52687/2582-1474/111
140. Grünwald N. Selbstheilende plasmagespritzte Mn1,0Co1,9Fe0,1O4-Schutzschichten in Festoxidbrennstoffzellen. [Jülich]: Forschungszentrum, Zentralbibliothek; 2018. (Schriften des Forschungszentrums Jülich Reihe Energie & Umwelt; Bd. 422).
141. Liebermann MA, Lichtenberg AJ. Principles of Plasma Discharges and Materials Processing, 2nd Edition. MRS Bull. 2005 Nov;30(11):899–901. doi:10.1557/mrs2005.242
142. Fauchais P, Vardelle A. Thermal Sprayed Coatings Used Against Corrosion and Corrosive Wear. In: Jazi HS, editor. Advanced Plasma Spray Applications. Intech; 2012.
143. Fauchais P, Vardelle A, Dussoubs B. <I>Quo Vadis</I> Thermal Spraying? J Therm Spray Technol. 2001 Mar 1;10(1):44–66. doi:10.1361/105996301770349510
144. Mutter MG. Herstellung thermisch gespritzter Schichten mit optimierten Spannungseigenschaften. Jülich: Forschungszentrum Jülich GmbH, Zentralbibliothek, Verlag; 2016. 198 p. (Schriften des Forschungszentrums Jülich. Reihe Energie & Umwelt = Energy & Environment).
145. Vaßen R, Traeger F, Stöver D. Correlation Between Spraying Conditions and Microcrack Density and Their Influence on Thermal Cycling Life of Thermal Barrier Coatings. J Therm Spray Technol. 2004 Sep 1;13(3):396–404. doi:10.1361/10599630420443
146. Vaßen R, Hathiramani D, Mertens J, Haanappel VAC, Vinke IC. Manufacturing of high performance solid oxide fuel cells (SOFCs) with atmospheric plasma spraying (APS). Surf Coat Technol. 2007 Dec;202(3):499–508. doi:10.1016/j.surfcoat.2007.06.064
147. Vaßen R, Grünwald N, Marcano D, Menzler NH, Mücke R, Sebold D, et al. Aging of atmospherically plasma sprayed chromium evaporation barriers. Surf Coat Technol. 2016 Apr;291:115–22. doi:10.1016/j.surfcoat.2016.02.005
148. Grünwald N, Sebold D, Sohn YJ, Menzler NH, Vaßen R. Self-healing atmospheric plasma sprayed Mn1.0Co1.9Fe0.1O4 protective interconnector coatings for solid oxide fuel cells. J Power Sources. 2017 Sep;363:185–92. doi:10.1016/j.jpowsour.2017.07.072
149. Ruder A, Buchkremer HP, Jansen H, Malléner W, Stöver D. Wet powder spraying—a process for the production of coatings. Surf Coat Technol. 1992 Jul;53(1):71–4. doi:10.1016/0257-8972(92)90105-J
150. Zhao L, Bram M, Buchkremer H, Stover D, Li Z. Preparation of TiO composite microfiltration membranes by the wet powder spraying method. J Membr Sci. 2004 Nov 15;244(1–2):107–15. doi:10.1016/j.memsci.2004.07.010
151. Talic B, Falk-Windisch H, Venkatachalam V, Hendriksen PV, Wiik K, Lein HL. Effect of coating density on oxidation resistance and Cr vaporization from solid oxide fuel cell interconnects. J Power Sources. 2017 Jun;354:57–67. doi:10.1016/j.jpowsour.2017.04.023
152. Hong JE, Bianco M, Van Herle J, Steinberger-Wilckens R. Properties of Spinel Protective Coatings Prepared Using Wet Powder Spraying for SOFC Interconnects. ECS Trans. 2015 Jun 2;68(1):1581–7. doi:10.1149/06801.1581ecst

153. Falk-Windisch H, Claquesin J, Svensson JE, Froitzheim J. The Effect of Metallic Co-Coating Thickness on Ferritic Stainless Steels Intended for Use as Interconnect Material in Intermediate Temperature Solid Oxide Fuel Cells. Oxid Met. 2018 Feb;89(1–2):233–50. doi:10.1007/s11085-017-9782-9
154. Brinker CJ. Dip Coating. In: Schneller T, Waser R, Kosec M, Payne D, editors. Chemical Solution Deposition of Functional Oxide Thin Films [Internet]. Vienna: Springer; 2013 [cited 2026 Mar 24]. p. 233–61. Available from: https://doi.org/10.1007/978-3-211-99311-8_10 doi:10.1007/978-3-211-99311-8_10
155. Da Conceição L, Dessemond L, Djurado E, Souza MMVM. La0.7Sr0.3MnO3-coated SS444 alloy by dip-coating process for metallic interconnect supported Solid Oxide Fuel Cells. J Power Sources. 2013 Nov;241:159–67. doi:10.1016/j.jpowsour.2013.04.082
156. Fu QX, Sebold D, Tietz F, Buchkremer HP. Electrodeposited cobalt coating on Crofer22APU steels for interconnect applications in solid oxide fuel cells. Solid State Ion. 2011 Jun;192(1):376–82. doi:10.1016/j.ssi.2010.03.010
157. Wu J, Jiang Y, Johnson C, Liu X. DC electrodeposition of Mn–Co alloys on stainless steels for SOFC interconnect application. J Power Sources. 2008 Mar 1;177(2):376–85. doi:10.1016/j.jpowsour.2007.11.075
158. Wei W, Chen W, Ivey DG. Oxidation resistance and electrical properties of anodically electrodeposited Mn–Co oxide coatings for solid oxide fuel cell interconnect applications. J Power Sources. 2009 Jan 15;186(2):428–34. doi:10.1016/j.jpowsour.2008.09.114
159. Mao J, Wang E, Wang H, Ouyang M, Chen Y, Hu H, et al. Progress in metal corrosion mechanism and protective coating technology for interconnect and metal support of solid oxide cells. Renew Sustain Energy Rev. 2023 Oct;185:113597. doi:10.1016/j.rser.2023.113597
160. Corni I, Ryan MP, Boccaccini AR. Electrophoretic deposition: From traditional ceramics to nanotechnology. J Eur Ceram Soc. 2008 Jan;28(7):1353–67. doi:10.1016/j.jeurceramsoc.2007.12.011
161. Boccaccini AR, Dickerson JH. Electrophoretic Deposition: Fundamentals and Applications. J Phys Chem B. 2013 Feb 14;117(6):1501–1501. doi:10.1021/jp211212y
162. Besra L, Liu M. A review on fundamentals and applications of electrophoretic deposition (EPD). Prog Mater Sci. 2007 Jan;52(1):1–61. doi:10.1016/j.pmatsci.2006.07.001
163. Ferrari B, Moreno R. EPD kinetics: A review. J Eur Ceram Soc. 2010 Mar 1;3rd International Conference on Electrophoretic Deposition: Fundamentals and Applications30(5):1069–78. doi:10.1016/j.jeurceramsoc.2009.08.022
164. Boccaccini AR, Keim S, Ma R, Li Y, Zhitomirsky I. Electrophoretic deposition of biomaterials. J R Soc Interface. 2010 Oct 6;7(suppl_5). doi:10.1098/rsif.2010.0156.focus
165. Sarkar P, Nicholson PS. Electrophoretic Deposition (EPD): Mechanisms, Kinetics, and Application to Ceramics. J Am Ceram Soc. 1996;79(8):1987–2002. doi:10.1111/j.1151-2916.1996.tb08929.x
166. Williams PM. Zeta Potential. In: Encyclopedia of Membranes [Internet]. Springer, Berlin, Heidelberg; 2016 [cited 2025 Nov 11]. p. 2063–4. Available from:

https://link.springer.com/rwe/10.1007/978-3-662-44324-8_612 doi:10.1007/978-3-662-44324-8_612

167. Stern O. Zur Theorie der elektrolytischen Doppelschicht. Z Für Elektrochem Angew Phys Chem. 1924;(30):508–16.
168. Hunter RJ. Zeta potential in colloid science: principles and applications. London San Diego New York: Academic press; 1988. (Colloid science; no. 2).
169. Lyklema J. Water at Interfaces: A Colloid-Chemical Approach. In: Plenary and Invited Lectures [Internet]. Elsevier; 1977 [cited 2023 Mar 12]. p. 257–65. Available from: https://linkinghub.elsevier.com/retrieve/pii/B9780124045019500274 doi:10.1016/B978-0-12-404501-9.50027-4
170. Amrollahi P, Krasinski JS, Vaidyanathan R, Tayebi L, Vashaee D. Electrophoretic Deposition (EPD): Fundamentals and Applications from Nano- to Micro-Scale Structures. In: Aliofkhazraei M, Makhlouf ASH, editors. Handbook of Nanoelectrochemistry [Internet]. Cham: Springer International Publishing; 2015 [cited 2023 Mar 12]. p. 1–27. Available from: http://link.springer.com/10.1007/978-3-319-15207-3_7-1 doi:10.1007/978-3-319-15207-3_7-1
171. Hamaker HC. Formation of a deposit by electrophoresis. Trans Faraday Soc. 1940;35:279. doi:10.1039/tf9403500279
172. Anné G, Vanmeensel K, Vleugels J, Van Der Biest O. Influence of the suspension composition on the electric field and deposition rate during electrophoretic deposition. Colloids Surf Physicochem Eng Asp. 2004 Sep;245(1–3):35–9. doi:10.1016/j.colsurfa.2004.07.001
173. Ma J, Cheng W. Electrophoretic Deposition of Lead Zirconate Titanate Ceramics. J Am Ceram Soc. 2002;85(7):1735–7. doi:10.1111/j.1151-2916.2002.tb00344.x
174. Biesheuvel PM, Verweij H. Theory of Cast Formation in Electrophoretic Deposition. J Am Ceram Soc. 1999;82(6):1451–5. doi:10.1111/j.1151-2916.1999.tb01939.x
175. Farnoush H, Mohandesi JA, Fatmehsari DH. Effect of Particle Size on the Electrophoretic Deposition of Hydroxyapatite Coatings: A Kinetic Study Based on a Statistical Analysis. Int J Appl Ceram Technol. 2013;10(1):87–96. doi:10.1111/j.1744-7402.2012.02818.x
176. Laska A, Bartmański M. Parameters of the Electrophoretic Deposition Process and Its Influence on the Morphology of Hydroxyapatite Coatings. Review. Inż Mater. 2020 Apr 24;1(1):20–5. doi:10.15199/28.2020.1.3
177. Ajdys L, Zurawska A, Kosiorek M, Naumovich Y, Zybert M, Wiecinska P, et al. Improving functional properties of protective coatings obtained by electrophoretic deposition on steel interconnects for solid oxide cells by tuning particle size distribution. Ceram Int. 2023 Nov;49(21):33818–27. doi:10.1016/j.ceramint.2023.08.074
178. Chakrabarti BK, Gençten M, Bree G, Dao AH, Mandler D, Low CTJ. Modern practices in electrophoretic deposition to manufacture energy storage electrodes. Int J Energy Res. 2022;46(10):13205–50. doi:10.1002/er.8103
179. Schäfer M, Vogt L, Raether F, Kurth DG. Towards local deposition of particles by electrophoresis in dc electric fields in polar and nonpolar media and mixtures thereof. Ceram Int. 2020 Aug;46(11):17857–66. doi:10.1016/j.ceramint.2020.04.092

180. Smeacetto F, De Miranda A, Cabanas Polo S, Molin S, Boccaccini D, Salvo M, et al. Electrophoretic deposition of Mn1.5Co1.5O4 on metallic interconnect and interaction with glass-ceramic sealant for solid oxide fuel cells application. J Power Sources. 2015 Apr;280:379–86. doi:10.1016/j.jpowsour.2015.01.120
181. Molin S, Sabato AG, Javed H, Cempura G, Boccaccini AR, Smeacetto F. Co-deposition of CuO and Mn1.5Co1.5O4 powders on Crofer22APU by electrophoretic method: Structural, compositional modifications and corrosion properties. Mater Lett. 2018 May;218:329–33. doi:10.1016/j.matlet.2018.02.037
182. Sabato AG, Molin S, Javed H, Zanchi E, Boccaccini AR, Smeacetto F. In-situ Cu-doped MnCo-spinel coatings for solid oxide cell interconnects processed by electrophoretic deposition. Ceram Int. 2019 Oct;45(15):19148–57. doi:10.1016/j.ceramint.2019.06.161
183. Ishihara T, Sato K, Takita Y. Electrophoretic Deposition of Y2O3-Stabilized ZrO2 Electrolyte Films in Solid Oxide Fuel Cells. J Am Ceram Soc. 1996;79(4):913–9. doi:10.1111/j.1151-2916.1996.tb08525.x
184. Mathews T, Rabu N, Sellar JR, Muddle BC. Fabrication of La1−xSrxGa1−yMgyO3−(x+y)/2 thin films by electrophoretic deposition and its conductivity measurement. Solid State Ion. 2000 Feb 1;128(1):111–5. doi:10.1016/S0167-2738(99)00308-2
185. Lalau CC, Low CTJ. Electrophoretic Deposition for Lithium-Ion Battery Electrode Manufacture. Batter Supercaps. 2019 Jun;2(6):551–9. doi:10.1002/batt.201900017
186. Yilmaz E, Xiao P. Effects of suspension properties on the fabrication of Yb2Si2O7 coatings using electrophoretic deposition. J Eur Ceram Soc. 2022 Feb;42(2):638–48. doi:10.1016/j.jeurceramsoc.2021.10.038
187. Sakka Y, Uchikoshi T. Forming and Microstructure Control of Ceramics by Electrophoretic Deposition (EPD). KONA Powder Part J. 2010;28(0):74–90. doi:10.14356/kona.2010009
188. Sarkar P, De D, Rho H. Synthesis and microstructural manipulation of ceramics by electrophoretic deposition. J Mater Sci. 2004 Feb 1;39(3):819–23. doi:10.1023/B:JMSC.0000012909.46419.0e
189. Wang YC, Leu IC, Hon MH. Kinetics of Electrophoretic Deposition for Nanocrystalline Zinc Oxide Coatings. J Am Ceram Soc. 2004;87(1):84–8. doi:10.1111/j.1551-2916.2004.00084.x
190. Besra L, Uchikoshi T, Suzuki TS, Sakka Y. Bubble-Free Aqueous Electrophoretic Deposition (EPD) by Pulse-Potential Application. J Am Ceram Soc. 2008;91(10):3154–9. doi:10.1111/j.1551-2916.2008.02591.x
191. Besra L, Uchikoshi T, Suzuki TS, Sakka Y. Application of constant current pulse to suppress bubble incorporation and control deposit morphology during aqueous electrophoretic deposition (EPD). J Eur Ceram Soc. 2009 Jul;29(10):1837–45. doi:10.1016/j.jeurceramsoc.2008.07.031
192. Zhu Z, Pal U, Gopalan S, Hussain AM, Dong S, Dale N, et al. Alternating-Current Electrophoretic Deposition of Spinel Coatings on Porous Metallic Substrates for Solid Oxide Fuel Cell Applications. JOM. 2021 Sep 1;73(9):2764–70. doi:10.1007/s11837-021-04763-2

193. Sun Z, Gopalan S, Pal UB, Basu SN. Cu1.3Mn1.7O4 spinel coatings deposited by electrophoretic deposition on Crofer 22 APU substrates for solid oxide fuel cell applications. Surf Coat Technol. 2017 Aug;323:49–57. doi:10.1016/j.surfcoat.2016.09.028
194. Ishihara T, Sato K, Mizuhara Y, Takita Y. Preparation of Yttria-Stabilized Zirconia Films for Solid Oxide Fuel Cells by Electrophoretic Deposition Method. Chem Lett. 1992 Jun 1;21(6):943–6. doi:10.1246/cl.1992.943
195. Ishihara T. Electrophoretic Deposition of Stabilized Zirconia For Solid Oxide Fuel Cells. ECS Proc Vol. 1993 Jan;1993–4(1):65–73. doi:10.1149/199304.0065PV
196. Zhitomirsky I, Petric A. Electrolytic and electrophoretic deposition of CeO2 films. Mater Lett. 1999 Sep;40(6):263–8. doi:10.1016/S0167-577X(99)00087-7
197. Zhitomirsky I, Petric A. Electrophoretic and electrolytic deposition of oxide films. In: Oxide Films: Proceedings of the International Symposium. The Electrochemical Society; 2000. p. 403–11.
198. Zhang Y, Javed A, Zhou M, Liang S, Xiao P. Fabrication of Mn–Co Spinel Coatings on Crofer 22 APU Stainless Steel by Electrophoretic Deposition for Interconnect Applications in Solid Oxide Fuel Cells. Int J Appl Ceram Technol. 2014;11(2):332–41. doi:10.1111/ijac.12013
199. Wang R, Sun Z, Choi JP, Basu SN, Stevenson JW, Tucker MC. Ferritic stainless steel interconnects for protonic ceramic electrochemical cell stacks: Oxidation behavior and protective coatings. Int J Hydrog Energy. 2019 Oct 4;44(47):25297–309. doi:10.1016/j.ijhydene.2019.08.041
200. Talic B, Venkatachalam V, Hendriksen PV, Kiebach R. Comparison of MnCo2O4 coated Crofer 22 H, 441, 430 as interconnects for intermediate-temperature solid oxide fuel cell stacks. J Alloys Compd. 2020 Apr;821:153229. doi:10.1016/j.jallcom.2019.153229
201. Bednarz M, Molin S, Bobruk M, Stygar M, Długoń E, Sitarz M, et al. High-temperature oxidation of the Crofer 22 H ferritic steel with Mn1.45Co1.45Fe0.1O4 and Mn1.5Co1.5O4 spinel coatings under thermal cycling conditions and its properties. Mater Chem Phys. 2019 Mar 1;225:227–38. doi:10.1016/j.matchemphys.2018.12.090
202. Wang R, Sun Z, Pal UB, Gopalan S, Basu SN. Mitigation of chromium poisoning of cathodes in solid oxide fuel cells employing CuMn1.8O4 spinel coating on metallic interconnect. J Power Sources. 2018 Feb;376:100–10. doi:10.1016/j.jpowsour.2017.11.069
203. Aznam I, Mah JCW, Muchtar A, Somalu MR, Ghazali MJ. Electrophoretic deposition of (Cu,Mn,Co)3O4 spinel coating on SUS430 ferritic stainless steel: Process and performance evaluation for solid oxide fuel cell interconnect applications. J Eur Ceram Soc. 2021 Feb;41(2):1360–73. doi:10.1016/j.jeurceramsoc.2020.09.074
204. Ekhlasiosgouei O, Bik M, Smeacetto F, Jasinski P, Molin S. Electrophoretic deposition of novel hybrid MnCo2O4: Mn1·7CuFe0·3O4 spinel protective coating on stainless-steel metallic interconnects for SOFCs application. Int J Hydrog Energy. 2025 Aug 14;158:150569. doi:10.1016/j.ijhydene.2025.150569

205. Yoo Y. The Effect of Protective Layers Formed by Electrophoretic Deposition on Oxidation and Performance of Metallic Interconnects. ECS Proc Vol. 2001 Jan;2001–16(1):837–46. doi:10.1149/200116.0837PV
206. Yang Z, Xia GG, Maupin GD, Stevenson JW. Evaluation of Perovskite Overlay Coatings on Ferritic Stainless Steels for SOFC Interconnect Applications. J Electrochem Soc. 2006 Aug 2;153(10):A1852. doi:10.1149/1.2239371
207. Mazur Ł, Domaradzki K, Winiarski P, Zych Ł, Brylewski T. Optimization of electrophoretic deposition and thermal treatment of Cu–Mn spinel matrix for spinel/perovskite composite coating used as SOC metallic interconnect. Ceram Int. 2024 Sep;50(18):34017–26. doi:10.1016/j.ceramint.2024.06.221
208. Zanchi E, Sabato AG, Molin S, Cempura G, Boccaccini AR, Smeacetto F. Recent advances on spinel-based protective coatings for solid oxide cell metallic interconnects produced by electrophoretic deposition. Mater Lett. 2021 Mar;286:129229. doi:10.1016/j.matlet.2020.129229
209. Huang W, Gopalan S, Pal UB, Basu S. Evaluation of Electrophoretically Deposited CuMn1.8O4 Spinel Coatings On Metallic Interconnects for SOFC Applications. ECS Trans. 2008 Dec 18;13(26):405–11. doi:10.1149/1.3050411
210. Zhang Y, Zhang Y, Wu C, Yang Y, Li Q, Chen Y. Oxidation behavior and electrical properties of metal interconnects with Ce-doped Ni–Mn spinel coatings. Ceram Int. 2022 Apr;48(7):9550–7. doi:10.1016/j.ceramint.2021.12.153
211. Irankhah R, Raissi B, Maghsoudipour A, Irankhah A, Ghashghai S. NiFe2O4 Spinel Protection Coating for High-Temperature Solid Oxide Fuel Cell Interconnect Application. J Mater Eng Perform. 2016 Apr 1;25(4):1515–25. doi:10.1007/s11665-016-1949-z
212. Zanchi E, Molin S, Sabato AG, Talic B, Cempura G, Boccaccini AR, et al. Iron doped manganese cobaltite spinel coatings produced by electrophoretic co-deposition on interconnects for solid oxide cells: Microstructural and electrical characterization. J Power Sources. 2020 Apr;455:227910. doi:10.1016/j.jpowsour.2020.227910
213. He C, Lu Y, Liu Y, Wang M, Jiang Z, Yang W. Preparation and properties of Co3O4–MnCo2O4 double-layered composite spinel coatings. Int J Hydrog Energy. 2025 Oct;177:151597. doi:10.1016/j.ijhydene.2025.151597
214. Dang THT, Lee IT, Kim J, Vo VK, Kim S, Lim HJ, et al. Enhanced protection of SOFC interconnects with dual coating using combined electrophoretic and sputtering methods. Int J Hydrog Energy. 2025 Apr;122:150–8. doi:10.1016/j.ijhydene.2025.03.366
215. Brylewski T, Molin S, Marczyński M, Mazur Ł, Domaradzki K, Kryshtal O, et al. Influence of Gd deposition on the oxidation behavior and electrical properties of a layered system consisting of Crofer 22 APU and MnCo2O4 spinel. Int J Hydrog Energy. 2021 Feb 3;46(9):6775–91. doi:10.1016/j.ijhydene.2020.11.169
216. Mirzaei M, Simchi A, Faghihi-Sani MA, Yazdanyar A. Electrophoretic deposition and sintering of a nanostructured manganese–cobalt spinel coating for solid oxide fuel cell interconnects. Ceram Int. 2016 May;42(6):6648–56. doi:10.1016/j.ceramint.2016.01.012

217. Bobruk M, Molin S, Chen M, Brylewski T, Hendriksen PV. Sintering of MnCo2O4 coatings prepared by electrophoretic deposition. Mater Lett. 2018 Feb 15;213:394–8. doi:10.1016/j.matlet.2017.12.046
218. Mikkola J, Couturier K, Talic B, Frangini S, Giacometti N, Pelissier N, et al. Protective Coatings for Ferritic Stainless Steel Interconnect Materials in High Temperature Solid Oxide Electrolyser Atmospheres. Energies. 2022 Feb 5;15(3):1168. doi:10.3390/en15031168
219. Sun Z, Wang R, Nikiforov AY, Gopalan S, Pal UB, Basu SN. CuMn1.8O4 protective coatings on metallic interconnects for prevention of Cr-poisoning in solid oxide fuel cells. J Power Sources. 2018 Feb;378:125–33. doi:10.1016/j.jpowsour.2017.12.031
220. Bidabadi MHS, Siripongsakul T, Thublaor T, Wiman P, Chandra-ambhorn S. Oxidation and Cr-evaporation behavior of MnCo based spinel and composite coated AISI 430 steel. Surf Coat Technol. 2022 Mar;434:128176. doi:10.1016/j.surfcoat.2022.128176
221. Zanchi E, Talic B, Sabato AG, Molin S, Boccaccini AR, Smeacetto F. Electrophoretic co-deposition of Fe2O3 and Mn1,5Co1,5O4: Processing and oxidation performance of Fe-doped Mn-Co coatings for solid oxide cell interconnects. J Eur Ceram Soc. 2019 Oct 1;39(13):3768–77. doi:10.1016/j.jeurceramsoc.2019.05.024
222. Zanchi E, Ignaczak J, Molin S, Cempura G, Boccaccini AR, Smeacetto F. Electrophoretic co-deposition of Mn1.5Co1.5O4, Fe2O3 and CuO: Unravelling the effect of simultaneous addition of Cu and Fe on the microstructural, thermo-mechanical and corrosion properties of in-situ modified spinel coatings for solid oxide cell interconnects. J Eur Ceram Soc. 2022 Jul 1;42(7):3271–81. doi:10.1016/j.jeurceramsoc.2022.02.008
223. Zanchi E, Sabato AG, Monterde MC, Bernadet L, Torrell M, Calero JA, et al. Electrophoretic deposition of MnCo2O4 coating on solid oxide cell interconnects manufactured through powder metallurgy. Mater Des. 2023 Mar;227:111768. doi:10.1016/j.matdes.2023.111768
224. Sabato AG, Zanchi E, Molin S, Cempura G, Javed H, Herbrig K, et al. Mn-Co spinel coatings on Crofer 22 APU by electrophoretic deposition: Up scaling, performance in SOFC stack at 850 °C and compositional modifications. J Eur Ceram Soc. 2021 Jul;41(8):4496–504. doi:10.1016/j.jeurceramsoc.2021.03.030
225. IEA Greenhouse Gas R&D Programme, Element Energy, E4tech. Analysis of Electrolytic Hydrogen Technologies with a Comparative Perspective on Low-Carbon (CCS-Abated) Hydrogen Pathways [Internet]. IEAGHG; 2024 Dec [cited 2026 Feb 11]. Available from: https://ieaghg.org/publications/analysis-of-electrolytic-hydrogen-technologies-with-a-comparative-perspective-on-low-carbon-ccs-abatedhydrogen-pathways/ doi:10.62849/2024-08
226. Salim KMA, Maelah R, Hishamuddin H, Amir AM, Ab Rahman MN. Two Decades of Life Cycle Sustainability Assessment of Solid Oxide Fuel Cells (SOFCs): A Review. Sustainability. 2022 Jan;14(19):12380. doi:10.3390/su141912380
227. Sarner S, Schreiber A, Menzler NH, Guillon O. Recycling Strategies for Solid Oxide Cells. Adv Energy Mater. 2022 Sep;12(35):2201805. doi:10.1002/aenm.202201805

228. Kaiser C, Buchwald T, Peuker UA. Ultrasonic decoating as a new recycling path to separate oxygen side layers of solid oxide cells. Green Chem. 2024;26(2):960–7. doi:10.1039/D3GC03189F
229. Sarner S, Menzler NH, Malzbender J, Hilger M, Sebold D, Weber A, et al. Towards a scalable recycling process for ceramics in fuel-electrode-supported solid oxide cells. Green Chem. 2025;27(8):2252–62. doi:10.1039/D4GC05883F
230. Yenesew GT, Quarez E, Le Gal La Salle A, Nicollet C, Joubert O. Recycling and characterization of end-of-life solid oxide fuel/electrolyzer ceramic material cell components. Resour Conserv Recycl. 2023 Mar;190:106809. doi:10.1016/j.resconrec.2022.106809
231. Saffirio S, Pylypko S, Fiorot S, Schiavi I, Fiore S, Santarelli M, et al. Hydrothermally-assisted recovery of Yttria- stabilized zirconia (YSZ) from end-of-life solid oxide cells. Sustain Mater Technol. 2022 Sep;33:e00473. doi:10.1016/j.susmat.2022.e00473
232. Al Assadi A, Goes D, Baazouzi S, Staudacher M, Malczyk P, Kraus W, et al. Challenges and prospects of automated disassembly of fuel cells for a circular economy. Resour Conserv Recycl Adv. 2023 Nov;19:200172. doi:10.1016/j.rcradv.2023.200172
233. Kaiser C, Ahn S, Brünner M, Goes D, Lastam J, Mongoljiibuu SO, et al. Recycling of Solid Oxide Electrolyzer Stacks [Internet]. SSRN; 2025 [cited 2025 Nov 30]. Available from: https://www.ssrn.com/abstract=5119643 doi:10.2139/ssrn.5119643
234. Lastam J, Sergeev D, Grüner D, Müller M, Schwaiger R. Unlocking the Value of End-of-Life JÜLICH Solid Oxide Cell Stack Interconnect Assembly: A Combined Experimental and Thermodynamic Study on Metallic Resource Recyclability. Metals. 2024 Apr;14(4):406. doi:10.3390/met14040406
235. Lastam J, Mongoljiibuu SO, Specht A, Grüner D, Sergeev D, Peuker UA, et al. Recycling End-of-Life Solid Oxide Cell Interconnect Assemblies into Commercial-Grade AISI 304 Stainless Steels. Steel Res Int. n/a(n/a):2500384. doi:10.1002/srin.202500384
236. Pihkola H, Isasa M, Bachmann TM, van der Kamp J, Zanchi L, Zamagni A, et al. ORIENTING 2024 (D2.9) LCSA Handbook. 2024. (EU Horizon 2020 project ORIENTING (GA No 958231)).
237. Curran MA. Life Cycle Assessment: a review of the methodology and its application to sustainability. Curr Opin Chem Eng. 2013 Aug;2(3):273–7. doi:10.1016/j.coche.2013.02.002
238. ISO. Environmental Management — Life Cycle Assessment — Requirements and Guidelines [Internet]. Geneva, Switzerland; [cited 2025 Dec 10]. Available from: https://www.iso.org/standard/38498.html
239. Sachitanand R, Sattari M, Svensson JE, Froitzheim J. Evaluation of the oxidation and Cr evaporation properties of selected FeCr alloys used as SOFC interconnects. Int J Hydrog Energy. 2013 Nov;38(35):15328–34. doi:10.1016/j.ijhydene.2013.09.044
240. Kuhn B, Jimenez CA, Niewolak L, Hüttel T, Beck T, Hattendorf H, et al. Effect of Laves phase strengthening on the mechanical properties of high Cr ferritic steels for solid oxide fuel cell interconnect application. Mater Sci Eng A. 2011 Jul;528(18):5888–99. doi:10.1016/j.msea.2011.03.112

241. Vakhrameev D. Mechanistic studies and modelling of degradation of ferric stainless steel during application in solid oxide electrolyser cells [in preparation]. [Aachen]: RWTH Aachen University; 2026.
242. VDM Metals. Crofer22APU Data sheet [Internet]. 2022 [cited 2025 Apr 13]. Available from: https://www.vdm-metals.com/fileadmin/user_upload/Downloads/Data_Sheets/Data_Sheet_VDM_Crofer_22_APU.pdf
243. VDM Metals. Crofer22H Data sheet [Internet]. 2021 [cited 2025 Apr 13]. Available from: https://www.vdm-metals.com/fileadmin/user_upload/Downloads/Data_Sheets/Data_Sheet_VDM_Crofer_22_H.pdf
244. Thyssenkrupp Materials (UK). AISI430 Data Sheet [Internet]. 2017 [cited 2026 Mar 25]. Available from: https://www.thyssenkrupp-materials.co.uk/stainless-steel-430-14016.html
245. Vargas MJG, Zahid M, Tietz F, Aslanides A. Use of SOFC Metallic Interconnect Coated with Spinel Protective Layers using the APS Technology. ECS Trans. 2007 May 25;7(1):2399–405. doi:10.1149/1.2729362
246. Steinberger-Wilckens R, Blum L, Buchkremer HP, De Haart LGJ, Pap M, Steinbrech RW, et al. Recent Results in Solid Oxide Fuel Cell Development at Forschungszentrum Juelich. ECS Trans. 2009 Sep 25;25(2):213–20. doi:10.1149/1.3205528
247. Blum L, Batfalsky P, Fang Q, De Haart LGJ, Malzbender J, Margaritis N, et al. SOFC Stack and System Development at Forschungszentrum Jülich. J Electrochem Soc. 2015;162(10):F1199–205. doi:10.1149/2.0491510jes
248. Dusoulier L, Cloots R, Vertruyen B, Moreno R, Burgos-Montes O, Ferrari B. YBa2Cu3O7−x dispersion in iodine acetone for electrophoretic deposition: Surface charging mechanism in a halogenated organic media. J Eur Ceram Soc. 2011 Jun;31(6):1075–86. doi:10.1016/j.jeurceramsoc.2011.01.008
249. Fakouri Hasanabadi M, Kokabi AH, Faghihi-Sani MA, Groß-Barsnick SM, Malzbender J. Room- and high-temperature torsional shear strength of solid oxide fuel/electrolysis cell sealing material. Ceram Int. 2019 Feb;45(2):2219–25. doi:10.1016/j.ceramint.2018.10.134
250. Zanchi E, Ignaczak J, Kamecki B, Jasiński P, Molin S, Boccaccini AR, et al. Manganese–Cobalt Based Spinel Coatings Processed by Electrophoretic Deposition Method: The Influence of Sintering on Degradation Issues of Solid Oxide Cell Oxygen Electrodes at 750 °C. Materials. 2021 Jul 9;14(14):3836. doi:10.3390/ma14143836
251. Tu H, Stimming U. Advances, aging mechanisms and lifetime in solid-oxide fuel cells. J Power Sources. 2004 Mar 10;Eighth Ulmer Electrochemische Tage127(1):284–93. doi:10.1016/j.jpowsour.2003.09.025
252. Merkus HG. Particle Size Measurements: Fundamentals, Practice, Quality. Springer Science & Business Media; 2009. 535 p.
253. Brunauer S, Emmett PH, Teller E. Adsorption of gases in multimolecular layers. J Am Chem Soc. 1938;60(2):309–19.

254. Ambroz F, Macdonald TJ, Martis V, Parkin IP. Evaluation of the BET Theory for the Characterization of Meso and Microporous MOFs. Small Methods. 2018;2(11):1800173. doi:10.1002/smtd.201800173
255. Hovis D b., Heuer A h. The use of laser scanning confocal microscopy (LSCM) in materials science. J Microsc. 2010;240(3):173–80. doi:10.1111/j.1365-2818.2010.03399.x
256. Egerton RF. Physical Principles of Electron Microscopy. Cham: Springer International Publishing; 2016. doi:10.1007/978-3-319-39877-8
257. Rein H. Scanning electron microscopy. DAZ. 2010 Sep 9;150:50–6.
258. Pandey A, Dalal S, Dutta S, Dixit A. Structural characterization of polycrystalline thin films by X-ray diffraction techniques. J Mater Sci Mater Electron. 2021 Jan 1;32(2):1341–68. doi:10.1007/s10854-020-04998-w
259. Grolig JG, Froitzheim J, Svensson JE. Coated stainless steel 441 as interconnect material for solid oxide fuel cells: Evolution of electrical properties. J Power Sources. 2015 Jun 15;284:321–7. doi:10.1016/j.jpowsour.2015.03.029
260. Froitzheim J, Ravash H, Larsson E, Johansson LG, Svensson JE. Investigation of Chromium Volatilization from FeCr Interconnects by a Denuder Technique. J Electrochem Soc. 2010;157(9):B1295. doi:10.1149/1.3462987
261. El Jardali K, Feyzi V, Iribarren D, Dufour J. Sustainability characterisation of the electrode and interconnect concepts based on advanced coating technologies. NOUVEAU project; 2024.
262. Scataglini R, Wei M, Mayyas A, Chan SH, Lipman T, Santarelli M. A Direct Manufacturing Cost Model for Solid-Oxide Fuel Cell Stacks. Fuel Cells. 2017 Dec;17(6):825–42. doi:10.1002/fuce.201700012
263. Wernet G, Bauer C, Steubing B, Reinhard J, Moreno-Ruiz E, Weidema B. The ecoinvent database version 3 (part I): overview and methodology. Int J Life Cycle Assess. 2016 Sep;21(9):1218–30. doi:10.1007/s11367-016-1087-8
264. European Commission. Joint Research Centre. Updated characterisation and normalisation factors for the environmental footprint 3.1 method. [Internet]. LU: Publications Office; 2023 [cited 2025 Apr 26]. Available from: https://data.europa.eu/doi/10.2760/798894
265. Molin S, Sabato AG, Javed H, Cempura G, Boccaccini AR, Smeacetto F. Co-deposition of CuO and Mn1.5Co1.5O4 powders on Crofer22APU by electrophoretic method: Structural, compositional modifications and corrosion properties. Mater Lett. 2018 May 1;218:329–33. doi:10.1016/j.matlet.2018.02.037
266. Masi A, Bellusci M, McPhail SJ, Padella F, Reale P, Hong JE, et al. The effect of chemical composition on high temperature behaviour of Fe and Cu doped Mn-Co spinels. Ceram Int. 2017 Feb;43(2):2829–35. doi:10.1016/j.ceramint.2016.11.135
267. Wang B, Li K, Liu J, Zhang T, Yang T, Zhang N. Promoting electric conductivity of MnCo spinel coating by doping transition metals (Cu, Fe) or rare-earth elements (La, Y) for solid oxide fuel cell interconnect. Int J Hydrog Energy. 2024 Apr;61:216–25. doi:10.1016/j.ijhydene.2024.02.198

268. Suo K, Zhu Z, Mulligan JR, Gopalan S, Pal UB, Hussain AM, et al. Processing and performance of protective Ni-doped Cu Mn spinel interconnect coatings. Int J Refract Met Hard Mater. 2025 Jan;126:106947. doi:10.1016/j.ijrmhm.2024.106947
269. Ebrahimifar H, Zandrahimi M. Oxidation and electrical behavior of AISI 430 coated with cobalt spinels for SOFC interconnect applications. Surf Coat Technol. 2011 Oct;206(1):75–81. doi:10.1016/j.surfcoat.2011.06.046
270. Talic B, Wulff AC, Molin S, Andersen KB, Zielke P, Frandsen HL. Investigation of electrophoretic deposition as a method for coating complex shaped steel parts in solid oxide cell stacks. Surf Coat Technol. 2019 Dec;380:125093. doi:10.1016/j.surfcoat.2019.125093
271. Siviji M. Electrophoretic Deposition of Protective Coatings for Solid Oxide Cell Interconnects: Optimization of Organic Suspension Media [unpublished Master thesis]. Aachen: RWTH Aachen University; 2026.

Acknowledgements

My time at Forschungszentrum Jülich was accompanied by numerous people, substantially contributing to the pathway and success of this work. Here, I would like to express my wholehearted thanks for the various facets of support I could receive.

A grateful thank is directed to Prof. Norbert H. Menzler, Dr. Christian Lenser, Prof. Olivier Guillon, Prof. Wilhelm A. Meulenberg and Prof. Martin Bram for the given trust in offering me the chance to extend my stay at IMD-2 from my previous research projects by this dissertation and even a moment beyond. I sincerely thank Prof. Joachim Mayer for taking over as second examiner and all related efforts for this dissertation.

A very special thank goes to my doctoral advisor Prof. Norbert H. Menzler, for integrating me ongoingly in the Solid Oxide Cells department after my MSc thesis, and accompanying and supporting me in my early years in science. Especially, the open-door policy and the given degrees of freedom in organizing my research is highly appreciated and not taken for granted. Also, I am deeply grateful for my day-to-day-supervisor Dr. Christian Lenser, who in all the creative flexibility in my work always knew to set the right accents and strategically adjust the work. Thank you for all the fruitful input, the encouraging words again and again, and lending hands, even when it has been densely packed for you as well.

Though, to make this work to what it became, more support was required, which should not be forgotten here – within the IMD-2 and beyond.

At first, I would like to thank Irmgard Mingers, Vicky Tirtey, Yvonne Lichtenfeld and Stefan Weitz for their administrative support, especially when it got short-term occasionally, enabling full focus on the research. Also, I appreciate various support of technical and scientific nature. Thus, my thank is directed to Andrea Hilgers and Sigrid Schwartz-Lückge for the powder characterization, and Volker Bader not only for operating the sintering furnaces, but also for the ongoing exchange and hands-on support all round creating the EPD setup. In terms of coating deposition, I also gratefully thank Jan-Philipp Treitz, beyond different assisting activities, as in cell manufacturing, for the support with the WPS coatings. Here, my thank further goes to Dr. Alexander Schwiers for the rather short but sweet episode. I want to extend my thanks to Dr. Michael Wolff for the discussions when I joined the world of protective coatings and Dr. Tim Van Gestel for the regular exchange on progress and possibilities. I am gratefully thankful for the support of our in-house workshop team, especially Carsten Gebhart, Jesse Müller and Erhan Sucuoglu, enabling to scale the developed EPD coatings to real component size, due to their straightforward and creative contributions. Moreover, I thank Prof. Robert Vaßen, Frank Kurze and Karl-Heinz Rauwald for providing the APS-reference-coatings and process data, as well as all related efforts and discussions. In terms of characterization, a special thank goes to Michael Xhonneux for the proactive and tireless support in the metallographic preparation, Dr. Yoo Jung Sohn for the help all around XRD analysis, as well as Dr. Doris

Sebold and Dr. Christian Dellen for SEM imaging and related discussions. My thank extends to Mukund Siviji for the contributions within his MSc thesis.

But beyond all the professional support, I could receive and everything I learned within this, it where the great people behind that made the time such special for me. Back in the days, starting off together in Cosy, Dr. Denise Ramler always was a step ahead and an important fixed point for me. Amazing that we could go this track together! Arrived in office 111, it still felt very cosy. Here, a special thank goes to Dr. Tim Sievert, Eugen Susakin and Oskar Höwer for the fidele-phantastic time. More in general, I always gratefully acknowledged the supportive atmosphere, created by the community of PhD students, as via sharing experience, assistance in the lab, and discussions of scientific or even more non-scientific character at lunch. Here, a unique thank is directed to Dr. Stephan Sarner. From the supervisor of my MSc thesis, you not only became a colleague, but even an irreplaceable friend. Thank you for the unforgettable years in Jülich, Cologne and wherever we ended up. Thank you for the numerous rides, the shared love for slow music, and the certainty to have your support, whenever needed!

On campus, I also received support from outside of IMD-2. My thanks go to Daniil Vakhrameev and Dr. Dmitry Naumenko at IMD-1 for the fruitful collaboration within the project NOUVEAU. At ITE, I especially thank Dr. Sonja Groß-Barsnick, Dirk Federmann and Wilhelm A. Mertens for the inspired exchange on stack level, all about the glass sealants and the nice drawings. Also, I acknowledge the support from Ute de Haart at IET-1 for the stack run and the belief in the EPD coatings.

Though, support from outside of Jülich was essential for this work and taught me a lot. Here, thank is directed to Prof. Federico Smeacetto, and especially Francesco Gallo und Francesco Da Prato at POLITO for the insightful episodes in Jülich and Turin and our emerging friendship. At IMDEA Energy, my thank goes to Khaled El Jardali, Dr. Vafa Feyzi and Dr. Diego Iribarren for the meaningful collaboration within the LCA study. I want to thank Thorbjørn Krogsgaard, Dr. S. Shrikanth and Prof. Jan Froitzheim at Chalmers University of Technology for productive collaboration and the possibility for my stay in Gothenburg.

Finally, my biggest thank you goes to the probably most important group with my social environment. A special thank is directed to my closest friends, partially accompanying me since early school days and where always a reliable anchor to me. Thank you for repeatedly checking up, motivating me, and taking me into account, in phases where it felt more difficult for myself. This gratitude extends to my WG, Sarah and Valle. With our final theses that wanted to be prepared in parallel and more exhausting passages involved, these were certainly not the easiest days. And some have had even more hurdles thrown in the path. But in the end, even the last piece of work was meant to find a happy conclusion, and the chapter at Liebigstraße was a shaping one and your support was indispensable. Thank you for this memorable episode! A very special thank is addressed to those, who enabled not

only this thesis, but all my educational path before – my family. A major thank goes to my parents, Angela and Lothar. Thank you for setting the ground for me, to become the person, I am today, and for paving the way for me, where needed. Thank you for staying persistent, even as I asked for withdrawing me from primary school after week 1. The thank extends to my grandparents whose support and belief in me felt always so secure, and to my older siblings, Nadja and Daniel, whose steps I could always follow and who knew to reinforce or even slow me down, where necessary.

Lastly, an indispensable thank goes to you, Lotta. Along the journey of this work, also the journey of us evolved and with all the given support and your perspective on the things, you became an irreplaceable pillar in my life. The journey of this work might find an end here, but ours will certainly have some lovely surprises in store!

Abbreviations

3/8YSZ	3/8 mol% yttrium-stabilized zirconium oxide
ASR	Area-specific resistance
APS	Atmospheric plasma spraying
BET	Brunauer-Emmet-Teller
BoP	Balance-of-Plant
BSE	Backscatter electron
CMF	$CuMn_{1.9}Fe_{0.1}O_4$
CMN	$CuMn_{1.8}Ni_{0.2}O_4$
CVD	Chemical vapor deposition
d10	Percentile value in cumulative PSD > 10% of the powder fraction
d50	Percentile value in cumulative PSD > 50% of the powder fraction
d90	Percentile value in cumulative PSD > 90% of the powder fraction
DLVO	Derjaguin-Landau-Verwey-Overbeek
EBSD	Electron backscatter diffraction
EDS	Energy-dispersive X-ray spectroscopy
EIS	Electrochemical impedance spectroscopy
ELD	Electrolytic deposition
EoL	End-of-Life
EoU	End-of-Use
EPD	Electrophoretic deposition
ESC	Electrolyte-supported cell
FESC	Fuel-electrode-supported cell
FSS	Ferritic stainless steel
FZJ	Forschungszentrum Jülich
GDC	Gadolinium-doped ceria
GD-OES	Glow discharge optical emission spectroscopy
HT-XRD	High-temperature X-ray diffraction
IEP	Isoelectric point
IET	Institute of Energy Technologies
IMD	Institute of Energy Materials and Devices
ITE	Institute of Technology and Engineering
IT-SOC	Intermediate-temperature solid oxide cell
LCA	Life cycle assessment
LCC	Life cycle costing
LCI	Life cycle inventory
LCSA	Life cycle sustainability assessment
LSC(F)	$(La,Sr)(Co(Fe))O_3$

LSCM	Laser scanning confocal microscope
LSM	$(La,Sr)MnO_3$
MCF	$MnCo_{1.9}Fe_{0.1}O_4$
MCO	$MnCo_2O_4$
MSC	Metal-supported cell
PCC	Proton-conducting cell
PEM	Proton exchange membrane
PMT	Photomultiplier tube
PSD	Particle size distribution
PVD	Physical vapor deposition
REO	Reactive element oxide
S-LCA	Social life cycle assessment
SE	Secondary electron
SEM	Scanning electron microscope
SRU	Single repeating unit
SSA	Specific surface area
TEM	Transmission electron microscope
TLR	Technology readiness level
TPB	Triple phase boundary
USB	Ultrasonic bath
WPS	Wet powder spraying
XRD	X-ray diffraction

Tables and Figures

Supporting Information

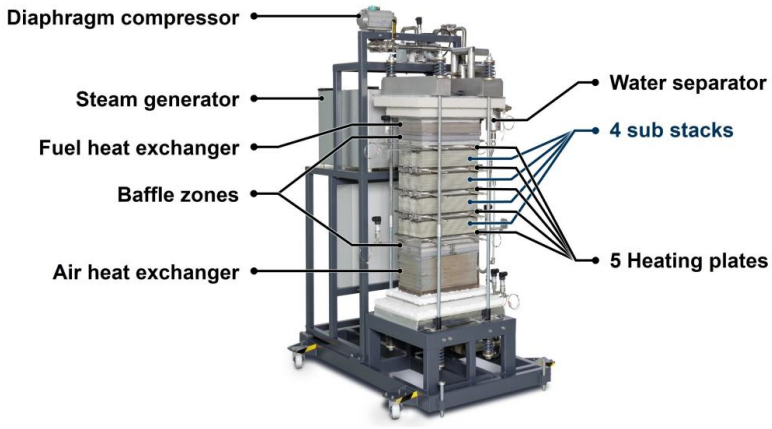

SI 1: Jülich rSOC system; © Forschungszentrum Jülich, IET-1. Photo: Ralf-Uwe Limbach.

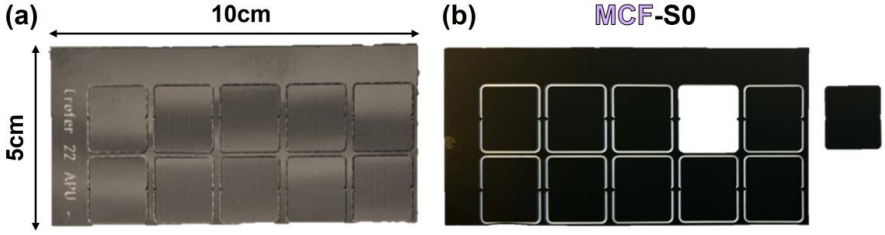

SI 2: Perforated Crofer22APU sheets, as established for exposure tests at Chalmers University of Technology; (a) prior to coating and (b) fully EPD-coated (MCF-S0).

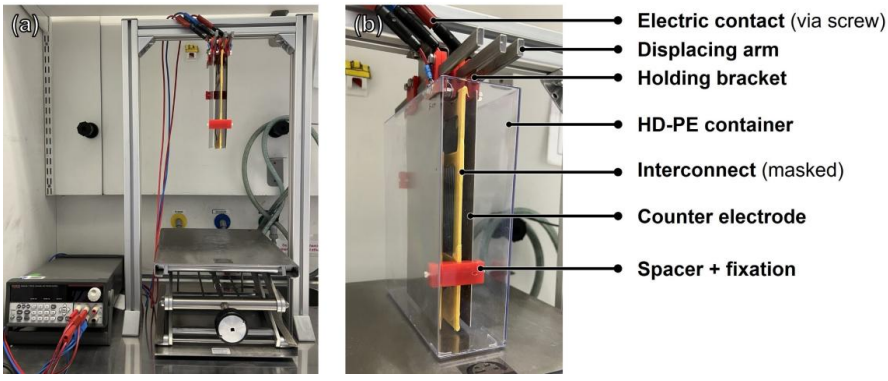

SI 3: Photograph of EPD up-scaling setup, as employed to coat real-size interconnect components; (a) Broad view displaying the entire setup with mounted electrodes and incorporating a masked F10 interconnect component, and (b) detailed view of the component-electrode-configuration, naming the main parts.

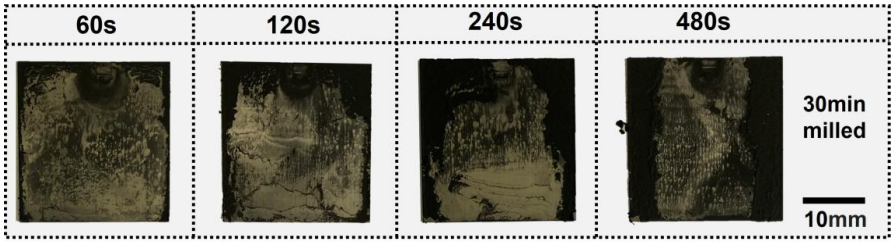

SI 4: EPD deposition time study with 30 min ball-milled MCF powder, using standard parameters. Photographs of sample surfaces after 60, 120, 240 and 480 s deposition time, showing overall poor deposition with pronounced "dog bone" effect.

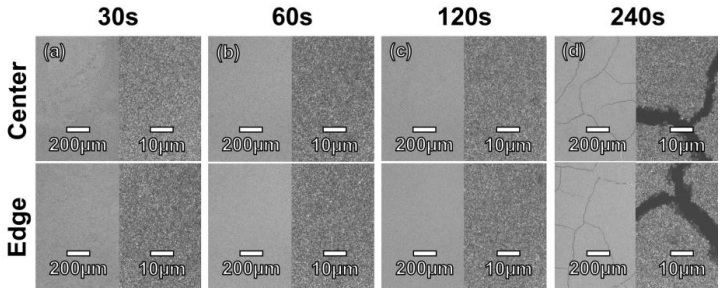

SI 5: LSCM images of EPD deposition study with 45 min ball-milled MCF powder; (a–d) Deposition over 30, 60, 120, and 240 s.

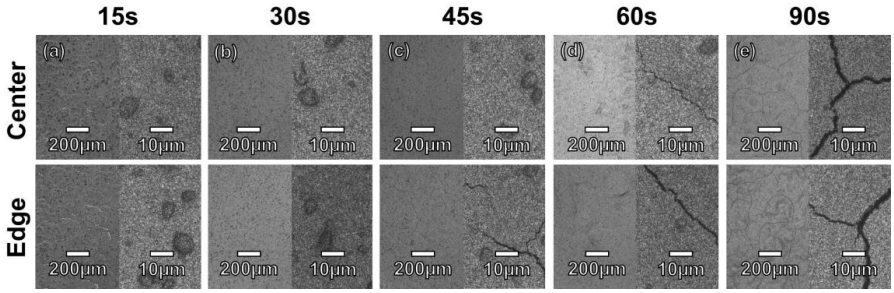

SI 6: LSCM images of EPD deposition study with 120 min ball-milled MCF powder; (a–e) Deposition over 15, 30, 45, 60, and 90 s.

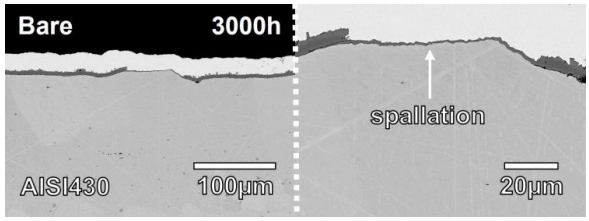

SI 7: SEM crosscuts of a non-coated AISI430 substrate after 3000 h exposure in air at 800°C showing oxide scale spallation and new scale formation.

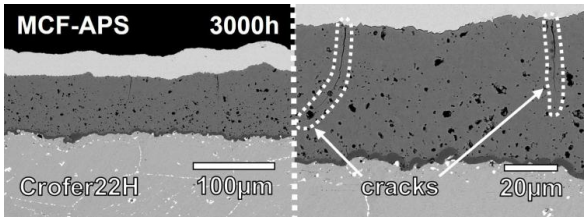

SI 8: SEM crosscuts of an MCF-APS-coated Crofer22H substrate after 3000 h exposure in air at 800°C showing macro-crack formation perpendicular to the coating.

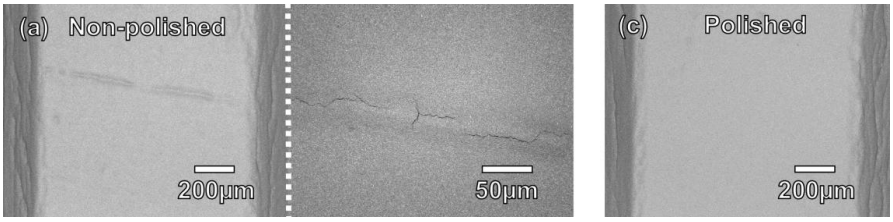

SI 9: Topographical LSCM images of EPD-MCF-coated F10 flow-field specimen (a) without and (b) with previous polishing step to enable crack-free coating formation and drying.

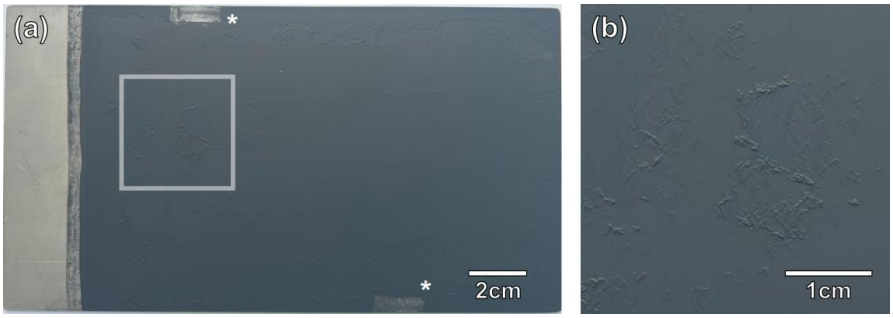

SI 10: Inhomogeneities on large-scale component (flat 20 cm × 10 cm steel plate) resulting in water-ethanol-based EPD process with MCF powder. *Positioning clamp imprints/masking marks.

Band / Volume 722
Combining Lattice Boltzmann Simulation and Synchrotron Imaging to Study Bubble Dynamics in Electrodes of Vanadium Redox Flow Batteries
K. Duan (2026), xxiii, 116 pp
ISBN: 978-3-95806-954-1 (Print)
ISBN: 978-3-95806-955-8 (E-Book)

Band / Volume 723
Geophysical characterization of landscapes along a climate and vegetation gradient in the Chilean coastal cordillera
I. Dal Bo (2026), 138 pp
ISBN: 978-3-95806-956-5 (Print)
ISBN: 978-3-95806-957-2 (E-Book)

Band / Volume 724
Model informed assessment of observation impact for emission rate optimization using four-dimensional variational data assimilation
A. Hermanns (2026), xvi, 109 Seiten
ISBN: 978-3-95806-958-9 (Print)
ISBN: 978-3-95806-959-6 (E-Book)

Band / Volume 725
Synthese und Bewertung hochaktiver Katalysatoren zur Herstellung höherer Alkohole aus Methanol als Kraftstoff
J. Häusler (2026), xiii, 265 Seiten
ISBN: 978-3-95806-962-6 (Print)
ISBN: 978-3-95806-963-3 (E-Book)

Band / Volume 726
Development and Characterization of Ni_3Fe Layered Double Hydroxide-Based Oxygen-Evolution Electrodes for Anion Exchange Membrane Water Electrolysis
I.Galkina (2026), vii, 173, xxxiii Seiten
ISBN: 978-3-95806-966-4 (Print)
ISBN: 978-3-95806-967-1 (E-Book)

Band / Volume 727
Surface Regeneration of Plasma-Facing Components by Wire-Based Laser Metal Deposition
J. Tweer (2026), XX, 186 pp
ISBN: 978-3-95806-970-1 (Print)
ISBN: 978-3-95806-971-8 (E-Book)

Band / Volume 728
Reducing the noble metal and titanium content of anode PTLs in PEM water electrolysis – performance and degradation
S. Zerressen (2026), XIII, 235 pp
ISBN: 978-3-95806-972-5 (Print)
ISBN: 978-3-95806-973-2 (E-Book)

Schriften des Forschungszentrums Jülich
Reihe Energie & Umwelt / Energy & Environment

Band / Volume 729
Gasfernleitungsnetze und deren Umstellung auf Wasserstoff
T. A. Triesch (2026), 364 pp
ISBN: 978-3-95806-978-7 (Print)
ISBN: 978-3-95806-979-4 (E-Book)

Band / Volume 730
Land-Atmosphere Coupling in a Changing Climate: Understanding Variability, Extremes, and Human Influence through Regional Climate Modeling
Y. Zhang (2026), 135 pp
ISBN: 978-3-95806-980-0 (Print)
ISBN: 978-3-95806-981-7 (E-Book)

Band / Volume 731
Abbildung gekoppelter Infrastrukturen in Energiesystemmodellen
P. Freitag (2026), XIX, 322 pp
ISBN: 978-3-95806-984-8 (Print)
ISBN: 978-3-95806-985-5 (E-Book)

Band / Volume 732
Cost-reduced and Sustainable Interconnects and their Coatings for Solid Oxide Cells
M. Hilger (2026), viii, 185 pp
ISBN: 978-3-95806-988-6 (Print)
ISBN: 978-3-95806-989-3 (E-Book)

Weitere ***Schriften des Verlags im Forschungszentrum Jülich*** unter
http://wwwzb1.fz-juelich.de/verlagextern1/index.asp

Energie & Umwelt / Energy & Environment
Band / Volume 732
ISBN 978-3-95806-989-3

Mitglied der Helmholtz-Gemeinschaft

JÜLICH
Forschungszentrum